Universidade de Aveiro Departamento de Física
2016

Seyedeh Pegah Mirzadeh Vaghefi

Estudo das Propriedades Estruturais e Físicas de Filmes e Heteroestruturas de Óxidos Multiferroicos

Structural and Physical Properties Studies on Multiferroic Oxide Films and Heterostructures

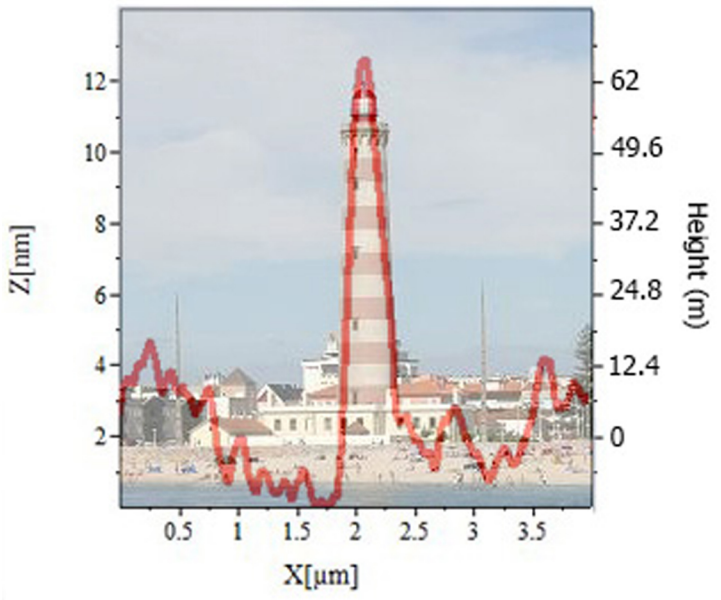

Universidade de Aveiro Departamento de Física
2016

Seyedeh Pegah Mirzadeh Vaghefi

Estudo das Propriedades Estruturais e Físicas de Filmes e Heteroestruturas de Óxidos Multiferroicos

Structural and Physical Properties Studies on Multiferroic Oxide Films and Heterostructures

Tese apresentada à Universidade de Aveiro para cumprimento dos requisitos necessários à obtenção do grau de Doutor em Engenharia Física, realizada sob a orientação científica do Doutor Vítor Brás de Sequeira Amaral, Professor catedrático do Departamento de Física da Universidade de Aveiro e co-orientação do Doutor Joaquim Agostinho Gomes Moreira, Professor Auxiliar do Departamento de Física e Astronomia, Faculdade de Ciencias da Universidade do Porto.

Apoio financeiro da FCT e do FSE no âmbito do III Quadro Comunitário de Apoio.

COMPETE 2020 PROGRAMA OPERACIONAL COMPETITIVIDADE E INTERNACIONALIZAÇÃO
PORTUGAL 2020
UNIÃO EUROPEIA Fundo Europeu de Desenvolvimento Regional
FCT Fundação para a Ciência e a Tecnologia MINISTÉRIO DA EDUCAÇÃO E CIÊNCIA
universidade de aveiro theoria poiesis praxis

To Ali, who made my dreams come true.

o júri / the jury

presidente / president

Professor Doutor Rui Luís Andrade Aguiar
Professor Catedrático, Departamento de electrónica, telecomunicaçãoes e informática, Universidade de Aveiro

vogais / examiners committee

Professor Doutor Vítor Brás de Sequeira Amaral
Professor Catedrático, Departamento de Física, Universidade de Aveiro

Professora Doutora Maria Margarida da Fonseca Beja Godinho
Professora Catedrático, Departamento de Fisica, Faculdade de Ciências, Universidade de Lisboa

Professor Doutor Andrei Leonidovitch Kholkin
Investigador Coordenador, Laboratorio Associado CICECO e Departamento de Física, Universidade de Aveiro

Professor Doutor Pedro Manuel de Melo Bandeira Tavares
Professor Associado, Departamento de Quimica, Universidade de Tras os Montes e Alto Douro

Professor Doutor João Pedro Esteves de Araújo
Professor Auxiliar, Departamento de Fisica e Astronomia, Faculdade de Ciencias da Universidade do Porto

Professor Doutor Armando António Cardoso dos Santos Lourenço
Professor Auxiliar, Departamento de Fisica, Universidade de Aveiro

Professor Doutor Bernardo Gonçalves Almeida
Professor Auxiliar, Departamento de Fisica, Escola de Ciencias, Universidade do Minho

agradecimentos /
acknowledgements

First I want to thanks my advisor professor Vítor Brás Sequeira Amaral, who has been a tremendous mentor for me. He has taught me, both consciously and unconsciously, how good experimental physics is done. I appreciate all his contributions of time, ideas, and funding to make my Ph.D. experience productive and stimulating. The joy and enthusiasm he has for her research was contagious and motivational for me, even during tough times in the Ph.D. pursuit. I would like to acknowledge his patience and helpful comments, which had major impact on my work.

I would like to thanks my co-advisor, professor Joaquim Agostinho Gomes Moreira, for being the best co-advisor. His helps for giving me the chance to visit several schools and conferences made my confidence to work harder in this field.

My sincere thanks for professor Armando António Cardoso dos Santos Lourenço for his great help, teaching all about the sputtering and helping me to prepare the thin films and heterostructures.

The members of the magnetic group, who had contributed immensely to my personal and professional time. The group has been a source of friendship as well as good advice and collaboration. I am especially grateful to João for his enthusiasm, his pure friendship and his guidance in magnetic discussion, during this period.

Other past and present group members that I had pleasure to work with or alongside of are João Nuno, Tiago, Maria João, Carlos, Amin and Farzin. I enjoyed the atmosphere, their sincere friendship and their support.

Special thanks to Nuno Fortunato, for being a great supporter and also teaching me the LATEX.

Many thanks to Fábio, Maxim Ivanov and Dzmitry Karpinski (Karpinsky) for their motivations and giving me the knowledge for force microscopy techniques.

Many thanks to Luis Gomes for his endless help for magnetoresistance measurements and teaching me working with LabView.

Many thanks to Dra. Maria do Rosário Teixeira Soares for her help on XRD subject.

My endless thanks for Dr. Eduardo Alves, from Instituto de Plasmas e Fusão Nuclear, Laboratório de Aceleradores e Tecnologias de Radiação, for his help on RBS measurements in a very short notice and his invaluable comments, on the structure of the film.

Special thanks to Dr. Marc George Willinger, for his interesting and fruitful discussions and for the great collaboration on HRTEM and for the cool time I had spent in his group, in Fritz-Haber institute, Berlin, especially grateful thanks to Eng. Achim Klein-Hofmann for his patience and kind behaviour, and for teaching me sample preparation method for electron microscopy and all his helps and supports, since 3 years ago.

agradecimentos /
acknowledgements

And my special thanks to the electron microscopy group of university of Aveiro for their help and patience during last years. Exclusively, professor Joaquim Manuel Vieira for his valuable discussions over (La,Sr)MnO_3 thin films. His points of view on growth mechanism of films gave my thesis a step higher level. Also his moral support of my family, during these years was a unique support.

I would also like to acknowledge the staffs and technicians of physics department, especially Sr. Francisco Reis to help me about technical problem, very often with my computer.

I gratefully acknowledge the funding sources that made my Ph.D. work possible. I was funded by several project fellowship, including "Multifox: Modificação e estudo à escala nanomética de óxidos multiferróicos" (PTDC/FIS/105416/2008), "Experiências de Correlações Angulares Perturbadas e de Canalização de Electrões no ISOLDE-CERN –Investigação aplicada a materiais con técnicas nucleares, formmação e desenvolvimento (CERN/FP/123585/2011), "HEAT@UA" (RECI/CTM-CER/0336/2012) and "Multiferroic materials: Study and modification of properties" (BI/UI89/5758/2012). This work was developed within the scope of the project CICECO-Aveiro Institute of Materials, POCI-01-0145-FEDER-007679 (FCT Ref. UID /CTM /50011/2013), financed by national funds through the FCT/MEC and when appropriate co-financed by FEDER under the PT2020 Partnership Agreement. My time at Universidade de Aveiro was made enjoyable in large part due to the many friends and groups that became a part of my life.

I would like to thank my family for all their love and encouragement. For my parents who raised me with a love of science and supported me in all my pursuits. For the moral support of my brothers and their families, my whole life.

And at the last, but for sure the most, my sincere and special thanks to my husband, Ali, who is not only a great company in life, but the best colleague, one can dream. His help on electron microscopy was a valuable asset, which will stay with me whole life. His help in making the thesis ready for submission was invaluable help. His patience and kindness helped me through past years and his presence was a full-time energy source for me.

Palavras Chave

Materiais Multiferroicos, Filmes finos, Heterostructure, Manganitas, Magnetization, Magneto-resistência, Microscopia de ponta, Microscopia electrónica.

Resumo

O presente trabalho de doutoramento é um estudo de propriedades físicas e aspectos estruturais de filmes de óxidos e heteroestruturas multiferróicas, englobando técnicas de caracterização do nível macroscópico ao microscópico. O objectivo principal é a compreensão de novas heteroestruturas epitaxiais multifuncionais e as suas interfaces para junções de túnel magnetoelétricas e filtros de spin.

Os principais materiais em estudo foram manganitas à base de La dopadas com iões divalentes (ba, Sr), apresentando efeito magnetoelétrico, sendo preparadas em diferentes substratos e diferentes técnicas de crescimento, optimizadas para epitaxia e qualidade de interface. O estudo combinado de propriedades eléctricas e magnéticas permitiu estabelecer as condições necessárias para a aplicação dos materiais multiferróicos em estudo, por técnicas experimentais apresentadas neste trabalho.

O trabalho consistiu no estudo sistemático de microestrutura de filmes finos de $La_{0.7}Sr_{0.3}MnO_3$ em substratos de $SrTiO_3$, preparados por pulsed laser deposition, o filme fino de $La_{0.9}Ba_{0.1}MnO_3$ e a heteroestrutura $La_{0.9}Ba_{0.1}MnO_3/BaTiO_3/La_{0.9}Ba_{0.1}MnO_3$ em substrato de Al_2O_3, e filme fino de $La_{0.9}Ba_{0.1}MnO_3$, $BaTiO_3$ e heteroestrutura de $La_{0.9}Ba_{0.1}MnO_3/BaTiO_3/La_{0.9}Ba_{0.1}MnO_3$ em substrato de Si, preparado por RF magnetron sputtering. A caracterização estrutural das amostras foi feita principalmente por difracção de raio-X (XRD) convencional e de alta resolução e Microscopia de Transmissão de Alta Resolução (HRTEM). A composição química foi analisada por Electron Dispersion Spectroscopy (EDS), Rutherford backscattering spectroscopy (RBS) e energy filtered transmission electron microscopy (EFTEM). As medidas de magnetização forram realizada com a um magnetómetro superconducting quantum interference device (SQUID). A análise da topografia e efeitos locais foi realizada por microscopia de varimento de ponta usando microscopia da Força Atómica (AFM) e de resposta piezoeléctronica (PFM).

Os resultados mostram claramente uma evolução da microestrutura dos filmes finos de $La_{0.7}Sr_{0.3}MnO_3$, á medida que aumenta a sua espessura, passando de uma estrutura policristalina no filme mais fino (13.5 nm) a colunar inclinado (45 nm e 200 nm), a uma estrutura ramificada no filme mais espesso (320 nm). A alteração na estrutura do filme é devida à tensão pelo substrato e deformação da estrutura nas etapas iniciais de crescimento, onde se detectaram fronteiras anti-phase e maclas. A evolução da estrutura modificou as propriedades magnéticas dos filmes a baixa temperatura (abaixo da temperatura de transição estrutural do substrato de $SrTiO_3$), mostrando magnetização em excesso e defeito, para espessuras abaixo e acima de 100 nm, respectivamente. Análises STEM-EELS e EFTEM mostraram a diferença em composição elementar dos filmes perto das fronteiras e na interface com o substrato.

Resumo

No âmbito do plano de trabalhos de doutoramento, o segundo substrato consiste em estudar as propriedades físicas e estruturais de filmes finos de $La_{0.9}Ba_{0.1}MnO_3$ e heteroestruturas $La_{0.9}Ba_{0.1}MnO_3/BaTiO_3/La_{0.9}Ba_{0.1}MnO_3$ em substratos de Al_2O_3, revelando estruturas altamente orientadas. A razão La/Ba do filme e heteroestrutura é drasticamente diferente do alvo providenciado, $La_{0.7}Ba_{0.3}MnO_3$, como provado por XRD, RBS e transições de fase magnéticas. As propriedades magnéticas e eléctricas das estruturas mostraram uma forte dependência na cristalinidade do filme e da heteroestrutura.

A parte final do trabalho é dedicada aos filmes de $La_{0.9}Ba_{0.1}MnO_3$, $BaTiO_3$ e a heteroestrutura de $La_{0.9}Ba_{0.1}MnO_3/BaTiO_3/La_{0.9}Ba_{0.1}MnO_3$ em substrato de Si, que em comparação com as estruturas em substrato de ALO, provaram o efeito da cristalinidade nas propriedades magnéticas, eléctricas e de magneto-resistência do filme e heteroestrutura. Foi mostrado que um grau superior de cristalinidade leva a uma mais elevada magnetização, reduzindo a resistividade das estruturas.

Pela primeira vez, um estudo de deformação de topografia por aplicação de uma tensão dc externa foi feito num filme fino de $BaTiO_3$ em Si, usando uma técnica de poling num microscópio de força piezoresponse. Os resultados mostraram a capacidade de uma modificação controlada da superfície, por aplicação de uma voltagem externa nointervalo 14V < V_{app} < 20V. Abaixo destes valores, não se observou alguma deformação na topografia, enquanto acima deste intervalo, a 30V, a superfície foi completamente danificada. A mudança topográfica produzida mostrou estabilidade no tempo, onde após a aplicação de 20V, a área modificada alcançou 83$\%$ da altura as-poled ($\sim$9 nm) em 90 minutos, a 7,4 nm. A resposta assimétrica de piezoresponse da área poled foi associada à existência de um campo eléctrico interno na amostra, que foi também provado através de medidas de espectroscopia de switching no filme fino. A heteroestrutura no substrato de Si mostraram o mesmo fenómeno que a mono-camada de $BaTiO_3$, onde o arranjo de heteroestrutura realça o efeito de voltagem aplicada na topografia. Aplicando 10V, a estrutura da superfície foi alterada na heteroestrutura e houve uma modificação visível da camada de $BaTiO_3$, alterando também a topografia da camada superior de $La_{0.9}Ba_{0.1}MnO_3$.

Keywords Multiferroic materials, Thin films, Heterostructure, Manganites, Magnetization, Magnetoresistance, Probe microscopy, Electron microscopy.

Abstract

This present PhD work made a study of structural aspects and physical properties of the oxide films and multiferroic heterostructures, encompassing the techniques from macroscopic level to microscopic description. The understanding of novel multifunctional epitaxial heterostructures and their interfaces for magneto-electrically driven tunnel junctions and spin-filters is the central objective. The main materials in study were La based doped manganites with magnetoelectric effect prepared on different substrates and growth conditions, optimized for epitaxy and interface quality. The combined study of electric and magnetic properties allowed us examining the conditions required for application of the studied multiferroic materials and experimental techniques are presented in this work.

The work consists of three main substrates, a systematic study of microstructure of $La_{0.7}Sr_{0.3}MnO_3$ thin films on $SrTiO_3$ substrate, prepared by pulsed laser deposition, the $La_{0.9}Ba_{0.1}MnO_3$ thin film and $La_{0.9}Ba_{0.1}MnO_3/BaTiO_3/La_{0.9}Ba_{0.1}MnO_3$ heterostructure on Al_2O_3 substrate, and the $La_{0.9}Ba_{0.1}MnO_3$ thin film, $BaTiO_3$ and $La_{0.9}Ba_{0.1}MnO_3/BaTiO_3/La_{0.9}Ba_{0.1}MnO_3$ heterostructure on Si substrate, prepared by RF magnetron sputtering.

Main structural characterization of samples was performed by conventional and high resolution X-Ray Diffraction (XRD), High Resolution Transmission Electron Microscopy (HRTEM); chemical composition was determined by Electron Dispersion Spectroscopy (EDS), Rutherford Backscattering Spectroscopy (RBS) and Energy Filtered Transmission Electron Microscopy (EFTEM); Magnetization measurements done with a Superconducting Quantum Interface Device (SQUID) magnetometer. Surface probing of topography and local effects was performed, using Atomic Force (AFM) and Piezo-Response (PFM) Microscopy.

Results clearly showed that there is an evolution in the microstructure of the $La_{0.7}Sr_{0.3}MnO_3$ thin films, by increasing their thickness, changing from polycrystalline structure in the thinnest film (13.5 nm) to tilted columnar structure(45 nm and 200 nm) and to a branched structure in the thickest film (320 nm). The change in the structure of the film is due to the strain from the substrate and deformation of the structure in the early stages of the growth, where anti-phase boundaries and twinning were detected. The evolution of the structure modified the low temperature (below structural phase transition of $SrTiO_3$ substrate) magnetic properties of the films, showing in-excess and in-defect magnetization, below and above 100 nm thickness, respectively. Also, STEM-EELS and EFTEM analysis showed the difference in the elemental composition of the films near the boundaries and interface with the substrate.

Abstract

In the scope of the PhD work plan, the second substrate consists of studying the structural and physical properties of $La_{0.9}Ba_{0.1}MnO_3$ thin film and $La_{0.9}Ba_{0.1}MnO_3/BaTiO_3/La_{0.9}Ba_{0.1}MnO_3$ heterostructure on Al_2O_3 substrate, where they showed highly oriented structure. The La/Ba ratio of the single layer film and heterostructure is drastically different from the target, $La_{0.7}Ba0.3MnO_3$, proven by XRD, RBS, and magnetic phase transitions. The magnetic and electrical properties of the structures showed strong dependence on the crystallinity of the samples.

The final part of the work is devoted to the $La_{0.9}Ba_{0.1}MnO_3$ and $BaTiO_3$ thin films and $La_{0.9}Ba_{0.1}MnO_3/BaTiO_3/La_{0.9}Ba_{0.1}MnO_3$ heterostructure on Si substrate, which in comparison with the structures on Al_2O_3 substrate, highlights the influence of crystallinity on magnetic, ferro-electrical and magnetoresistance properties of the film and heterostructure. It is shown that higher degree of crystallinity leads to higher magnetization and lowers the resistivity. For the first time, a study of the topography deformation by applying a dc-external voltage was done on $BaTiO_3$ thin film on Si, using a poling technique in a piezoresponse force microscope. The results show the ability of controlled modification of the surface, by applying an external voltage/electric field in the range of 14V< V_{app}<20V. Below this range, no deformation is observed on the topography, and above this interval, at 30V, the surface is completely damaged. The produced topographical change show stabilization in respect to time, where after applying 20V, the modified area reaches its 83$\%$ of the as-poled height ($\sim$9nm) in 90 minutes, to 7.4 nm. The asymmetrical response in the piezoresponse of the poled area is related to the existence of an internal built-in electric field in the sample, which is also confirmed by performing switching spectroscopy measurements on the single layer. The heterostructure on the Si substrate shows the same phenomena, as the BTO single layer, where the heterostructure arrangement enhances the applied voltage effect on the topography. With applying 10V, the structure of the surface changes in the heterostructure and a visible modification of $BaTiO_3$ layer, changing also the topography of $La_{0.9}Ba_{0.1}MnO_3$ top layer is observed.

الا یا ایها الساقی، ادر کاسا و ناولها

که عشق آسان نمود اول، ولی افتاد مشکل‌ها

شب تاریک و بیم موج و گردابی چنین هایل

کجا داند حال ما، سبکباران ساحل‌ها

Contents

List of Figures

List of Tables

Symbols

M_r	Remanent magnetization
M_s	Saturation magnetization
H_c	Coercive field
T_c	Curie Temperature
t_0	Inter-site hopping interaction
μ_B	Bohr magneton
k_B	Boltzmann's constant
δ	Oxygen deficiency
Δf	frequency shift
g	Landé g-factor
D_n	Dielectric displacement vector
T_{kl}	Second-rank stress tensor
d_{nkl}	Third-rank tensor of piezoelectric coefficient
ϵ_{nm}^T	Dielectric permittivity at constant stress
E_m	Electric field vector
d_{33}	z-direction strain of piezoelectric tensor
E_c	Electric coercive field
d_{hkl}	Interplanar distance
μ	Magnetic moment
ϵ	Electromotive force
ρ	Resistivity
F	Shape correction factor

a	Lattice mismatch
Y	Sputter yield
t	Goldschmidt tolerance factor
$r_{A,B}$	Ionic radii
τ	Mean size of crystallite domain

Abbreviations

RE	Trivalent rare-earth ion
AL	Divalent alkaline-earth ion
MR	magentoresistance
CMR	Colossal magnetoresistance
TMR	Tunnelling magnetoresistance
GMR	Giant magnetoresistance
SCES	Strongly correlated electron system
RF	Radio frequency
PLD	Pulsed laser deposition
MTJ	Magnetic tunnel junction
fcc	Face centred cubic
MR	Magnetoresistivity
LSMO	$La_{0.7}Sr_{0.3}MnO_3$
LBM	$La_{0.9}B_{0.1}MnO_3$
LBMBT	$La_{0.9}B_{0.1}MnO_3/BaTiO_3/$ $La_{0.9}B_{0.1}MnO_3$
BTO	$BaTiO_3$
STO	$SrTiO_3$
CA	Citric acid
APB	Anti phase boundary
PM	Paramagnetic
SR	Short-range oeder
FM	Ferromagnetic
PM	Paramgnetic

PS	Phase seperated
CVD	Chemical vapour deposition
PVD	Physical vapour deposition
ICDD	International centre for diffraction data
XRD	X-Ray diffraction
XRR	X-ray reflectometry
FWHM	Full width half maximum
RBS	Rutherford backscattering spectroscopy
SPEM	Scanning probe microscopy
AFM	Atomic force microscopy
PFM	Piezoresponse force microscopy
PR	Piezoresponce
RMS	Root mean square
TEM	Transmission electron microscopy
HRTEM	High resolution transmission electron microscopy
DF	Dark field
BF	Bright field
SAED	Selected area electron diffraction
FRAM	Ferroelectric non-volatile random access memory
EDS	Energy dispersive X-Ray Spectroscopy
STEM	Scanning transmission electron microscope
HAADF	High angle angular dark field
EELS	Electron Energy Loss Spectroscopy
FFT	Fast Fourier Transform
EFTEM	Energy Filtered Transmission Electron Microscopy
SQUID	Superconducting Quantum Interface Device
VSM	Vibrating sample magnetometry
ZFC	Zero-field cooled
FC	Field cooled

Chapter 1

Introduction

In perovskite $RE_{1-x}AL_xMnO_3$ manganites (RE: trivalent rare-earth, AL: divalent alkaline-earth ions) the coupling between lattice, spin, charge and orbital degrees of freedom led to discovery of colossal magnetoresistance (CMR) [1] and multiferroic behaviour [2]. The existence of electric and magnetic order, simultaneously, gives rise to electrically controlled magnetocrystalline anisotropy [3, 4, 5, 6], exchange bias [7, 8] and spin transport [5, 9, 10]. The aforementioned phenomenon can be tuned by external parameters such as pressure, magnetic/electric fields and radiation [11]. In particular, many researches have been shown that their electrical (resistivity, magnetoresistance, magnetocapacitance), magnetic (anisotropy, Curie temperature) and structural properties can be modified by imposing lattice strains on the samples [11, 12].

In thin films, strains are usually present due to lattice mismatch between film and substrates, with various thicknesses, on different types of substrate [13]. However, this is not the only parameter that induces the strain. Other variables affecting oxide thin film properties can be: oxygen stoichiometry, crystalline quality, changes in composition at the interfaces and lattice relaxation [14, 15, 16].

1.1 Thesis outline

This thesis presents the work developed in the past years, with the goal of structural characterization and optimization of the structure in manganite thin films and heterostructures. It is organized by the influence of single crystal substrates, $SrTiO_3$, Al_2O_3 and Si substrate. In this context, the thesis is outlined as follows:

- In chapter 1 the motivation of this work is mentioned, along with the thesis outline.
- In chapter 2 a brief review of the fundamental concepts is discussed, regarding the multiferroic manganites, as well as thin films and heterostructures.

- In chapter 3 the experimental techniques used in the production of structures and their structural, magnetic and transport characterization are presented. The method for preparing the ceramics used in pulsed laser ablation, as well as the deposition techniques, pulsed laser deposition and RF magnetron sputtering, are also described. The structural characterization techniques (X-ray diffraction, transmission electron microscopy, energy dispersive X-ray spectroscopy, Rutherford backscattering spectroscopy) are briefly reviewed. The methodology and the experimental setups for the electrical resistivity, magnetoresistance measurements, atomic and piezoresponse force microscopy and SQUID magnetometry are also described.
- Chapter 4 summarizes the high resolution transmission electron microscopy studies of $La_{0.7}Sr_{0.3}MnO_3$ thin films deposited on $SrTiO_3$ substrate. The structural properties of the films, and the influence of the microstructure on the magnetic properties of the produced films are assessed.
- In chapter 5 the deposition and microstructure of $La_{0.9}Ba_{0.1}MnO_3$ and $La_{0.9}Ba_{0.1}MnO_3$ / $BaTiO_3$ / $La_{0.9}Ba_{0.1}MnO_3$ (LBMBT) heterostructure on Al_2O_3 substrate are reviewed. The magnetic and magnetoresistance properties and surface properties of the film and heterostructure are also discussed.
- In chapter 6 the structure of $La_{0.9}Ba_{0.1}MnO_3$ and $BaTiO_3$ thin films and $La_{0.9}Ba_{0.1}MnO_3$ / $BaTiO_3$ / $La_{0.9}Ba_{0.1}MnO_3$ heterostructure on Si substrate are studied. Furthermore, the physical properties of the films and heterostructure have been investigated and compared with structures on Al_2O_3 substrate.
- In chapter 7 the modification of the surface/structure by applying local voltages of $BaTiO_3$ thin film and $La_{0.9}Ba_{0.1}MnO_3$ / $BaTiO_3$ / $La_{0.9}Ba_{0.1}MnO_3$ heterostructure is described.
- In chapter 8 the main conclusions of this work are presented, as well as an outlook toward the work to be carried out in the future. Some concrete ideas and lines of investigations, as well as the motivation to pursue them are proposed.

Chapter 2

Fundamental concepts

The increasing attention in the study of the strongly correlated electron systems (SCES) lead to more research on this category of materials. The main interest in this type of materials is the possibility of controlling the electrical currents through applying a magnetic field, which results in spintronics industry [2]. Multiferroic materials have been studied, extensively, for their significant magnetoelectric effects [17, 18]. Rare-earth manganites and transition metal oxides, such as high T_c superconductors and CMR manganites, are examples of SCES [17, 18, 19]. The degree of correlation can be controlled by the crystal structure in perovskite oxides with the formula of (RE,AL)MnO_3, where RE and AL stand for rare earth and alkaline earth elements, respectively. In these manganites, the size of the substitutional ions, as well as the amount of the dopants, can determine the main properties of the manganite compounds.

2.1 Multiferroic materials

Complex oxides represent a broad class of materials that have a wide range of crystal structures and functionalities. Among them the study of magnetic, ferroelectric, and multiferroic properties has considerable attention. The study of multiferroic and magnetoelectric materials has been developed by the emerging thin film growth techniques, radio frequency (RF) Sputtering and Pulsed Laser Deposition (PLD). The most interesting manifestation of functional oxide materials is the emergence of the coupled behaviour, in which the lattice, orbital, spin, and charge degrees of freedom are coupled through engineering design of artificial heterostructures or quantum mechanism [20].

In accordance with the original definition of multiferroicity [21], multiferroics are a class of materials which combines two or more ferroic order, i.e. ferroelectricity, ferromagnetism, ferrotoroidicity or ferroelasticity [22].

Table 2.1: The four primary ferroic classes of materials.

	Orientation states	Switching force	Example
Ferroelectric	Spontaneous polarization (P)	Electric field (E)	$BaTiO_3$
Ferroelastic	Spontaneous strain (S)	Mechanical stress (T)	$Au_xCu_{1-x}Zn$
Ferromagnetic	Spontaneous magnetization (M)	Magnetic field (H)	Fe_3O_4
Ferrotoroidic	Spontaneous toroidial moment	Toroidial moment	A solenoid in the form of a torus with an even number of windings

Table 2.1 shows the four primary ferroics [23]. On the other hand, magnetoelectric coupling can, but need not, exist in ferroic order of the material, for example it can occur in paramagnetic ferroelectric.

In present work, we focus on materials which combines the magnetic order with ferroelectricity. Therefore in following pages multiferroics are a class of materials which brings the spontaneous long-range magnetic and dipolar orders together and represent an attractive class of compounds, combining rich fundamental physics and technologically appealing potential for applications in spintronics and magnetic tunnel junctions (MTJ).

Most of the early works on multiferroic materials were done on structural magnetic ferroelectrics, to identify mechanisms for ferroelectricity, compatible with simultaneously magnetic order. Also, conventional ferroelectrics, such as $BaTiO_3$, show hybridization effects between the filled oxygen p states and unfilled transition metal d states that are essential for the structural instability, leading to ferroelectricity [24].

The required overlap of ferroic materials to be in the classification of multiferroic is shown schematically in Figure 2.1. Only a small subgroup of all magnetically and electrically polarizable materials are either ferromagnetic or ferroelectric and even smaller subgroup simultaneously shows both order parameters [25].

2.1.1 Crystallographic structure

The oxide perovskite structure of simple ABO_3 is a face centred cubic (fcc), with $Pm\bar{3}m$ symmetry, where A-ion is located in corner of the cube, in the (0,0,0) position, while the B-ion is octahedrally coordinated by oxygen ions, located in $(\frac{1}{2},\frac{1}{2},\frac{1}{2})$. The oxygen atoms form an FCC-like cell with atoms missing from the corners which are occupied by A-atoms (see Figure 2.2). Replacing the B-ion position by a mixed-valence state Mn^{3+}/Mn^{4+}, and by substituting the A-cation, a large number of perovskite-like

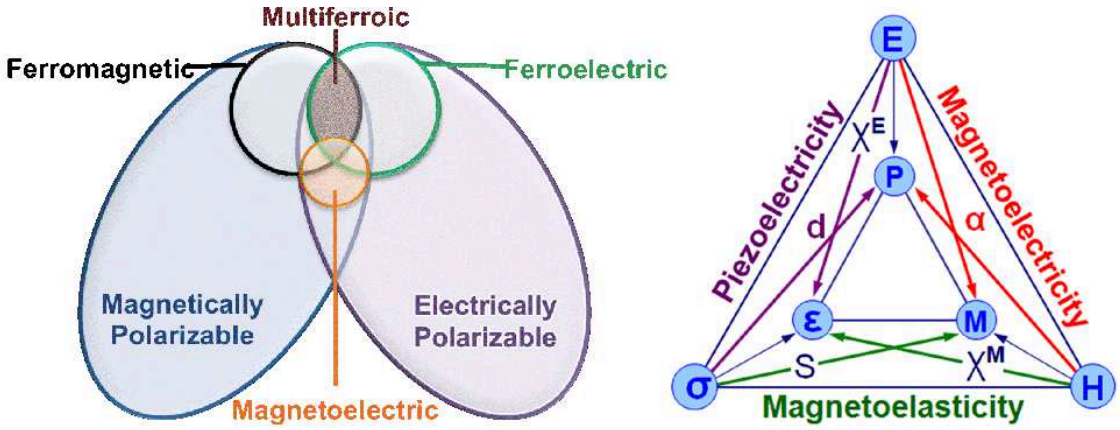

Figure 2.1: (Left) Relationship between multiferroic and magnetoelectric materials (adapted from [23]). (Right) Schematic illustrating different types of coupling present in materials. Much attention has been given to materials where electric and magnetic order is coupled (adapted from [26]).

oxides with different structures and physical properties can be obtained [27]. For the stoichiometric oxide, the ratio of Mn^{3+}/Mn^{4+} is equal to (1-x)/x. Perovskite-type structure can be stabilized in distorted symmetries such as orthorhombic, rhombohedral, tetragonal and hexagonal. The stabilization of the structure is determined by the Goldschmidt tolerance factor that depends on the A and B ionic radii, r_A and r_B, and on the oxygen ionic radius, r_O [28]:

$$t = \frac{r_A + r_O}{\sqrt{2}(r_B + r_O)}. \tag{2.1}$$

In the ideal cubic perovskite structure, t=1, e.g. in strontium titanate ($SrTiO_3$) [29]. However, as the value differs from 1, internal stress increases and the cubic lattice becomes unstable. The common perovskite-type compounds usually exhibit tolerance factor of 0.78<t<1.05 [30]. For manganites at low temperature, a rhombohedral or orthorhombic structure is more probable, which varies t appreciably different from 1.

For t<1, that is the small misfit between the sizes of B and O ions, the MnO_6 octahedra cooperatively rotate, giving rise to a rombohedral distortion [32]. This type of distortion is characteristic of $La_{0.67}Sr_{0.33}MnO_3$ (LSMO).

The distortions of the cubic perovskite can lead to dramatic changes in the properties of manganites. For instance, the Curie temperatures of two lanthanum manganites at the same doping level, but with different A-site doping is the influence of the tolerance factor on these materials. While $T_C \approx 370$ K for the distorted $La_{0.67}Sr_{0.33}MnO_3$, $La_{0.67}Ba_{0.33}MnO_3$ has $T_C \approx 340$ K, which has lower tolerance factor, as can be seen in Figure 2.3).

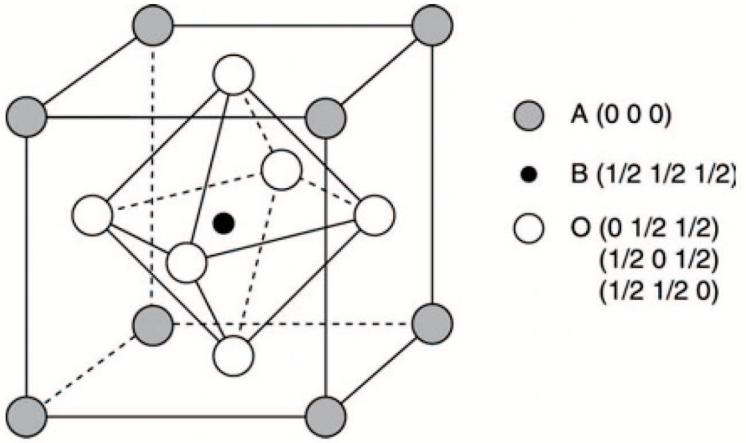

Figure 2.2: Scheme of a perovskite cubic-crystalline ABO_3 structure, with A (0,0,0), B $(\frac{1}{2},\frac{1}{2},\frac{1}{2})$ and O at $(\frac{1}{2},0,0)$ position, adapted from [31].

2.1.2 Antiphase boundary

Antiphase boundaries (APBs) are the displacement boundaries within a crystal. The vector R, parallel to the boundary is the crystallographic operator, which generates an APB, specifying the displacement of one part with respect to the other, Figure 2.4).

Antiphase boundaries in cubic close-packed metal crystals arise as a result of the movement of a partial dislocation, where the cubic close-packed metal atom stacking sequence ...ABCABCABC... is disordered to give a sequence ...ABC**AC**ABC... where the antiphase boundary lies between the layers in bold type [34].

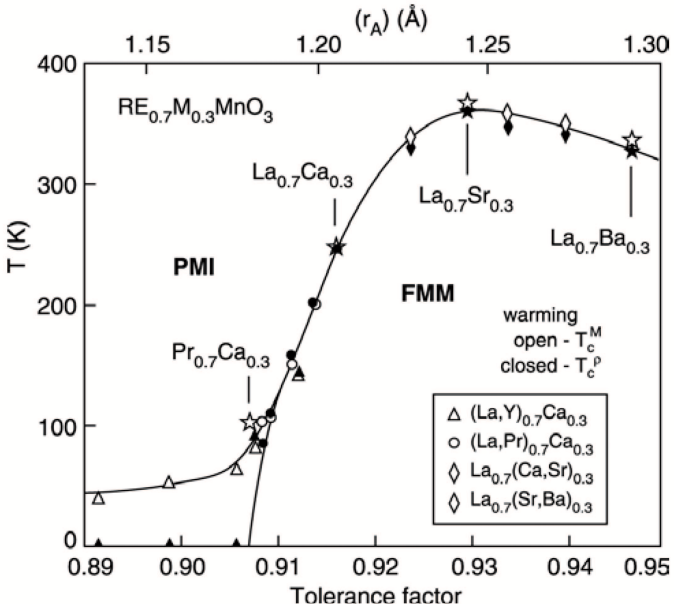

Figure 2.3: Phase diagram of Curie temperature vs. tolerance factor and average AL cation size for the $RE_{0.7}AL_{0.3}MnO_3$ system [33].

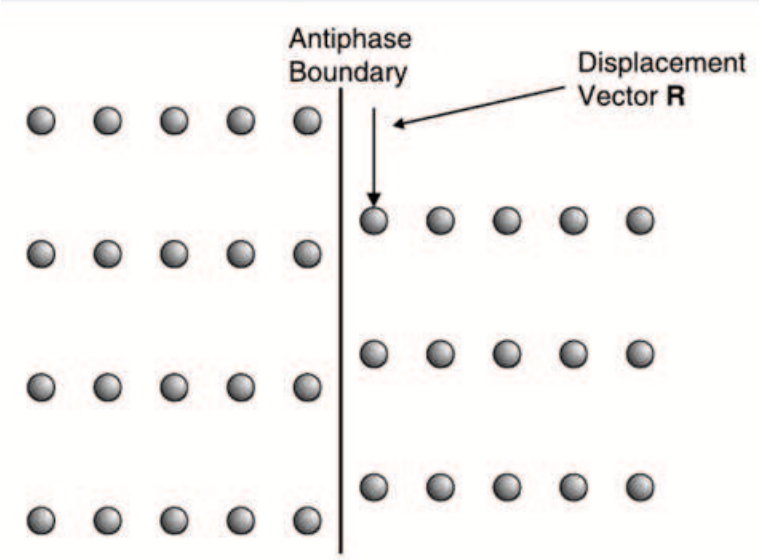

Figure 2.4: Schematic of antiphase boundary, formed when one part of a crystal is displaced with respect to the other part by a vector parallel to the boundary [34].

2.2 Ferromagnetism

The origin of magnetism lies in the orbital and spin motions of electrons and the way that electrons interact with one another. The best manifestation of magnetism in solids is the spontaneous magnetization of ferromagnetic materials, which is due to the alignment of magnetic moments on atomic scale inside the lattice, and exists even in absence of an applied magnetic field. Magnetization is defined as the magnetic dipole moment per unit volume of material.

The hysteresis loop of a ferromagnet is shown in Figure 2.5), initially in an unmagnetized state. Magnetization appears as the sample is imposed by magnetic field, H. The hysteresis loop combines information on an intrinsic magnetic property, M_s, exist in magnetic domain and two extrinsic properties; remanent magnetization, M_r and coercive field, H_c, depending on different factors, such as sample shape, surface roughness, microscopic defects and thermal history [35]. The phrase "hard magnetic materials" refers to materials that show broad M(H) loops i.e. having high coercivity, once saturated in magnetization by $H \geq M_s$, they remain in magnetized state even by removing the applied field. On the other hand, "soft magnetic materials" are the ones with very narrow loops i.e. having low coercivity, and lose magnetization as the applied field is removed.

The idea of magnetic domains was introduced by French physicist Pierre-Ernest Weiss [36] and the principle of domain theory was established in 1935 by Lev Landau and Evgenii Lifschitz. It was first proposed that a ferromagnet contains a number of small regions, called domains; within each, the local magnetization reaches the saturation

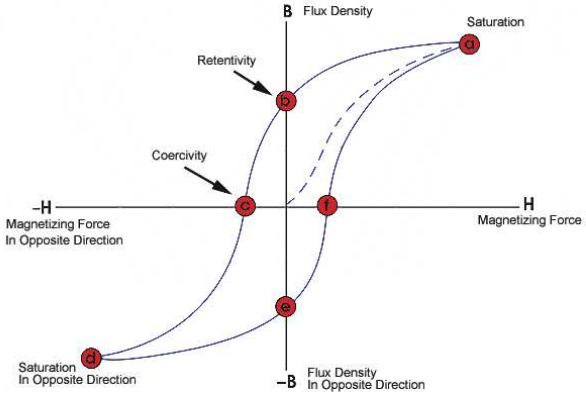

Figure 2.5: The hysteresis loop of a ferromagnet.

value. The direction of magnetization in each domain does not need to be parallel. The existence of domains can explain attaining the saturation magnetization by applying a very weak magnetic field, in soft magnetic materials [8]. The possibility of having a net zero in a ferromagnetic specimen shows that the magnetization is saturated inside domains, but the directions of the magnetization of each single domain are ordered in a way that the net magnetization of the specimen is equal to zero.

2.2.1 Curie temperature

The spontaneous magnetization of the specimen, due to the alignment of the magnetic moments inside the domains rely on temperature and it falls rapidly to zero (paramagnetic phase) at a specific transition temperature. This transition temperature, referred as Curie temperature, can be obtained within the Weiss model of a ferromagnet [37], formulated as:

$$T_c = \frac{g_J \mu_B (J+1) \lambda M_s}{3k_B}. \tag{2.2}$$

where g_J is the Landé g-factor, μ_B is Bohr magneton, k_B is the Boltzmann's constant and λ is a constant which parametrizes the strength of the molecular field as a function of magnetization. Above the Curie temperature the material is in the paramagnetic phase without spontaneous magnetization [38].

2.3 Antiferromagnetism

By having a negative exchange interaction, the molecular field is oriented to favour the nearest neighbour magnetic moments to lie antiparallel to one another [37]. Considering an antiferromagnetic material as a sum of two sublattices with antiparallel magnetic

moments and applying Weiss model, we can find the transition temperature, referred as Néel temperature:

$$T_N = \frac{g_J \mu_B (J+1)|\lambda| M_s}{3k_B}. \tag{2.3}$$

2.4 Exchange and Magnetic interactions

The magnetic properties of a CMR manganite depends on the balance of the competition between double-exchange (ferromagnetic) and super-exchange interaction (mostly antiferromagnetic). The complex phase diagrams of manganites is a result of the interplay between these magnetic interactions, coulombic and lattice-electron interactions [31, 39]. The parent compound $LaMnO_3$ is an A-type antiferromagnetic material, with Néel temperature T_N=140 K [32]. In an A-type antiferromagnetic materials, the magnetic moments ferromagnetically are aligned within (001) planes, but antiferromagetically coupled with each other along c-axis [11, 32, 39], as shown in Figure 2.6.

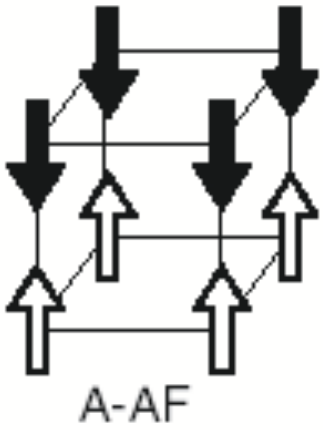

Figure 2.6: A-type antiferromagnetic structure in a 2×2×2 cluster [40].

Experimental [29, 41] and theoretical [42, 43] studies on $La_{1-x}AL_xMnO_3$ perovskites showed ferromagnetic-metallic behaviour over a wide range of concentration, x, between 0.15 and 0.5 [31], while at low and high x concentrations, the antiferromagnetic insulating behavior is obtained The phase diagram of $La_{1-x}Sr_xMnO_3$ is shown in Figure 2.7. In general, this striking behavior can be explained by the theory of double-exchange.

However, the colossal magnetoresistance in manganese oxide compounds cannot be explained by double exchange mechanism alone, while it should be explained along by strong electron-lattice coupling through the Jahn-Teller mechanism. That is caused by

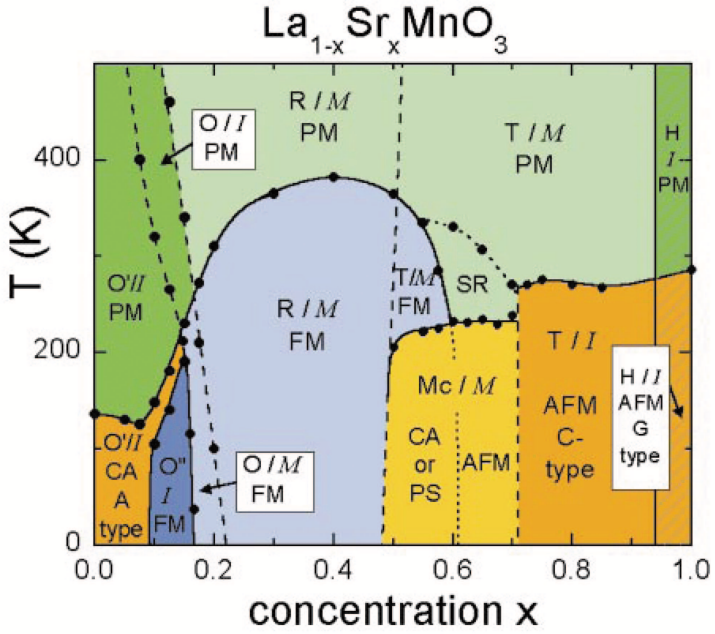

Figure 2.7: Phase diagram of a single crystal $La_{1-x}Sr_xMnO_3$, showing the transition temperature vs. concentration, where the crystal structures (Jahn-Teller distorted orthorhombic: O', orthorhombic O; orbital-ordered orthorhombic: O", rhombohedral: R, tetragonal: T, monoclinic: Mc, and hexagonal: H) are indicated as well as the magnetic structures (paramagnetic: PM (green), short-range order (SR), canted (CA), A-type antiferromagnetic structure: AFM (yellow), ferromagnetic: FM (blue), phase separated (PS), and AFM C-type structure) and the electronic state (insulating: I (dark); metallic: M (light)) [44].

MnO_6 octahedra deformations [45].

2.4.1 Double exchange

The double exchange mechanism is defined as an indirect coupling between Mn ions in manganites through both localized and delocalized 3d electrons [35]. This interaction was first proposed by Zener [42] in 1951, and after developed by Anderson [43], Hasegawa [43], Goodenough [46] and de Gennes [47]. As an example in manganites, $La_{0.7}Ca_{0.3}MnO_3$ compound has Mn^{3+} and Mn^{4+} ions in octahedra sites (d^3 and d^4). The d^3 electrons of both octahedrally coordinated ions are localized in $t_{2g}{}^{\uparrow}$ band, but in Mn^{3+}, the fourth d electron stays in $e_g{}^{\uparrow}$ band, hybridized with oxygen. It can hop from one d^3 to another freely, if according to Hund's rule interaction, the spins are parallel [35].

The transfer integral between two Mn-ions depends on the angle between the Mn spins, θ and can be expressed by t as [48, 43, 47]:

$$t = t_0 \cos\frac{\theta}{2}. \tag{2.4}$$

where t_0 is the inter-site hopping interaction, depending on the Mn-O-Mn angle.

Therefore, if neighbouring ions have antiparallel spins,θ=π, the transfer integral is zero. When the θ=0, the neighbouring ions are parallel and the exchange must be ferromagnetic [35]. The scheme of double exchange interaction is shown in Figure 2.8.

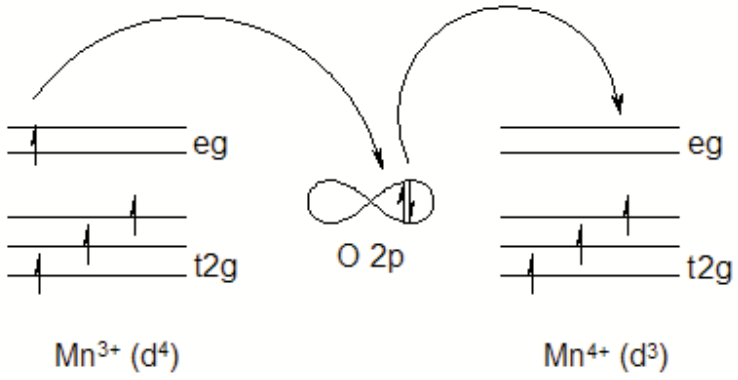

Figure 2.8: Double exchange mechanism between Mn^{3+} and Mn^{4+} ions.

2.4.2 Super exchange

Super exchange is another indirect exchange. This interaction consists of a virtual electron transfer between Mn^{3+} ions or Mn^{4+} ions, via an oxygen ion. The scheme of typical super exchange bond is shown in Figure 2.9.

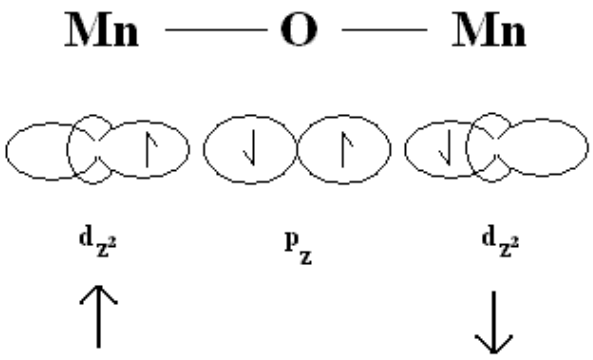

Figure 2.9: A typical super exchange bond between Mn^{3+} and Mn^{4+} ions.

Considering t as the p-d transfer integral and U as the on-site 3d coulomb interaction, the exchange interaction is of order $-2t^2/U$. The overlap integral tends to be larger than zero, according to Goodenough-Kanamori rules, leading super exchange to be more antiferromagnetic, rather than ferromagnetic [35].

2.5 Colossal magnetoresistivity

Colossal magnetoresistive manganites are known for their steep decrease of their resistivity when a magnetic field is applied near the critical temperature. The magnetoresistivity is given by the ratio of the change in resistivity in an applied magnetic field relative to the zero-field value:

$$MR = \frac{\rho(H) - \rho(0)}{\rho(0)}. \tag{2.5}$$

Below T_C, the spontaneous alignments of Mn spins makes a delocalization of e_g electrons, and consequently leads to a low resistivity ferromagnetic phase. By applying an external magnetic field, the maximum effect is obtained close to T_C, as is seen in Figure 2.10. The high value of the magnetoresistance of ferromagnetic La-based manganites near the Curie temperature is related to the effect of the magnetic field in a temperature region, where spin disorder and susceptibility are large. The magnetic field aligns the core spins and leads to a decrease in the resistivity [49]. The magnitude of this effect is associated with the competition between double exchange and other mechanism, near T_C. Previous studies showed that the resistivity of the paramagnetic phase increases with decreasing T, whereas in ferromagnetic phase, it decreases, therefore the CMR is larger as T_C is smaller [17, 31, 33, 49, 50].

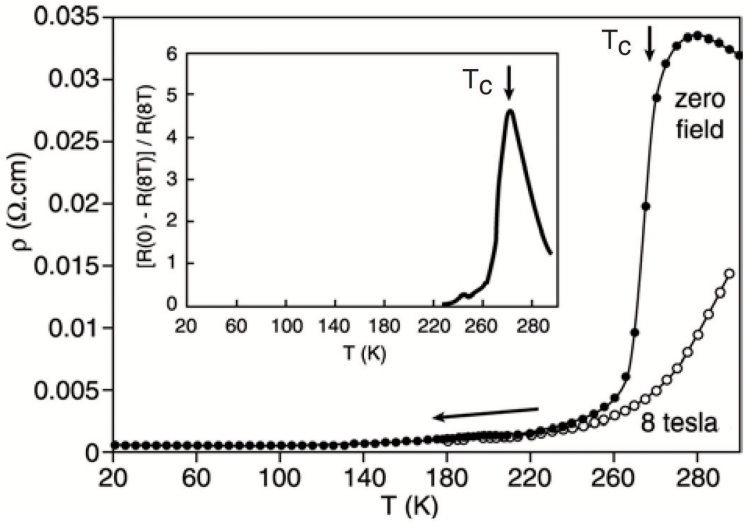

Figure 2.10: Resistivity in zero field and in a 8T applied field versus temperature, for a single crystal $La_{0.825}Sr_{0.175}MnO_3$. Inset: magnetoresistance ratio vs. temperature [51].

2.6 Multiferroicity and Magnetoelectricity

The magnetoelectric effect was first stablished by Pierre Curie [52] in 1894 while the name of magnetoelectric was given to this phenomenon in 1926 by P. Debye [53]. It was only in 1960 that a precise formulation of a linear coupling between electric polarization and magnetization was given by L.D. Landau and E. Lifshitz. Magnetoelectric coupling refers to the linear effect, that is an induction of magnetization by an electric field or electrical polarization by a magnetic field [22].

The significant property of perovskite is the large variety of functional responses, such as ferroelectricity, pyroelectricity, antiferromagnetism, ferromagnetism, etc. that provide a very rich basic science in CMR and tunnel magnetoresistance (TMR) manganites. Different responses, simultaneously, are possible within the framework of the oxygen coordination octahedron by changing the cationic occupations of the A- and B-sites.

2.6.1 The mechanism

There are several mechanisms that underlies the magnetoelectric effect:

- Intrinsic magnetoelectric coupling: this coupling occurs in compounds with no time-reversal, neither space-inversion symmetries [54]. In this group, an external electric field displaces the magnetic ions, leading to a change in the exchange interaction between them and magnetic properties of the compound [55].
- Induction of magnetization by strain effect: this mechanism occurs in composites of piezoelectric and magnetostrictive compounds. In these structures an applied electric field induces strain in piezoelectric component, which is transferred to the magnetostrictive component, where induces a magnetization [56].
- Pure electronic mechanism: the displacement of atoms at the ferromagnetic-ferroelectric interface changes the overlap between atomic orbitals at the interface that change suddenly the interface magnetization [57].
- Spin-dependent screening: in this mechanism, an applied electric field produces an accumulation of spin-polarized electrons or holes at the metal/insulator interface, resulting in a change in the interface magnetization [57, 58].
- Magnetic reconstruction: this mechanism occurs at ferromagnet-ferroelectric interface, due to switching of electric polarization [59].

It is well known that the doped La-based manganites, $La_{1-x}A_xMnO_3$ (A can be Ca^{2+}, Sr^{2+}, or Ba^{2+}) possess a rich phase diagram as a function of hole concentration, x, and temperature that induces metal-insulator transitions as well as the CMR effect [60], shown in Figure 2.7 for $La_{1-x}Sr_xMnO_3$. Following the magnetic phase of La manganites, it is obvious that they follow the same phase transition sequence, from antiferromagnetic

to ferromagnetic and back to antiferromagnetic, as x is increasing from 0 to 0.6, with the maximum T_c for $x = 0.3$. These phase transitions sequences can be defined as a consequence of the competition between super exchange interaction, attributed to antiparallel alignment of neighbouring Mn magnetic moments, and double exchange interaction, attributed to parallel alignment [47], as described in Section 2.4. Therefore, altering the population of electrons can change the exchange interaction mechanism, which lead to the rich series of magnetic transitions.

2.7 Piezoelectric and ferroelectricity

Generally, there are two main effect of changing the structure of material with electric field: electrostriction and piezoelectricity.

Electrostriction is defined as the elastic deformation of a dielectric material, under the force, due to its interaction with an electric field. This phenomenon is due to the change in the charge distribution of the material.

It should be noted that this phenomenon is not visible in un-compressible materials, due to rigidly bonding of particles, where in slightly compressible materials, such as polymers and ceramics, it may be detectable [61, 62]. Electrostriction is traditionally described as a tensor of electrostriction coefficients, γ_{ijkl}, such as:

$$u_{ij} = \gamma_{ijkl} E_k E_l \tag{2.6}$$

which links the strain tensor of $u_{ij} = (1/2)(\partial u_i/\partial x_j + \partial u_j/\partial x_i)$ with the components of the electric field [63].

The second effect is the applying of an external stress to develop an electrical polarization. This effect is called piezoelectricity. According to the definition of the piezoelectric effect, all the components of piezoelectric tensor should vanish in centrosymmetric crystal. Only 21 crystal classes out of 32 are non-centrosymmetric, and among them 20 shows piezoelectricity, as summarized in Table 2.2 [61, 62, 64, 65].

The piezoelectric effect can be described by:

$$D_n = d_{nkl} T_{kl} + \epsilon^T_{nm} E_m \tag{2.7}$$

where D_n is n^{th} component of the electric displacement vector, T_{kl} is the second-rank stress tensor and d_{nkl} is a third-rank tensor of piezoelectric coefficients, ${\epsilon^T}_{nm}$ is the dielectric permittivity at constant stress, and E_m is the m^{th} component of electric field vector [66].

Ferroelectric materials show hysteresis and nonlinear behaviour between the polar-

Table 2.2: Classification of the 20 non-centrosymmetric crystallographic point groups, showing piezoelectric effect [61].

Triclinic	Tetragonal	Hexagonal	Monoclinic	Orthorhombic	Trigonal	Cubic
1	4	6	2	222	3	23
	$\bar{4}$	$\bar{6}$	m	mm2	32	$\bar{4}$3m
	422	622				
	4mm	6mm				
	$\bar{4}$2m	$\bar{6}$2m				

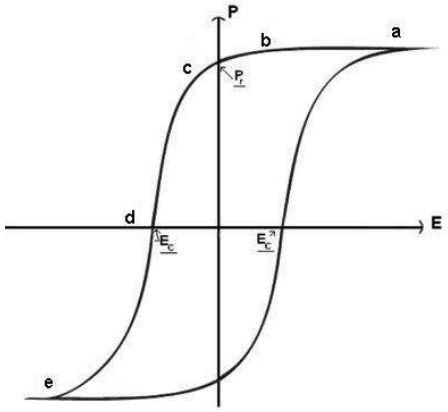

Figure 2.11: The hysteresis loop of a ferroelectric material.

ization and the applied electric field [62], observable in measuring the magnitude of the electric polarization, P, as a function of the strength of the applied ac electric field, E. Figure 2.11 shows a typical P(E) hysteresis measurement in a ferroelectric material.

The maximum of piezoelectricity is achievable by aligning the ferroelectric domains [65]. The process of saturating the spontaneous by applying a strong electric field to

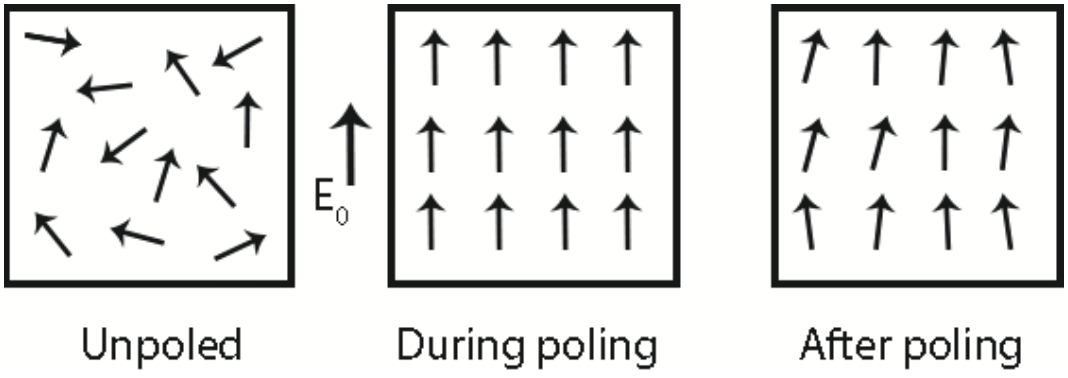

Figure 2.12: Alignment of electric dipoles represented by arrows in a material before poling (left), during the poling process (middle) and at the end of poling (right).

the material is called poling [62, 65], as shown in Figure 2.12.

2.8 Thin films

2.8.1 Interface effects in perovskite thin films

The importance of spin valves or spin injectors gives the manganite thin films a head on into the technology [67, 68]. It is mandatory to note the role of (i) homogenous substrate strain [69], (ii) electronic and/or chemical phase separation related to structural inhomogenities at the interface [70] and (iii) manganese e_g orbital reconstruction [71] in an oxide film to the loss of magnetization near the interface with the substrate [72].

A so-called "dead-layer", as the thinnest layer for which metallic as well as ferromagnetic behaviours are observed, is usually of a few unit cells width at the interface between the manganite film and most perovskite substrates. The existence of a dead-layer can be due to a phase-separation between ferromagnetic insulator and metallic phase at nanometric scale [60, 73]. This phase-separation may be related to the structural inhomogenities at the interface between film and substrate. It also can exist due to orbital reconstruction at the interface, where a crystal-field splitting of e_g levels with lowering ($3z^2$-r^2) orbitals over the (x^2-y^2) orbitals are present. This results in C-type antiferromagnetic structure at the interface [74, 75]. As an example, the $La_{0.67}Sr_{0.33}MnO_3$ (LSMO) manganite is a rhombohedrally distorted perovskite at room temperature [32]. This distortion is due to the smaller size of the B-site cations, i.e. La^{3+} and Sr^{2+}, relative to the size of oxygen ions, resulting in a compression and tilting of the Mn-O bonds and tension in the B-O bonds, which in turn lead to a cooperative tilting of the octahedra about a [111] axis in order to minimize the resulting stress [32, 49].

In thin films, additional stress may arise from the lattice mismatch between the manganite and the substrate. It is known that the transport and magnetic properties of manganite thin films are strongly influenced by the strain imposed by the substrate [31, 67, 76].

The interface effects between a manganite and an oxide substrate with perovskite structure can be modelized as an energy balance at the interface [72].

1. The strongest effect of the substrate is to constraint the film in-plane cell parameters to fit the substrate ones:

$$a_{film} = a_{substrate}; b_{film} = b_{substrate}, \tag{2.8}$$

Therefore, the film relaxes slowly. The difference between the lattice parameters

of the film and the substrate, i.e. the lattice mismatch, is a source of stress which can be very important and strongly influence the properties of the films. The lattice mismatch δ along the interface is formulized as:

$$\delta_i = \frac{i_{substrate} - i_{bulk}}{i_{substrate}} \tag{2.9}$$

where $i_{substrate}$ and i_{bulk} are the i^{th} lattice parameters of the substrate and the film (i = a, b, c), respectively. Positive δ corresponds to tensile strain, Figure 2.13(a), whereas negative values are related to compressive stresses, Figure 2.13(b). The substrates mismatch strain induces a lattice deformation, which can be analysed from the unit cell distortion [31]. The effect of the temperature on the cell parameter mismatch is considered by thermal expansion, given by:

$$\delta_T = (600^{\circ}C) \times (C_{T_f} - C_{T_s}) \tag{2.10}$$

where C_{T_f} and C_{T_s} are thermal expansion coefficients of film and substrate, respectively.

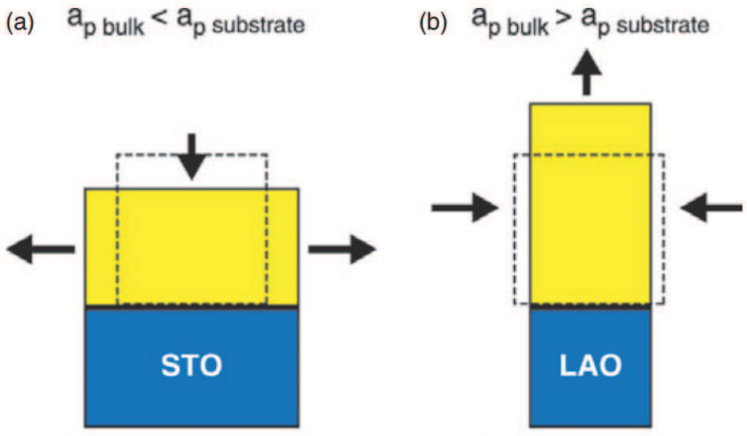

Figure 2.13: Schematic draft of the lattice cell distortion in a strained epitaxial LSMO film (abulk = 0.3873nm), (a) under tension (a_{STO}= 0.3905 nm) or (b) compression (a_{LaAlO_3} = 0.3788nm).

2. The substrate imposes to the film its in-plane symmetry operations. This interaction is weak, since it is related to low energy vibrational modes. After a few first cells at the interface, these constraints start to relax according to the energy of the associated vibrational mode.

3. The electronic structure of the film and substrate interact at the interface. In particular, the possible delocalization effects at the interface should be taken into account [72]. The physics of a manganite films and a perovskite substrate at the interface results from a competition between:

(a) The elastic energy (c<a) and

(b) The delocalization energy (c>a); this energy is originated from the delocalization of orbitals, between film and substrate's atoms, usually in first few monolayers of film, right at the interface. The delocalization dominates the elastic energy that leads to elongation of film in the c-direction, despite their already in-plane tensile strain [72].

After a few unit cells, there is no more delocalization energy. At the same time, the in-plane symmetry operations imposed by the substrate should start to relax. The consequence of this constraint relaxation is that the c monolayer parameter should start to decrease toward the value expected from the elastic energy minimization.

2.8.2 Horizontal multilayer heterostructures

An approach to obtain a magnetoelectric effect is through multi-layered heterostructures. Significant advances have been made in the area of composite magnetoelectric systems. These systems are based on mechanical coupling between ferromagnetic and ferroelectric properties between two layers, via piezoelectric effect. The mechanism is defined as the creation of a piezoelectric strain by an applied electric field. This produces a corresponding strain in the ferromagnetic material and consequently piezo magnetic change in magnetization or in magnetic anisotropy [25]. In 1990s, theoretical studies showed the possibility for strong magnetoelectric coupling in multilayers configuration [77]. The experimental tests on ferromagnets, including $La_{0.7}Sr_{0.3}MnO_3$ and $La_{0.7}Ca_{0.3}MnO_3$ [78], proved the results, obtained from calculations. The work has been continued on investigating thin film heterostructures by combining ferroelectrics, such as $BaTiO_3$ [79] with ferromagnets; however, these experiments were not capable of producing magnetoelectric voltage coefficient higher than few tens of $mVcm^{-1}Oe^{-1}$. Running studies show that the in-plane magnetoelectric interfaces limits the magnitude of magnetoelectric voltage coefficient, due to the clamping effect of the substrate on the ferroelectric phase [80].

Epitaxial growth presents a powerful pathway to control the phase stability and electronic properties in thin film and heterostructure systems [68].

2.8.3 Engineering new functionalities with multiferroics

Nowadays, the principle question in multiferroic materials is how to apply them into room-temperature devices. In 2005, a new member of magnetoelectric based devices had been presented [81].

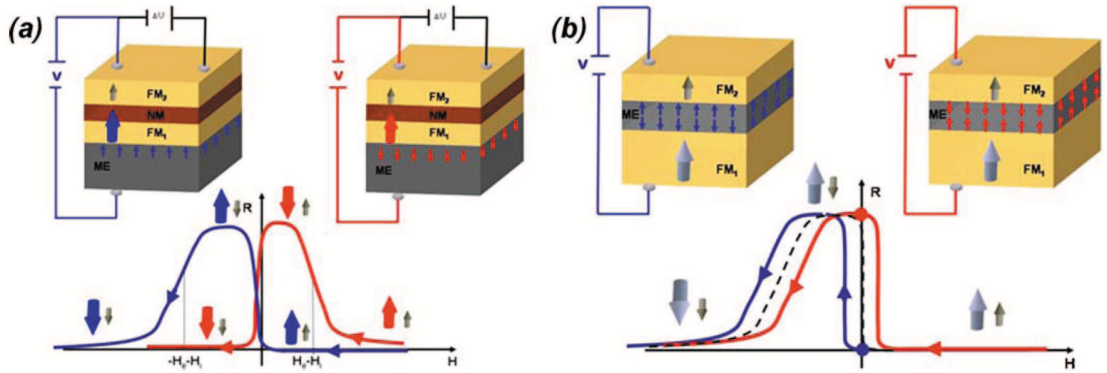

Figure 2.14: Schematics multiferroic based magnetoelectric, (a) the magnetoresistance curve of a GMR device involving a magnetoelectric, multiferroic film as a pinning layer, and (b) the magnetoresistance curve of a TMR device involving a magnetoelectric, multiferroic film as a tunnel barrier [25].

The simple idea was based on using the net magnetic moment created by electric field in a magnetoelectric thin film to change the magnetization of a neighbour ferromagnetic layer by means of exchange coupling. The proposal of some giant magnetoresistance (GMR) (Figure 2.14(a)) and tunnel magnetoresistance devices (Figure 2.14(b)) had been made. The other flourishing field of applying magnetoelectric systems can be spintronic. Spin-based electronics or spintronic has found its way into magnetic read-heads and sensors [82, 83].

2.8.3.1 Electric field control of ferromagnetism

Is it possible to control ferromagnetism at room temperature with an electric field? The answer is not very simple, but: YES. One solution is using heterostructures of existing multiferroic materials, such as $BaTiO_3$. This concept is shown in Figure 2.15. The idea includes of two different types of coupling in materials: intrinsic magnetoelectric coupling, which allows the electrical control of antiferromagnetism, and an extrinsic exchange coupling between ferromagnetic and antiferromagnetic materials (Figure 2.15(a)). By combining these different types of coupling, it is possible to couple ferroelectric and ferromagnetic order at room temperature and create a pathway to electrical control of ferromagnetism (Figure 2.15(b)).

2.9 Introduction to the used materials

In Electronic Magnetic Ferroelectrics (EMFs), the primary order parameter of the phase transition is related to electronic (i.e. spin, charge, or orbital) degrees of freedom [84]. In these materials, polarization is magnetically induced and it is reasonable to expect a strong correlation between magnetic and ferroelectric properties, because both

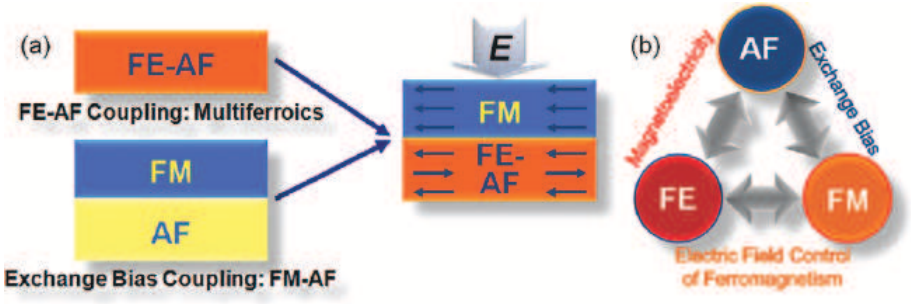

Figure 2.15: Schematic illustrating the design algorithm for gaining electrical control of ferromagnetism. (a) By combining multiferroics together with traditional ferromagnet, we can create heterostructures that might have new functionalities. (b) These structures rely on two types of coupling, magnetoelectric and exchange bias, to gain electrical control of ferromagnetism [26].

of them share the same origin and occur at the same temperature [85]. The EMFs can be divided into two main classes: (i) spin-ordering driven and (ii) charge-ordering driven materials.

The presence of strong electron-lattice correlations in transition-metal oxides with perovskite-type structures imply that the lattice distortion plays a crucial role on physical properties in this category of materials, such as magnetoresistance, super-conductivity, charge-ordering, etc. It already has been proven that the physical properties of this category of materials are strongly coupled to the distortion in the shape and/or rotation of MnO_6 octahedra [45, 86].

The distortion in lattice in thin epitaxial La-based doped perovskite, $La_{1-x}AL_xMnO_3$, films can happen due to substrate-induced biaxial stress, that can modify the electron-lattice coupling [87].

Perovskite-like compounds of ABO_3 type have become a strategic materials in fundamental science and technological applications. Their high-temperature phase has a cubic crystal structure, where they show a large variety of physical properties. In this family, it is easy to find different physical properties, like superconductivity ($K_xBa_{1-x}BiO_3$) [88], giant magnetoresistance ($LaMnO_3$) [89], orbital ordering ($YTiO_3$) [90] and ferroelectricity ($BaTiO_3$) [88, 89, 90].

2.9.1 Properties of $La_{1-x}Sr_xMnO_3$ (x=0.33)

The $La_{1-x}Sr_xMnO_3$ compound possess a rich phase diagram, Figure 2.7, being the CMR ferromagnetic manganite with the highest $T_c \approx 370$ K, for $x \approx 0.33$. The temperature dependence of the magnetization of single crystal and two polycrystalline $La_{0.67}Sr_{0.33}MnO_3$ samples is shown in Figure 2.16.

The behaviour of magnetization with temperature is almost similar and the Curie temperature is the same for both single crystal and polycrystalline samples, with the

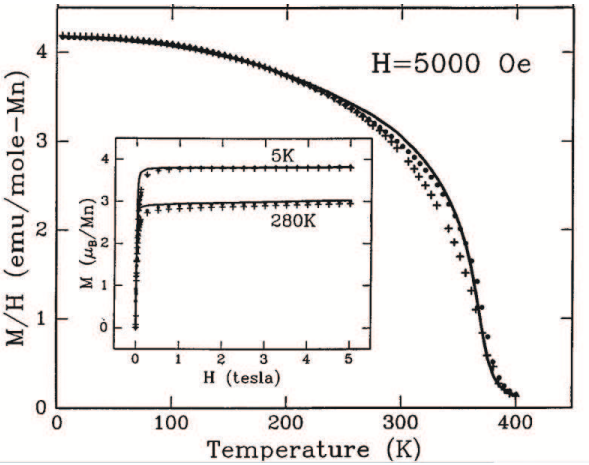

Figure 2.16: Temperature dependence of magnetization of a single crystal (solid line) and two polycrystalline samples of $La_{0.67}Sr_{0.33}MnO_3$ manganite sintered at 1300 °C (+) and 1700 °C (•). the inset shows the magnetization as a function of magnetic field for all samples at 5K and 280K [33].

value T_c=365K [33]. The inset shows the isothermal field dependent magnetization at 5 and 280 K for the three samples. The small differences between samples at low fields are due to the different demagnetization factors. All the samples were cut to the same geometry, although the polycrystalline samples have an additional factor, mostly caused by their slight porosity [33] and random orientation of the grains.

At low temperatures, lower than T_c, $T \ll T_c$, the spontaneous magnetization of high-T_c $La_{0.7}Sr_{0.3}MnO_3$ can be described by Bloch law [11, 32]:

$$M = M_0(1 - (T/T_c)^{3/2}) \tag{2.11}$$

In the bulk form of $La_{0.67}Sr_{0.33}MnO_3$, the magnetic properties depend on valence effect by varying the content of oxygen [91, 92], charge mismatch, nature of the Mn site doping element, magnetic field during cooling, electron irradiation, crystal orientation etc. [33, 92, 93]. However, in thin films, the saturation magnetization and Curie temperature depend also drastically on the thickness, and consequently on the strains at the interface of the samples [70, 76, 92, 94, 95, 96], in addition to film orientation [76, 97, 98] and oxygen content [95, 99]. The influence of substrate-induced strain on the Curie temperature of thin films with composition $La_{0.67}Sr_{0.33}MnO_3$ is shown in Figure 2.17(b). However, taking into account all the factors to understand the way that properties are modified is very difficult, due to hard control of parameters. All the films have the same thickness of t=22 nm. The substrates induce different values of biaxial strain, because of different values of lattice mismatch [67]. Figure 2.17(b), showing the magnetization of $La_{0.67}Sr_{0.33}MnO_3$ film on different substrates, illustrates that the film with highest mismatch, which is $NdScO_3$, has the lowest Curie temperature [67]. The influence of strain on Curie temperature of the $La_{0.67}Sr_{0.33}MnO_3$ films can be described

as [67]:

$$T_c(\epsilon_B, \epsilon^*) = T_c(0,0)[1 - \alpha\epsilon_B - b\epsilon^{*2}] \tag{2.12}$$

where α=$(1/T_c)(dT_C/d\epsilon_B)$) and b=$(1/T_c)(d^2T_C/d\epsilon^{*2})$, with typical values of 6 and 1.4E3, respectively [100]. The parameter ϵ_B is related to the uniform strain affecting electron hopping probability and ϵ^* shows the biaxial strain that influence Jahn-Teller localization mechanism [67].

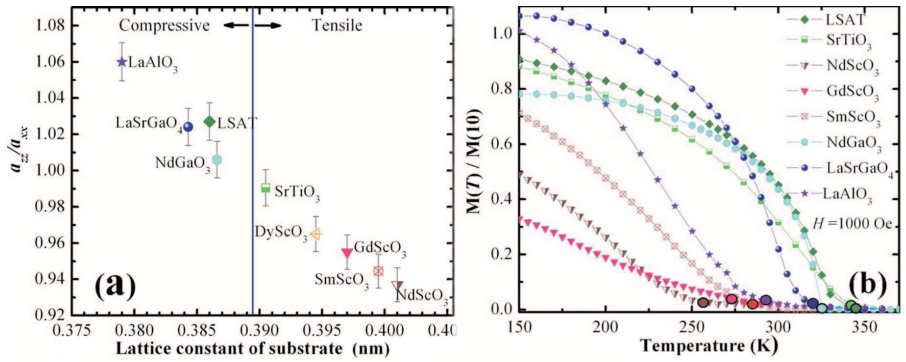

Figure 2.17: a) Ratio between the out-of-plane and in-plane lattice spacing of commensurately $La_{0.7}Sr_{0.3}MnO_3$ films as a function of the pseudocubic in-plane substrate lattice parameter. b) The temperature dependence of the magnetization normalized at 10 K of samples cooled in a 1000 Oe field. Circles indicate the Curie temperature, T_c [67].

The other key that has an important effect on the magnetic properties of the $La_{0.67}Sr_{0.33}MnO_3$ thin films is the presence of the dead layer, which causes a decrease in the saturation magnetization with the increase of film thickness [74]. This layer provides disordered spins, causing the loss of magnetic polarization [31, 32, 94, 101].

2.9.2 Properties of $La_{1-x}Ba_xMnO_3$

The Ba-doped La-based manganites are very interesting compounds of manganites, due to their Curie temperature, that can reach up to 340 K [102]. It possess the largest ionic radii among the $La_{1-x}AL_xMnO_3$ manganites, $r_{Ba^{2+}}$=1.47 Å, compared with $r_{Ca^{2+}}$=1.18 Å and $r_{Sr^{2+}}$=1.24 Å, that leads to an intrinsically strained structure [102]. The $La_{0.7}Ba_{0.3}MnO_3$ composition crystallises in rhombohedral ($R\bar{3}c$) crystal lattice below room temperature and in orthorhombic lattice of Imma space-group symmetry below 1.6 K [102, 103]. According to the phase diagram, $La_{1-x}Ba_xMnO_3$, with x=0.3, has paramagnetic insulating behaviour above Curie temperature; and a ferromagnetic metal behaviour below T_c [102, 104]. The film form of this composition is also attractive for application in resistive sensors, because its ferromagnetic ordering of spins, in Mn ions, happens at a close-to-room temperature, which shows $T_c \approx 300$ K [105, 39].

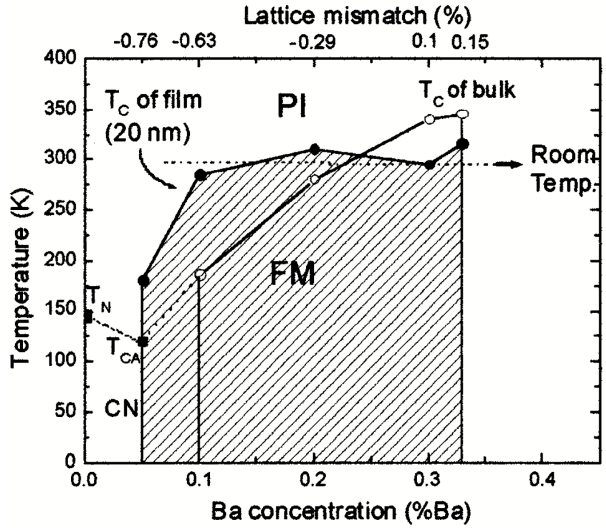

Figure 2.18: Phase diagram of LBM 20 nm-thin film on $SrTiO_3$ substrate and bulk form [39].

Studies showed that tensile strained thin films (20 nm thick) of $La_{1-x}Ba_xMnO_3/SrTiO_3$ with lower doping levels (x=0.1-0.2) have a higher T_c in comparison with doping levels of x=0.3 or x=0.33. The phase diagram of $La_{1-x}Ba_xMnO_3$ bulk and result for 20-nm thin films are shown in Figure 2.18 [39]. Some representative values of temperature dependence of magnetization for bulks under the applied magnetic field of 200 Oe and thin films, under the applied magnetic field of 1000 Oe, are presented in Figure 2.19(a) and (b), respectively.

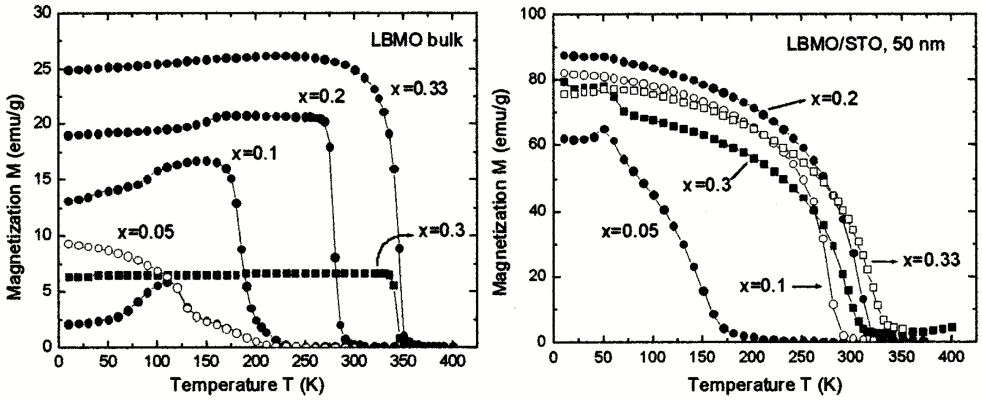

Figure 2.19: Temperature dependence of magnetization of $La_{1-x}Ba_xMnO_3/SrTiO_3$; (left) bulk values, under the 200 Oe applied field and (right) 50-nm thin film, applied field is 1000 Oe [106].

The magnetoresistance behaviour of $La_{1-x}Ba_xMnO_3$ is found to be the largest around T_c [102, 107], due to the reduction in magnetization fluctuation, expected in ferromagnetic materials. Studies on the temperature dependence of the magnetoresistance at/above room temperature for x= 0.2 shows that the peak is located at T=315 K for the MR value of 25%, under a magnetic field of only 0.8 T. Furthermore, with increasing

the level of x, the peak temperature is increasing, while the MR value decreases.

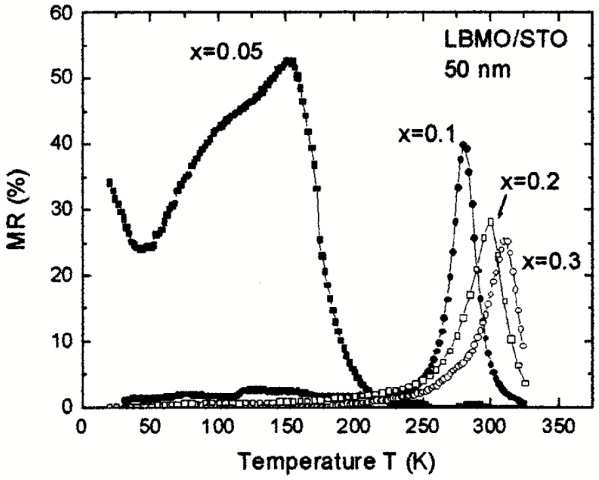

Figure 2.20: Temperature dependence of MR ratio for $La_{1-x}Ba_xMnO_3/SrTiO_3$ thin films, adapted from [39].

2.9.3 Properties of $BaTiO_3$

Some ferroelectric materials, such as perovskite-like $BaTiO_3$, are single-valent. The valence and conduction bands of the compound are formed by p states of oxygen and d states of titanium [108]. At high temperature, it has a cubic phase ($Pm\bar{3}m$), with the lattice parameter, a=4.009 Å. As the temperature decreases, $BaTiO_3$ experiences a succession of phase transitions to ferroelectric structures with tetragonal, orthorhombic, and rhombohedral symmetry, as shown in Figure 2.21.

Due to strong covalence effects, the relative displacement of the ionic sub-lattice with respect to the cationic sub-lattice gives rise to the spontaneous and switchable polarization.

2.10 State of the Arts and Objectives

The increasing need for storing and transferring information in smaller devices at faster temporal rates leads to search for new multifunctional materials [110]. The interest in multiferroic materials arises from the possibility of magnetically control of the polarization and electrical control of magnetization, through a magnetoelectric coupling [111]. This coupling adds new functionalities to devices for encoding information independently both in electrical polarization and magnetization. Therefore it is possible to obtain four different logic states as well as electrical control of the transmission through a tunnel barrier [112]. Available magnetic driven spintronic devices, usually,

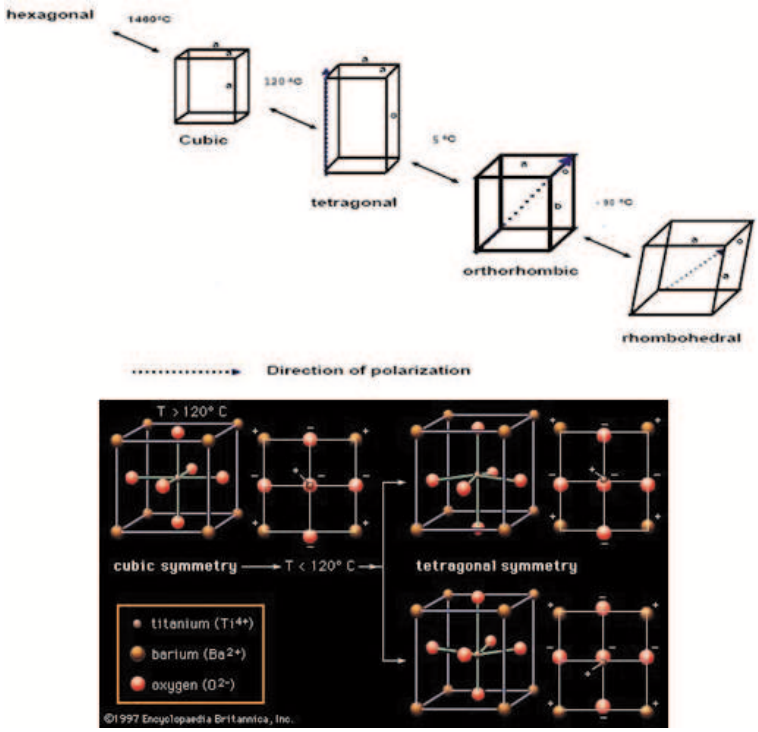

Figure 2.21: (Up) Changes in the crystal structure of $BaTiO_3$, and (down) Ferroelectric properties of BTO. Above 120 °C the structure of the $BaTiO_3$ crystal is cubic, and there is no net polarization of charge; below 120 °C the structure changes to tetragonal, shifting the relative positions of the ions and causing a concentration of positive and negative charges toward opposite ends of the crystal [109].

require high magnetic fields to obtain adequate changes in electrical resistance. Often, the current needed to create such a strong magnetic fields are not achievable, from industrial point of view, due to their power requirements. This can be the reason why CMR systems have not been commercially viable. It is clear that by using multiferroic heterostructures, the electrical driven effect becomes more attractive in technological applications [86]. By using a multiferroic insulator, it is possible to have an additional degree of freedom to MTJs, because the barrier can store information, through the polarization state. Therefore, creating thin films and new heterostructures of materials is a crucial component of controlling and manipulating magnetism with electric fields [113].

The electric control of the spin transport properties of devices is based on the coupling between the ferroelectric and magnetic orders [113]. The main physical phenomena in order to manipulate electrically the spin transport are:

- Exchange bias effect,
- Domain coupling,
- Converse piezoelectric effect, and
- Screening effect of the interfacial electric charges.

The ability of engineering or tuning the physical properties of the mentioned materials

is one of the most interesting points of this science. The engineering can be done by replacing, substituting, or varying the ratio of the cationic species in the A-site or B-site in thin films. Selection of proper doping elements can impact the structural, electronic magnetic polar, etc. properties of these materials [26]. The alkaline earth doped rare earth manganites have huge attraction in understanding the fundamental of physics and their potential technological applications [114, 39, 25].The electronic structure and coordination chemistry of the cationic species control the physical properties of these materials [25]. Choosing of materials for the thin films and heterostructures was based on the different factors, including the mismatch between film and substrate, the film ferromagnetic and ferroelectric behaviour, and etc. The used substrates was chosen based on the close cell parameter ($La_{0.7}Sr_{0.3}MnO_3$ film on $SrTiO_3$ substrate)[115], epitaxial growth of the film (thin film and heterostructure on Al_2O_3 substrate) and capability of application in semiconductor industry (thin films and heterostructure on Si substrate).

Also, in recent years, much attention has been attracted to nanoscale phenomena in ferroelectric films as explored by piezoresponse force microscopy (PFM). The notable examples include ferroelectric domain patterning [116, 117, 118] and polarization-mediated electronic transport [119, 120].

The scientific work within this thesis, presenting the multiferroic materials and their properties, is a part of personal experience obtained during PhD graduation period.

Understanding the properties of multiferroic oxide materials and the connection between their structural aspects and their properties, from macroscopic scale to domain-size level and microscopic level is the main objective of this work. The materials include manganite and titanate thin films and multiferroic heterostructures at room temperature. Analysing and comparing the structural properties of the thin films and heterostructures, grown on chosen thermodynamic conditions, by altering growth and strain condition, by changing substrates is the basis of this PhD thesis.

As the first step, the work consists of investigating on microstructural influence of substrate on the deposited films and the interfaces between film and substrate. This has influence on the physical properties of the grown film, changing the Curie temperature, magnetic/electric behaviour and topographical arrangements of the structures. Following the plan work, engineering the multiferroic heterostructures through combining of ferromagnetic and ferroelectric thin films and detailed analysis of magnetic and electric properties of engineered heterostructures is the next step. The effect of poling the ferroelectric film and multiferroic heterostructure, grown on conductive Si substrate, by a dc bias voltage in local (nanometric) scale, is going to be studied. The changes on the ferroelectric domain orientation promote modifications at the interfaces associated

with the ferroelectric polarization.

The morphology, domain configuration and the crystal structure of the obtained films will be analyzed by scanning force microscopies (AFM and PFM) and electron microscopy (TEM). The macroscopic characterization of the magnetic and electric properties will be carried out through magnetic susceptibilities and magnetic and polarization measurements. The obtained experimental results are going to be used for evaluating and improving the growth conditions of the films and give the preliminary information for growth of multiferroic heterostructures. The same techniques for thin films processing and characterization will be used and the transport properties as a function of applied magnetic field will be studied and compared to the thin films, on the same substrate.

The goals in the present work can be summarized as:

- Analysing the microstructure of the grown films and heterostructure, using Force microscopies (atomic force microscopy and piezoresponse force microscopy) and electron microscopy (Transmission electron microscopy) to investigate the strains and defects, created by the substrate effect on the sample.
- Understanding the modification of magnetic/electric properties of heterostructures, composed of oxide (manganite and ferroelectric) layers.
- Studying the ability of thin films and heterostructures to sustain electric-field induced dielectric/ferroelectric phases, and understanding the nature of bias-induced phases in materials under study.
- Investigating on the effect of applying a dc-bias-voltage field on the thin films and heterostructures, in the local scale, on topography and surface modifications.

The studies on this thesis were done by using various techniques, from XRD and RBS to TEM, for structural analysis, and SQUID, linear four-point probe technique for magnetic, and electrical analysis, respectively. Also, the surface analysis is done by force microscopy technique, which gives a great view of the surface behaviour under the studied conditions. Compositional studies were done by various methods, including RBS, PIXE, EDS, EDS mapping, EELS-mapping and EFTEM. The used techniques will be described in chapter 3. Also the results of the performed measurements and discussions are introduced in chapters 4, 5, 6 and 7.

Chapter 3

Thin Films Production and Characterization Techniques

The thin films and heterostructures are produced by pulsed laser deposition and sputtering techniques, described later. Contrary to chemical methods, such as chemical vapour deposition (CVD) and sol-gel method, in physical vapour deposition (PVD) methods, target is the key point for producing films and heterostructures.

3.1 Production of targets

In this section, the procedure followed in the preparation of the samples is presented.

3.1.1 Laser ablation target

Polycrystalline target with nominal composition of $La_{0.7}Sr_{0.3}MnO_3$ (LSMO) was prepared by the gel combustion method, done by professor Pedro Tavares, and previously characterized in order to assess its quality and physical properties [121]. Stoichiometric amounts of La_2O_3, $SrCO_3$ and $MnNO_3$:$4H_2O$ (as reactant) were used as starting materials. This oxide was converted into metal nitrates by adding nitric acid and dissolved in distilled water to obtain a clear solution. Urea was used as fuel/ complexing agents with a molar ratio of [urea]/[salts]=3 and [CA]/[salts]=2. By adding ammonia the pH of solution was adjusted to 6.5. Subsequently, the solution was heated with stirring to evaporate most of the solvent water. The resultant gel precursor powder was obtained. In order to get the desired laser ablation targets, this powder was ground and pelletized and then annealed at temperatures from 500°C to 1400 °C [122].

3.1.2 RF-Sputtering targets

The depositions were performed using a circular target, $La_{0.7}Ba_{0.3}MnO_3$, 2-inch diameter, provided by Kurt J. Lesker Co. The level of the doping is x=0.30 (confirmed by the XRD pattern of target, shown in Figure 3.1). The peak indexation was done based on the Powder Diffraction File (PDF), published by International Centre for Diffraction Data (ICDD), and agrees with the cubic system, $Pm\bar{3}m$ (221) space group, with a = 0.391 nm and molecular weight of 241.37 gr/mol.

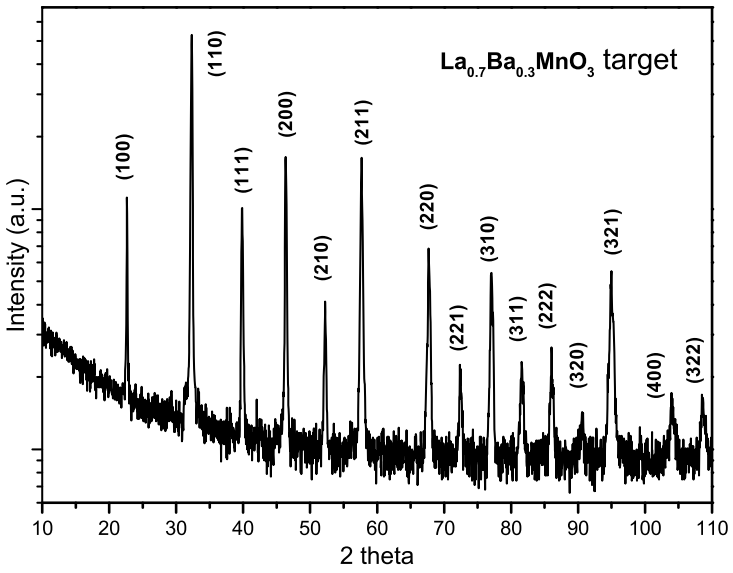

Figure 3.1: XRD Pattern for the used target $La_{0.7}Ba_{0.3}MnO_3$, recorded at room temperature.

The commercially $BaTiO_3$ (BTO) target was checked by XRD and shown in Figure 3.2. The XRD of the target shows a polycrystalline structure, according to ICDD database with the space group of P4mm (99), of tetragonal family, with a = 0.57 nm, c = 0.7 nm and molecular weight of 227.95 gr/mol.

3.2 Thin film deposition

3.2.1 Pulsed laser deposition (PLD)

Since mid-1980s PLD become popular among the thin film deposition techniques [123, 124], because of its simplicity and the stoichiometry of the target material is often kept during deposition. It has been applied in the production of a variety of materials from high-T_C superconductor [123, 124, 125] to multiferroics [92, 126, 127, 128] and

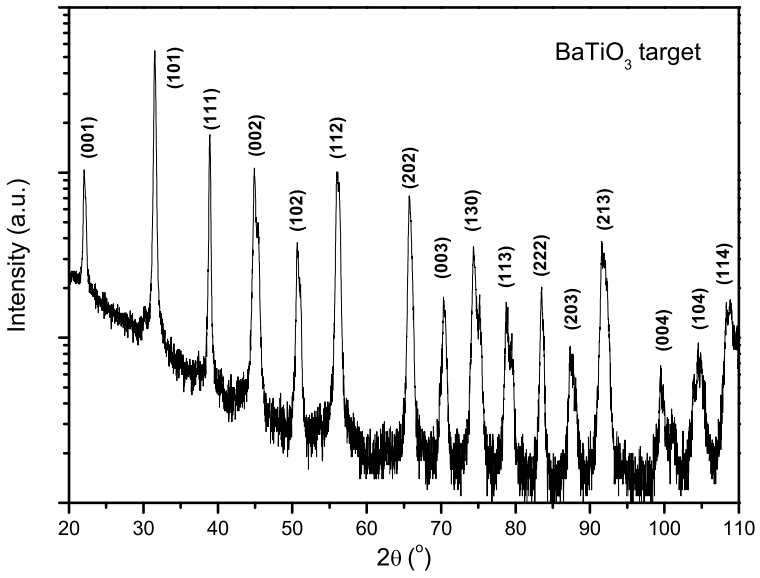

Figure 3.2: XRD Pattern of the $BaTiO_3$ target, showing the P4mm (99) space group, obtained at room temperature.

metal oxides [129, 130, 131, 132].

This technique consists of a high energy laser beam (with typical pulse duration of 25 ns, energy intensity of 1.0E8 W/cm^2 and repetition rates around 10 Hz) on the surface of a dense target inside a vacuum chamber, see Figure 3.3. The extreme energy density at the target causes the breakage of the chemical bonds in target, and a few surface layers are ejected at high kinetic energy in the form of an ablation "plume". The plume composition is made of energetic species, such as atoms, molecules, ions, clusters and particles of different sizes, propagating perpendicularly to the target's surface. The high impact energies cause the particles to stick to the surface, and compressed, forming a dense continuous film. Subsequent laser pulses gradually build up the thickness of the film from a few atomic layers to microns.

The PLD process is dependent on numerous parameters, chosen to be optimum for the microstructure, transport and magnetic properties of the film, such as wavelength, target material, background gas pressure, laser-to-target distance, substrate temperature, target-substrate distance, and etc.

3.2.1.1 Growth of the film on the substrate

The final stage is the arrival and diffusion of the particles on the substrate, chemical bonding between adsorbed species and consequently growth of a film on its surface [134]. The kinetic energy of the arriving particles, the substrate temperature and the

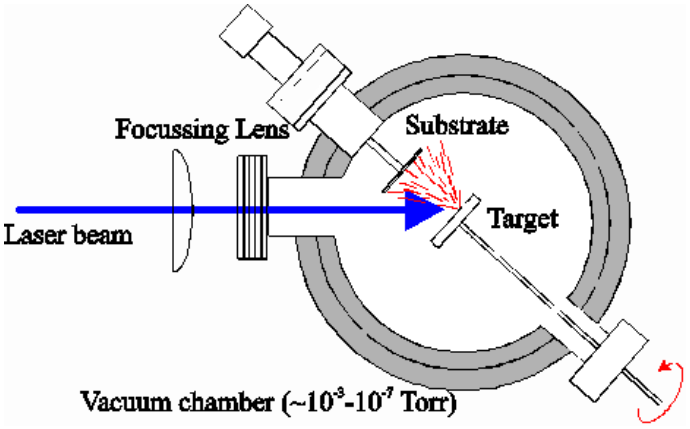

Figure 3.3: Schematics of a typical pulsed laser deposition setup, adapted from, adapted from [133].

sticking probability are determinant factors in the morphology and crystallinity of thin films. The fact that the particles in the plume are having a high kinetic energy, makes pulsed laser deposition a good technique for obtaining high quality and epitaxial films of many different types of materials [131, 135].

High substrate temperatures and low deposition rates in general facilitate epitaxy, allowing for the diffusion of the adatoms on the substrate until they find equilibrium lattice sites [136]. Thin films deposited at low temperatures and/or high deposition rates have a tendency to become amorphous. Other important factor is that of the substrate, particularly through lattice mismatch.

There are few disadvantages to this deposition method, the most important one is the presence of particulates with sizes ranging from ∼1nm to several μm and also target corrosion [123, 137, 138].

3.2.2 Sputtering

Sputtering as a phenomena was first observed in 1850s by Sir. W.R. Grove, while studying neon lights [138], but stayed a scientific curiosity until 1940s, when found its way into application. The basic of the work was laid on modern plasma physics. With the introduction of modern vacuum pumping technology, it became possible to use the sputtering process commercially.

The advantages of sputtering over other deposition methods are: (1) High deposition rates, (2) Ease of sputtering any materials, metals, oxides and etc., (3) High-purity films, (4) Extremely high adhesive films, (5) Excellent coverage of steps and small features, (6) Ability to coat heat-sensitive substrates, (7) Ease of automation, and (8) Excellent uniformity on large-area substrates [139]. However, the disadvantage of this technique is the change in composition between target and the film, due to different sputtering yields.

3.2.2.1 Sputtering mechanism

Sputtering is a process, wherein atoms or molecules are ejected from the target, using the bombardment of high-energy particles, usually by positive ions derived from an electrical discharge in a gas. In this process the pressure of the chamber must be low enough that ejected atoms will be able to move freely towards the substrate and coat directly on the substrate [139].

The "sputter yield" is the fundamental parameter which measures the efficiency of the sputtering process. This parameter, named Y, is defined as the mean number of atoms or molecules ejected from the surface per incident particle [136]:

$$Y = \frac{atomsremoved}{incidentions}. \tag{3.1}$$

Sputtering rate is also determined by different factor [140]:

- Gas pressure,
- Discharge current flowing,
- Type of gas (mass, energy and angle of incident of bombarding ions),
- Target material (mass, crystal orientation, temperature).

Some applications require deposition rates higher than 1 Å/s. This may happen for film structural reasons, since deposition rates influence the film microstructure and purity. The highest deposition rates can be achieved by using a magnetron discharge system.

In order to run the sputtering system working, the plasma can be generated by dc or RF-power. Considering plasma in a low-pressure gas, the tube can be divided into several regions. One of the regions is cathode dark space and the positive glow, which is the most important region for sputtering use. Electrons are emitted from the cathode, during stable conduction conditions. The emitted electrons are accelerated toward the positive electrode until they have sufficient energy to ionise the gas molecules.

Using the magnetron source, the cathode's surface is immersed in a magnetic field such that electron traps are created and drift current close in on themselves [139]. Figure 3.4 shows a scheme of the essential arrangement for planar magnetron sputtering system.

3.2.2.2 RF magnetron sputtering technique

This section aims to present and describe the basis of the fundamental RF-sputtering process. The power supply usually has a voltage up to 1 kV, and typical RF frequencies employed range from 5 to 30 MHz, while the most common used value is 13.56 MHz, established by the Federal Communications Commission for plasma processing [142].

Sputtering, as a method of deposition, encounters an important limitation in its

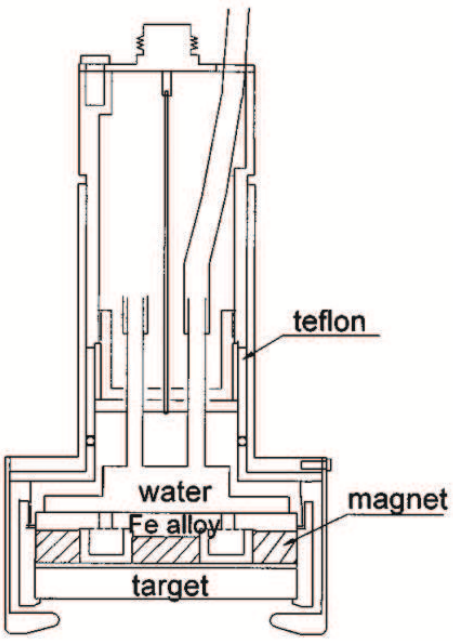

Figure 3.4: Scheme of a 2-inch magnetron sputtering gun, used for deposition [139, 141].

dc mode: ONLY conducting targets can be used. Using radio frequency sputtering (RF-sputtering), it is possible to deposit thin films using insulating targets, as well. In comparison with dc sputtering the RF method has lower deposition rates [143]. However, this disadvantage is neutralized by the combination of RF-sputtering with magnetron sputtering. The magnetic field intensifies the plasma in that area by trapping electrons and enhancing ion bombardment of the target.

The magnetic circuit behind the target forms a tunnel of semi toroidal magnetic field B which, along with E, creates a sort of endless racetracks where primary and secondary electrons are trapped, increasing greatly the chances of them colliding with a gas atom. Therefore, ion bombardment of the target becomes a much more efficient process and impedance of the plasma drops, which will allow the use of much lower voltages: 500-600 V (or lower) compared to several kV [144].

Besides the already mentioned advantages that magnetron sputtering can bring, there is also an additional positive feature of allowing the use of lower sputtering gas pressure. However, it presents the disadvantage of more inhomogeneous target erosion [143].

Beside all the equipment needed for RF-sputtering, it requires an impedance matching network to ensure that the maximum power is absorbed into the plasma [139].

3.3 The deposition setup

3.3.1 Laser ablation deposition

The deposition of LSMO thin films on $SrTiO_3$ (STO) substrates were done in the PLD facilities in Centro de Física da Universidade do Minho. The STO imposes very small strain (δ=0.81%) on the epitaxial LSMO film. The setup consists of a cylindrical-shaped stainless steel vacuum chamber, with 30 cm in diameter.

The substrates were placed on the central plate of a resistive heater, where the temperature of heater can reach to 900°C, measureable by a thermocouple behind the central plate. A resistive oven is also available, heated from the inside by a halogen lamp. The substrate has the possibility to move perpendicular to the target.

The laser used for this setup is a Lambda Physik LPXpro 210 pulsed excimer KrF with λ=248 nm and pulse duration of 20 ns. The maximum energy per pulse was 800 mJ and the pulse repetition rate may be tuned up to 100 Hz. The dimension of the laser beam at the output is $10\times24mm^2$ and it is focused on the target by a lens with the aid of set of mirrors suitable for this wavelength range, as shown in Figure 3.5. The laser enters the deposition chamber through a fused silica window and impinges on the target at an angle of 45° with its surface.

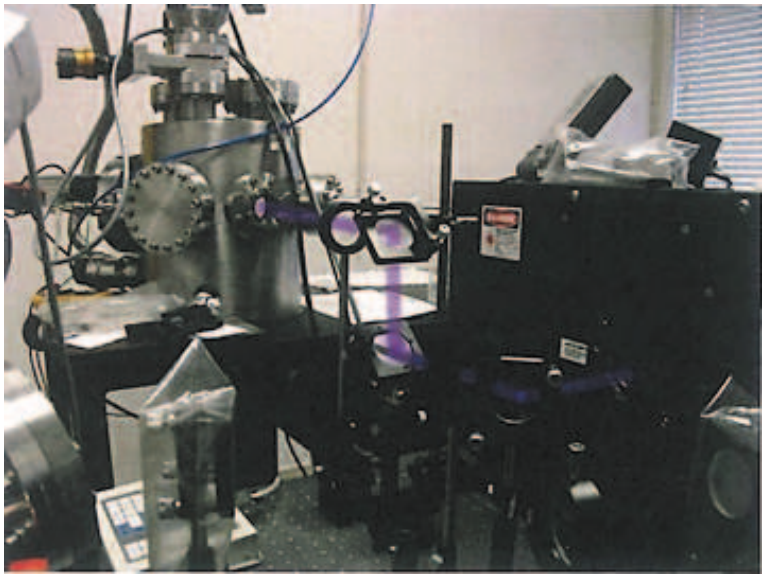

Figure 3.5: The optics of the pulsed laser deposition setup in Centro de Física da Universidade do Minho - Cooperative Phenomena in Dielectrics group. The purple line marks the path of the laser beam.

The oxygen flux into the chamber is controlled by a needle valve, and the pressure is measured by an AML Pirani gauge for rough vacuum and an MKS 943 cold cathode Penning gauge for high vacuum.

3.3.2 RF-sputtering setup

The thin films and heterostructures were sputtered with a RF magnetron sputtering device, Figure 3.6 (a), on well-cleaned substrates of:

- Sapphire; which is a single crystal form of corundum, Al_2O_3. It can be used for various semiconductor applications, with hexagonal structure, a=b=0.4785 nm and c=1.2991 nm. The c-axis cut [0001]-Al_2O_3 is used as a substrate in this work.
- p-doped silicon (Si), which has a cubic $Fd\bar{3}m$ (227) structure, with a=0.54311 nm is a very common semiconductor. The (100) cut of Si is used in this work.

The used sputtering system is a 2 inch planar circular RF sputtering gun, as shown in Figure 3.6. It consists of : (1) a sputtering gun head with 6.5 cm diameter and 4.5 cm height, to improve the film uniformity by adjusting the distance between target and substrate, (2) Teflon, to insulate the electrical part, (3) O-ring for vacuum seal between two electrodes, (4) permanent magnets, separated from cooling water to prevent erosion, (5) target holder, designed in a form to change the target, easily, pure oxygen free copper as the back plate of the target to reduce the impedance for ceramics targets, (6) a RF source, (7) a heating source to set the temperature of the substrates, which were fixed on a substrate holder, up to 950° C ± 2%. The configuration of the deposition system allows depositing up to four substrate, at the same time. Also a part of this sputtering system is the vacuum equipment which allowed the control of atmosphere inside the deposition chamber, which composed of two pumps, a rotary pump to achieve the 1E-3 mbar vacuum and afterward, there is a turbo-molecular pump to gain pressure $<$ 5E-8 mbar inside the chamber.

After mounting the substrates (Al_2O_3/Si) on the holding plate (heater), the chamber is closed and pumped below 5E-8 mbar. The next step includes heating up and stabilizing the temperature of substrate, then Argon gas (Ar) is introduced into the chamber to reach the desired pressure, which should not exceed from 1E-3 mbar. Argon is flushed and finally it is set into desired deposition pressure. This step is done to flush out the air molecules, if there is any left after evacuation. The next step is turning on the plasma power and RF source. The pre-sputtering step is done with the shutter closed to clean the target surface, removing oxide layer and other contaminations from previous depositions. The pre sputtering time depends on the sort of material to be deposited. After pre-sputtering, the substrate shutter opens and the main deposition begins.

After deposition is done, the RF power supply is turned off. Argon gas inlet is closed, turning off the heater, oxygen flow increases, usually up to ∼500 mbar, and wait until substrate cools down to room temperature. Then chamber vent valve is opened.

The cleaning of the substrates involved two steps. The first one consists of 10

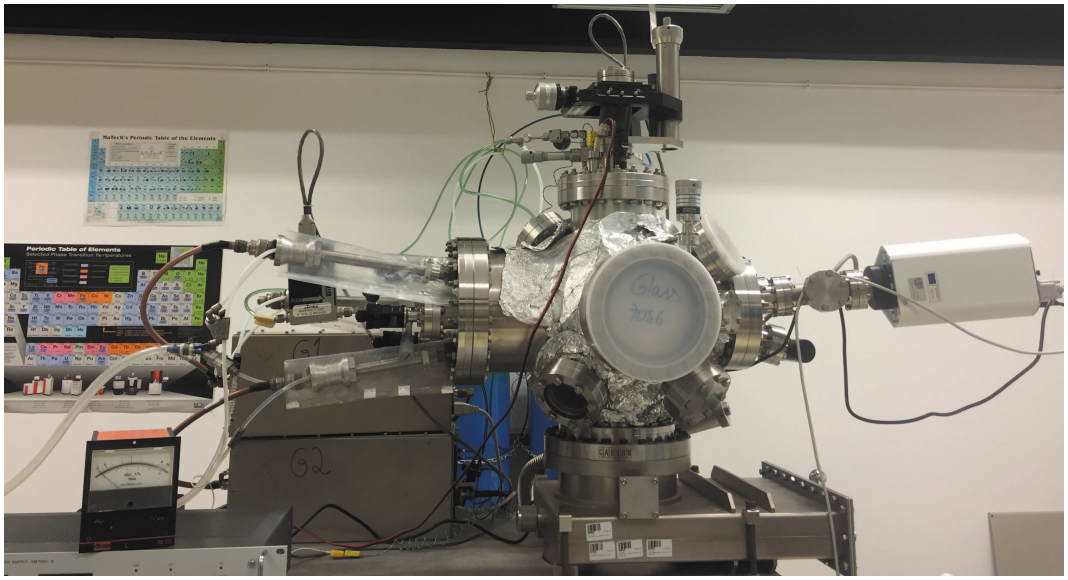

Figure 3.6: The sputtering setup in Departamento da Física da Universidade de Aveiro.

minutes immersing in acetone in ultrasonic bath to remove any existing grease. The second step is removing the acetone from the substrates by immersing them in an ultrasonic bath of ethanol for 10 minutes. Deposition parameters, used to grow thin films by RF sputtering is listed and shown later, in Chapters 5 and 6.

3.4 Structural characterization

3.4.1 X-ray diffraction (XRD)

The primary structural characterization of the deposited films were performed by X-ray diffraction. Since the X-ray wavelength is comparable to the interplanar distances in crystalline materials and it is a non-destructive method, it is a very useful technique in detecting crystalline phases, allowing for the determination of preferential crystallographic orientations in the samples, lattice parameters and strain states and the grain sizes. The conditions satisfying the X-ray diffraction are shown in Figure 3.7.

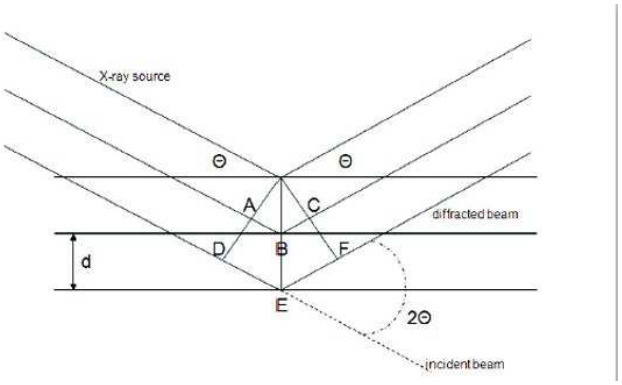

Figure 3.7: Diffraction of X-rays by a crystal [36].

When X-rays receive at an angle θ to the surface and separated by the distance of d_{hkl}, they generate a diffraction pattern. Obeying the Bragg's law, the diffraction maximum occurs at:

$$\sin\theta = \frac{n\lambda}{2d_{hkl}} \tag{3.2}$$

where λ is the wavelength of the incident radiation and n is an integer. Also the crystalline size and strain can be determined from the width of the XRD peaks using the Williamson-Hall equation:

$$\tau^2 = (\frac{k\lambda}{\beta\cos\theta})^2 + (4\epsilon\tan\theta)^2 \tag{3.3}$$

where τ is the mean size of the crystallized domains, k is the shape factor, that varies from 0.89 for spherical to 0.94 for cubic particles, λ is the X-ray wavelength, β is the FWHM and θ is the Bragg angle. Assuming cubic crystalline, the k = 0.94 is used in the calculations.

The peak broadening caused by instrumentation, β_{inst} can be estimated using the substrate diffraction peak and were fitted with a Gaussian profile. The width of this peak was subtracted from the diffraction peak of the film to obtain the FWHM of the film, via equation:

$$\beta^2 = \beta^2_{exp} - \beta^2_{inst} \tag{3.4}$$

In a typical θ-2θ technique, the data is only collected along $\omega = \theta$ line, consequently, there is no information along ω. By collecting the full map, it is immediately possible to have direct information on the structure.

The physical properties of the film is better revealed if the map is shown in the reciprocal space. The conversion can be done by using:

$$q_x = k(\cos(\omega+) - \cos(\omega-)) \tag{3.5}$$

$$q_z = k(\sin(\omega+) + \sin(\omega-)) \tag{3.6}$$

where $\omega+$ and ω- are the incidence and emergence angles of the X-ray beam relatively to the surface and k=K_i=K_s=$2\pi/\lambda$, as shown in Figure 3.8. The alignment along q_y indicates gradients of the c lattice constant in the film.

The measurements presented in this work were carried out in a Philips X'Pert MRD diffractometer, with a Bragg-Brentano ($\theta - 2\theta$) geometry schematically shown in Figure 3.9.

The most common measurement is performed in the θ-2θ geometry, in which the X-ray source does not move and the distance between the sample and the detector is constant for all values of θ. The sample is rotated around its axis by θ, while the detector simultaneously rotates by an angle of 2θ around the goniometric circle [146].

The peaks in the diffractograms of the samples were fitted with Pesudo-Voigt functions and the distances d_{hkl} between lattice planes in the films were determined by Bragg's law (Equation 3.2). After the determination of the interplanar distances, the crystallographic phases present in the sample were identified by comparison with the powder diffraction files from International Centre for Diffraction Data Database (ICDD). Diffraction peak broadening may be caused by several factors, including instrumentation, strain and heterogeneous composition of the samples, thickness, temperature and etc. [36].

The equipment uses Cu K_α radiation with a wavelength λ=1.54056 Å, generated by a tube running at 40 mA and 40 kV.

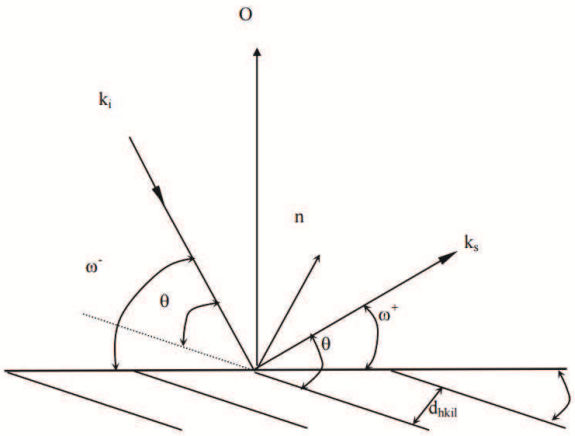

Figure 3.8: Geometry of the typical diffraction experiment, with ki and ks as the incident and scattered wave vectors, respectively, O as the surface normal, n as the normal of the reflecting planes.

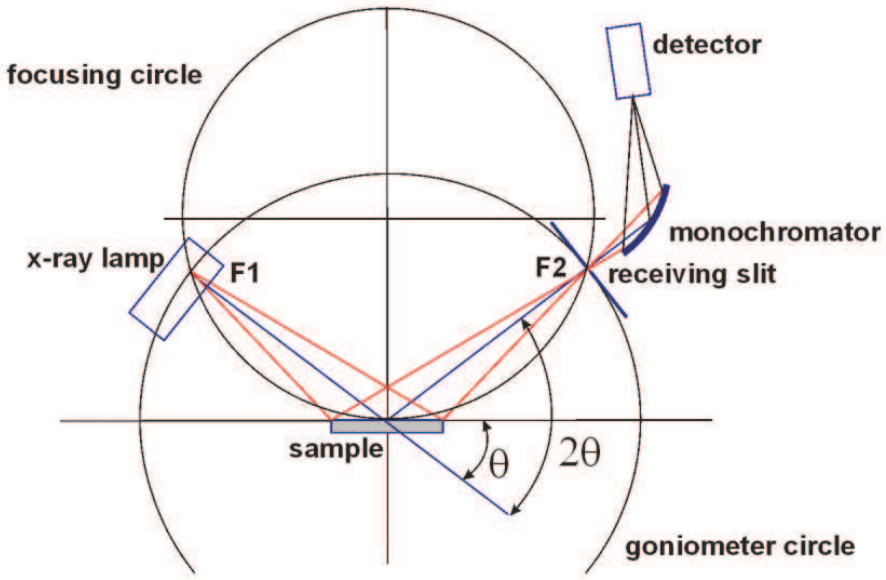

Figure 3.9: Diagram of the Bragg-Brentano geometry used in XRD measurements [145].

3.4.2 Rutherford Backscattering Spectroscopy (RBS)

RBS is one of the most used Ion Beam spectroscopic techniques for interface analysis, composition and crystallographic investigations. The basis of the technique is originated from the famous gold foil experiment done by E. Rutherford in 1911 on backscattering of α-particles from metal foils, i.e. gold foil, to study the fine structure of atoms, also resulted in mathematical description of the scattering, which nowadays, is used in RBS. The technique was developed mostly when the access to dc accelerators like Van de Graaff with 2 to 3 MeV energies became available. Since RBS technique deals with near surface region of materials, progress on thin film technology, mostly silicon based devices on 1970s, pushed researchers to use this technique for the characterization of the films and substrate.

Basically RBS technique can be used to elemental identification, composition, thickness, interfaces and diffusion process. Conventionally, RBS is done using light particles like alpha, proton, and deuterium in Van de Graaff accelerators, in the energy range of 0.5 MeV to 3 MeV, and in high vacuum. However, introducing of Tandem accelerators has improved significantly the capabilities on using range of light to heavy ions with higher energies more than 10 MeV, also proper for surface modification purposes. The resolution of this technique for thickness analysis on Si is 10 nm, in case of having a 15 keV detector.

The fundamental physics behind RBS technique is categorized to four important phenomena:

- Kinematic factor: This factor is simply the classical mechanics rules of the collision

of moving charged particles to a stationary atom inside a material. Since this factor depends only on mass of incident and target ions and the scattering angle after collision, it creates a way to identify elements in targets as in real experiment, the incident ion and scattering angles are two known parameters, and the only unknown parameter is the mass of the atom in the target material.

- Scattering cross section: This concept is directly linked to famous Rutherford "gold foil experiment". The mathematical description was developed to explain the backscattering of α-particles from metal foils. Cross section of the scattered ions depends on the atomic numbers of probing ion and target, scattering geometry and inversely to the energy of the incident ion. Basically it gives the number of scattering events, occurring during the collision of incident ions to the target atoms. Therefore the higher energy of the charged particles would result in less scattering events; on the other hand, heavier elements produce more scattering events.
- Stopping power and energy loss: The concept of energy loss comes from the scattering process upon entering a charged particle into the target materials. Because the charged particle has high energy, it can penetrate into the material, depending on its energy, atomic number, elements in the material, and also geometry of the experiment. The incident ion would suffer from penetration process and many collisions, until it is stopped and backscattered. Hence the amount of energy loss, for a known composition and density, corresponds to the thickness of the layers. In a RBS spectrum, the x-axis is given either per channel or energy of the backscattered ions, which is actually energies of the ions backscattered at different depths from elements present in the material. Our understanding on the thickness and diffusion process comes from this concept.
- Energy loss straggling: Upon entering charged particles into the material, the statistical collision process would cause the energy of the incident beam to spread, reaching the maximum depth inside the material. It does not show the same energy spread as it had already in vacuum. This phenomenon is important on setting the final energy resolution mostly on dealing with thin films or low content impurities and dopants in a material.

3.4.2.1 RBS-channelling

Our description of the RBS technique, was mostly valid for amorphous materials where preferential orientation does not exist. However, introduction of RBS concepts would be also very useful for many purposes when the incident ions can penetrate into a single crystal material. Since in a single crystal material, along main crystallographic

axes, the density of atoms of the target is lower than the one in an amorphous material, therefore the backscattering events are also lower. This concept is based on a very important technique, so-called RBS-Channelling, where the incident beam is directed along one of the main crystallographic axes of the crystal like (100) direction of silicon single crystal. Compared to random scattering when the beam is not aligned to any main direction of the crystal (also called random RBS or conventional RBS), the backscattering events drop even 100 times. Different atomic densities along main crystal directions would give rise to different backscattering events, this is used to identify the main directions. Also interfaces of the epitaxial layers or presence of impurities in single crystal bulk or film, which favours either substitutional positions of the lattice or interstitial sites, can be nicely resolved in RBS-Channelling technique.

RBS measurements were made at the Van de Graaff accelerator of LATR/IST, with 2 MeV $^4He^+$, in a small chamber, where three detectors are installed: standard at 140°, and two pin-diode detectors located symmetrical each other, both at 165°. Angle of incidence was 0° (normal incidence) and 30°. The RBS data were analysed with the IBA Data Furnace NDF v9.6h [147].

3.4.3 Scanning Probe Microscopy (SPM)

Scanning simultaneously in two perpendicular directions, which forms a square or rectangular area of specimen (called a raster) is employed in a scanning probe microscope, where the sharp-point tip is mechanically scanned in close distance of the surface of the sample to detect local properties. A remarkable feature in SPM is achieving the high spatial resolution; usually in order of 1nm in the Z-direction [145].

One type of SPM is atomic force microscope (AFM), in which the tip is brought close to the surface of the sample, in order to feels an interatomic force. The z-motion of the cantilever is usually detected by deflection of the reflected laser beam during scanning of the sample, as shown in Figure 3.10.

Piezoresponse force microscopy (PFM) measures the mechanical response caused by applying of electrical voltage to the sample's surface, using a conductive nano-sized tip of an AFM. In response to the electrical field, the sample will expand or contract, locally, as shown in Figure 3.11. When the tip is in contact with the surface and the local piezoresponse is detected as the first harmonic component of the tip deflection, the phase, ϕ, of the electromechanical response of the surface yields information on the polarization direction below the tip.

PFM requires detection of tip's small displacements induced by high frequency, and high amplitude voltages.

The relationship between the strain and the applied electric field in piezoelectric

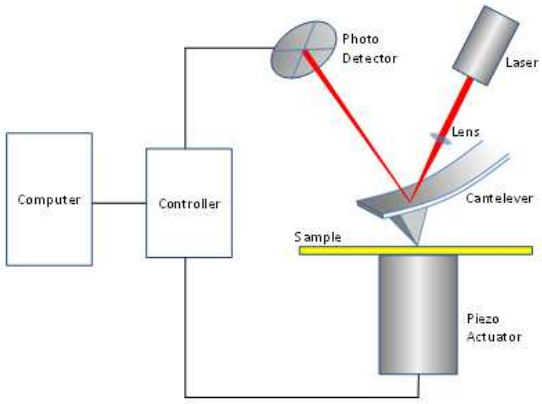

Figure 3.10: Principle of a scanning probe microscope; in the x- and y- direction, the tip is stationary and the sample is raster-scanned by piezoelectric drives [145].

materials is described as a 3-rank tensor. The most important component of this tensor for PFM is the d_{33} [148], since it couples into the vertical motion of the cantilever. When the voltage is driven at a frequency well below the contact resonance of the cantilever [149], the z-displacement of the tip is equal to:

$$z = d_{33}V_{dc} + d_{33}V_{ac}\cos(\omega t + \theta) \tag{3.7}$$

where we have assumed d_{33} depends on the polarization state of the material. From Equation 3.6 and Figure 3.11 the magnitude of the oscillating response is a measure of the magnitude of the d_{33} and the phase is sensitive to the polarization direction of the sample. On the other hand, the polarization direction of the sample determines the sign of the response. Figure 3.12 illustrates the idea.

When the polarization is parallel and aligned with the applied electric field, the piezo effect will be positive, and the sample will locally expand, and vice versa. This sign-dependent behaviour means that the phase of the cantilever provides an indication of the polarization orientation of the sample, while an oscillating voltage is applied to the sample.

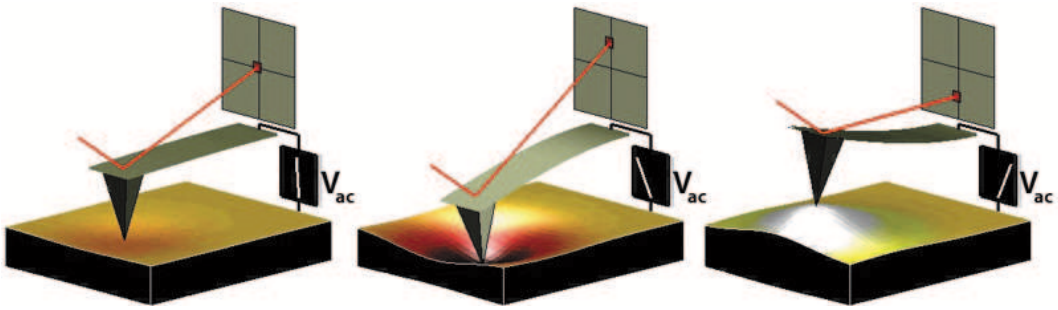

Figure 3.11: Depiction of PFM operation. The sample deforms in response to the applied voltage. This causes the cantilever to deflect, measured and analysed into a piezoresponse of the sample.

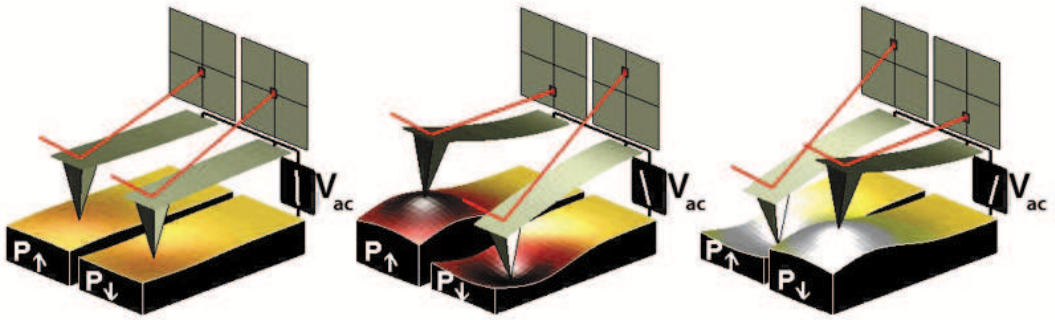

Figure 3.12: Sign dependence of the sample strain. When the domains have a vertical polarization that is pointed downwards and a positive voltage is applied to the tip, the sample will locally expand. If the polarization is pointed up, the sample will locally contract. The phase of the measured response is thus proportional to the direction of the domain polarization [149].

In vertical PFM imaging, out-of-plane polarization is measured by recording the tip deflection signal at the frequency of modulation. For ferroelectric applications, PFM can be used also to modify the ferroelectric polarization and also topography of the sample through the application of a bias. When the applied field is large enough, it can induce ferroelectric polarization reversal. This method can be used to 'write' single domains, domain arrays, and complex patterns without/with changing surface topography (poling). Other option using force microscopy is extracting the PFM spectroscopy i.e. the locally hysteresis loops in ferroelectric materials. From them, the information on local ferroelectric behaviour, such as local work of switching and nucleation biases can be obtained.

This can be the basis of the development and optimization of applications such as ferroelectric, non-volatile random access memory (FRAM). Figure 3.13 shows the basis of PFM spectroscopy.

The PFM measurements were done by the NTEGRA PRIMA and NTEGRA ARUA systems, provided by NT-MDT company, and installed in CICECO, Aveiro institute of materials, in Universidade de Aveiro. The cantilever used in this work is provided by NanoSensorstm co., made of silicon, coated by aluminium on the detector side (ppp-nchr-50). The tip height is 10-15 μm, owning the resonance frequency of 204-497 kHz. Their force constant is in interval of 10-130 N/m.

3.4.4 Energy Dispersive X-Ray Spectroscopy (EDS)

EDS is a chemical microanalysis technique, which uses the X-ray spectrum emitted by a sample, bombarded with a focused beam of electrons, to obtain a localized chemical analysis. When the sample is bombarded by the electron beam; electrons are ejected from the sample's surface, Figure 3.14(a). The resulting electron vacancies are filled

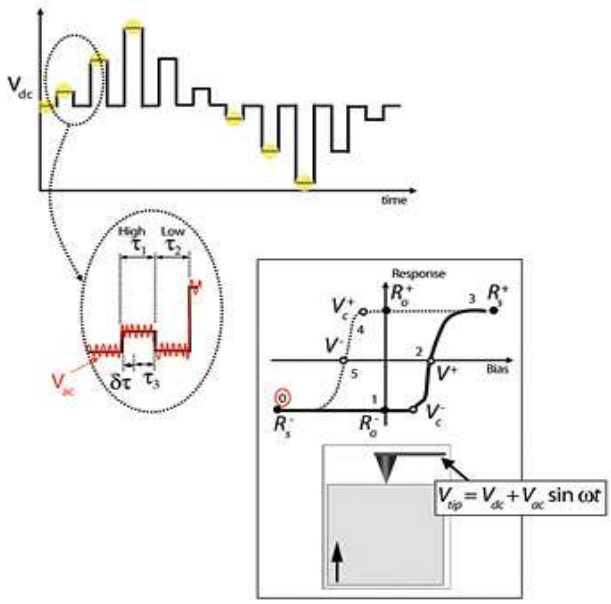

Figure 3.13: Switching spectroscopy PFM diagram [149].

by electrons from a higher state, and X-ray is emitted to balance the energy difference between states. This technique detects all elements from atomic number 4 (Be) to 92 (U). Having incidence of X-ray to the detector, a charge pulse is created proportional to the energy of X-ray. By an amplifier, the charge pulse is converted to a voltage pulse, and then is sent to the analyser, where they are sorted according to voltage. By displaying the intensity of a selected X-ray line, element distribution images or 'maps' can be produced. Also, images produced by electrons, collected from the sample, reveal surface topography or mean atomic number differences according to the mode selected. Features or phases as small as 1 μm or less can be analysed within this technique [150]. The output is displayed as a histogram of counts versus X-ray energy, as represented in Figure 3.14(b).

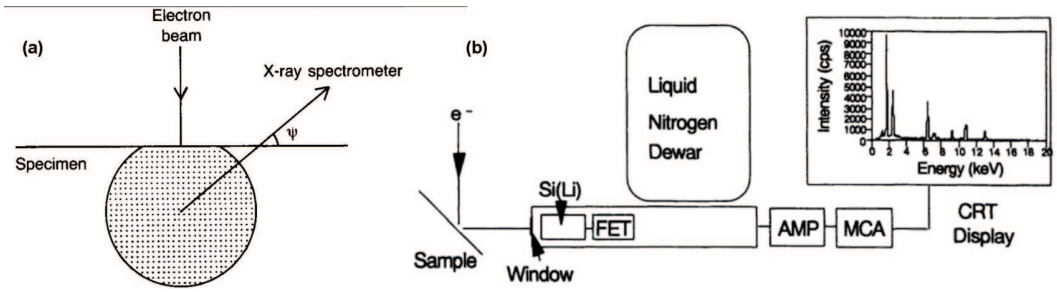

Figure 3.14: (a) X-ray source region, with path of X-rays to the spectrometer, (b) basic EDS schematics.

In the study of thin films, it is usually desirable to minimize the electron penetration in the sample and use a moderate voltage of 5 to 15 keV in SEM, ultimately being

able to detect even a monolayer of metal film on a substrate using K_α lines in lighter elements and L_α lines for heavier elements ($Z > 38$).

EDS systems are easy to use and controlled by computer, the basic operations include spectrum collection, peak identification, and background subtraction, while peaks deconvolution and quantitative analysis is software processed.

3.4.5 Particle-induced X-ray emission (PIXE)

Another method for determining of the elemental make-up of samples is particle-induced X-ray emission (PIXE). By exposing the sample to an ion beam, atomic interactions take place and X-rays are released. PIXE is a powerful technique for elemental analysis, first proposed in 1970 by Sven Johansson and developed over next few years by Roland Akselsson and Thomas B Johansson. Trace element analysis using PIXE has a detection limit orders of magnitude lower than can be attainable by x-ray spectrometry techniques using electron excitation. There are three type of spectra, which can be collected from PIXE experiment:

- X-ray emission spectrum,
- Rutherford backscattering spectrum and,
- Proton transmission spectrum.

The PIXE experiments were done in High Resolution High Energy Particle Induced X-ray Emission (HRHE-PIXE) facility, installed in Instituto Superior Técnico de Lisboa (IST), able to provide PIXE X-ray spectra covering an almost 120 keV window energy (from just below 1 keV up to above the 110 keV of the $^{19}F(p,p'\gamma)^{19}F$ nuclear reaction γ ray), while presenting a state-of-the-art relative resolution reaching 0.25% and always better than 1.5%.

3.4.6 Transmission Electron Microscopy (TEM)

To study the structure of thin films and interfaces and to have deeper understanding of materials near the interfaces, we need to look at the film not from top view, but from the cross-section view, which is significantly viable by using electron microscopes with nano-meter probes. In TEM as a common method for characterization of the layered materials, it is possible to do various analysis on the crystallographic structure, thickness, interfaces, atomic planes, probable defects and so on. It is also possible to compare the result of the experiments with other analytical methods like X-ray diffraction, and the results of simulations using available software for the microscopy.

In TEM a thin specimen is irradiated with an electron beam of uniform current density. This working voltage of TEM is in the range of 100-400KeV to get the image of

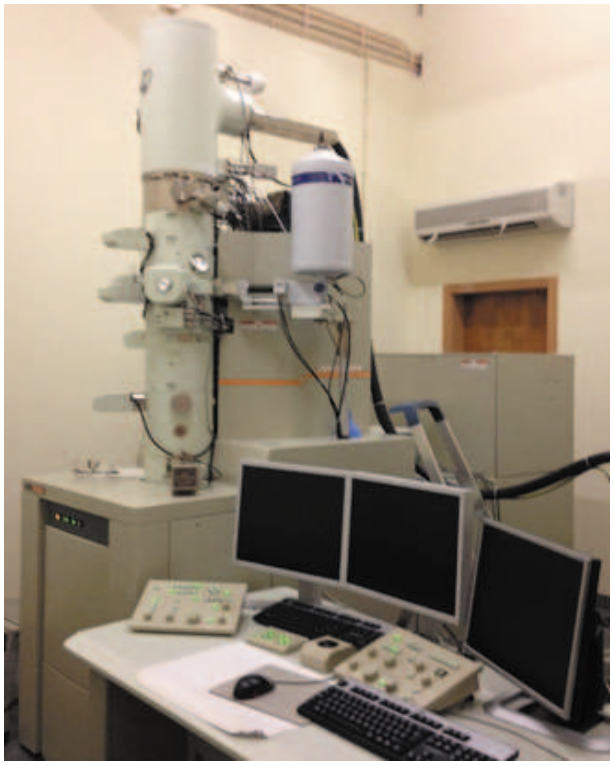

Figure 3.15: JEOL TEM microscope, used in thesis, Universidade de Aveiro.

samples. Electrons are emitted by the electron gun that can be thermionic, Schottky or field emission. The scattering process, which is used for the formation of electro-optical images by the electrons transmitted through the sample, is elastic scattering. The electrons emitted by the gun are accelerated through the accelerating anodes.

By the means of the three-stage lenses system, condenser, objective and intermediate lenses, Figure 3.15, the electron beam will be mono-energetic and also controlling the beam convergence is possible. The lenses system is responsible for forming, focusing, and magnifying the image on the viewing screen and the camera to record the image. The aberrations of the objective lens are so great that it is very important to work with very small objective apertures, to achieve a resolution needed.

The sample is illuminated by a broad parallel beam and the image is formed by the imaging lenses on the other side of the sample. Magnification has nothing to do with the size of the illuminated area; it is determined by the imaging lenses. The image is formed on an electroluminescent screen (or detector) in a fixed position in both modes of operation (imaging mode and diffraction mode). In imaging mode, the image plane of the objective lens is projected to the screen. In diffraction mode, the focal plane of the same objective lens is projected on the screen, which contains a diffraction pattern. A high vacuum system is necessary to remove interfering air molecules from the column.

In TEM using high resolution mode (HRTEM), dark field (DF) and bright field

Figure 3.16: Philips CM200 FEG microscope, used in thesis, FHI, Berlin.

(BF) mode, we will be able to realize any distortion related to the mismatching of the lattices or other effective factors, and additionally we can have an accurate assessment of the diffusion during deposition and presence of dislocations as two common observed phenomenon in thin film growth.

To overcome issues of preparing TEM thin cross sections of due quality, time was invested on sample preparation, using cross sectional kit of Gatan model 01.07. However, finally we came up with a more common sample preparation procedures of mechanical polishing and ion milling using dummy silicon, glued to sample. The essentials of the method of TEM thin section preparation were learnt from the experience of staff in Microscopy group of Fritz Haber Institute, Berlin. The list of in-house facilities used for sample preparation and mounting materials is given below.

1. Wire saw (WELL 3241)
2. Two polishing/grinder units: METASERV 2000 and PACE Technologies Nano 1000T Grinder/Polisher.
3. Dimple Grinder Gatan model 656
4. Gatan Cross Section Kit model 601.07000
5. UHU (PLUS SCHNELLFES) glues, their use depends on the preparation steps
6. Homemade Tripods for holding the samples during mechanical polishing

7. Gatan Precision Ion Polishing System (PIPS) dual milling model 691

8. Nanoclean Plasma cleaner model 1070 (4 min. under 50 W power of plasma)

9. Dummy silicon, CrysTec, P-type, 1-20 Ωcm, (100) orientation.

The preparation starts by gluing the film on dummy silicon to control the thickness of the sample during mechanical polishing. After curing, the prepared sample was mechanically polished down to 10 μm or less, the thickness being evaluated by the color of silicon made transparent (red color for 10 μm thickness). For diamond polishing, lapping papers were used in sequence of 30, 15, 9, 6, 3 and 1 μm particle sizes. Mechanical polishing was done on both sides of the prepared sample, on the second side it is done down to silicon transparency (red color of silicon). Final step of thinning to electron transparency was made by gentle ion milling of the samples. The Ar ion energy starts from 5 keV (10 min) then is successively decreased to 4 keV (20-40 min), 3 keV (10-20 min), 2 keV (10 min) and finally to 1 keV (10 min) with fixed angle of 4° for both, the top ion gun and the one from below. As an option of the PIPS equipment, the ion thinning can be done either in single mode or in double mode. In single mode, ions hit the sample once in each revolution of sample. In double mode, each ion gun is activated twice per revolution of sample. Experience showed that using the option of double mode modulation creates unwanted artifacts on thin edges of the particles under study. Therefore single mode option was always used in the first steps of ion milling with high energy of the Ar beam. Only in the final step of ion etching at low energy (1 keV) the double mode was used to remove the surface damaged region on the edge of thin sections created by ion thinning at higher energy. Copper rings are most commonly used to hold TEM samples. It was shown that the use of copper rings resulted in re-deposition of copper on the surface of the thin sections coming from hitting the ring by Ar ions during ion milling. Because the etching rate of Mo or Ti rings by the Ar ions is lower than for copper, mostly Mo rings were used to reduce re-deposition. All samples before TEM analysis were passed to plasma cleaner to remove surface contaminations.

Most samples were studied by JEOL JEM2200FS FEG TEM/STEM electron microscope using the electron gun energy of 200 kV, equipped with Omega filter for filtered energy TEM imaging and EELS in TEM mode and the EDS detector. The EDS analysis was done in STEM mode using 0.2 nm beam spot as the ultimately fine spot of this microscope. All HRTEM images were taken by introducing 10 eV energy slit to filter out the high angle scattered electrons and enhancing the contrast. None of the main TEM/STEM microscopes widely used during PhD work had Cs-corrector and sub-Å resolution or energy monochromator for better resolution in EELS.

3.4.6.1 Scanning transmission electron microscope

Another configuration of beam optics for electron in TEM is scanning transmission electron (STEM). In this mode of analysis, the optics of the microscope has been designed to transfer a probe with the size of electron beam, coming out of electron gun, to the sample. Because the formed electron beam is usually very fine, in the order of one angstrom, the probe, which will hit the sample, is very fine. This fine probe would provide point by point scanning of the sample, as it is done in SEM technique.

In STEM configuration the main part of beam optics is related to the condenser lens, where the size of electron probe can be defined, and on the contrary of TEM mode objective lenses do not play any role in the final image. Because the transmitted electrons from sample come from each point of the sample, the corresponding image is the real image of the sample, not the contrast image, as in TEM. This makes the interpretation of the image more straight-forward. Like TEM, in STEM one can look at electron beams parallel to optical axis of the microscope, bright fields image and for those which have been scattered from the optical axis dark field image. To take DF and BF images in STEM mode, there are different detectors, where in DF image there is high angular angle dark field (HAADF) detector, which capture electrons scattered with large angle from optical axis of the microscope. Because this kind of scattering is very sensitive to atomic number of the elements in the sample, the identification of light elements in matrix of heavy elements would be much easier than TEM. Also by removing the objective lenses and recent improvements on forming sub-angstrom electron probe the microscopes can reach a resolution as low as 50 pm.

3.4.6.2 Electron energy loss spectroscopy

When a fast ($\sim$ 100 kV) electron traverses a thin foil of a material, it may create various excitations by transferring (losing) energy to the material. Electron energy loss spectroscopy (EELS) probes the primary excitation and registers each excitation event independently of the exact de-excitation mechanism.

There are three energy regions identified in energy loss spectra. Energy losses of a few meV to a few hundred meV are predominately due to vibrational excitations (phonons), but unfortunately they only can be studied with energy resolution significantly better than is typical of most EELS systems. Collective excitation (plasmons), intraband and interband transitions cause energy losses between a few eV and about 40eV. At energy losses above 40 eV, there is the inner shell excitations. These occur at energies:

$$\Delta E = E_F - F_B \tag{3.8}$$

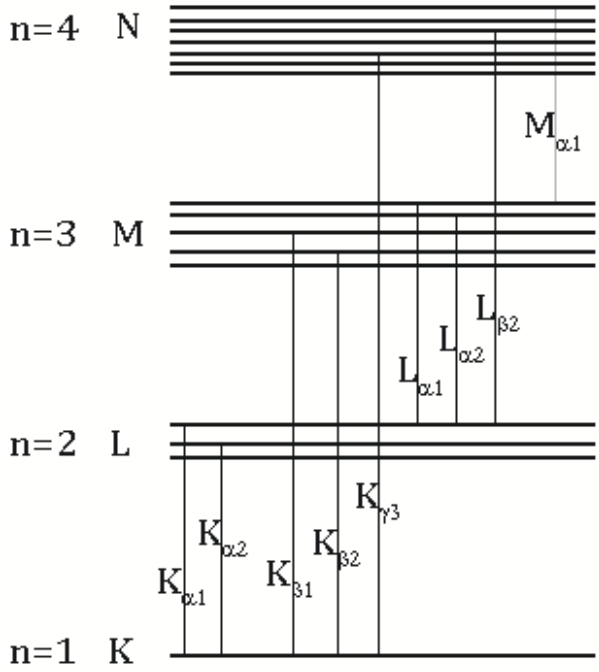

Figure 3.17: Inner shell edges label in standard spectroscopic notation, for cupper.

where Δ E is the energy loss, E_F is the Fermi energy level, and E_B is the binding energy of the inner shell. The corresponding feature in an energy loss spectrum is an inner shell loss edge, whose threshold energy agrees to within a few eV with the known ionization for the appropriate electron shell of the atom. EELS of inner shell losses therefore provides a convenient method of identifying atoms of different types in a thin foil of a material.

The various inner shell edges that can arise are labelled following standard spectroscopic notation as shown in Figure 3.17. Not all the transitions listed occur in every atom.

In general, there is always at least one strong edge in the usable energy region 100-3000 eV for every element.

3.4.6.3 EELS mapping

Demand for higher (atomic) resolution in chemical mapping, based on fine edge of elements, pushed people to develop EELS mapping technique in STEM mode. Because in STEM mode the electron probe is very fine, in order of sub-angstrom, to record an image, this features of STEM would make it possible to perform point by point analysis. Keeping all advantages of imaging based on fine edges of elements, explained in EFTEM, in EELS-STEM mapping there is possibility of choosing more than one edge, means that two or three elements can be mapped simultaneously. Current resolution of

chemical analysis in EELS mapping can reach as good as better than 80 pm. Another advantage of EELS mapping in STEM is resolving atoms with large difference in atomic numbers, due to the EELS HAADF detector.

3.4.6.4 Energy filtered TEM

One of the intriguing Analysis, which can be done in TEM by combination of imaging and spectroscopy, is EFTEM. In this technique specific edge of an element, which can first be checked in EELS spectra, would be chosen and then a TEM image will be taken by filtering out the signal of other elements, present in the sample. Therefore, energy filtered transmission electron microscopy (EFTEM) will provide chemical information about the presence and distribution of specific element in the sample. Although this kind of elemental analysis is done regularly in EDS spectroscopy, the advantage of EFTEM is the ability to detect more precisely light elements, also those elements which have close atomic number, and in EDS, their signals overlap together and makes the identification and quantification difficult, can be diminish.

To perform EFTEM imaging, the TEM instrument should be equipped to energy filter system which include lenses designed to apply energy shift from zero to normally 2000 eV on the energy of electron beam coming from electron gun. Another advantage of EFTEM is the time needed to acquire an image, which is less than two minutes, useful to avoid damaging of the sample or drift problem, at high magnification. However, the disadvantage of EFTEM is that still it does not provide the lattice resolution, as well as the normal image, and usually it is possible to take image of only one element. To take the image of few elements, we need to shift the energy filter lenses to the edge of that specific elements which may introduce some break between different image acquiring of few elements or slight change in the alignment of the microscope.

Main characteristics of TEM microscopes of general for the works of the PhD thesis:

1. LaB_6 Hitachi TEM H-9000NA 300 kV TEM/STEM microscope with BF STEM detector, of ultimate point resolution 0.20 nm at 300 kV in TEM, equipped with a 4 Mp digital camera and EDS detector from Bruker (Laboratory of Electron Microscopy, CICECO/DEMaC). Offers the advantage of easy use, the high gun voltage 300 kV, less sensitive sample preparation compared to 200 FEG microscopes, large angle of double tilting holder. It limited to the only mode ADF-STEM and of lesser resolution.

2. JEOL TEM-2200FS 200 kV FE-TEM/STEM microscope equipped with in-column Omega Filter for EELS of 0.8 eV zero-loss resolution and filtered energy TEM image, BF/DF STEM detectors, electron diffraction SAED and CEBD, EDS of

Oxford, INCA system (Laboratory of Electron Microscopy, CICECO/DEMaC). Ultimate point resolution 0.19 nm in TEM, 0.20 nm (BF) and 0.13(6) nm (ADF) in STEM. It offers several advantages: the high resolution with the SFEG in conventional TEM/STEM, omega filter for EELS and energy filter imaging, BF/DF STEM imaging, light element EDS detector and EDS mapping. The disadvantages are the more complex alignment of the electron beam for each image mode of microscopy and smaller tilt angles of double tilt holder. As in all HRTEM imaging it demands very careful TEM thin section elaboration.

3. Philips CM200 FEG TEM/TSEM 200 kV microscope with maximum resolution of 0.18 nm, equipped to GIF camera (Tridiem) and EDS Genesis 4000 unit. (FHI, Berlin, http://www.fhi-berlin.mpg.de). In high resolution in TEM, post-column Gatan Camera for EELS and energy filter imaging, EELS spectroscopy presents a true advantage and makes operations much easier than omega filter in JEOL. There are however some disadvantages for the advanced user: not efficient STEM, not as robust for image filtering and less efficient for EDS.

3.4.7 Magnetometry

Magnetic measurements were carried out with Superconducting Quantum Interference Device (SQUID) magnetometer in Departamento da Física, Universidade de Aveiro. SQUID magnetometer uses a Josephson junction and a resonant radio frequency circuit, as shown in Figure 3.18(left), in order to measure the magnetic moment of the sample in absolute values. The electric current density through a weak contact between two superconductors is proportional to the phase difference of the wave functions of the superconductors. The great sensitivity of the SQUID devices is associated with measuring the changes in magnetic field associated with one quantum flux. In the used instrument, Quantum Design MPMS3 in Departamento da Física da Universidade de Aveiro, the measurements are performed via the VSM (Vibrating Sample Magnetometry) and dc detection modes. dc scan mode provides continual plotting and capturing raw data points at static or sweeping fields and temperatures, while in the VSM mode, the sample oscillates at frequency ω about the very centre of the detection coils. These oscillations induce the magnetic flux and generates a SQUID signal, V, as a function of time, t:

$$V(t) = AB^2 \sin^2(\omega t). \tag{3.9}$$

because V(z) = Az^2 for small vibration amplitudes, and z(t) = Bsin(ωt). Here A is a scaling factor related to the magnetic moment of the sample and B is the amplitude

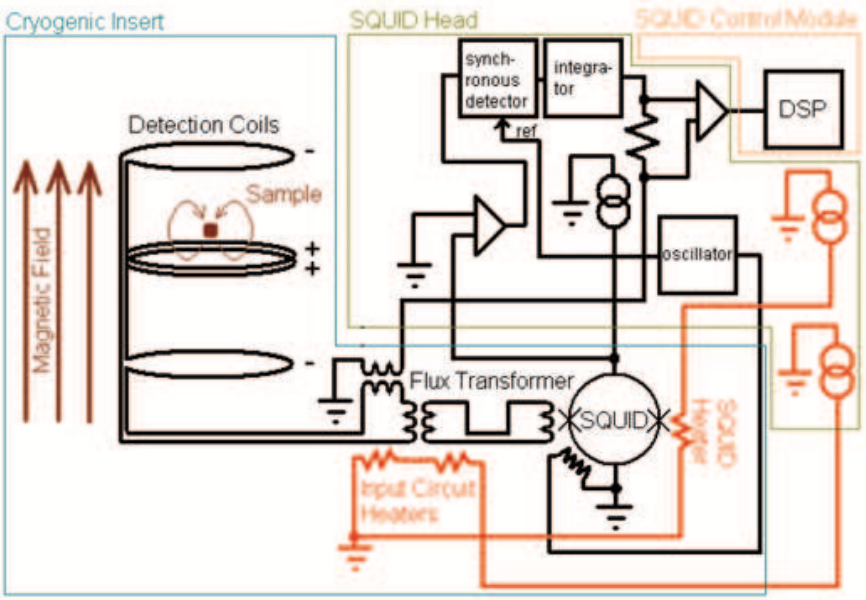

Figure 3.18: (Left) A simplified model of the MPMS SQUID VSM detection hardware, (right) the MPMS3 SQUID system, Universidade de Aveiro, Departamento de Física.

of sample vibration. It provides the ability to achieve the sensitivity of 1.0E-8 emu for applied magnetic field below 2500 Oe and 8.0E-8 emu for applied magnetic field above 2500 Oe. In this work VSM mode is used, due to higher data points, which provide higher precision for the user. The default vibration frequency is 14 Hz and has been selected by the manufacturer to optimize sensitivity based on the mechanical properties of the instrument.

The M-T measurement at zero magnetic field and M-H at T=5 K, on the quartz sample holder+ GE varnish, is shown in Figure 3.19. The data is used to remove the contribution of the sample holder from the measurements.

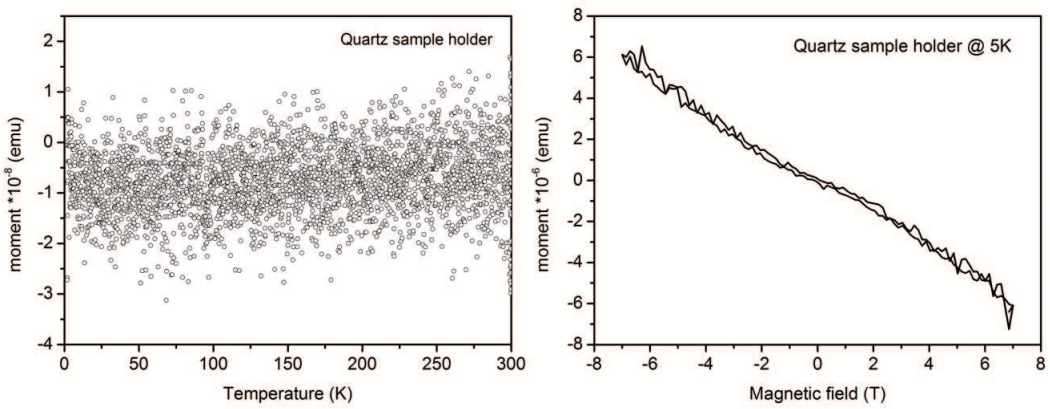

Figure 3.19: The signal of the quartz sample holder, during the M-T measurement at zero magnetic field (RMS= 7E-9 emu) (left) and M-H measurement at T= 5K (left). Both measurements were done in VSM mode.

Considering the fact that sample dimensions are much smaller than the dimensions of the detection coils, the current in the detection coils is a function of the sample position. The current in the detection coils is inductively coupled to the instrument's SQUID, which serves as an extremely sensitive current-to-voltage converter. The SQUID voltage is amplified and digitized by the instrument electronics.

The instrument is calibrated with a circular cylinder of palladium that is supplied with the system, with diameter 2.8 mm and height 3.8 mm.

The samples are mounted on a quartz sample holder, by using of GE Varnish, inside the plastic straw, as shown in Figure 3.20. The holder is then attached to the tip of sample rod. Centring the sample is done before measurements, using the provided software, in order to maximize the SQUID signal and ensure that the signal is acquired in the sample region.

Figure 3.20: Thin film sample mounted for magnetization measurements.

Measurements of the magnetization versus temperature were performed by cooling the samples without any applied magnetic field (zero-field cooling (ZFC)) to 20K, using the rate of 10K/min. Reaching the desired temperature, a small magnetic field (100 Oe) was applied in the heating up to 350 K, in 3 K/min, and measure the magnetic moment of the sample. The second cooling down of the sample happens with the applied field (field cooling (FC)) and the measurements is done during heating. The magnetic hysteresis cycles were done at stabilized temperature and the magnetization were measured versus applied magnetic field in range of -20000 Oe to +20000 Oe, using the rate of 100 Oe/min for magnetic field, in logarithmic space filling.

3.4.8 Four-point linear probe technique

The four-point probe is a common method for measuring electrical resistivity and was originally developed by Wenner in 1915 for geological investigations and adapted for semiconductor resistivity by Valdes in 1954 [151]. The technique is a very simple technique and as its name implies, is composed of four equally spaced points which are placed on the surface of the material. Two of the points lying on the inside, are used

to measure the potential difference. By passing a current through two outer probes and measuring the voltage through the inner probes allows the measurement of the sample resistivity. In this work this method is used to measure the resistivity and magnetoresistance of the films prepared. In Figure 3.21, there is a schematic of the four point method presented.

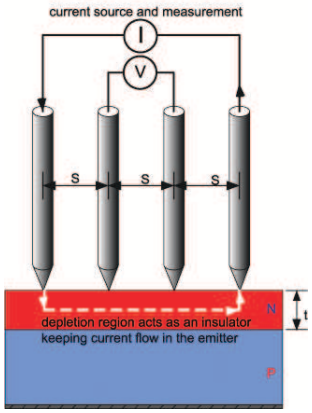

Figure 3.21: Schematic presentation of the four point method [152].

The relationship between the resistivity, the voltage and current present in the sample is given by [152]:

$$\rho = \frac{V}{I}\frac{l \times t}{s} \tag{3.10}$$

where ρ is the resistivity of the film (Ω.m), V is the voltage (V), I is input current (I), t is the thickness of the film (m), s is the distance between electrodes (m) and l is the width of the sample (m).

The resistivity and magnetoresistance measurements were done in the equipment in Departmento da Física, Universidade de Aveiro, using 1.0 μA current. The system consists of an Agilaent 34420A Nanovolt/Micro-ohm Meter and a Keithley 6221 stabilized electric current source. The temperature is controlled via a Lakeshore 325 temperature controller, capable of 0.001 K precision. Also a Multimag magnetic field generation system was used to provide the required field, which consists of a NdFeB permanent magnet, able to geometrically combined to generate a continuous magnetic field, up to 1 Tesla intensity and a 360° horizontal orientation. The samples were fixed to the holder using GE-VarnishTM, and electric contacts were made by thin 0.1 mm copper wired and silver paint from the connectors. The measurements of the resistivity versus temperature were performed by cooling to 150 K and warming up the samples without magnetic field. The magnetoresistance measurements were done in fixed temperature, by changing the applied magnetic field in parallel to the current, ranging from 0.0T to 1.0T, by step of 0.1T. The magnetoresistance is defined as:

$$MR\% = \frac{\rho(H) - \rho(0)}{\rho(0)} \times 100 \tag{3.11}$$

where ρ(H) and $\rho(0)$ are the resistivities at magnetic field H and at zero magnetic field, respectively.

3.4.9 Software for data analysis and simulation

- TEM based techniques: TEM/EELS image recording and data acquisition were done both using proprietary Gatan Digital Micrograph 1.84.1282. Image processing to reduce the noise and to subtract the background from EELS spectra were also performed using Gatan package.
- TEM image simulation: The simulation HRTEM images was done using proprietary JEMS package and Multislice approach embedded in the package, by introducing a relevant crystal structure. Depending on the TEM microscope used to acquire specific image, a set of experimental parameters such as energy of electron beam, energy spread of the gun, values of the spherical C_s and chromatic C_c aberration coefficients, the half angle value for incoming electrons to the sample was inserted into program. The kinematical diffraction pattern simulation was often carried out in JEMS for relevant cases in this study.
- AFM/PFM image processing: WSM 5.0 Develop 7.0 free package was used to carry out image processing, data analysis and noise reduction of the AFM/PFM data. As complementary software, Image Analysis 3.5.0.13365 NT-MDT was used to calculate the piezoelectric coefficient for selected samples.
- XRD/RSM pattern analyzing: PANalytical X-Pert Epitaxy was used for XRD analysis, in calculating the instrumental contributions for XRD of the diffractometers machines used in the present study.
- XRR analysis: Open access Parratt 32 was the package selected for XRR reflection analysis and simulations.
- Magnetic simulations: Mean-Field Simulation Suite software was used to simulate the magnetic phases.
- Data analysis: OriginPro was generally used to analyze and plotting data and to write short iterative programs for Curie-Weiss fitting.

Chapter 4

Structures on $SrTiO_3$ substrate

4.1 $La_{0.67}Sr_{0.33}MnO_3$ thin film deposition

The deposition of the thin films were carried out on (100)-$SrTiO_3$ substrate, using a pulsed laser deposition setup facility in Centro da Física da Universidade de Minho. A KrF excimer laser (λ=248nm) was used with pulse duration of 25 ns and energy density of 1.5 J/cm^2, focused onto LSMO manganite target prepared by solid state method [153, 115]. A 0.8 mbar oxygen atmosphere was introduced during deposition and the cooling down of the samples was done at pure oxygen atmosphere at 7 °C/min after deposition. The target-to-substrate distance was kept at 5.5 cm constantly, during deposition. The produced samples are varied in thickness, between 13.5 nm to 320 nm (13.5, 45, 110, 200 and 320 nm), extracted from TEM analysis. The deposition parameters of the LSMO samples are shown in Table 4.1.

Table 4.1: Deposition parameters of LSMO thin films, by PLD system.

Sample	Deposition					Cooling (oxygen)
	Temperature	Energy Density	Distance	P_{O_2}	Time	Rate
	°C	J/cm^2	cm	mbar	min	°C/min
LSMO 13.5	700	1.5	5.5	8.0 E-1	15	7
LSMO 45	700	1.5	5.5	8.0 E-1	30	7
LSMO 100	700	1.5	5.5	8.0 E-1	45	7
LSMO 200	700	1.5	5.5	8.0 E-1	60	7
LSMO 320	700	1.5	5.5	8.0 E-1	80	7

4.2 X-ray diffraction characterization

The X-ray diffraction diffractogram, shown in Figure 4.1 for the 200 nm LSMO film, presents the crystalline growth of the film, following the (100) orientation of the substrate. Regarding the splitting of the peak at higher angles of the spectrogram, the film structure is indexed to the Rhombohedral $R\bar{3}c$ (167) space group [153, 115], which was verified by HR-XRD measurements at the most representative allowed reflections.

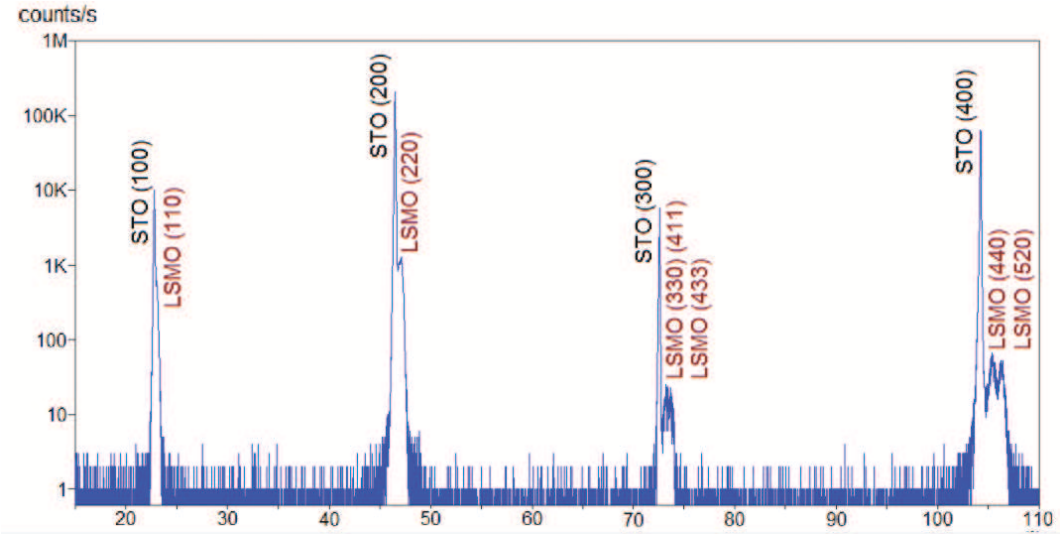

Figure 4.1: X-ray diffraction pattern of the 200 nm LSMO thin film, showing the preferential growth in the [110] direction, following the [100] direction of $SrTiO_3$ substrate, from ref. [115].

However, a detailed look at the splitting of the peak at higher angles of the diffractogram, the film structure is composed of two composition, indexed from PDF files of $La_{0.7}Sr_{0.3}MnO_3$ ((012) family) and $La_{0.98}Sr_{0.02}MnO_3$ ((002) family) with Orthorhombic Pbnm (62) space group. The close look at peaks of substrate, along with film peaks are shown in Figure 4.2. The existence of a second phase is also proved by STEM results, presented in following pages.

Specific details of the structure are further revealed through of the asymmetric pole figures and reciprocal space mapping (RSM), shown in the following for some representative samples. For the 200nm LSMO thin film, the HR-XRD results point to approximately 0.44% compressive deformation relative to the conventional bulk form (a = 5.472Å, $\alpha = 60.354°$) [154] for the $d_{(110)_R}$ planes. The 2D asymmetric pole figure performed at the most intense reflection ($2\theta = 32.60°$), shown in Figure 4.3(a), suggests some relaxation of $(101)_R$ and (211)R planes of LSMO film relative to the substrate $(110)_C$ plane, denoted by the four peaks elongation in Ψ angle. The Ω versus 2θ map, shown in Figure 4.3(b), centred at $2\theta = 46.50°$ and $\Omega = 23.25°$, covers the STO $(200)_c$ peak and the $(220)_R$ peak of the LSMO film. The strong spread $\Delta\Omega$ (2°) of the latter peak, diverging from the substrate peak shape, evidences the existence of a significant

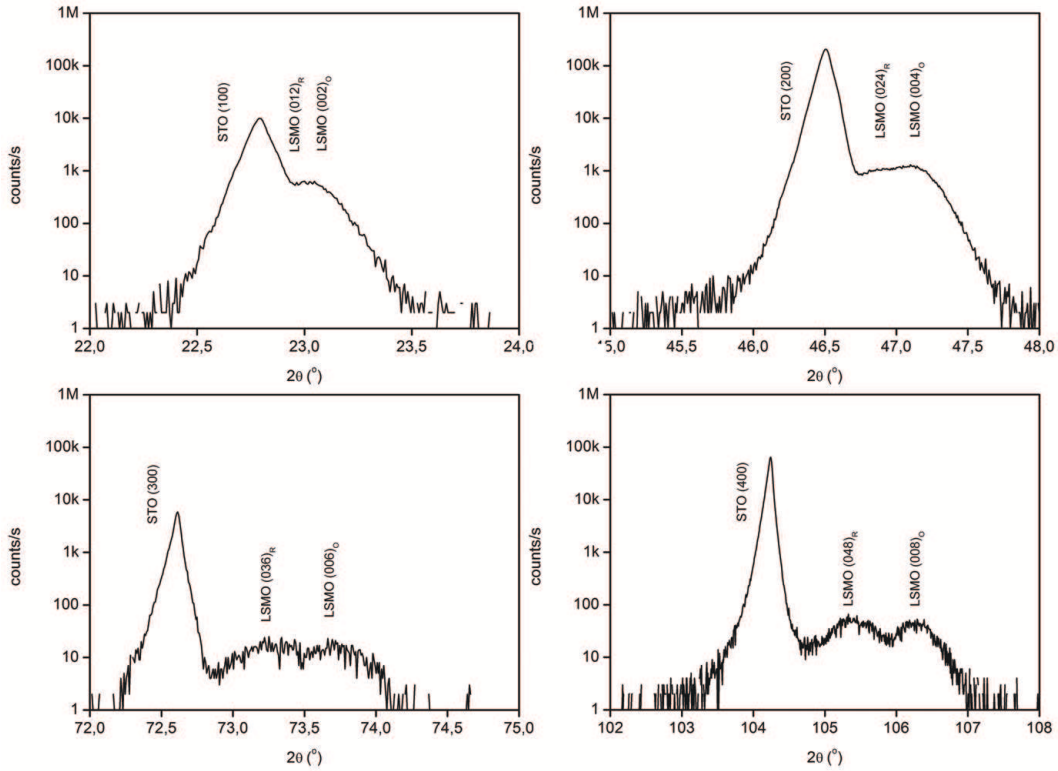

Figure 4.2: Zoom in the XRD pattern of 200 nm-LSMO thin film shows the existence of a secondary phase.

mechanical tension, which yields a partial bending of the film planes. Moreover, the elongation of the peak in $\Delta\theta$ (0.5°) can be associated with $d_{(220)_R}$ plane relaxation across the film growth direction. This relaxation may not be homogeneous as observed by Ranno et al [155].

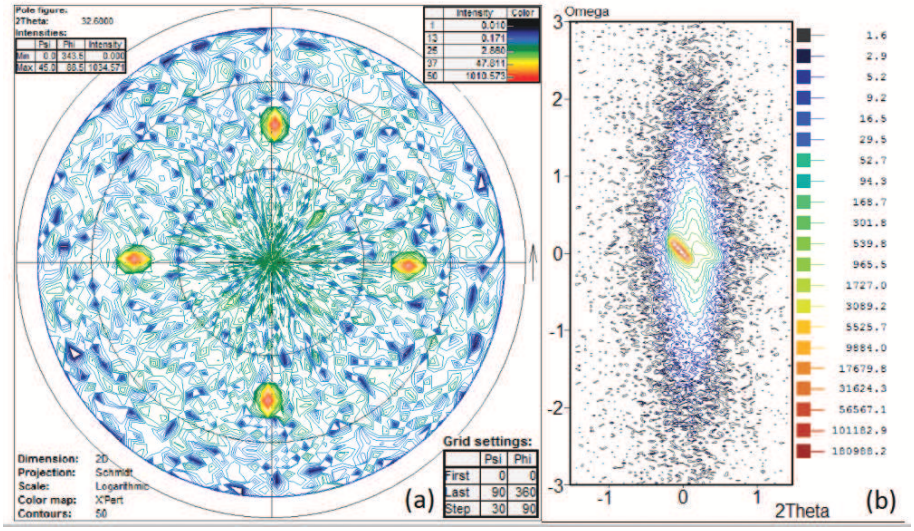

Figure 4.3: 2D asymmetric pole figure at 2θ= 32.6° of the 200nm LSMO thin film (a) and HR-XRD map centered at 2θ=46.50° and Ω=23.25° (b) [115].

4.3 Magnetic properties of LSMO samples

The magnetic properties of the as-processed thin films show an abnormal behaviour in temperature dependent magnetization M(T) below antiferrodistortive $SrTiO_3$ phase transition, at T≈ 100 K [115]. Films with thicknesses above 100 nm show an in-defect magnetization, as shown in Figure 4.4, where below 100 nm, the magnetic behaviour of the samples show an in-excess magnetization, in the same temperature region.

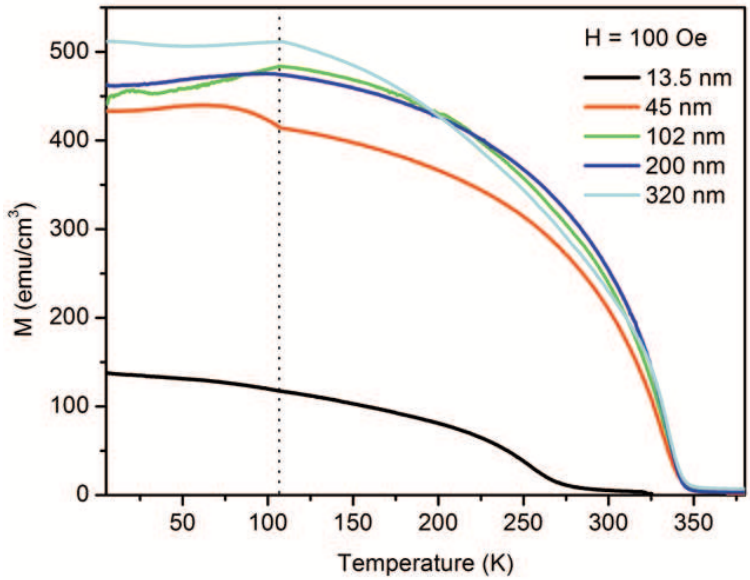

Figure 4.4: M-T curves of LSMO thin films, with different thicknesses.

Figure 4.5(a) and (b) show the dc magnetization for the 45 nm and 200 nm LSMO film, respectively, measured after field cooling the sample under an applied magnetic field of 100 Oe, parallel to the film plane. The temperature dependence of the dc magnetization, recorded above 110 K, follows a smooth behaviour, from fitting a Brillouin like curve to the experimental results, but it deviates from the Brillouin curve below 110 K. The film exhibits a ferromagnetic-like behaviour, with a Curie temperature T_c = 344 K, which is in good agreement with earlier published results [156]. Below T_{STO}= 105 K, the low field magnetization exhibits two distinct anomalous behaviours, starting to deviate from the smooth Brillouin like curve, depending on the film thickness. The 'in-excess' and 'in-defect' magnetizations in Figure 4.5(a) and (b) refer to non-thermodynamic equilibrium magnetic deviations from the expected Brillouin behaviour observed at T_{STO}, when magnetic fields below the saturation value are used. In this regard, this terminology refers only to low field magnetizations. Such deviations are associated with distinct magnetic domain patterns created by the clamping to the substrate for low film thicknesses and by the film strain relaxation for higher film thicknesses.

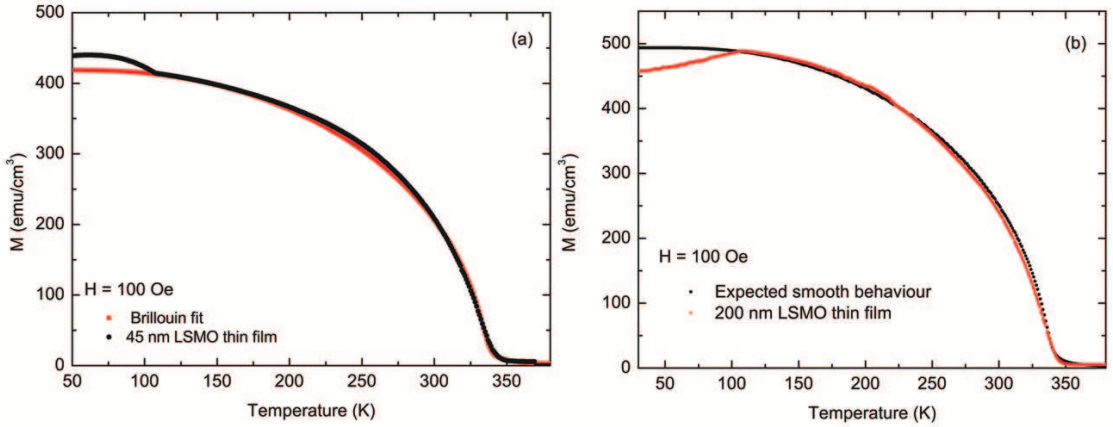

Figure 4.5: Temperature dependence of the 45nm (a) and 200 nm (b) LSMO thin film magnetization, measured in FC conditions with 100 Oe applied magnetic field. The expected smooth behaviour dots are obtained from a simulated Brillouin-like curve [153, 115].

Figure 4.6 shows the coercive field measured at 60 K and 120 K, as a function of film thickness [115]. It is obvious that for lower thicknesses, the coercive field, measured at 60K, is much larger than the one measured at 120 K. The results show the existence of a critical thickness, close to 100 nm. The films with the thickness below 100 nm are more sensitive to structural changes induced by the substrate. To study the effect of film structure, TEM and HRTEM studies were done on the set of samples.

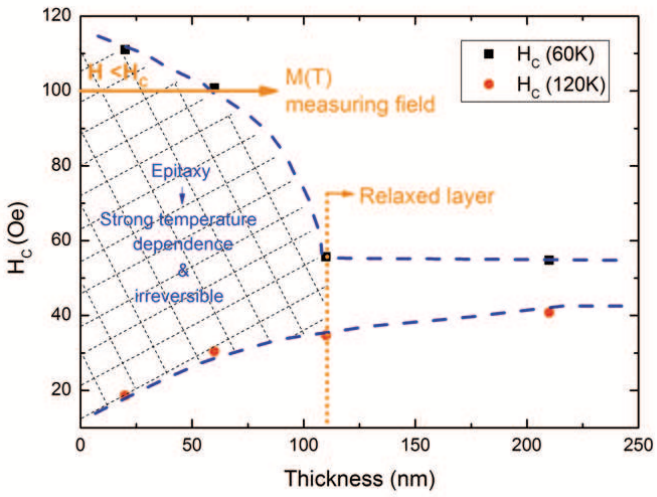

Figure 4.6: Thickness dependence of the coercive field measured at 60 K and 120 K, adapted from the work of Mota et al. [115].

4.4 Microstructure analysis

To investigate the distortion in magnetic properties of produced films, microstructure, strain and lattice order must be taken into account. Basically, strain is a function of

lattice and thermal expansion mismatch between film and substrate, which can results in additional distortion/rotation of MnO_6 octahedron [157, 158]. In this manner, epitaxial strain imposed by substrate is additional factor to tune the functional properties [71, 76]. To study the microstructure of the LSMO, TEM studies on the cross-section 320 nm LSMO sample were performed in Laboratoire de Cristallographie et Sciences des Matériaux (CRISMAT), Caen, France, and for the 200 nm LSMO sample, in Fritz Haber Institute of the Max Planck Society, Berlin, Germany. The other samples (13.5 and 45 nm-thick film) were measured by JEOL TEM-2200 FS-200 kV, field emission TEM equipped with in-column Ω filter, in Departamento de Engenharia de Materiais e Cerâmica, Universidade de Aveiro.

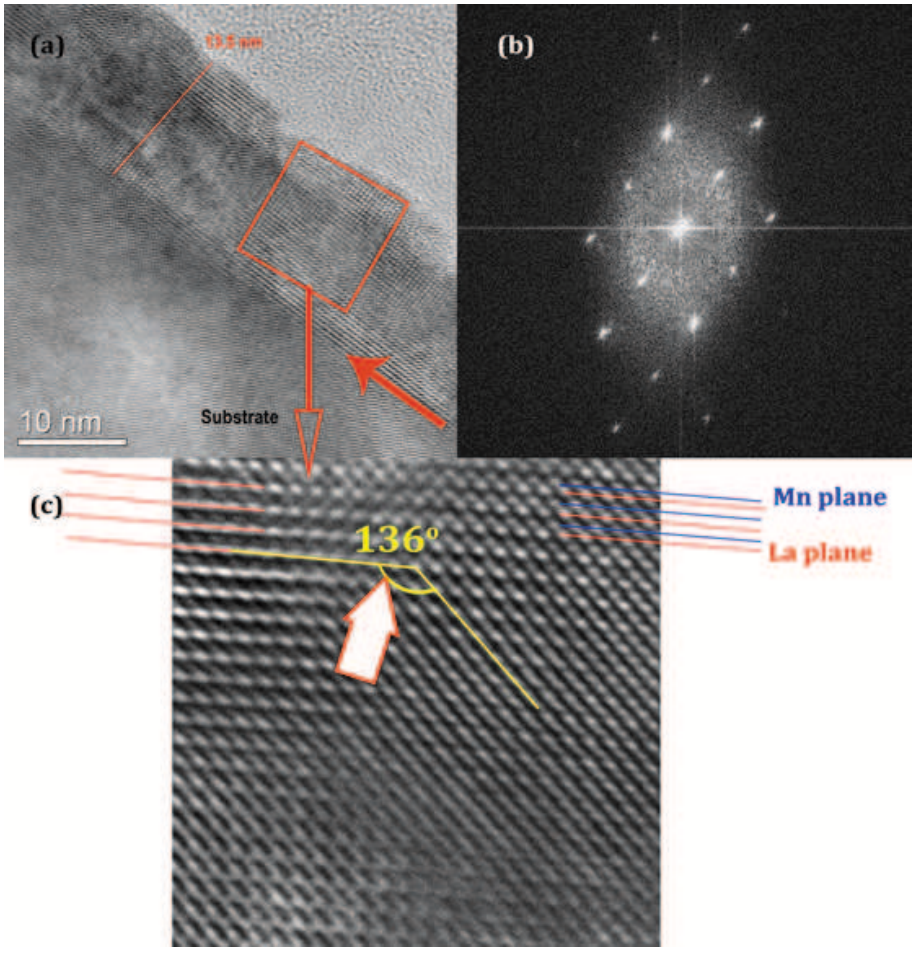

Figure 4.7: (a) Cross-section micrograph of LSMO thin film on $SrTiO_3$ substrate. The growth direction of the film is found to be $<201>_{LSMO}$ on $<100>_{STO}$. The film thickness is shown in TEM, 13.5 nm, (b) the FFT shows epitaxial growth of the film, and (c) a detailed micrograph of film shows a twinning, where Mn planes become clear in the structure, as well.

Figure 4.7 shows the cross-section micrograph of LSMO thin film, with 13.5 nm thickness. The crystallinity of the film is evidenced in the micrograph. FFT of the image shows the crystalline structure of the film, where the diffraction spots are elongated.

This points out for some strain in the structure of the film, in the growth direction. The growth direction of the film is found to be $<201>_{LSMO}$ (rhombohedral phase) on $<100>_{STO}$. Also, a close look at the film shows twinning in the structure, marked with an arrow in Figure 4.7(c).

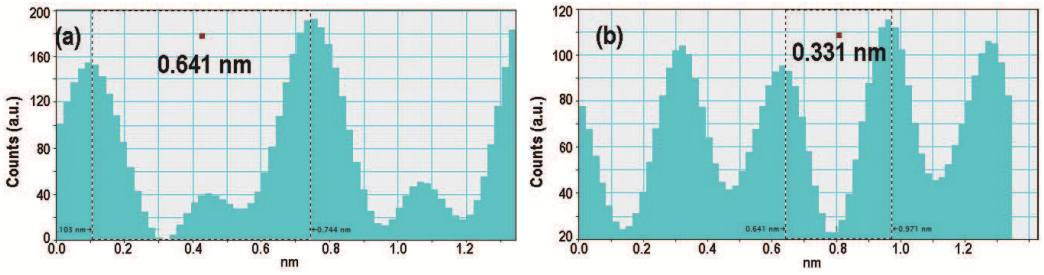

Figure 4.8: Intensity profile of 13.5 nm-LSMO film (a) and $SrTiO_3$ (b), the profiles show elongation in the film, along the growth direction of the film ($<201>_{LSMO}$ on $<100>_{STO}$).

The intensity profile of film and substrate, which gives the repetition of the counts, in distance on the growth direction is shown in Figure 4.8. The cell parameter of the substrate is 0.33 nm, while the distance of Mn plane in growth direction for the film is around 0.64 nm, different from the distance of same plane in bulk LSMO, 0.54 nm, which proves the elongation of the film along the growth direction.

Also, a trace of antiphase boundary is visible in 13.5 nm LSMO film, where the A-plane in ABO_3 structure, $(La_{0.7}Sr_{0.3})MnO_3$, is displaced by almost 2/3 of the plane distance, shown in Figure 4.9.

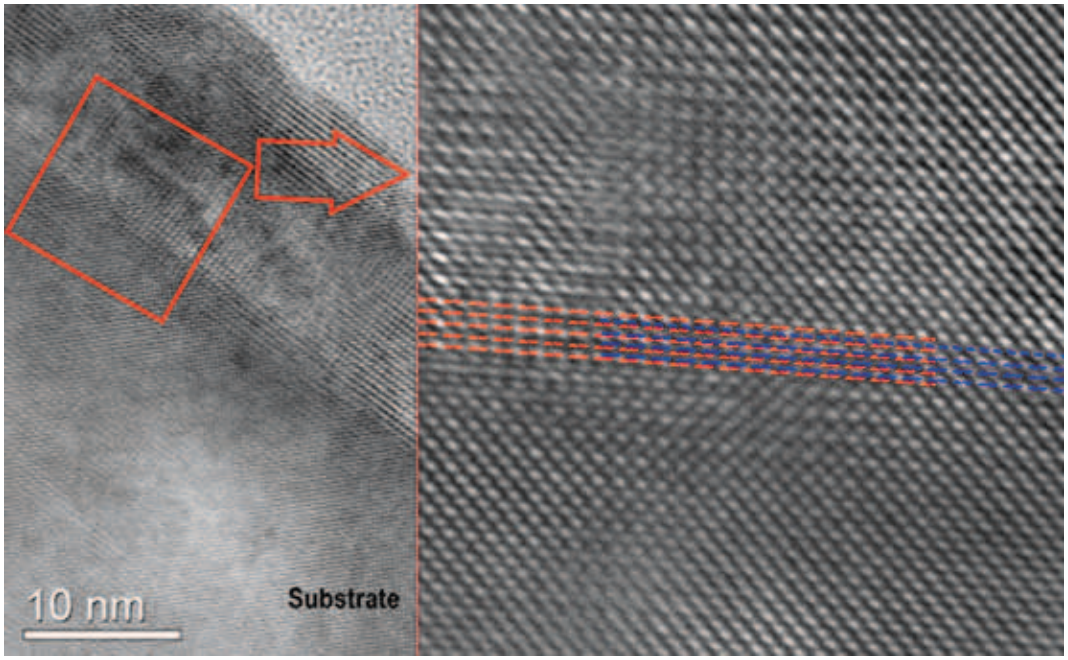

Figure 4.9: The 13.5 nm LSMO film shows anti-phase boundary, on top of interface, shown with blue and red lines.

While LSMO thin film with 13.5 nm thickness shows slightly strained film, thicker films show inclinated columnar structure, see Figure 4.10 and Figure 4.16. These films display boundaries, apart from horizontal interfaces, which in some materials, these boundaries/twin walls have shown different conductivity/magnetization than the contiguous domains [159, 120].

The formation of such columns can be attributed to as "self-shadowing" effect [160], which describes the evolution of of the surface morphology as a function of both pressure P and the target-to-substrate distance, D [161]. At low T and high inert gas pressure P, scattering occurs in the dynamic plasma (called plume), so that the incident particles are thermalized before reaching the growth surface. In PLD system, the plume is transported over large distance, and satisfies the $PD^3 = constant$ condition. The low energetic adatoms impinge on the surface with a random angle of incident, causing a "self-shadowing" effect occur [31].

A deep look into the interfaces of crystalline grains in the film and also Energy Filtered TEM (EFTEM) analysis shows the crystalline growth of the film, along with elemental composition in the film. The nucleation of the film on the substrate results in building up the triangle shapes with either their base or the apexes on the substrate. In some parts of the film, it is possible to see a columnar growth from the interface of film/substrate, up to the free surface of the thin film. In the enlarged view, presented in Figure 4.10, twining of the crystallites is evidenced; by comparing with thinner film (Figure 4.7) the growth mechanism, texture and twin boundaries are affected by film thickness. Guided by results of the interface of anti-phase boundaries in epitaxial thin films of an orthorhombic-$TbMnO_3$ [159], where the chemistry of the film changes in the interfaces, the analogous analysis was attempted on LSMO film, using EFTEM in JEOL 2200 FS microscope. The advantage of EFTEM is its short time of image acquisition, in order of one to two minutes, despite of a compromise in resolution of the image, compared to STEM-EELS mapping, where 50 pm resolution in aberration corrected microscope can be reached.

Figure 4.11 shows the high resolution TEM images of 45-nm LSMO, and the EFTEM analysis of top-right quarter, Figure 4.11(a) and (b), of TEM image, for $M_{5,4}$-La (Figure 4.11(c)) and $L_{3,2}$ edges for Mn (Figure 4.11(d)). There is a region, in the left side of EFTEM of Mn, where the concentration of Mn is lower than the rest of image. By comparing to the TEM image, a boundary is obvious in the region, which also shows deficiency of La in the mentioned region. Also, Figure 4.12 shows a high contrast image of the sample, including the interface with the substrate. It is clearly obvious that concentration of Mn is higher at film/substrate interface.

A close look to the columns in $\sim$45 nm film is shown in Figure 4.13(a), and illustrates

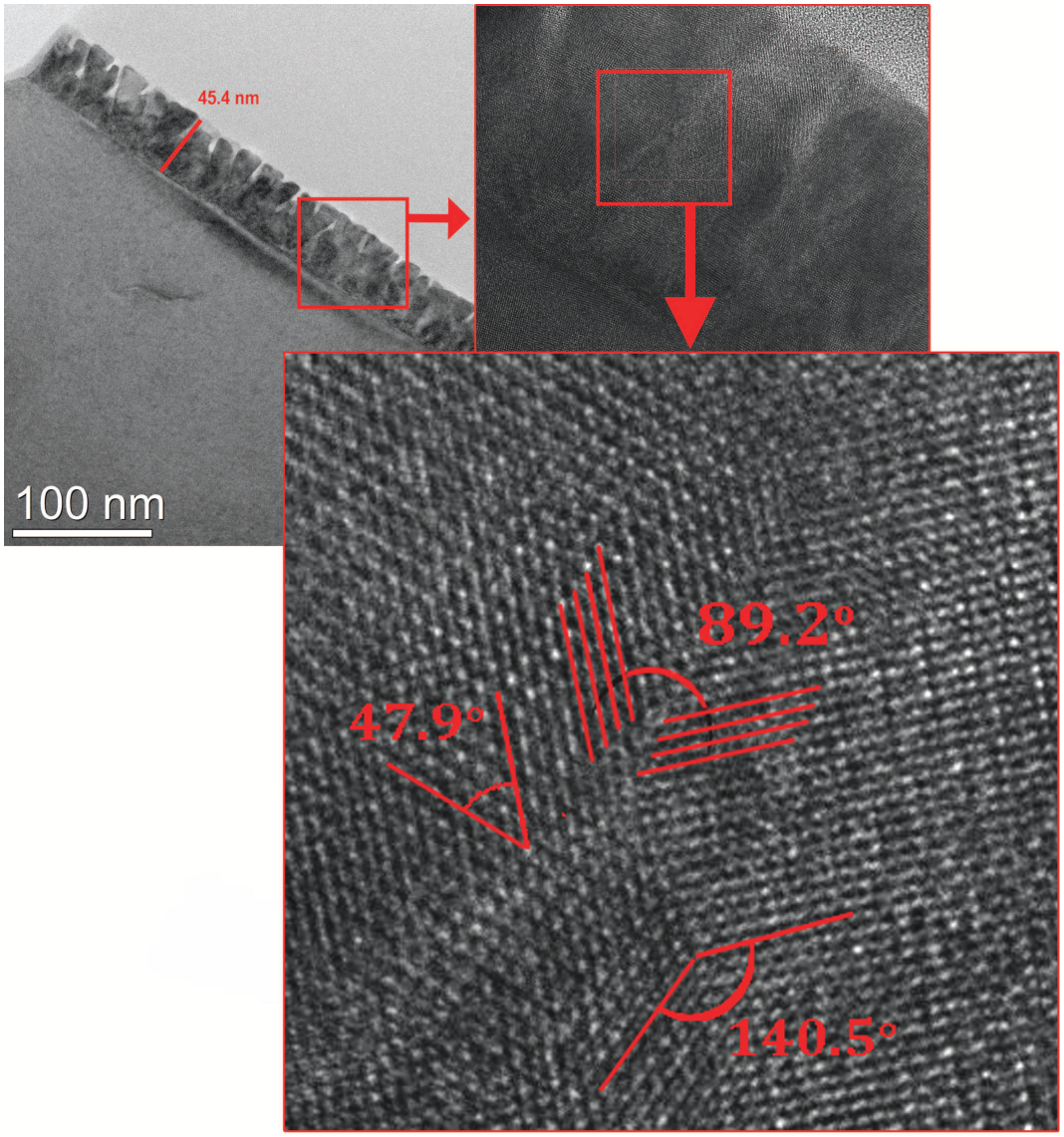

Figure 4.10: TEM micrograph of ∼45 nm LSMO thin film. The zone axis is [2 -1 0] for the film

the single crystal growth inside each columns, although the difference in the direction, is due to layers of superimposing of columns, in the area. The zone axis in this TEM micrographs is [2 -1 0] for the LSMO film.

Looking inside one of the columns, after energy filtering, the epitaxial growth of each columns is observable and confirmed by FFT micrograph, shown in Figure 4.14. With the intensity profile along one set of atoms, we can see the seperation of 0.36 nm, where some irregularity is seen in intensity profile.

The TEM image of the film/substrate interface, for the ∼45 nm LSMO film shows a deformation above the interface, limited by the dashed rectangle in Figure 4.15(a). This is also proved by diffraction pattern, where the circles are shown, in Figure 4.15(b).

TEM image on the 200 nm LSMO sample, are shown in Figure 4.16. An inclinated

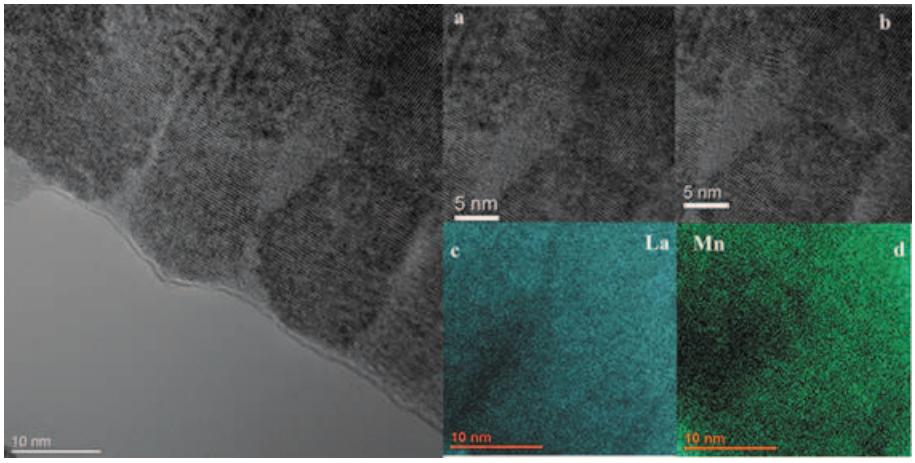

Figure 4.11: High contrast TEM image of 45 nm-LSMO film, corresponding image and EFTEM of $M_{5,4}$ edges of La (a,c) and $L_{3,2}$ edges of Mn (b,d).

columnar structure is visible in the thin film. The columns were grown with $\sim 67°$ in respect to the film/substrate interface and their width are ∼20 nm. A ∼40 nm- thick region of the layer is visible, with darker resolution.

A closer look to the dark region, in vicinity of the interface with the substrate, Figure 4.17, embodies an epitaxial growth of the film on the initial ∼40 nm stage of the film. An intensity profile across the region shows 0.44 nm cell parameter. The red lines, plotted in TEM micrograph shows small tilt of the crystalline plane from direct line, by ∼4° in 10 nm scale. The tension, caused by tilting is the basis of the columnar growth of the film. A DF-STEM analysis of the film shows the existence of second phase near the interface with the substrate, as seen in Figure 4.18. The bright region near the interface is related to the existence of heavier element (La) in the area. With assuming the constant Mn composition, the region has Sr-deficiency, which was also proved by

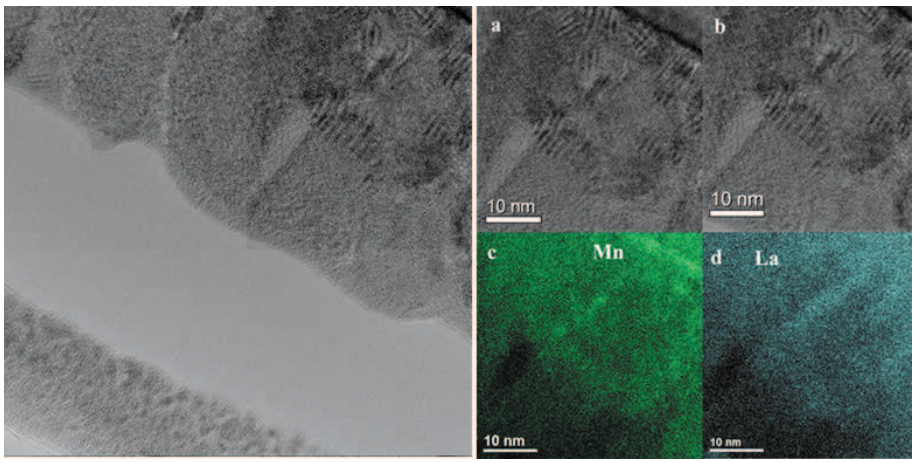

Figure 4.12: High contrast TEM image of the interface in 45 nm-LSMO film, corresponding image and EFTEM of of $L_{3,2}$ edges of Mn (a,c) and and $M_{5,4}$ edges of La (b,d).

XRD analysis, presented in Figure 4.2.

A close look to the area with columns and FFT from the region is shown in Figure 4.19. FFT shows the (2-10) zone axis, while the growth is in (100) orientation. Crystal structure continues unchanged, even in the boundaries of the columns.

Figure 4.20 shows the EFTEM analysis of a 200 nm LSMO film. Figure 4.20(a) gives the part of film chosen for EFTEM, whereas in image (b) and (c) the Mn and La mapping are shown although a slight shift. The EFTEM of the Mn and La elements was taken according to accessible edges in EELS spectra as shown in Figure 4.20(d). The EELS spectrum of the film in the energy range shown in Figure 4.20(d) covers O K-edge, Mn-$L_{3,2}$-edges and La-$M_{5,4}$-edges. The images are showing slight difference in the contrast of the La at the position of the interfaces. Such change of contrast is not visible in Mn mapping as clear as in La maps. It suggests a trend for La deficiency on the interfaces. In the Mn mapping, right down of the Figure 4.20(b) marked by an arrow, there is an interface rich of Mn where the contrast is more bright. It may be the region of excess Mn at Figure 4.20(a) marked by an arrow where the same wide interface is seen. In the corresponding place of the FETEM image (c), the darker contrast of La implies La deficiency where the excess of Mn appears at least at this interface.

TEM measurements on the 320 nm LSMO film is shown in Figure 4.21 and Figure 4.22. The columnar growth is visible in this sample, as well, although it is not as ordered as in the film with 200 nm thickness.

The existence of a branched growth is obvious in the structure. The columns become

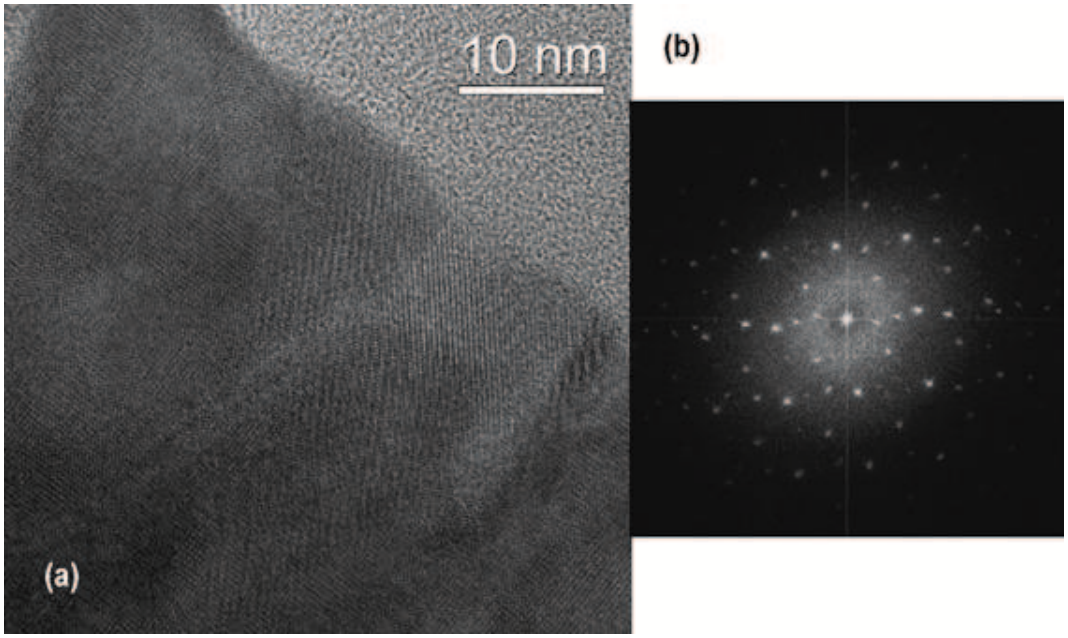

Figure 4.13: (a) Close look to column structure of LSMO (45nm) thin film and (b) FFT pattern, from the columns. The superimposed columns are visible.

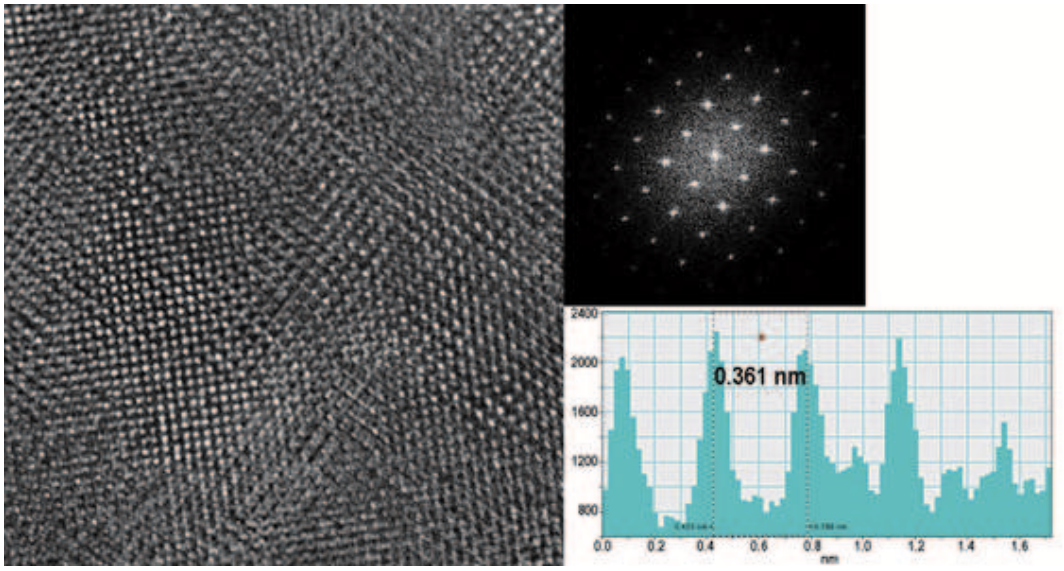

Figure 4.14: Structure inside one of the columns, in 45nm LSMO thin film, the FFT pattern and intensity profile of a chosen area.

more and more obvious in atomic scale. The selected area electron diffraction (SAED) pattern shows the epitaxial part of the film in the orientation of (011) LSMO || (100) $SrTiO_3$ (Figure 4.23). The red circles are showing the (011) planes of the LSMO film, while the green circles show the other growth direction, slightly different from the main orientation. Also, the partially amorphous growth is obvious, by a circle, around the central point.

A closer look at the interface between LSMO and the $SrTiO_3$ substrate shows epitaxial growth with small amount of misalignment, Figure 4.24. Although, FFT of the

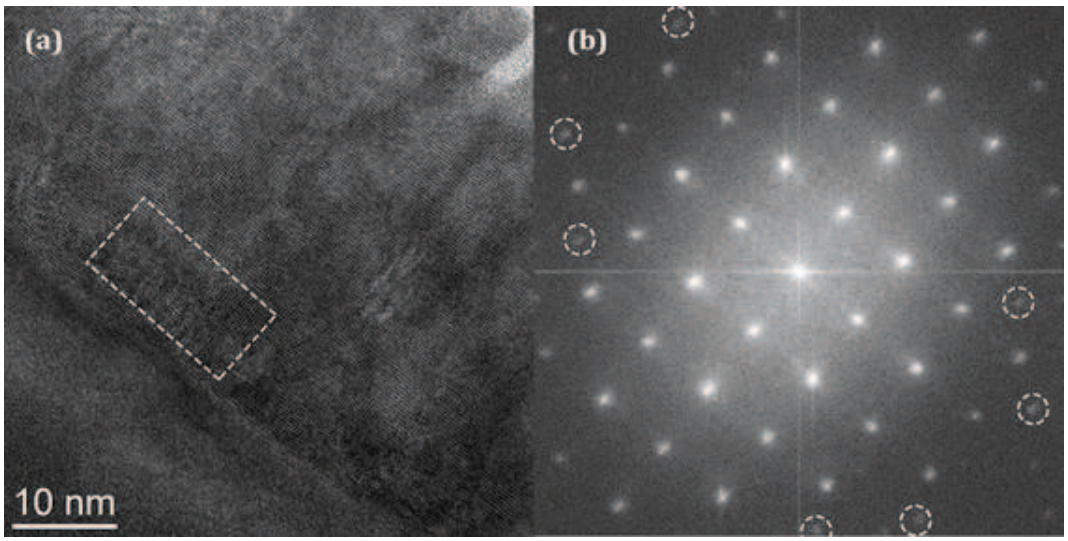

Figure 4.15: TEM image of the interface of 45 nm LSMO thin film. The marked area is showing a slight deformation of structure, illustrated by circles in the diffraction pattern.

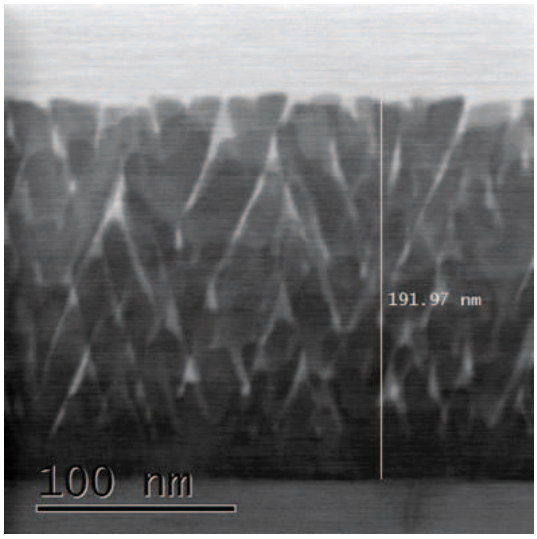

Figure 4.16: TEM micrograph of 200 nm LSMO thin film shows inclinated columnar structure, which are oriented neatly, in relation to each other.

film at the interface is showing epitaxial growth of the film, small distortion is visible at large scale. The ∼6 nm distance between the starting point of the misalignment states a stressed film. Right above the substrate, the misfit dislocations develop and relax the elastic strain of the film. It should be noted that the long dislocation line in the film, marked in Figure 4.24(right), is originating just above the interface of the film/interface.

Figure 4.25(a) shows the detail of the branch structure and the Fourier transform of the branch, indicating a rotation around the $(110)_R$ axis perpendicular to the film by an angle of 13°, Figure 4.25(b). A detailed look near the boundary of the branch shows 69° of twinning in respect to the branch edge, while the boundary has rotated 19° in

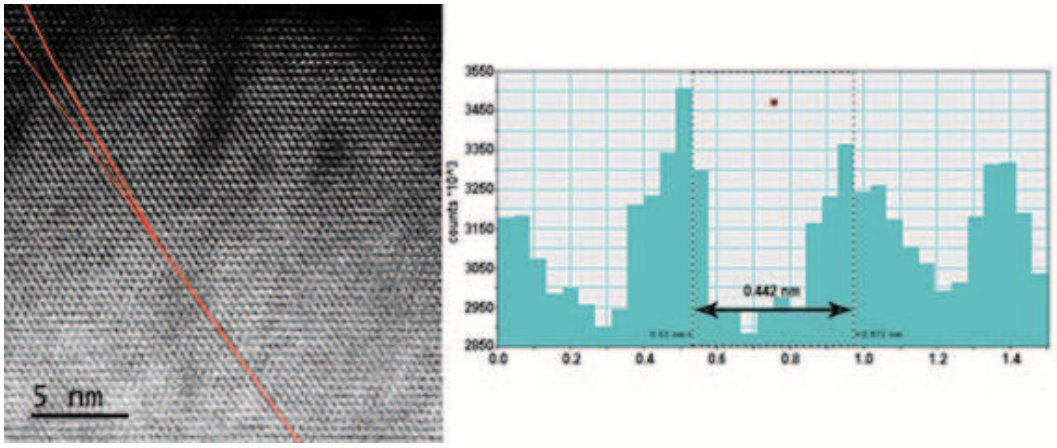

Figure 4.17: TEM of the darker region of Figure 4.16, in vicinity of the interface with substrate. Formation of columns is not visible in this area. Intensity profile shows the lattice parameter of 0.442 nm.

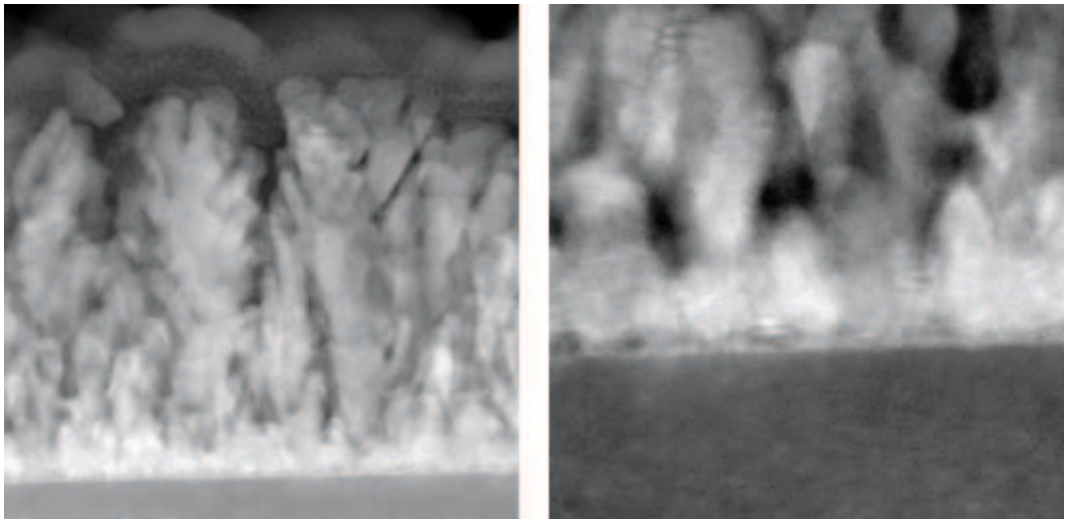

Figure 4.18: DF-STEM of 200 nm-LSMO thin film proves the existence of a Sr-deficient phase near the interface of the film-substrate.

respect to background of structure.

The HRTEM results demonstrate that the first ∼80 nm of the deposited film, closer to substrate, is still strained and the rest of thin layer is relaxed (in respect to a=0.387 nm in bulk form). Following, a 30 nm-thick layer of film can be observed, Figure 4.21, in different contrast with the rest of the film, in which the branched structure does not continue. Right above this intermediate layer and until the surface of the film, the branched structure becomes visible, again.

The STEM-EELS (scanning transmission electron microscopy-electron energy loss spectroscopy) results from the film are shown in Figure 4.26, accompanied by DF image, acquired simultaneously with EELS spectrum. The HAADF (high angle angular dark

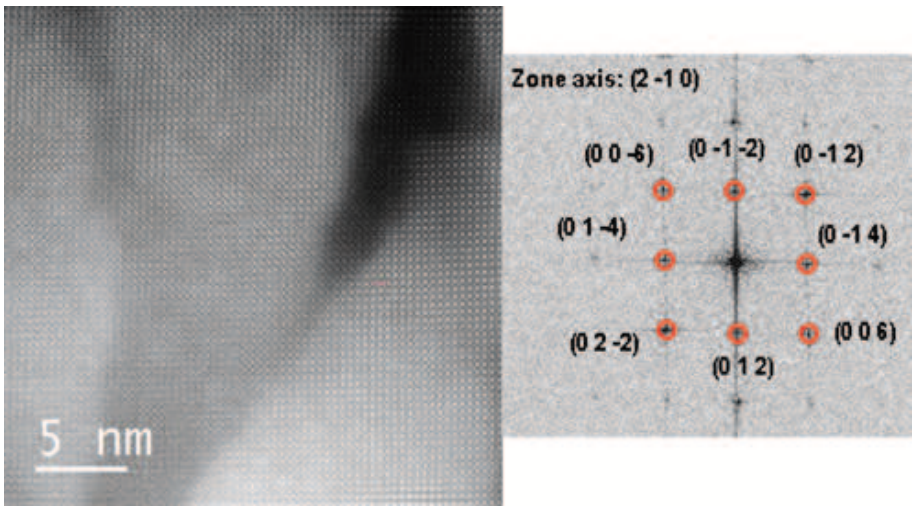

Figure 4.19: HRTEM of the 200 nm LSMO film and FFT image of the area. Simulations shows (2-10) zone axis.

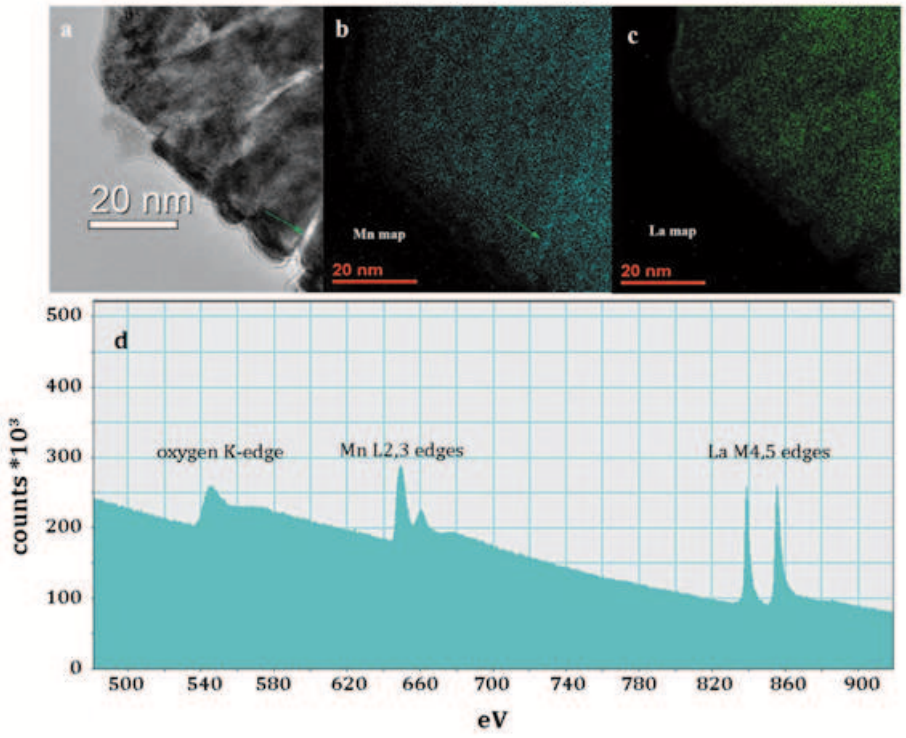

Figure 4.20: High contrast TEM image of LSMO film (200 nm thickness film), corresponding EFTEM of $L_{3,2}$ edges of Mn (b) and $M_{4,5}$ edges of La (c). d) EELS spectrum of the film which shows edges of three elements where EFTEM analysis is possible. Arrows in (a) and (b) point to the same interface showing excess of Mn at the interface.

field) image of the film suggests that the difference in contrast can be caused by heavier elements or higher thickness of the observed area in comparison with the rest of the film. The elemental maps, Figure 4.26(c) and (d) shows that the branch contrast is

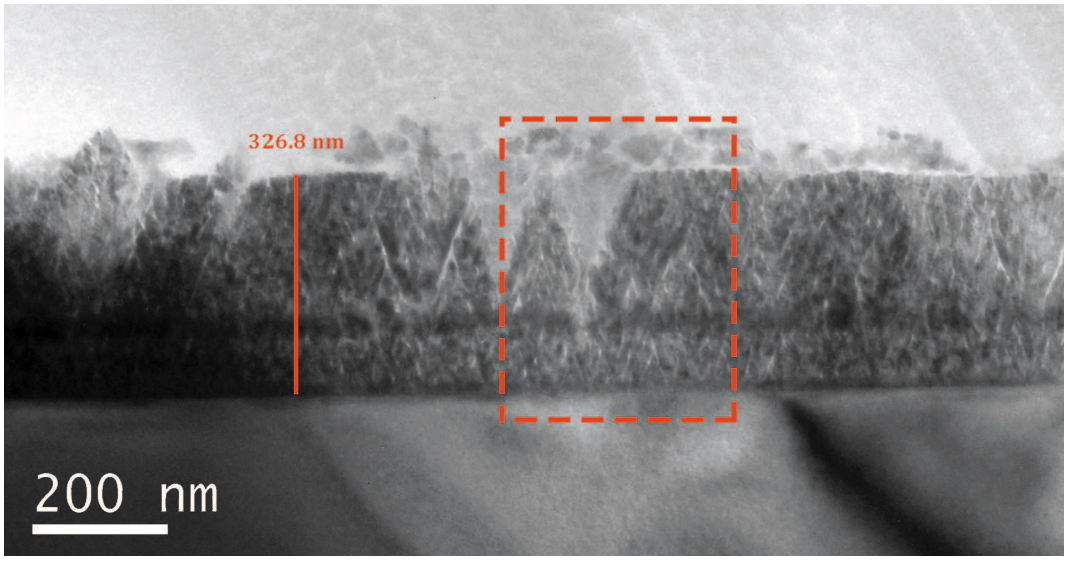

Figure 4.21: Cross-sectional bright field TEM micrograph of 320 nm LSMO thin film grown on (100) $SrTiO_3$ substrate.

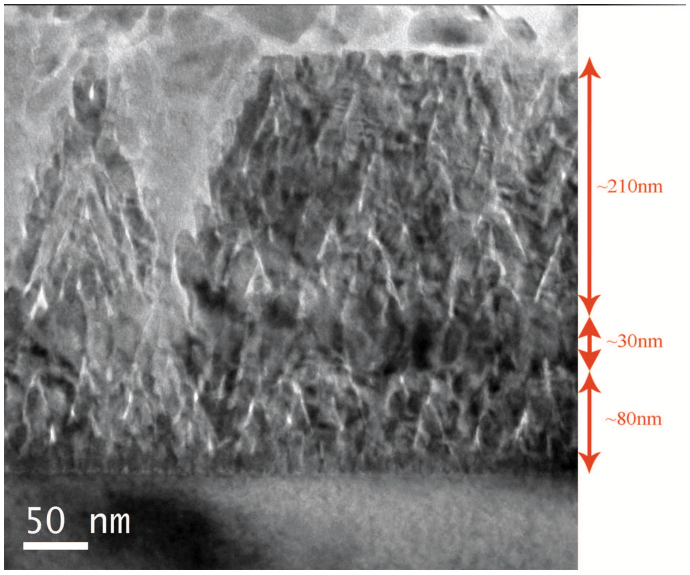

Figure 4.22: Detailed look in branched structure of 320-nm LSMO thin film. The film shows (011) LSMO || (100) $SrTiO_3$ growth direction.

mainly from the thickness of the observed area. However, the Mn/ (Mn+La) ratio map, Figure 4.26(e), shows that the edge of branches contain more Mn than inside the branches. Mn is deficient (47%) in the bright layer, indicated by a black arrow in Figure 4.26(a). The Sr mapping is not as clear as Mn and La because of its low content and its presence in $SrTiO_3$ substrate.

As a conclusion of the analysis on LSMO thin films, TEM results of the samples, show a transition in structure of thin film, from epitaxial in 13.5 nm film, to a branched structure in 320 nm film. In the middle thicknesses, the film is arranges into inclinated

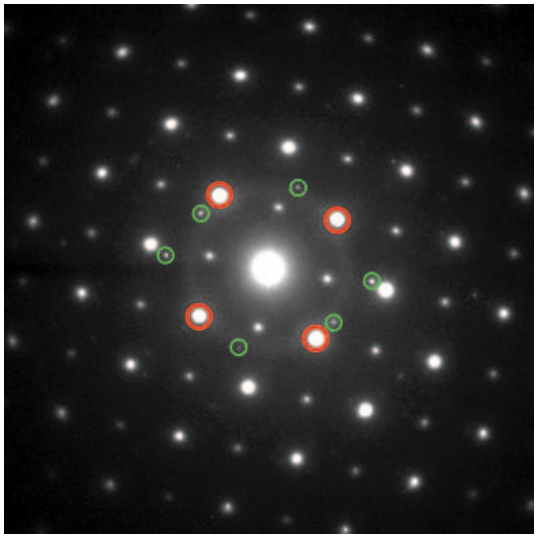

Figure 4.23: Selected area electron diffraction pattern from the film, the red circles are showing the (011) planes of the LSMO film, while the green circles show the other growth direction. The partially amorphous growth is obvious, by a circle, around the central point.

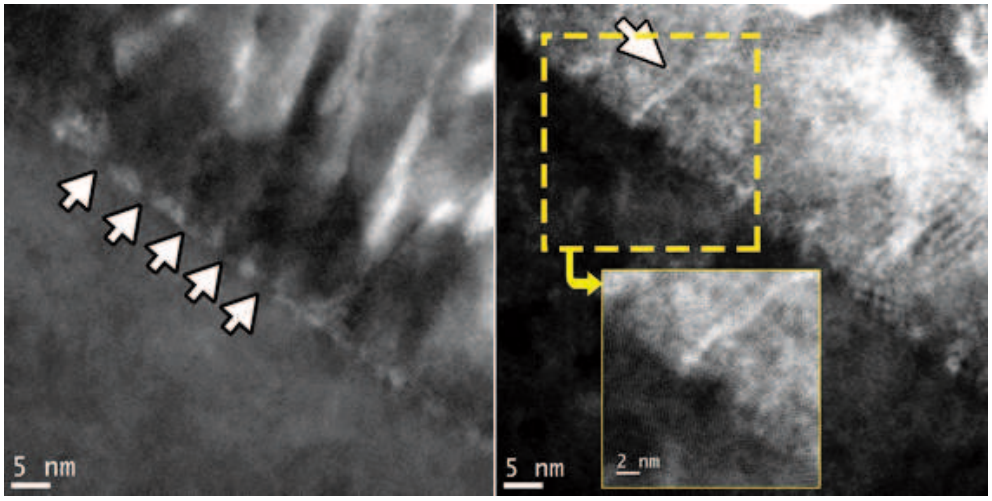

Figure 4.24: (Left) Cross-sectional TEM micrograph at high magnification, showing starting points of some misalignment in the grown film. The average distance between two closest starting points is ∼ 6 nm, (right) threading dislocation created in the LSMO thin film leads the film to relax.

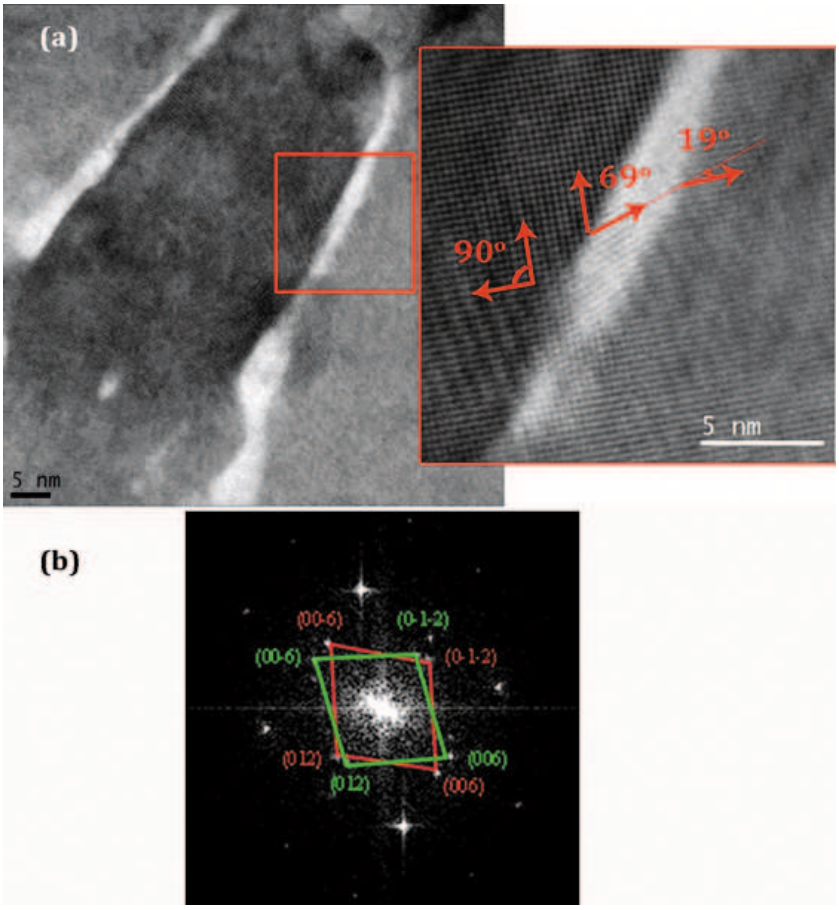

Figure 4.25: (a) The branch structure of the LSMO thin film, on $SrTiO_3$ and the twinning in the branch and also the boundary twinning, (b) The FFT from one of the LSMO branches reveals rotated crystals, inside each branch.

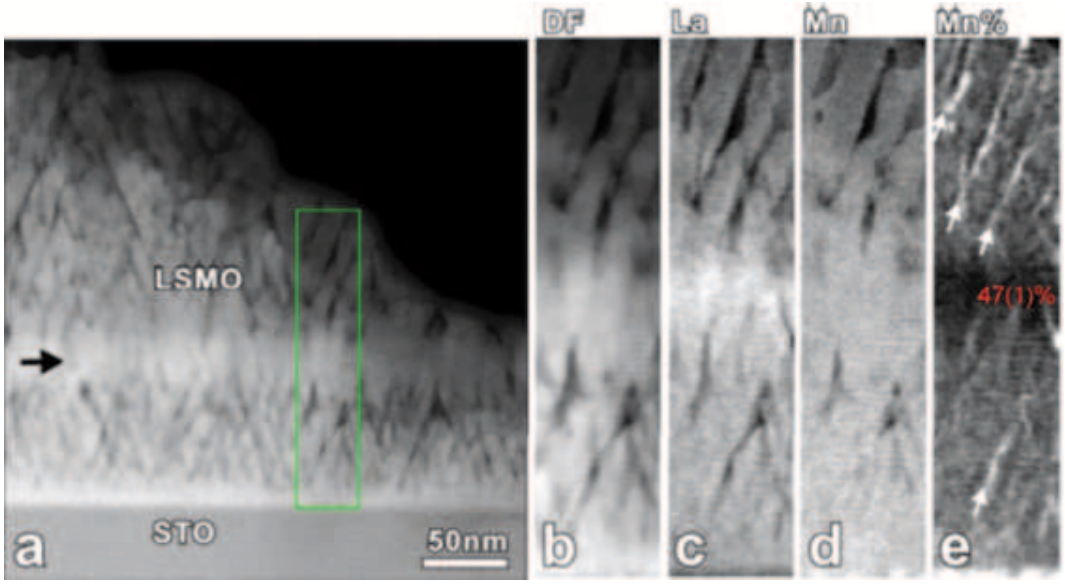

Figure 4.26: (a) STEM-EELS results from the area indicated by green box. (b) DF image is acquired simultaneously with EELS spectrum. The La-M_{45} edges and Mn-L_{23} edges are acquired in the same spectrum. The elemental maps (c and d) shows that the branch contrasts are mainly from the thickness. However, the Mn/(Mn+La) ratio map (e) shows that the edge of the branches contains more Mn than the core of the branches.

columns, with 67° growth direction, in respect to the substrate, as shown in Figure 4.27.

Regarding the magnetic behaviour of the system, it is obvious that antiferrodistortive ordering in STO, below 105 K, induces significant changes on the magnetic microstructure of the LSMO thin films. This is especially remarkable in thin films, thinner than 100 nm. These magnetic changes are most evident in the field cooling magnetization and in the coercivity, which largely increases with lowering the temperature below T_{STO}. On the contrary, the in-defect magnetization observed for thicker films can be understood by the formation of randomly oriented magnetic domain reconstructions as-

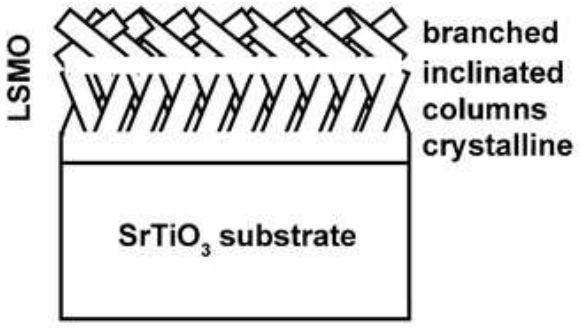

Figure 4.27: Scheme of LSMO thin fims, through change the thickness.

sociated with film relaxations confirmed by both XRD and HRTEM. This shows a close relation between the structural unit cells of both $SrTiO_3$ and LSMO film [115], where the structural coupling between the film and substrate, through the $SrTiO_3$/LSMO interface is the driving force of the structure of the film and magnetic properties of the film, consequently. The interface-mediated magneto-elastic coupling is playing the main role in the magnetization behaviour of the thin film [115].

Chapter 5

Structures on Al_2O_3 substrate

5.1 Film deposition conditions

The deposition of the thin film and heterostructures were done in RF-magnetron sputtering, in Departamento de Física, Universidade de Aveiro. The [0001]-sapphire substrates were cleaned, before inserting inside the chamber, within two steps, as described in section 3.3.2.

The (La,Ba)MnO_3 (LBM) thin film and LBM/$BaTiO_3$/LBM (LBMBT) heterostructure were deposited under total deposition pressure of 5.5E-03 and 6.0E-3 mbar, with P_{O_2}/P_{Ar} of 10% and 20% mbar, for single layer and heterostructure, respectively. All sputtering parameters, selected in the deposition of the $LaBaMnO_3$ samples, such as sputtering time and substrate temperature are listed in Table 5.1.

Table 5.1: Deposition parameters for LBM thin film and LBMBT heterostructure on Al_2O_3 substrate. The subscript "a" is the indication of the substrate.

Sample	Base pressure	Deposition						
		Temperature	dc bias	Distance	P_{Ar}	P_{O_2}	Time	Rate
	mbar	±5°C	V	mm	mbar	mbar	min	nm/min
LBM_a	4.8E-08	757	127	115	5.0E-03	5.0E-04	120	0.41
$LBMBT_a$	3.9E-08	697	155	105/105/105	6.0E-03	5E-04	30/30/30	1.3/1/1.3

5.2 $La_{1-x}Ba_xMnO_3$ thin film

5.2.1 X-ray diffraction characterization and Microstructure analysis

Figure 5.1 shows the XRD diffractogram of the thin film deposited on [0001]-Al_2O_3 substrate. The film shows the directed growth of (220) plane on (006) plane of substrate.

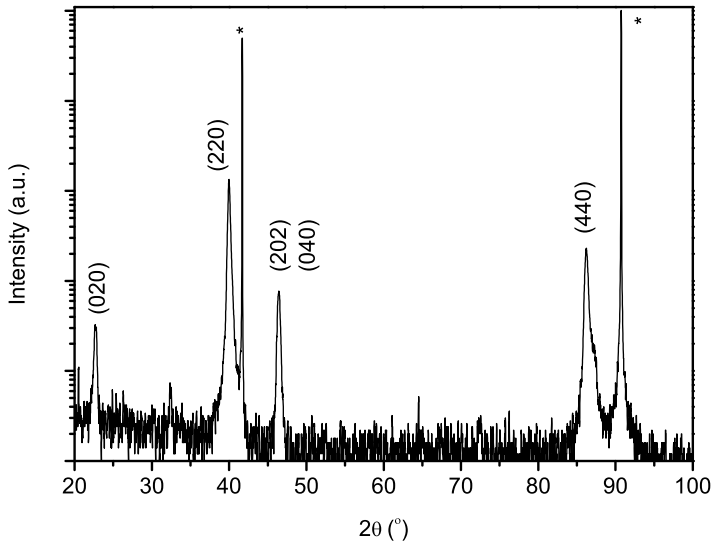

Figure 5.1: X-ray diffractogram of LBM_a thin film deposited on Al_2O_3. The peaks marked with an asterisk symbol (*) belong to the substrate, (a) without monochromator and (b) with monochromator.

The structure of the LBM_a thin film was deduced from the comparison with the available XRD peaks with the crystallographic data, from ICDD, which shows the structures of the film is closer to bulk form of $La_{0.9}Ba_{0.1}MnO_3$ (LBM), an orthorhombic structure (Pnma, 62), with a = 5.51 Å, b = 7.82 Å and c = 5.55 Å (PDF files are provided in Appendix A-3). Also, the difference between the content of Ba in target and the deposited film is expected to be due to its lower sputtering rate. The EDS data, presented in Table 5.2, evidenced the deficiency of Ba in the structure, however, due to the large error in Ba content, the absolute value of Ba content could not be ascertained.

The EDS measurement showed the ratio of Ba/La to be ∼0.12, which is close to the value of Ba content, considered in XRD measurements. However, it is obvious that extracting the exact composition is hard from XRD due to various parameters, such as oxygen deficiency in thin film structure and imposed strains by the substrate, among others.

Comparing the d_{220} of the film ($2\theta = 39.99°$) to the d_{006} (= 2.165 Å) of the substrate ($2\theta = 41.69°$), we conclude that the film on Al_2O_3 is under in-plane compressive strain,

Table 5.2: EDS data from $(La_{1-x}Ba_x)MnO_3$ thin film on Al_2O_3 substrate, showing low content of Ba, in comparison with target.

Element	O-K	Al-K	Ba-L	La-L	Mn-K	Total
Weight %	41.40	56.08	0.22	1.64	0.65	100
Atomic %	55.16	44.30	0.03	0.25	0.25	100

derived from the negative value for the lattice mismatch of δ=-4.0 %, calculated from Equation 2.8.

The observed diffraction peaks were fitted using Gaussian function in order to determine the peak position and width [162]. The fit of the (220) plane of the film is shown in Figure 5.2. The extra part, seen in the the deconvolution, at right side of the (220) peak is due to the $Cu_{k\alpha 2}$ in the spectra and also overlapping of (022) peak of substrate, as shown in Figure 5.3, which causes the broadening of the peak.

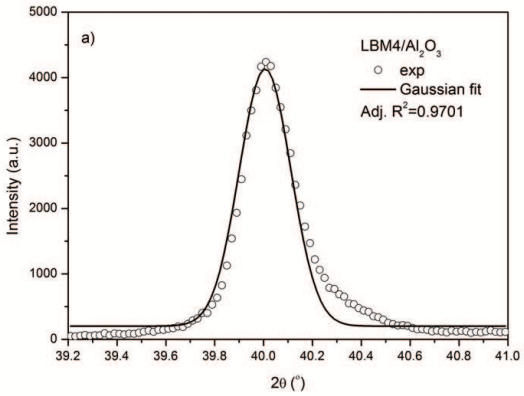

Figure 5.2: Fit of the (220) diffraction peak of LBM_a thin films deposited on (0001)-Al_2O_3.

The distance d_{220} between the (220) crystallographic planes was obtained from the Bragg relation, Equation 3.2, as well as the grain size, was determined from the width

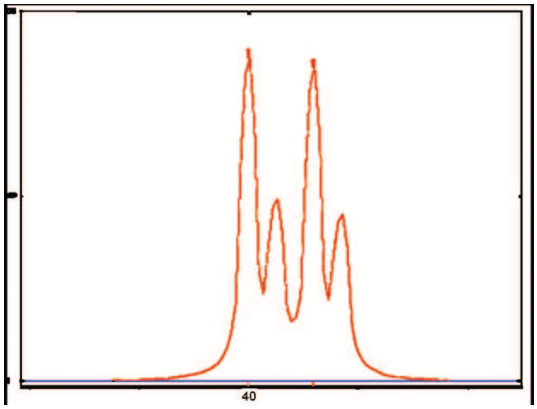

Figure 5.3: Simulation of (220) and (022) peak of LBM_a film on (0001)-Al_2O_3.

of the XRD peaks using the Scherrer equation:

$$\beta = \frac{k\lambda}{\tau \cos\theta} \tag{5.1}$$

and the results are shown in Table 5.3. However, it should be taken into account that due to low quality of the XRD data and the existence of $Cu_{k_\alpha 2}$, the calculations suffer from the high error.

Table 5.3: Parameters obtained from the X-ray diffractograms of LBM thin film deposited on Al_2O_3: diffraction angle for the (hkl) planes $2\theta_{hkl}$, width of the (hkl) diffraction peak β_M, instrument peak broadening β_s, (hkl) interplanar distance of the films d_{hkl}, and crystallite size τ.

Sample	Plane	$2\theta_{hkl}(^\circ)$	β_M (°)	β_s (°)	d_{hkl} (Å)	τ (nm)
LBM_a/Al_2O_3	020	22.75	0.28	0.06	3.91	30.9
LBM_a/Al_2O_3	220	40.01	0.25	0.06	2.25	36.5
LBM_a/Al_2O_3	202	46.49	0.30	0.06	1.95	30.7
LBM_a/Al_2O_3	440	86.25	0.51	0.06	1.13	22.4

The peak broadening caused by instrumentation was estimated using the (006) diffraction peak of Al_2O_3, at $2\theta = 41.69^\circ$.

Figure 5.4 shows the X-ray reflectivity (XRR) spectrum of the sample LBM_a on Al_2O_3 substrate. The calculated thickness for this sample was 49.5 nm, using the simulation on the program Parratt, with roughness of 0.8 nm. The density used in the simulation is 6.71 gr/cm^3 and the scattering length density (SLD) of 4.918E-5 - i5.966E-06, where the real part is related with the refraction index of the material and the imaginary part is connected to the absorption of the film, that is the decay of X-ray waves inside the film.

By collecting the full map, it is immediately possible to have direct information on

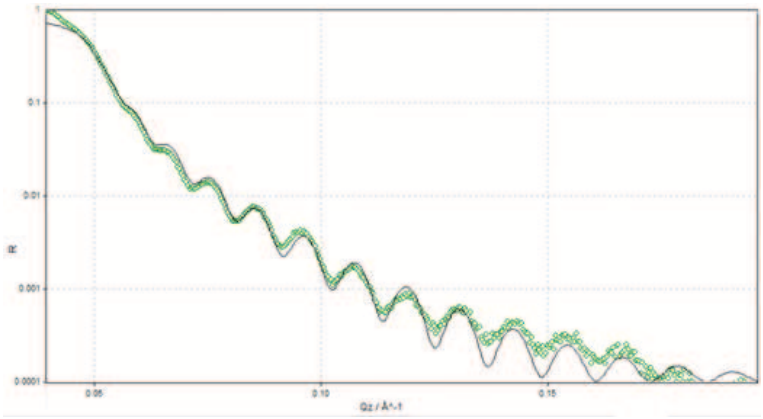

Figure 5.4: XRR spectra of LBM_a thin film on Al_2O_3 substrate.

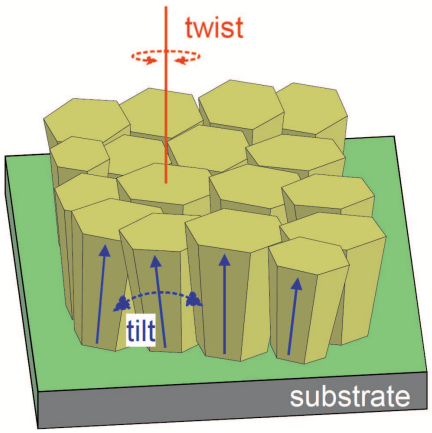

Figure 5.5: Schematic representation of the mosaic structure [163].

the mosaic spread in layer. The mosaic structure consists of number of small crystallite grains with their basal plane, approximately parallel to the substrate surface. The basal planes of the individual crystallites can be slightly tilted with respect to each other and the individual column axes tilted with respect to each other. The degree of tilting and twisting determines the macroscopic crystal quality. Microscopically, the tilting is correlated with the threading dislocation and twisting to the edge threading dislocation density [164]. A schematic diagram of the mosaic structure is shown in Figure 5.5.

The ω versus 2θ map, shown in Figure 5.6(a), centred at 2θ=40.00° and Ω=20.00°, covers the Al_2O_3 (006) peak, in addition to (220) and (202) peaks of the LBM_a film. The spectral broadening along the ω direction (∼0.8°) in the full map, is due to tilting between the mosaic blocks and small mechanical tension. Moreover, the elongation of the peak in $\Delta\theta$ (∼0.3°) can be associated with d_{220} plane relaxation across the film growth direction. This feature evidences both the high degree of epitaxy and the coherent growth of the film.

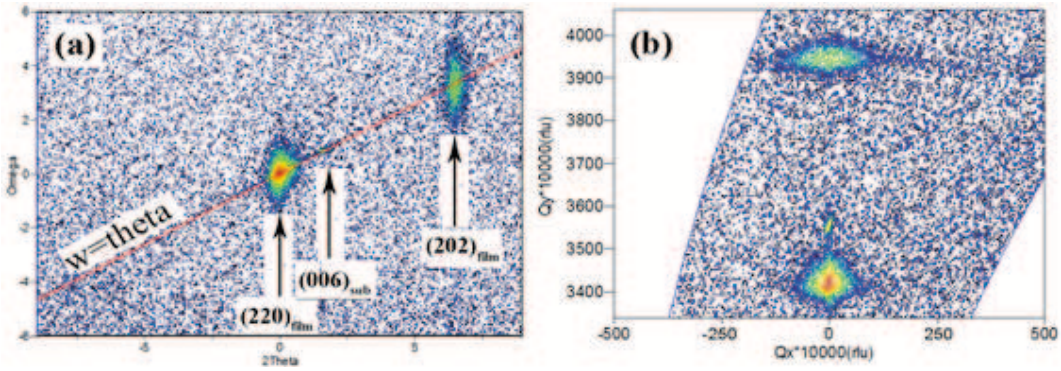

Figure 5.6: (a) ω-2θ map of the LBM_a film centred at 2θ=40.00° and ω =20.00°, (b) the reciprocal space map of the film.

The TEM analysis of the LBM_a thin film, Figure 5.7, shows the 50.4 nm thin film,

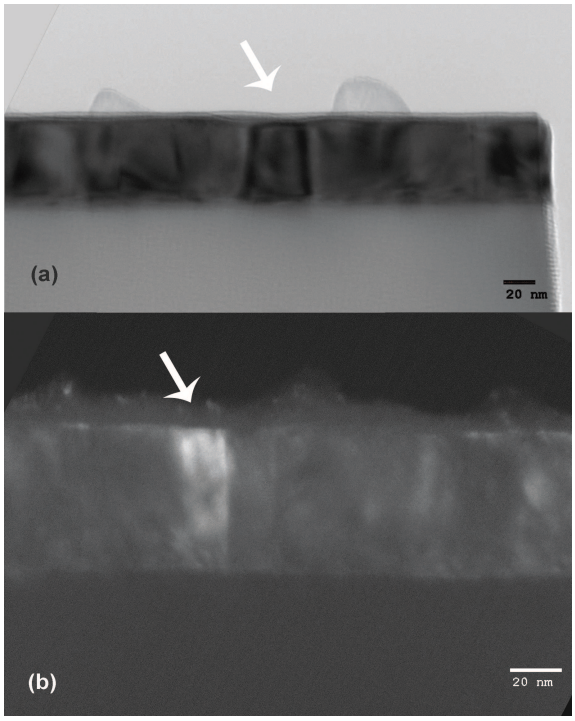

Figure 5.7: TEM micrograph of the LBM_a film on Al_2O_3 substrate, (a) bright field image shows the threading dislocations in the grown film, (b) dark field image shows the crystalline region in the film.

grown partially crystalline on the substrate. The mosaic structure can be seen in Figure 5.7(a) in bright field (BF) TEM micrograph. Some of the regions, with ∼40 nm width, are crystalline, as shown in DF TEM micrograph, Figure 5.7(b).

The mosaic structure can be proven by TEM results, as well. The high resolution TEM micrographs show a polycrystalline structure, which is due to the twisted mosaics with slightly changed orientations. Figure 5.8 shows the HRTEM micrograph of the interface of LBM_a thin film with Al_2O_3 substrate. The insets in Figure 5.8 represent the FFT of the selected areas on the substrate and the film.

To make sure that the crystalline structure is not due to non-homogenous elemental composition, EDS mapping was done, in STEM mode, along the film. The mapping shows the homogenous composition in mosaics along the film.

The EDS data proves the lack of Ba, in comparison with the target. Here Ba/La ratio is 0.03, well below the ratio in the target, which is 0.43. However, due to vicinity of the energy of La and Ba, it is hard to distinguish the exact value of these elements. Also (La+Ba)/Mn ratio is around 1.23. The existence of Cu is inevitable, due to the TEM sample holder.

In order to confirm the elemental composition of the film, RBS measurements were proposed. However, due to the dedication of the sample to TEM sample preparation, a LBM film, from another series (LBM5) was chosen, see Table A.1. RBS measurements

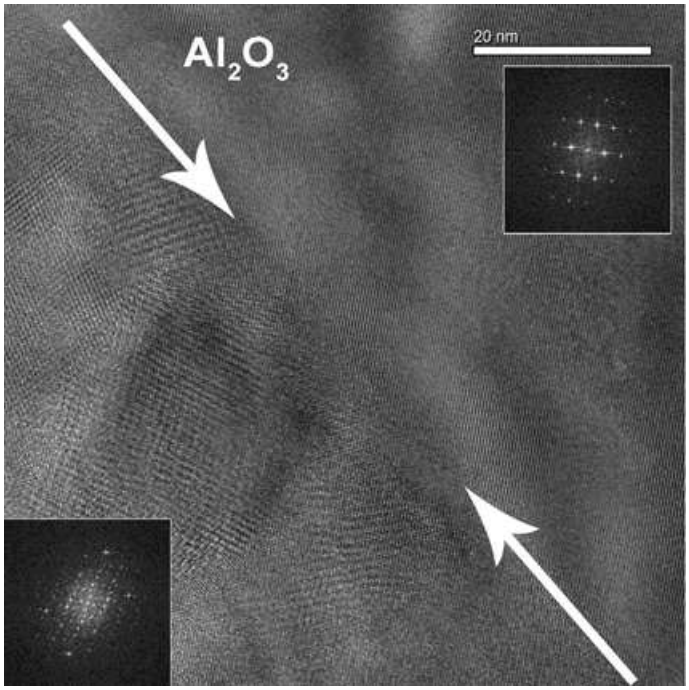

Figure 5.8: HRTEM of LBM_a thin film, the insets show the FFT of the substrate and film. The film shows polycrystalline structure.

were done at the CTN/IST Van de Graaff accelerator in the small chamber with three detectors installed at 140° (standard), and two pin-diode detectors, located symmetrically, both at 165°. Spectra were collected for 2 MeV $^4He^+$. PIXE experiments were also done to determine the Ba/La ratio, and the results are shown in Figure 5.10

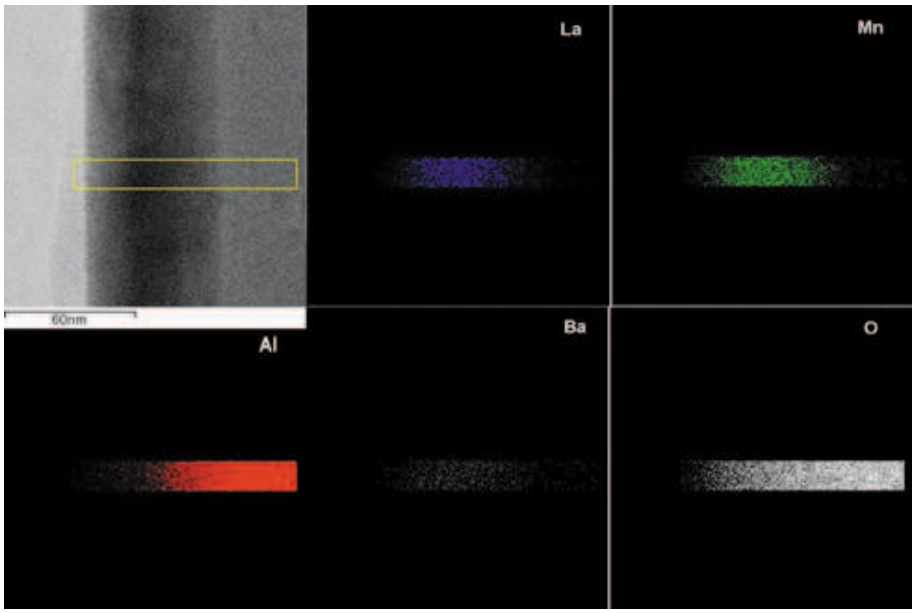

Figure 5.9: EDS mapping of LBM_a thin film, in STEM mode. The mapping show that elemental composition does not change along the film.

Table 5.4: EDS data, from the region, marked in Figure 5.9. The existence of Cu atom is due to the instrument.

Element	O-K	Al-K	Ba-L	La-L	Mn-K	Cu – K	Total
Weight %	40.14	30.17	0.67	20.63	6.87	1.52	100
Atomic %	63.85	28.45	0.12	3.78	3.18	0.61	99.99

[147] and Table 5.6 [165, 166].

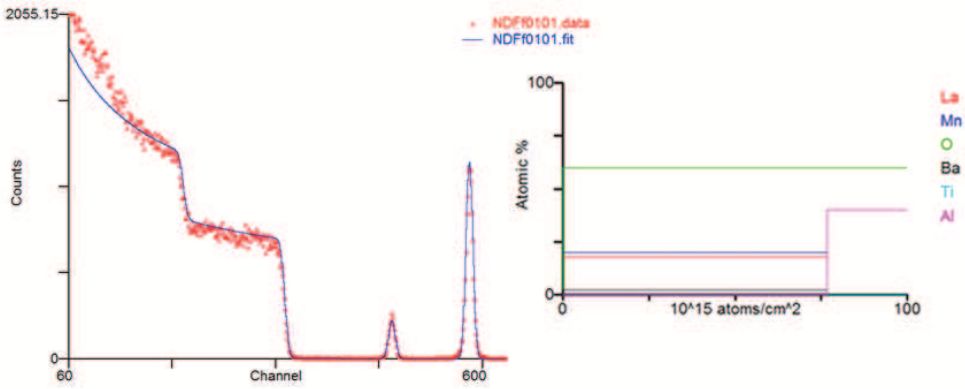

Figure 5.10: RBS analysis and simulations of LBM thin film on Al_2O_3 substrate (17 nm-thick), with the fitted depth profile in inset. The measured film is different from the sample in the rest of measurements in this section.

PIXE analysis shows the La/La+Ba ratio of 0.8889, which is very close to the determined ratio from EDS, TEM and XRD peak identification data, La/(La+Ba) = 0.9.

Table 5.5: The results of fitting on RBS spectrum of LBM thin film on Al_2O_3 substrate, where t is the areal thickness.

Layer	t	Density	Thickness	La	Mn	O	Ba	Al
	1E15 atom/cm^2	1E22 atom/cm^3	nm					
LBM	76.711	4.721	16.248	17.7778	20.0000	60.0000	2.2222	0.0000
Al_2O_3	119092.094	4.990	23864.236	0.0000	0.0000	60.0000	0.0000	40.0000

5.2.2 Magnetometry and Magnetoresistance

All the measurements in this section, which includes Magnetometry, magneto-resistivity and resistivity, were done on a sample with the dimension of 9 (mm) × 4.5(mm) × 50.4 (nm). Previous studies showed that metal-to-insulator phase transition (MIT) is explained in terms of competition between ferromagnetic metallic (FM) and

paramagnetic insulator (PI) phases [12, 167, 168]. Theoretically, the resistivity of manganites can be a superimposition of two independent resistivities, of ρ_{FM} and ρ_{PI}:

$$\rho(T) = f\rho_{FM} + (1-f)\rho_{PI} \tag{5.2}$$

where f is the volume fraction of FM region. In the PI phase, the resistivity, ρ_{PI}, is expressed by an exponential behaviour, Equation 5.3 [167, 169].

Resistivity measurements on LBM_a thin film at high temperatures, 150 to 300 K, shows an insulator-like behaviour, with no transition to metallic phase, as was predicted from the literature, on $La_{1-x}Ba_xMnO_3$ thin film (45 nm-thick), with x = 0.05 [106, 162]. In the high temperature region, one can expect to find an activated behaviour of:

$$\rho = \rho_0 exp[E_a/(k_B T)] \tag{5.3}$$

where ρ_0 is a constant and E_a is the activation energy. Hence, plotting the logarithmic scale of resistivity versus reciprocal temperature (1/T) would present a straight line. The existence of two regions, with two different asymptotic slopes is obvious in experimental curve, shown in Figure 5.11. The cross-over temperature, T_C^R, of these two trends is at 213 K. However, an inflection can be observed in the temperature dependence, this is more clearly seen by plotting the first derivative of resistivity, the inflection point has been shown, at ∼197 K. It is notable that the cross-over point in Ln(ρ) vs. 1/T plot matches slightly with the inflection point, obtained from the ρ-T plot, shown in Figure 5.11. Comparing with LBM polycrystalline bulk [162] and 45 nm-LBM thin film on $SrTiO_3$ substrate [106] matches obtained T_C^R. However, the magnitude of resistivity has increased, comparing with mentioned works.

The magnetoresistance of the film was measured with the setup, described in section

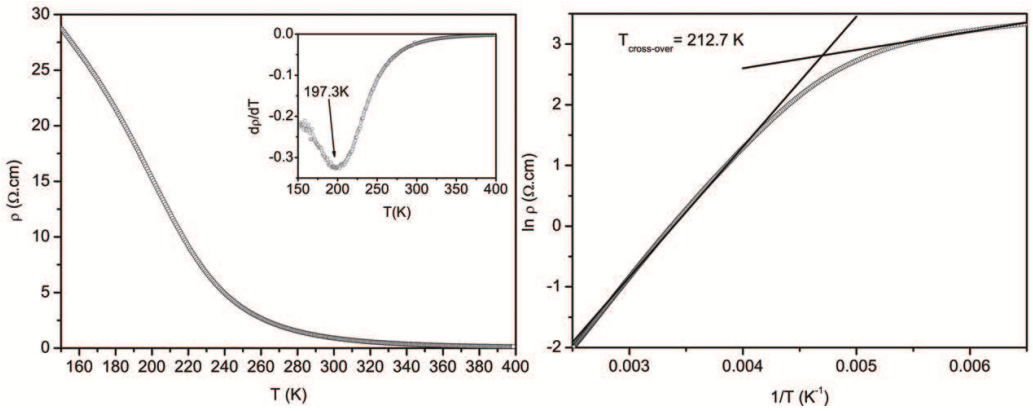

Figure 5.11: (Left) temperature dependence of resistivity of LBM_a thin film on Al_2O_3 substrate, (inset) derivative of resistivity vs. temperature shows the inflection point at ∼197 K, (right) Plot of ln ρ vs. (1/T) and corresponding linear fits for finding the cross-over temperature, T_C^R.

3.4.8. Figure 5.12 shows the magnetoresistance results obtained in the film on Al_2O_3 substrate, measuring as function of field, at selected temperature values, ranged between 150 K and 360 K. The change in the MR behaviour of the film, from linear, ferromagnetic phase, to quadratic, paramagnetic phase, is seen in the range of 180 K to 240 K, as shown in Figure 5.12 (b). A comparison between temperature dependence of the magnetoresistance at H=1.0T and H=0.2T, multiplied by a factor of 5, shows the region, where there is a sharp change in the magnetoresistance value, in accordance with Figure 5.12(a). The magnitude of magnetoresistance is decreasing as the temperature increases.

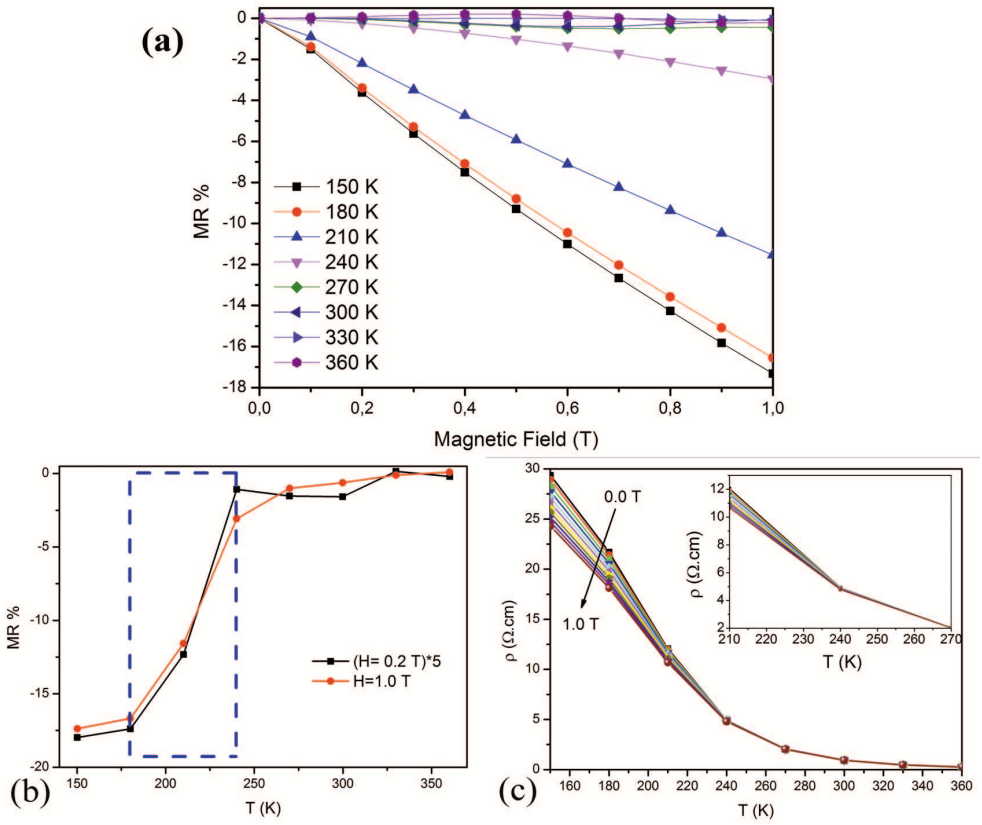

Figure 5.12: (a) Field dependence of magnetoresistance of LBM_a thin film, (b) Temperature dependence of the magnetoresistance at 1.0T and 0.2T, the magnetoresistance at 0.2T is multiplied by the factor of 5, (c) the temperature dependence of the resistivity of LBM_a on Al_2O_3 substrate.

The temperature dependence of the magnetization of the sample was measured with an applied field H=100 Oe after zero-field-cooling (ZFC) and field-cooling (FC), as described in section 3.4.7, and the results are presented in Figure 5.13. There is a separation between the ZFC and the FC curves at low temperatures, associated to the irreversibility, which is at ∼177 K for this case, while the Curie temperature, associated to the transition from the ferromagnetic to the paramagnetic phase, T_C^M is obtained at 203.3 K, from the extremum point of |dM/dT| curve. The transition

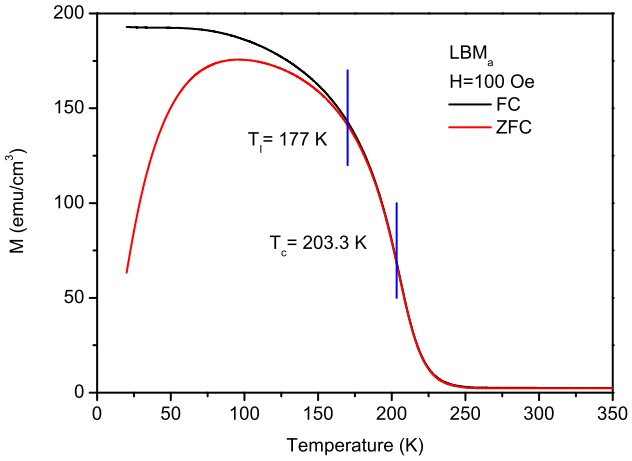

Figure 5.13: (a) Temperature dependence of the magnetization of LBM_a thin films deposited on Al_2O_3.

temperature, derived from magnetic measurements, is in a very good agreement with the cross-over temperature, obtained from resistivity measurements, T_C^R. Looking back at $La_{1-x}Ba_xMnO_3$ phase diagram, Figure 2 18, we can confirm that, from obtained Curie temperature, the composition of film is different from the target, $La_{0.7}Ba_{0.3}MnO_3$, with less Ba content (x< 0.1), as it was already refered to by XRD results. Also, the insulator-like behaviour of resistivity confirms the difference of Ba content in film and target, as the $La_{0.7}Ba_{0.3}MnO_3$ thin film shows the MIT temperature around 300 K [106].

In the reciprocal behaviour of magnetization versus temperature graph, in paramagnetic region, we expect that the samples follow linear Curie-Weiss law. In Figure 5.14, the inverse of the magnetic susceptibility is shown for the LBM_a sample and the linear Curie-Weiss behaviour of the sample is calculated from:

$$\chi(\frac{emu}{cm^3.Oe}) = \rho_0 + \frac{C}{T - T_{cw}} \tag{5.4}$$

where χ_0 (constant background, including the contribution of substrate), C (Curie constant) and T_{CW} (Curie-Weiss temperature) are three adjustable parameters. Fitting is based on least-square algorithm embedded in Origin Pro 9.0 package. The calculated susceptibility background, from the Curie-Weiss fit is 1.255 emu/Oe.cm^3. By considering the composition of $La_{0.9}Ba_{0.1}MnO_3$, we have 90% of Mn^{3+} (S = 2) and 10% of Mn^{4+} (S = 3/2), therefore with total spin of 1.95 and spin density of 1.67E22 atom/cm^3, from:

$$C = \frac{\mu_B^2}{3k_B} N g^2 S(S+1) \tag{5.5}$$

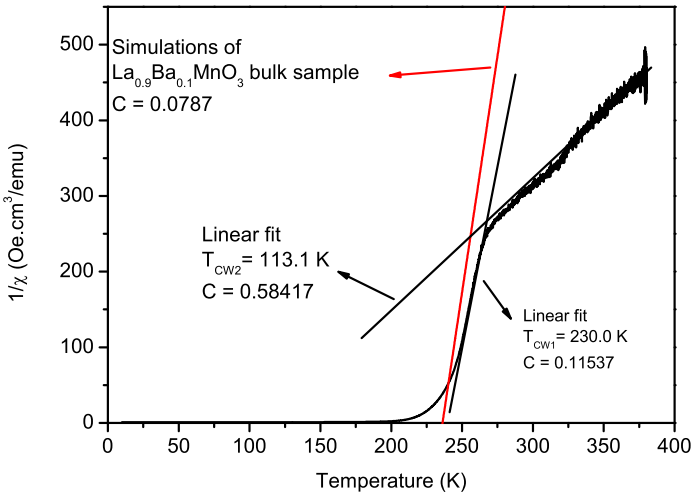

Figure 5.14: Temperature dependence of the susceptibilty of LBM_a thin film, after removing the background and substrate contribution and fitting Curie-Weiss law in paramagnetic phase. The red line shows the simulation of $La_{0.9}Ba_{0.1}MnO_3$ bulk sample.

we can calculate the Curie constant as 0.0787 $\frac{emu.K}{cm^3.Oe}$. These values are extracted from the bulk form of $La_{0.9}Ba_{0.1}MnO_3$, and as it can be seen, the slope of the linear fit in the range of 250 K<T<270 K, CW_1, in Figure 5.14 is in a good agreement with the simulations, using Mean-Field Simulation Suite [170, 171]. The magnetic results shows a mixed-phase sample, where by looking closely at the temperature range of 280 K-380 K, another phase can be detected with Curie-Weiss temperature, T_{CW}, of 113.1 K, which is an evidence for non-homogenous structure in crystal structure of the thin film, proven by TEM micrographs, Figure 5.7 and Figure 5.8, and also by EDS mapping, Figure 5.9.

Magnetic hysteresis loop at 350 K was used to calculate the substrate contribution. The magnetization was measured in the identical substrate, Al_2O_3, normalized to its volume and its contribution was subtracted to the measurement of the LBM_a sample, resulting in the curve in Figure 5.15.

Figure 5.16(a) shows the hysteresis loops at different temperatures for the sample, after subtracting the diamagnetic contribution from the substrate. It is clear from the figure that there is a saturation of the magnetization, M_s, at all temperatures The highest value of M_s observed for the loop, recorded at 20K, M_s=256 emu/cm^3. Figure 5.16(b) shows the saturation magnetization for the same sample. Comparing to polycystalline bulk sample of $La_{0.9}Ba_{0.1}MnO_3$, for which the saturation magnetization is ~100 emu/g (~600 emu/cm^3) [172], there is a decrease of saturation magnetization in thin film. This can be due to several factors, including a possible rearrangment in the oxygen and Mn position, oxygen deficiency in the film, crystal structure of the film

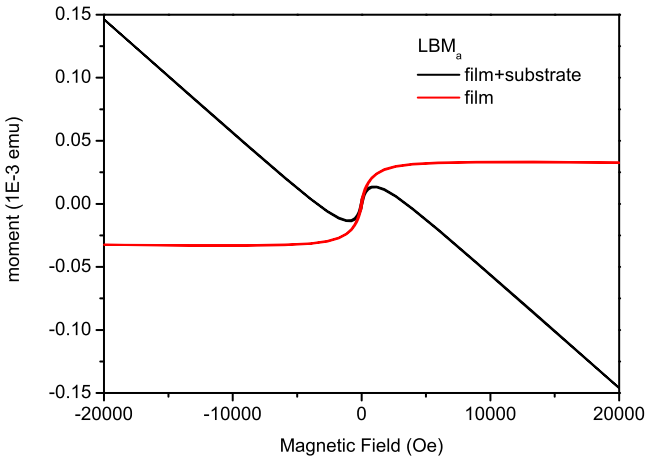

Figure 5.15: Magnetic hysteresis loop at 350 K of the film+substrate, and after subtracting the substrate contribution.

and etc.

The saturation magnetization curve versus temperature, at H= 20 kOe, Figure 5.16 (b), portrays the same behaviour of magnetization, at H= 100 Oe, where the sample shows highly magnetized behaviour at T= 50 K, which is around 200 emu/cm^3. The main difference shows itself at paramagnetic phase of the sample, above 250 K, where there is a visible magnetization of ∼30 emu/cm^3. This can be caused by an additional phase in the sample, which have higher T_c than the LBM_a phase, but strong enough, not to show contribution at low-field FC curve, as seen in Figure 5.13. Figure 5.16(c) illustrates the coercivities, obtained from hysteresis loops, where H_{c+} and H_{c-} represent coercivity at positive and negative magnetic field. The comparison between H_{c+} and H_{c-} shows that there is no exchange-bias, available in the sample. However, the change in the behaviour of the coercivity, around T_C^M is notable. It is expected the coercivity plot versus temperature tends to zero, around transition temperature, T_c^M, and remains at the same value , in paramgentic phase. However, we can see that around T_C^M, the M-H curves change their path, Figure 5.17, and causes coercivity to be negative. The reason of this behavior is the remanent field of the coil in the used system. In order to measure the remanent field of the system, M-H measurements of paramagnetic Pd reference sample (cylindrical shape, supplied by Quantum Design Company) was done on cycling μ_0 H in ±7T. Before the measurements, the coil was demagnetized, using magnet reset option, provided on the software. The remanent of such 7 T coil was measured as $\mu_0 H_{rem} \approx \pm$ 30 E-4 T (∼30 Oe). This causes a false effect, changing the sign of magnetization, sweeping from positive to negative field and vice versa. Silva et al. [173] reported this effect on reference Pd sample. This effect can be corrected by

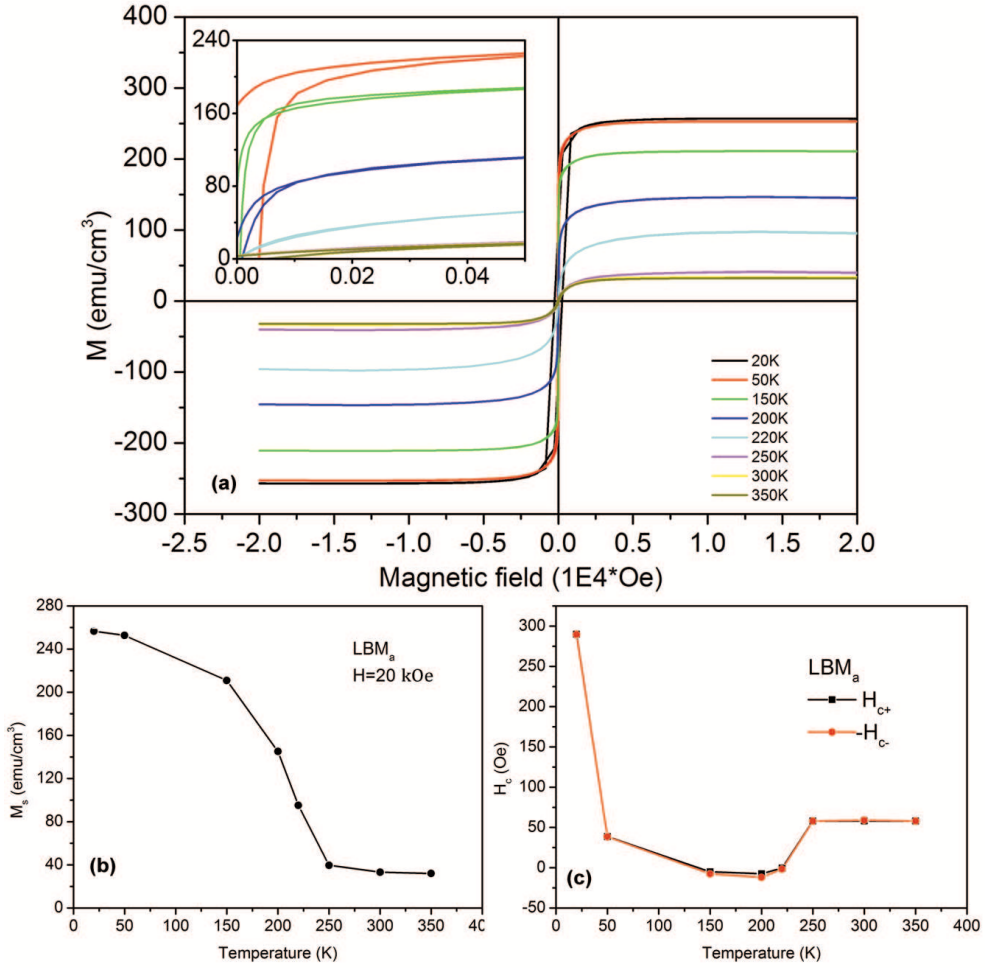

Figure 5.16: (a) Magnetic hysteresis cycles of LBM_a thin film deposited on Al_2O_3, (b) temperature dependence of the saturation magnetization and (c) the coercivity field plot versus temperature.

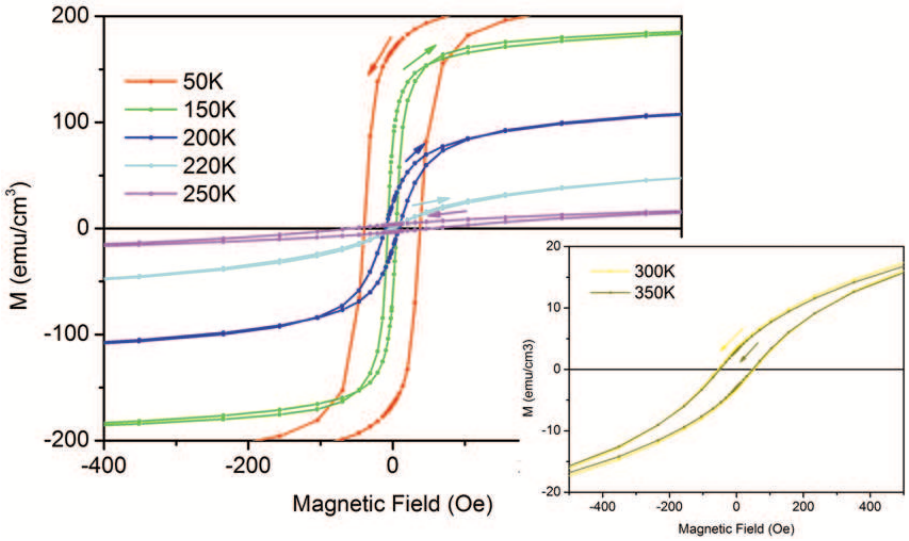

Figure 5.17: M-H curves of LBM_a show the origin of negative coercive field, shown in Figure 5.16.

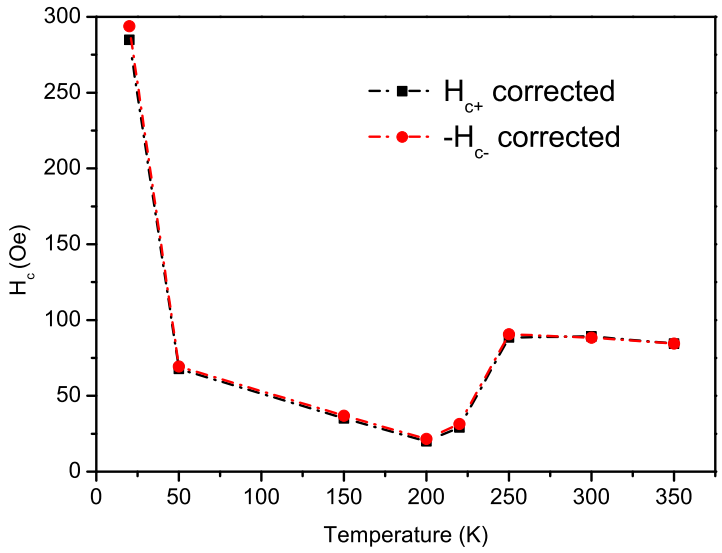

Figure 5.18: Corrected curve of coercivity versus temperature in LBM_a thin film proves the existence of a ferromagnetic phase at room temperature.

adding the mentioned value to the coercivity and the result is shown in Figure 5.18.

Meanwhile, the results of the coercivity at $T>T_C^M$ proves the existence of an extra ferromagnetic component, which was already proven by M_s-T curve, Figure 5.16(b).

5.2.3 Surface analysis

In contact-AFM mode, the contrast is generated by the detection of small variations in the tip-surface force acting on an oscillating tip scanning the surface at the sub-nm scale [174, 119]. The AFM images presented in this section were taken at room temperature using contact AFM, operated in the frequency modulation mode [175], where the tip-cantilever system is excited at its first-mechanical resonance frequency in close proximity of the surface. The forces between oscillating tip and the surface shift the resonance frequency of the tip-cantilever system, called frequency shift, Δf. The main goal for the AFM on LBM_a thin film is to detect the grain size in the film and the morphology of the surface, as shown in Figure 5.19(a) and (b). The average size of the grain structure on the surface of the film is 150 nm, as the profile of a random grain is presented in Figure 5.19(c). The histogram of the topography-scanned area shows the root mean square (RMS) roughness of 1.54 nm, and the average roughness of the surface, as 1.23 nm, which is in the range of data, extracted from the fit, done on XRR pattern, which is $\sim$0.8 nm. The difference of the roughness values, from XRR and AFM, is related to the scale of measured area. The scanned area was chosen randomly

on the sample, which could be from a highly rough region.

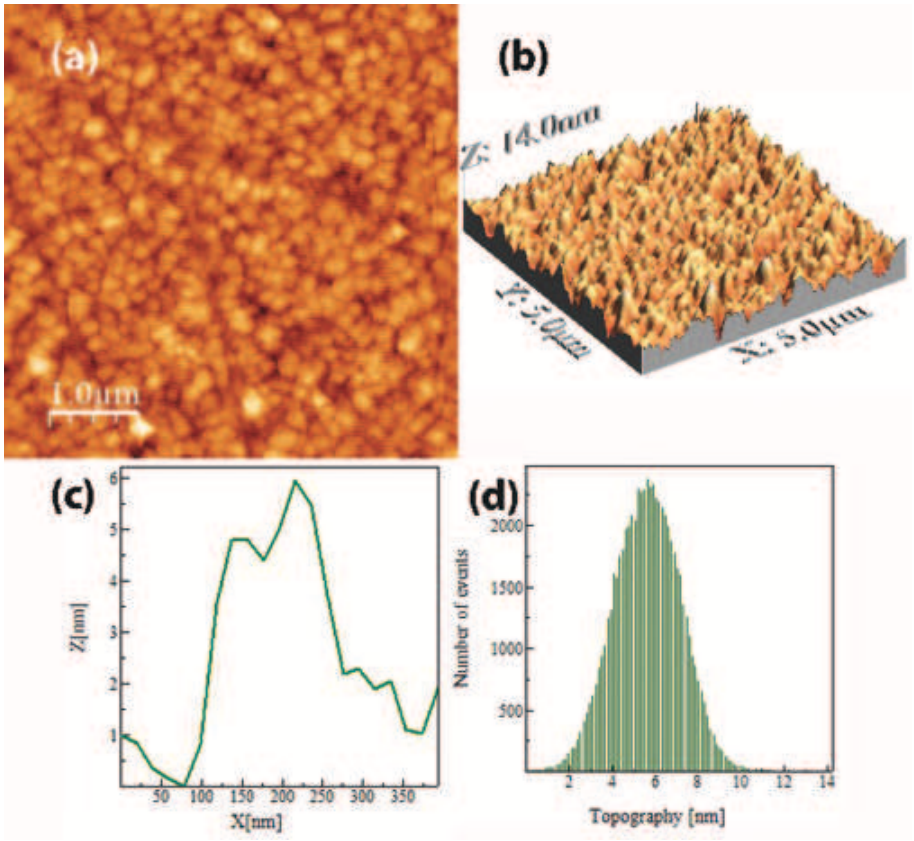

Figure 5.19: Topographic non-contact AFM image of the LBM_a surface (a) 2D view (b) 3D view, (c) profile of one of the grains, the average size of ∼250 nm and (d) histogram of the topography.

5.3 LBM/$BaTiO_3$/ LBM ($LBMBT_a$) heterostructure

The LBMBT heterostructure (LBM (40nm)/BTO (30nm)/LBM (40nm)) was deposited on Al_2O_3 substrate ($LBMBT_a$). The design of the heterostructure is shown in Figure 5.20.

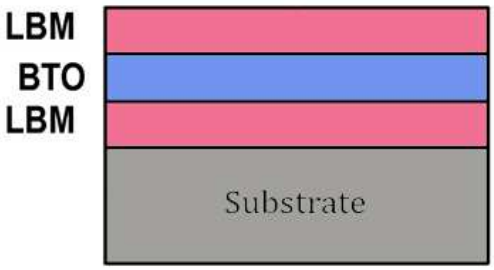

Figure 5.20: Schematic of the $LBMBT_a$ heterostructure.

5.3.1 X-Ray diffraction and Microstructure analysis

The high angle X-ray diffraction data is presented in Figure 5.21 for LBMBT$_a$ heterostructure deposited on Al_2O_3. The XRD pattern shows the highly oriented growth of the bottom LBM layer, with a (220) preferred growth direction on top of (006) plane of substrate. The out-of-plane interplanar distance, d_{220}=2.257 Å, is lower than the target (d_{220}, target= 2.259 Å), but slightly higher than the d_{220}=2.251 Å of bulk form $La_{0.9}Ba_{0.1}MnO_3$, indicating an out-of-plane relaxation of the LBM$_a$ lattice.

In comparison with single layer of LBM on the same substrate, Figure 5.1, there exists an extra peak of $(121)_L$ of LBM$_a$, which can be related to the top LBM layer, grown on top of $BaTiO_3$ (BTO) layer. The L and B indices are related to LBM and BTO, respectively. The BTO layer shows growth on $(003)_B$ direction, indicated in Figure 5.21. There is 0.28% compression of BTO layer, in comparison with bulk form, in which a=5.70 Å, from PDF files, presented in Appendix A.3.

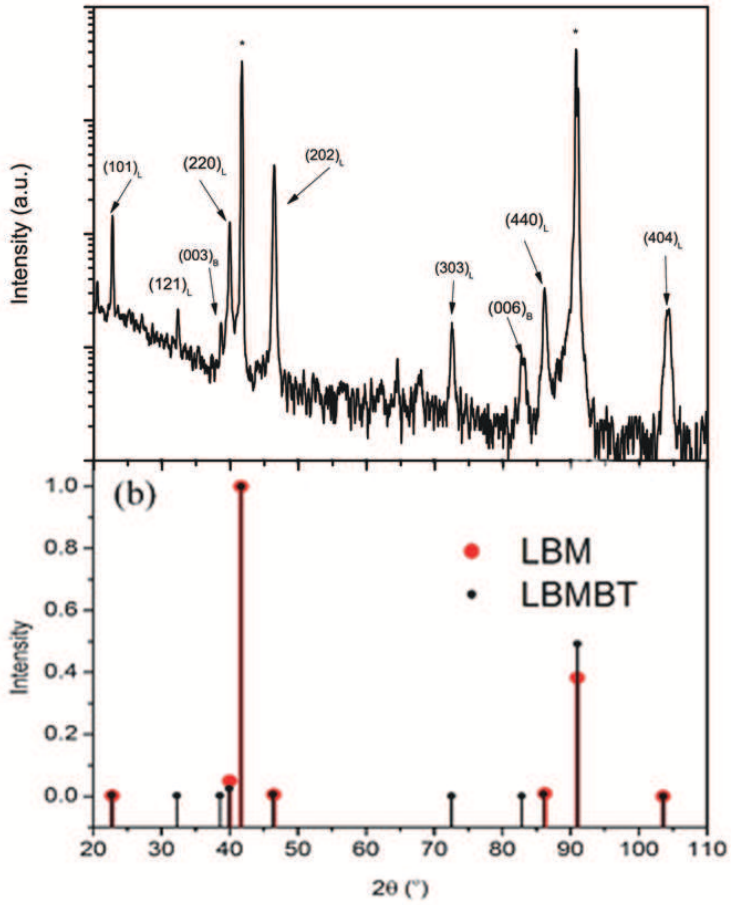

Figure 5.21: XRD pattern of LBMBT$_a$ heterostructure on Al_2O_3. The peaks, marked with asterisk are associated with (006) plane of the substrate, (b) comparison of the XRD peaks of LBM$_a$ and LBMBT$_a$, the extra peaks were assigned to the BTO and top LBM layer. The L and B indices are LBM and BTO, respectively.

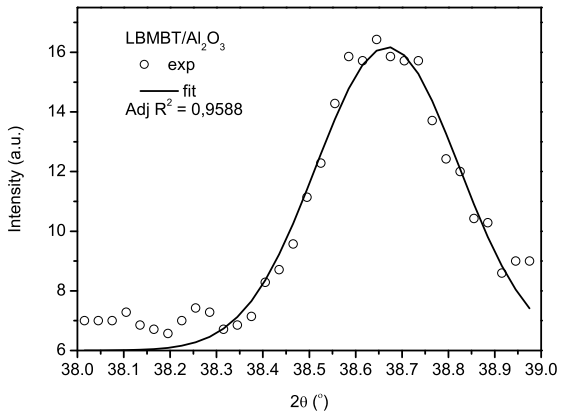

Figure 5.22: Fit of the $(003)_B$ diffraction peak of BTO layer, deposited on bottom LBM layer, on Al_2O_3 substrate.

The (220)L plane of bottom LBM_a structure is relaxed, regarding to the substrate, 4.26%. The next layer, BTO, the $(003)_B$ plane has 3.67% relaxation in regards to $(220)_L$ plane of LBM, where the highest amount of stress is observed between BTO layer and top LBM layer, 18.98%. Figure 5.22 shows the $(003)_B$ peak of BTO layer, at 38.66° and the Gaussian fit of the peak. Table 5.6 presents the crystallite size in the heterostructure, according to Scherrer equation. However, regarding the existence of $Cu_{k_\alpha 2}$ line in x-ray diffraction and low quality of X-ray measurements, the extracted values are not definite.

Table 5.6: Parameters obtained from the X-ray diffractograms of LBMBT heterostructure deposited on Al_2O_3; diffraction angle 2θ, width of the diffraction peak β_M, instrument peak broadening β_s, interplanar distances d, and crystallite size .Parameters obtained from the X-ray diffractograms of LBM thin film deposited on Al_2O_3: diffraction angle for the (hkl) planes $2\theta_{hkl}$, width of the (hkl) diffraction peak β_M, instrument peak broadening β_s, (hkl) interplanar distance of the films d_{hkl}, and crystallite size τ.

Sample	Plane	$2\theta_{hkl}(^\circ)$	β_M (°)	β_s (°)	d_{hkl} (Å)	τ (nm)
LBM/Al_2O_3	(220)	39.90	0.31	0.04	2.258	28.714
LBM/Al_2O_3	(202)	46.44	0.27	0.04	1.954	33.812
BTO/LBM	(003)	38.67	0.29	0.04	2.327	30.614
LBM/BTO	(121)	32.31	0.31	0.04	2.768	28.100

The TEM micrograph of the heterostructure, Figure 5.23, shows the growth orientation of the sample. The different crystallite regions are obvious in Figure 5.23(a). The width of these regions is varied between 30 nm to 50 nm, in width, verified by XRD, Table 5.6. The interface of the bottom LBM and the Al_2O_3 substrate, in one

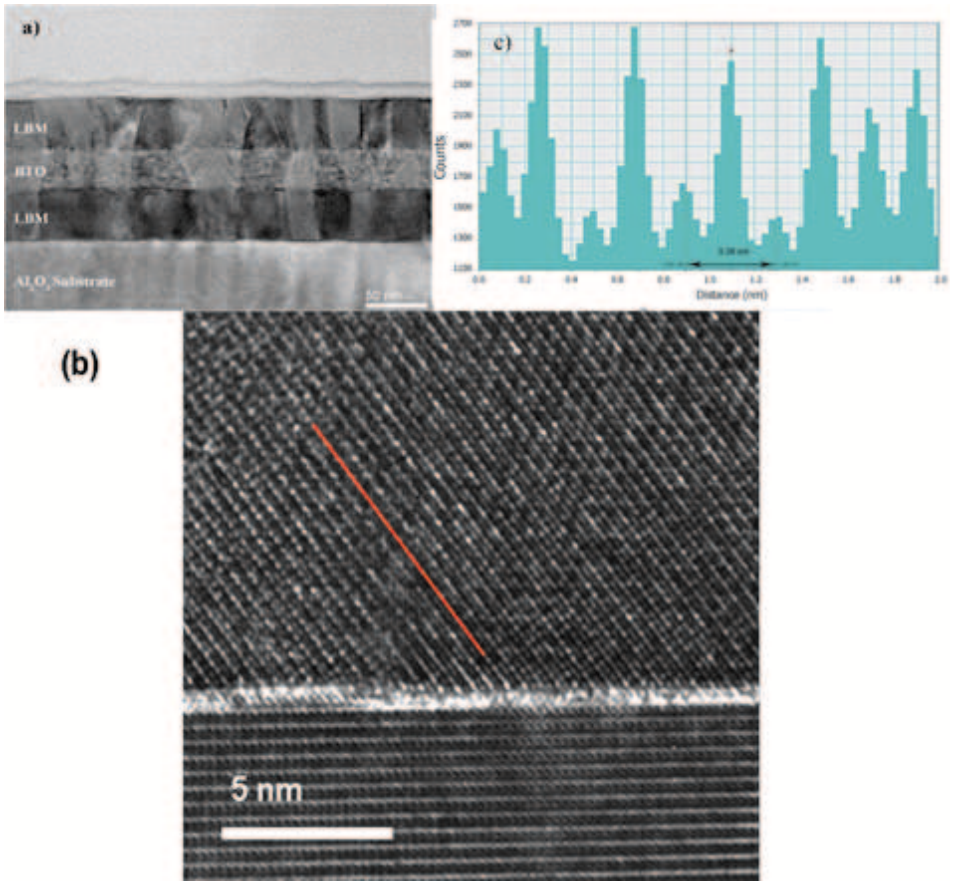

Figure 5.23: (a) TEM micrograph of LBMBT heterostructure, deposited on Al_2O_3 substrate, the thickness of the layers are 40/30/40 nm, respectively, (b) the interface between bottom LBM layer and substrate, the epitaxial growth of the film is obvious, (c) intensity profile of bottom LBM layer shows the inter-planar distances of the layer.

sample crystallite regions, is shown in Figure 5.23(b), in zone axis of [010] for the film, on [100] plane of the substrate. The Figure 5.23(c) shows the intensity profile of the film, pointing that the lattice parameter is 3.9 Å, along the shown line in Figure 5.23 (b). The simulations, done with JEMS software, show the position of the participating elements on the structure, as shown in Figure 5.24.

In Figure 5.24(a), the HRTEM micrograph of the bottom LBM film is shown. The atomic positions were determined by simulation, shown in Figure 5.24(b). It is obvious that the La/Ba atoms are positioned in a separate plane, while Mn and O atoms form a separate plane.

Figure 5.25 shows the different crystalline structure on the bottom LBM layer, in three adjacent regions. The zone axis in these structures change slightly from (100) and create various crystalline regions. The change in the zone axis of neighboring regions can be due to the overlay of two neighboring regions or the newly structure, being opposed to the stress from other neighbors.

The high resolution TEM micrograph of intermediate BTO layer is shown in Figure

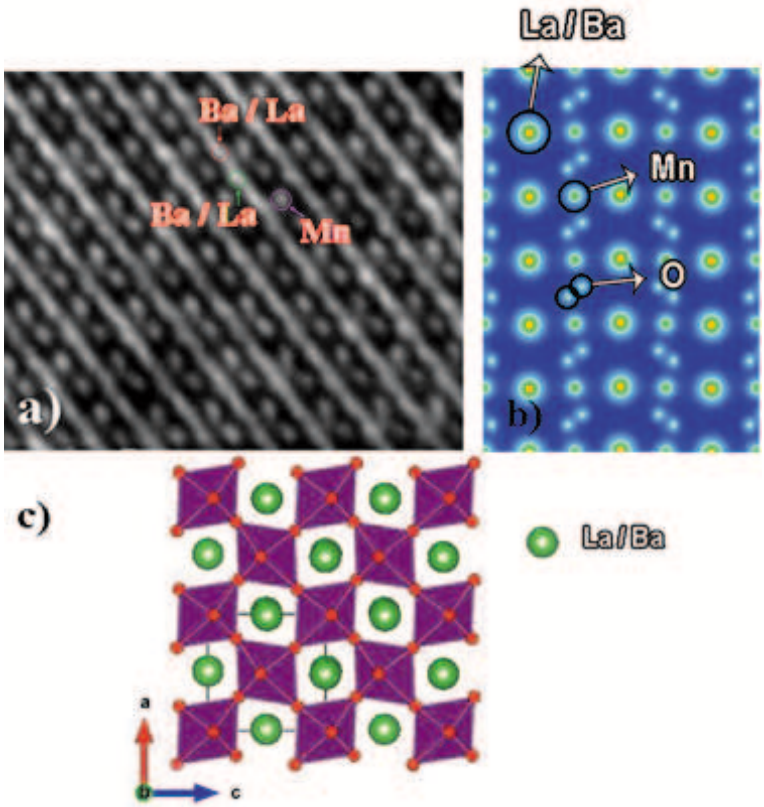

Figure 5.24: (a) High resolution TEM image of bottom LBM layer, the bright line shows the position of La and Ba atoms, (b) Simulation of the LBM thin film, with atoms indicated on it, c) atomic position of LBM bulk structure.

5.26(a). The thickness of the layer is ∼32.7 nm and its crystallinity is less than the bottom LBM layer, proved by XRD data, showing smaller crystallite regions. The periodicity of the lattice is measured in two different regions and shown in Figure 5.26(b), as 3.03 Å and 3.39 Å.

FFT of the marked region in Figure 5.26(c) is shown in Figure 5.27, and showing the interplanar distances of 3.04 Å (observed from intensity profile), 2.10 Å and 2.45 Å (d_{003}). The track of different crystallite in the bottom LBM continues inside BTO layer and the layer has unclear crystalline grains, as shown in Figure 5.26 (c).

As a qualitative comparison, the BTO layer has the least crystallinity, among all the layers, as shown in Figure 5.28. The FFTs, taken from each layer, show the crystallinity of the layers, proven by the FFT of BTO layer, which shows the least crystalline structures.

The STEM-HAADF micrograph and EELS-mapping of a chosen point in the $LBMBT_a$ heterostructure is shown in Figure 5.29. The micrograph shows the concentration of elements in layers.

Intensity profile of EELS-mapping, Figure 5.29, plotted in Figure 5.30, shows sharp

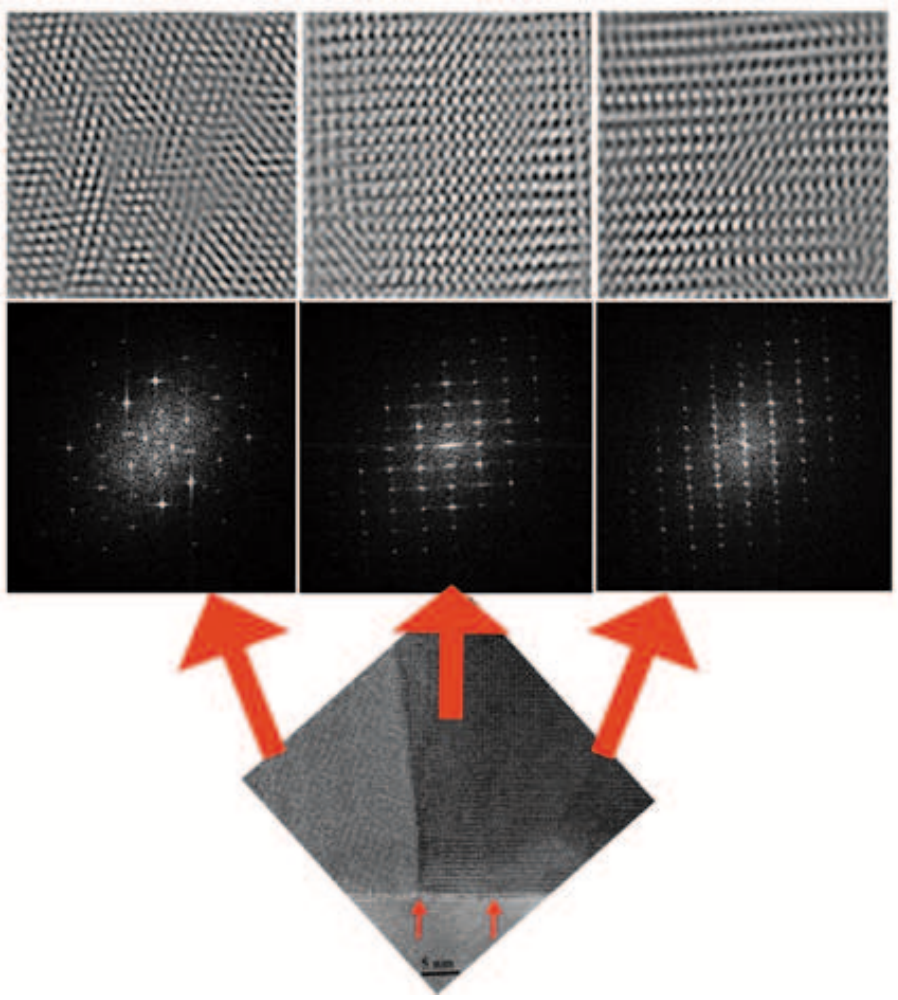

Figure 5.25: High-resolution TEM of different orientation of the bottom LBM layer.

edges on Mn ions, restricted in LBM layers, while its intensity is less in the top layer. La ion, also follows the same intensity pattern, where it also spread on BTO layer. The most interesting result is the spreading of Ti, where it diffused in both LBM layers, top and bottom LBM layers. However, the resolution of the EELS-mapping is not enough for any precise quantitative analysis. Diffusing the Ti ions into LBM layer, they replace Mn^{4+} sites and reduce the magnetic response of the layer, compared to single layer of LBM_a on Al_2O_3 substrate.

RBS mesurements were done on a LBMBT heterostructure (10nm/30nm/110nm), different from the heterostructure measured in TEM analysis (40nm/30nm/40nm), Figure 5.31. After sample preparation for TEM, there was not enough sample for RBS experiment, therefore a sample from another series was used. RBS confirms a heterostructure growth, therefore the thicknesses, derived from other experiments (such as reflectometry) is used to deduce atomic density of layers, as shown in Table 5.7 [165, 166]. As it is obvious, the diffusion of Ti and La in the heterostructure was not

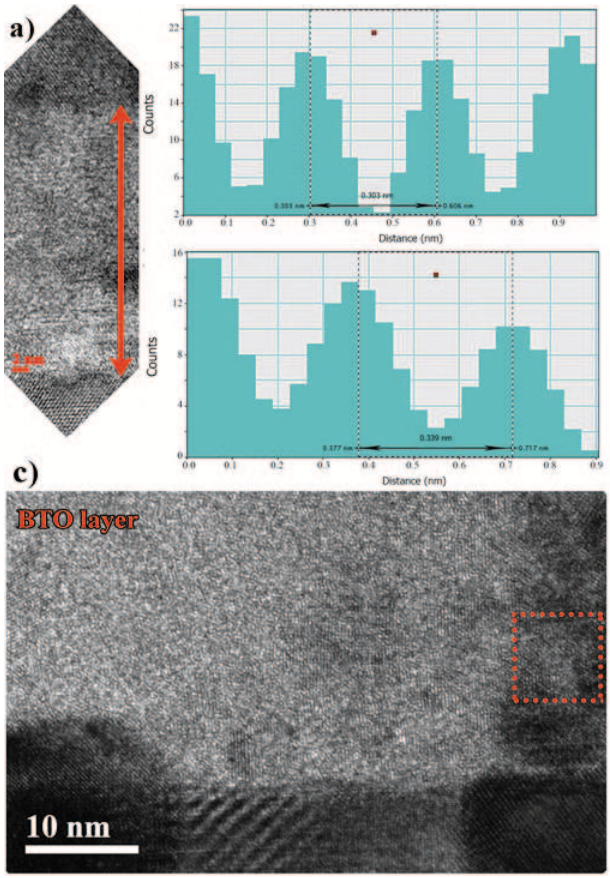

Figure 5.26: (a) High-resolution TEM of intermediate BTO layer; (b) the intensity profile in lattice distances, in different regions, are shown in intensity profile graphs; (c) the interface of LBM/BTO layers.

considered, in simulation. On the other hand, looking at $BaTiO_3$ layer (2nd layer), it is clear that the content of Ba is below Ti content, which was also presumed by deposition conditions, as was described in section 5.2.1. Although the deficiency of Ba is proved

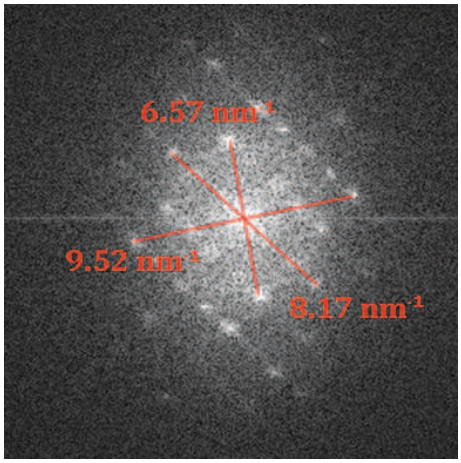

Figure 5.27: FFT of the marked region in Figure 5.26(c), showing the interplanar distances between planes in BTO layer.

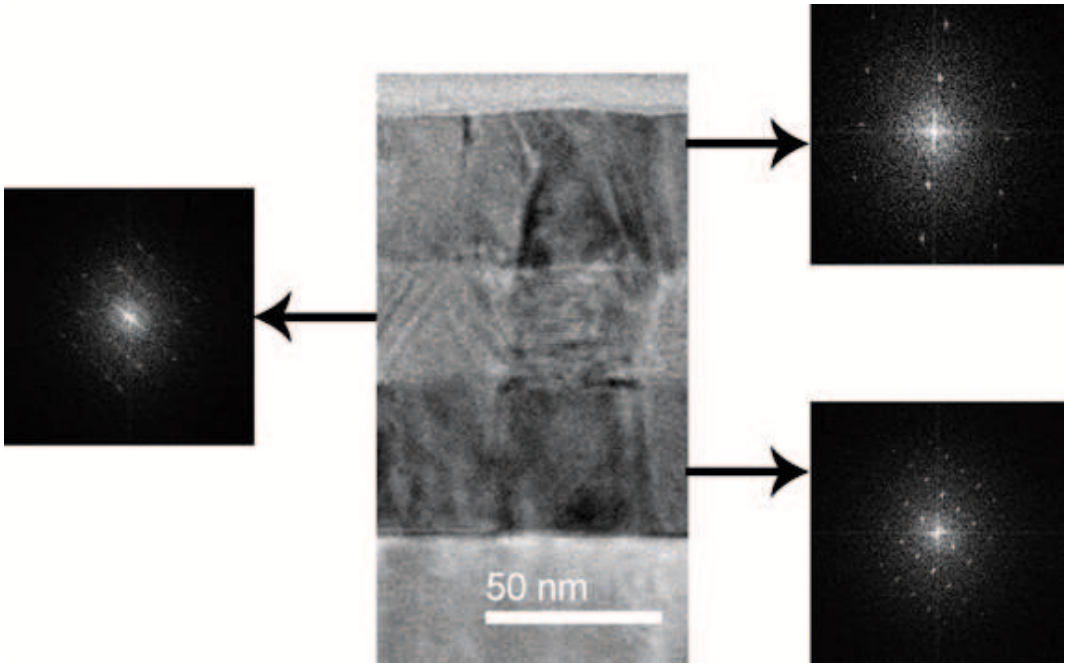

Figure 5.28: The structure of the tri-layer, with separated FFT for each layer. The FFTs show the crystalline quality of the layers.

by RBS, the La/Ba ratio is achieved 4/1, that is higher than the ratio, which was used for XRD. The difference in the ratio can correspond to ignorance of La diffusion in the calculations and also the overlapping of peaks of La and Ba, where makes it hard to distinguish the elements from each other, within the experimental method.

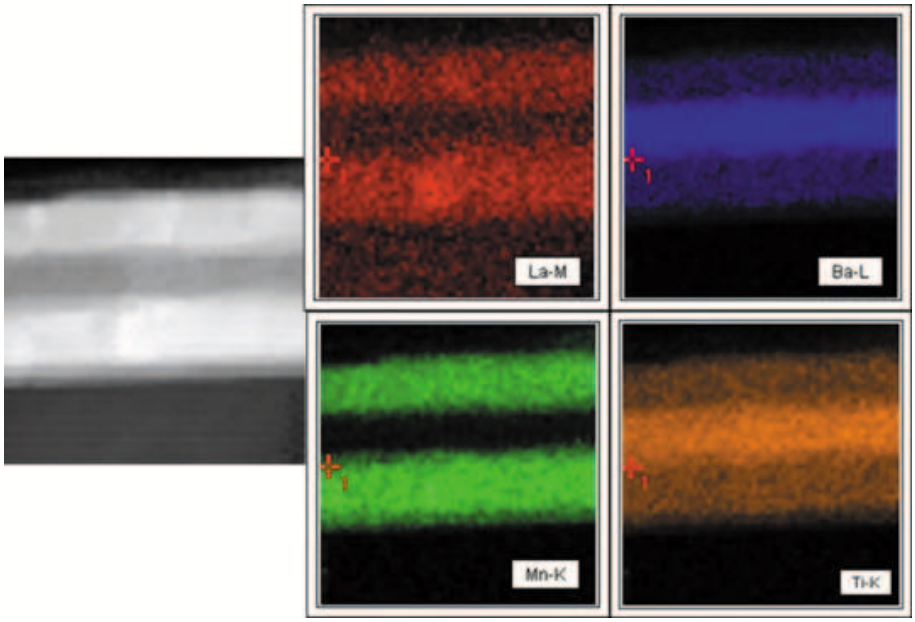

Figure 5.29: The STEM-HAADF micrograph and EELS-mapping of the LBMBT$_a$ heterostructure on Al_2O_3 substrate.

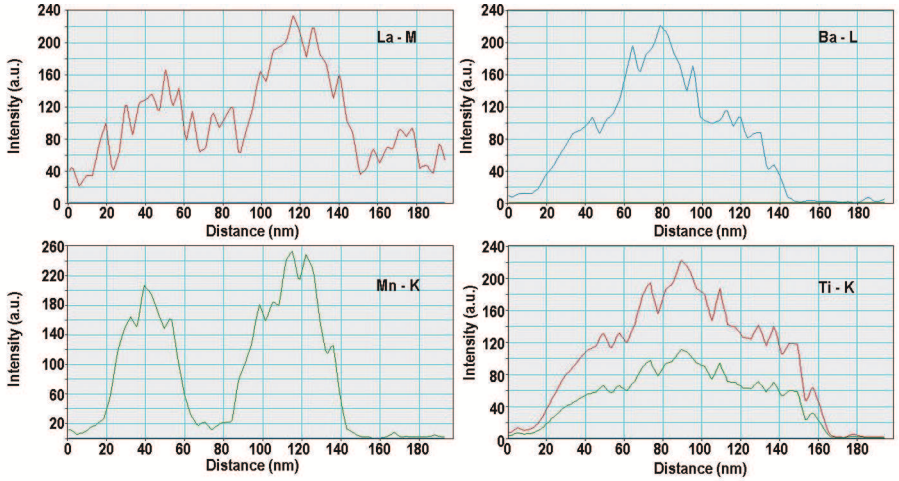

Figure 5.30: Intensity profile of EELS-mapping micrograph of $LBMBT_a$, shown in Figure 5.29, shows diffusion of La and Ti on whole structure. The top LBM is on the left.

Table 5.7: The results of fitting on RBS spectrum of LBMBT (LBM (110nm)/BTO (30 nm)/LBM (10nm)/Al_2O_3 substrate.

Layer	t	Density	La	Mn	O	Ba	Ti	Al
	10^{15} atom/cm^2	10^{22} atom/cm^3						
1 (top LBM)	1255.468	11.413	15.9514	20.0000	60.0000	4.0486	0.0000	0.0000
2 (BTO)	320.359	10.678	0.0000	0.0000	64.5399	6.3804	19.0797	0.0000
3 (bottom LBM)	84.912	8.491	15.9514	20.0000	60.0000	4.0486	0.0000	0.0000

5.3.2 Magnetic and Magnetoresistance behaviour

The sample dimension, used in these measurements is 8.9 (mm)×4.1(mm)×(40(nm) LBM_{bottom}+40 (nm) LBM_{top}). The 30 nm $BaTiO_3$ middle layer does not contribute in this part, because of its diamagnetic contribution in the magnetic measurements. The

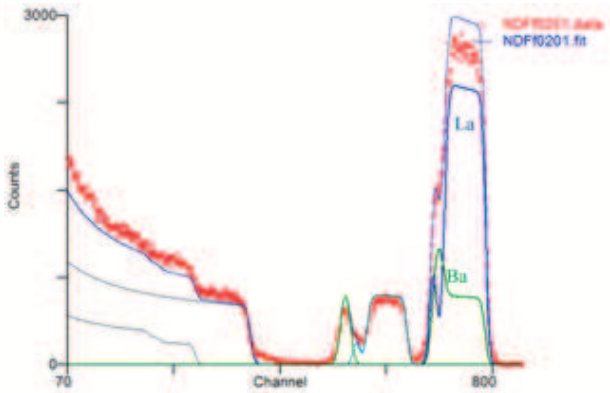

Figure 5.31: (Up) RBS analysis and simulations, (down) PIXE results of LBMBT heterostructure (LBM (110nm)/BTO (30 nm)/LBM (10nm)/Al_2O_3). The measured film is different from the sample in the rest of measurements in this section (LBM (40nm)/BTO (30 nm)/LBM (40nm)/Al_2O_3).

temperature dependence of the magnetization of LBMBT$_a$ heterostructure on Al_2O_3 is plotted in Figure 5.32 (a). The measurements were performed under a small magnetic field, H = 100 Oe. The T_C^M is observed at 209.0 K, derived from FC curve, from the maximum of |dM/dT|. The irreversibility temperature is calculated as 159.3 K, which is obtained from the separation between FC and ZFC curves.

According to the STEM-HAADF results of LBMBT$_a$ heterostructure,Figure 5.29, Ti had diffused in the top and bottom LBM layers, which change the composition of the film. Ti atoms can replace Mn^{4+} atoms in LBM structure and reduce the magnetic response of the sample, in comparison with pure LBM layer.

Figure 5.33 shows the inverse of magnetization of LBMBT$_a$ heterostructure, where the contribution of background and substrate were removed by Curie-Weiss fit. Unlike LBM$_a$ thin film, Figure 5.14, the main phase in the LBMBT$_a$ heterostructure is not so close to to simulated bulk $La_{0.9}Ba_{0.1}MnO_3$ phase.

The magnetic hysteresis loops are plotted in Figure 5.34(a), measured at different temperatures, ranging from 20 K to 350 K. The share of substrate and $BaTiO_3$ is subtracted from the curves, using the measurements done on an identical substrate. The results show saturation magnetization of M_s =210 emu/cm^3, at 20 K, shown in Figure 5.34(b). In comparison with the single LBM$_a$ layer on the same substrate, the magnetization of the heterostructure has decreased, ∼46 emu/cm^3, which is due to the lower crystallinity of top LBM layer [92, 176]. The BTO layer does not contribute in magnetization measurements, according to EELS-mapping results, showing no magnetic

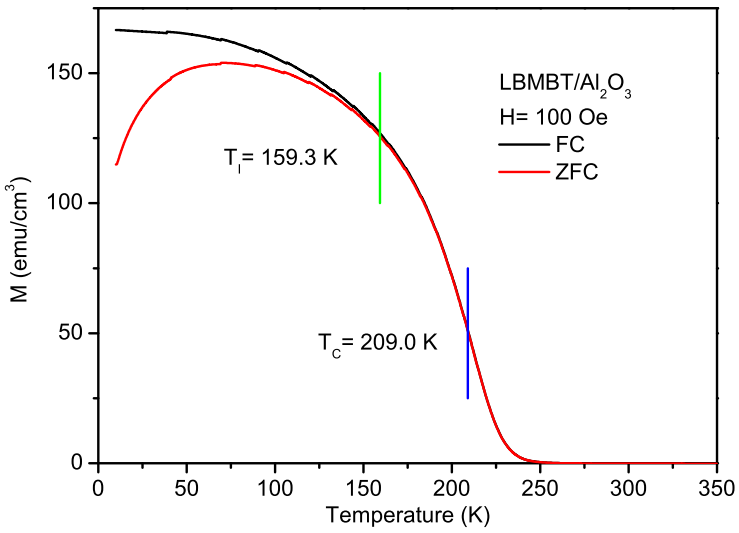

Figure 5.32: (a) Temperature dependence of the magnetization of LBMBT$_a$ heterostructure deposited on Al_2O_3.

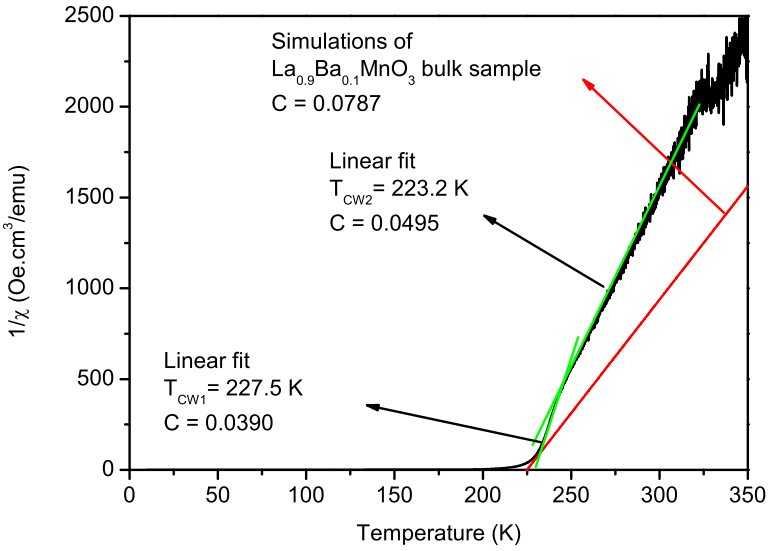

Figure 5.33: Temperature dependence of the inverse magnetization of LBMBT$_a$, after applying Curie-Weiss law in paramagnetic phase and removing the background.

(Mn) ions in the layer.

The negative coercivity in the temperature range in the range between 150 and 300 K, encompassing the Curie temperature (T_C^M ~209 K), is visible in Figure 5.34(c), while at lower temperature, the cycles have normal appearance (i.e. H_c>0). This is clearly a spurious effect, related to the superconducting coil, which produces a remanent magnetic field, as explained in section 5.2.2. The remanent magnetic field changes sign as the field is swept from positive to negative values, shifting the M(H) curve to positive fields in the decreasing branch and to negative fields in the increasing field branch. Close look at the hysteresis loops, around M = 0 emu/cm^3 shows the shift in the coercive field, clearly, Figure 5.35, and the corrected coercivity plot is shown in Figure 5.36.

The temperature dependence of the electrical resistivity was measured, where it presents an insulating-like behaviour, as expected, in comparison with the resistivity behaviour of single layer of LBM$_a$, shown in Figure 5.11(a). However, no inflection point is observed, and the derivative dρ/dT is monotonous Also, the logarithmic scale of resistivity is depicted in Figure 5.37(b), showing the cross-over temperature at 216.3 K, close to T_C^M determined from magnetization. The resistivity in the heterostructure has increased slightly from the LBM$_a$ single layer. This can be due to the lower degree of crystallization of the LBM layer; namely the top LBM in the LBMBT$_a$ heterostructure, as proofed by TEM micrograph. It is worth to note that in resistivity measurements on the heterostructures, only the contribution of top layer is taking into account, because

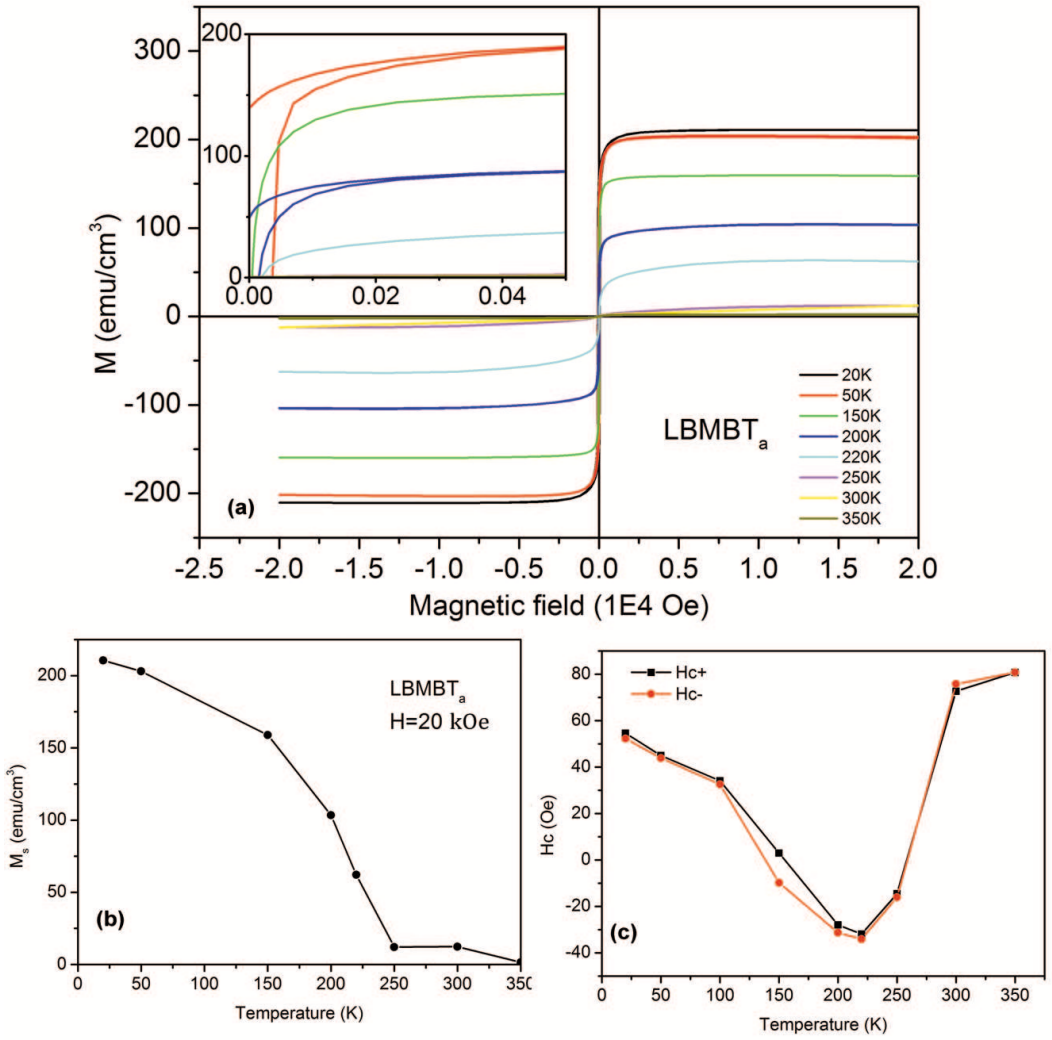

Figure 5.34: (a) Magnetic field dependence of the magnetization of $LBMBT_a$ heterostructure deposited on Al_2O_3, (b) temperature dependence of the saturation magnetization and (c) coercivity versus temperature curve, showing a drop, near T_c^M.

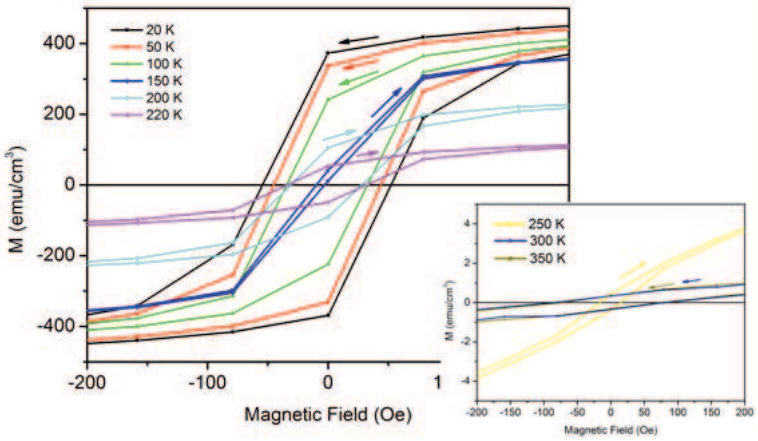

Figure 5.35: M-H curves of $LBMBT_a$ show the origin of negative coercive field, shown in Figure 5.34.

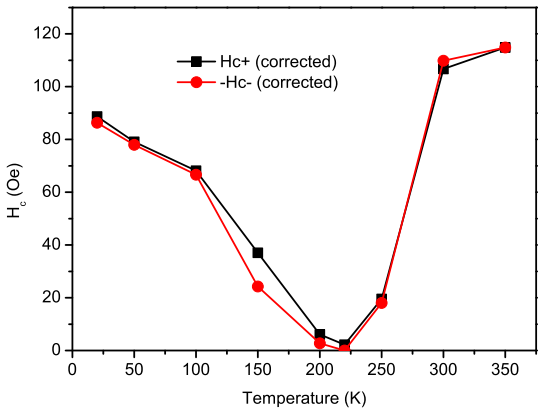

Figure 5.36: Corrected coercivity plot of $LBMBT_a$ heterostructure on Al_2O_3 substrate.

middle BTO layer is a strong insulator and does not let the current pass through.

The magnetoresistance measurements were done with the current of 1.0 μA and field up to 1.0 T. The results show decreasing MR magnitude with increasing temperature, as shown in Figure 5.38(a) and (b). However, the slope of MR changes is more gradual, in comparison with single layer of LBM_a. The fluctuations in Figure 5.38(a) are due to the fluctuations in temperature, during experiment. The resistivity of the heterostructure is decreasing while increasing the magnetic field,Figure 5.38 (c). The maximum magnetoresistance at 1.0 T is close to the pure LBM_a thin film (18%), Figure 5.12.

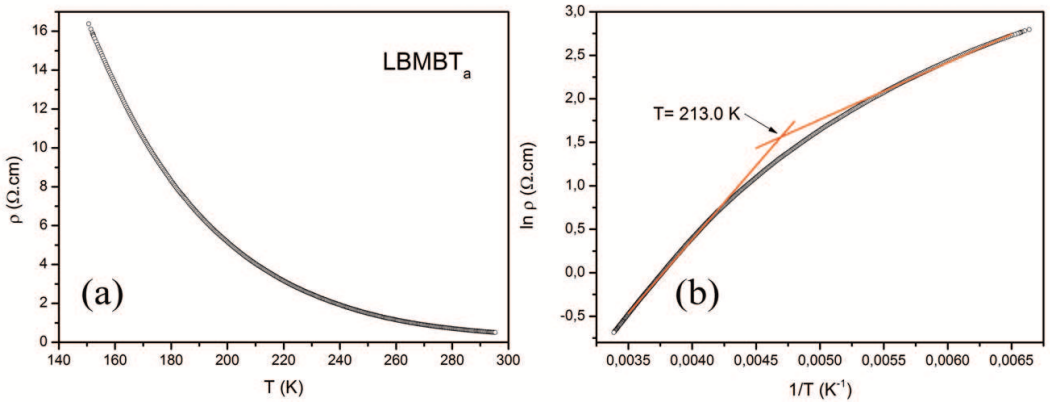

Figure 5.37: (a) The plot of resistivity versus temperature does not show the transition temperature, inset: plot of derivative of resistivity versus temperature does not show any transition temperature, (b) 1/T dependence of logarithmic scale of resistivity of $LBMBT_a$ heterostructure on Al_2O_3 substrate, shows the transition temperature at 209.5 K.

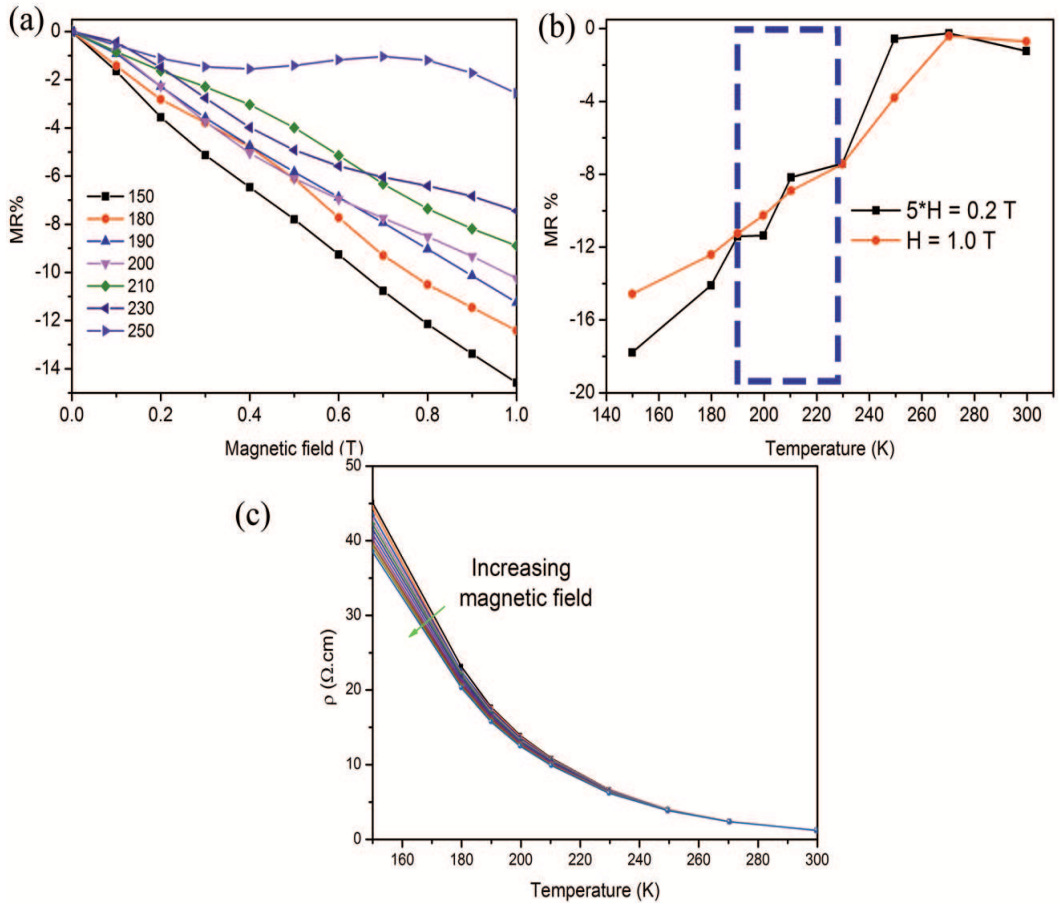

Figure 5.38: (a) Field dependence of magnetoresistance of $LBMBT_a$ heterostructure, (b) Temperature dependence of the magnetoresistance at 1.0 T and 0.2 T, the magnetoresistance at 0.2 T is multiplied by the factor of 5, (c) the temperature dependence of the resistivity of $LBMBT_a$ heterostructure.

5.3.3 Surface analysis

The contact AFM image, taken at room temperature, shows the topography of the surface of the heterostructure, Figure 5.39. The scan was done over 1.5μm×1.5μm area, showing the RMS of 1.09 nm, the roughness average of 0.83 nm, and the average height is 4.74 nm. Figure 5.39(a) and (b) show the 2-D and 3-D raster of $LBMBT_a$ heterostructure on Al_2O_3 substrate. The average size of a sample grain is around 300 nm, Figure 5.39(c). Also, the histogram of the AFM raster shows that most of the grains have the height between 4 to 5 nm. Comparing to average roughness of LBM_a single layer, the heterostructure has rough surface. This is shown, also, in grain size, where in single layer, the sample grain size is 150 nm. Deposition of each layer starts by nucleating over the previous layer, which is the source of the layer roughness. In heterostructure, the top LBM layer is deposited on top of $BaTiO_3$ layer, which enhances the roughness of the top layer, as shown, also, by TEM image.

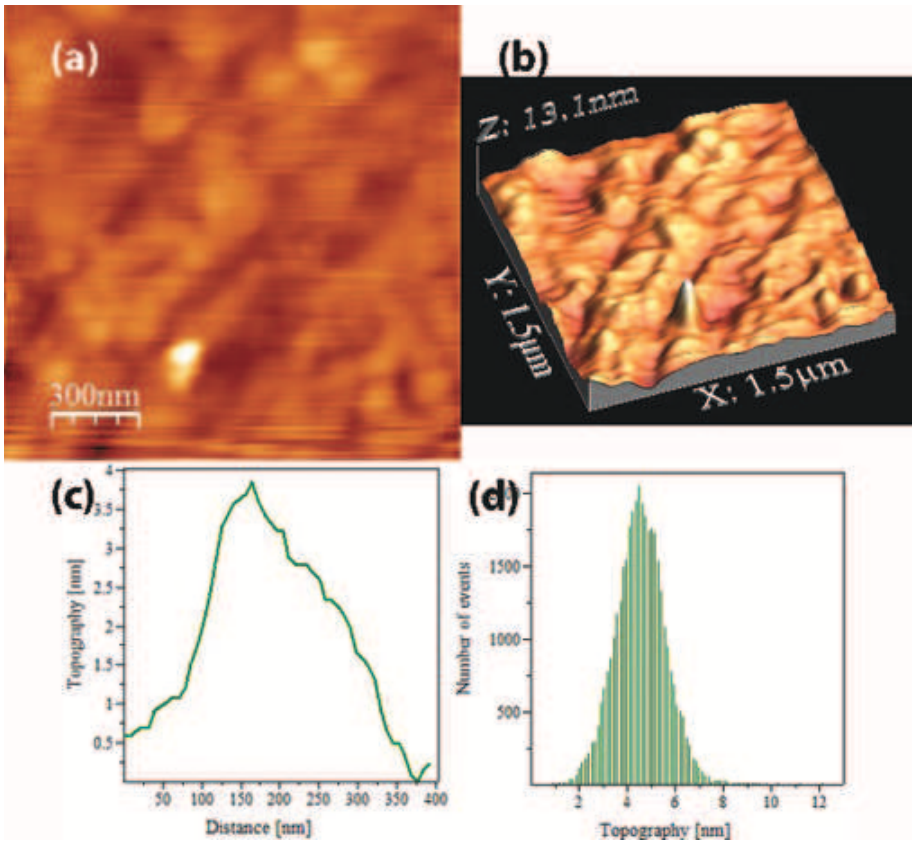

Figure 5.39: Topographic AFM image of the LBMBT$_a$ surface (a) 2D view (b) 3D view, (c) profile of one of the grains, the average size of ∼300 nm and (d) histogram of the topography.

Chapter 6

Structures on Si substrate

The thin films of LBM_s and BTO and also the heterostructure of $LBMBT_s$ have also been grown on Si, with different deposition parameters, as summarized in Table 6.1. It should be noted that during deposition of LBM_s thin film, there was a power cut in the system, two minutes after starting the deposition. During this period, the shutters were closed, and reopened after the deposition conditions were stable.

Table 6.1: Deposition parameters for the thin films and heterostructures, (LBM_s, BTO, and $LBMBT_s$, respectively) grown on (100) single crystal Si substrate.

Sample	Substrate	Base pressure	Deposition						
			Temperature	dc bias	Distance	P_{Ar}	P_{O_2}	Time	Rate
		mbar	±5°C	V	mm	mbar	mbar	min	nm/min
LBM_s	100 Si-SiO_2	3.1E-08	696	30.7	105	5.0E-03	1.0E-03	135	1.07
BTO	100 Si	1.8 E-07	633	122	97	5.0 E-03	5.0 E-04	60	0.66
BTO	100 Si-SiO_2	4.9E-08	696	110	85	2.5E-03	5.0E-3	8	1.2
$LBMBT_s$	100 Si-SiO_2	3.9E-08	512	155	105/105/105	6.0E-03	5.0E-04	30/30/30	1.3/1/1.3

6.1 $La_{1-x}Ba_xMnO_3$ thin film

6.1.1 X-ray diffraction characterization and Microstructure analysis

Figure 6.1 presents the XRD spectra of LBM_s thin film, deposited on (100)-Si/SiO_2 substrate. The film shows weakcrystallinity. Following the composition, which we select for LBM_a thin film, the growth directions is labelled (111).

Table 6.2 shows the crystallite size and inter-planar distances of (111) and (200) directions of the LBM_s films on silicon substrate. Based on the use of $Cu_{k_\alpha 2}$ line in X-ray diffraction, the values suffer from high error.

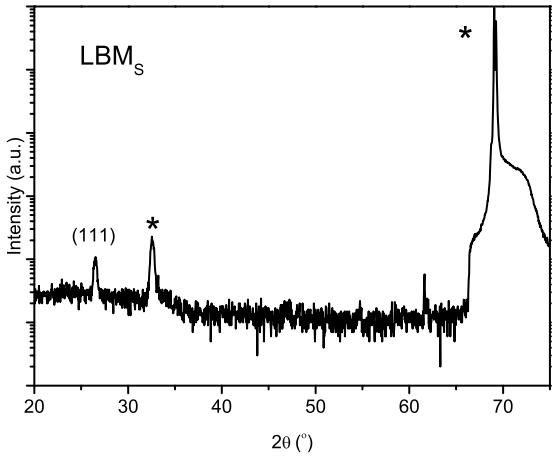

Figure 6.1: X-ray diffractogram of LBM$_s$ thin film deposited on Si/SiO_2. The peaks marked with an asterisk symbol (*) belong to the substrate.

Table 6.2: Parameters, crystallite size and inter-planar distance, obtained from the X-ray diffractograms of LBM thin film deposited on silicon.

Sample	Plane	$2\theta_{hkl}(^\circ)$	β_M (°)	β_s (°)	d_{hkl} (Å)	τ (nm)
LBM$_s$	(111)	26.54	0.463	0.044	3.36	17.70

The thickness and the microstructure of the film on silicon substrate were assessed by TEM and the main results are shown in Figure 6.2. The flat surface of the film is obvious in TEM micrograph. The thickness of the local amorphous SiO_2 layer is 17 nm, on top of the silicon substrate. The micrograph shows different structures, which can be due to change in the condition of deposition, caused by the energy cut. The bottom part is grown on local SiO_2 layer, amorphously, for ∼55 nm. After the power-cut, there was a pause for the system to stabilize, and restore the initial growth conditions. Above 55 nm, the structure tends to show some crystallinity, which is not homogenous, along the film. However, by increasing the thickness, degree of crystallinity is increased. This crystallization was detected in XRD, as it is shown in Figure 6.1. The total thickness of the LBM$_s$ layer is 145 nm. Figure 6.2(c) shows one of the grains of the film, where planes of atoms can be observed.

RBS analysis of the sample is shown in Figure 6.3. RBS shows extensive roughness and/or interdiffusion. This is completely in accordance with TEM images.

Due to high roughness in the sample, it is impossible to have a good fit for RBS measurement.

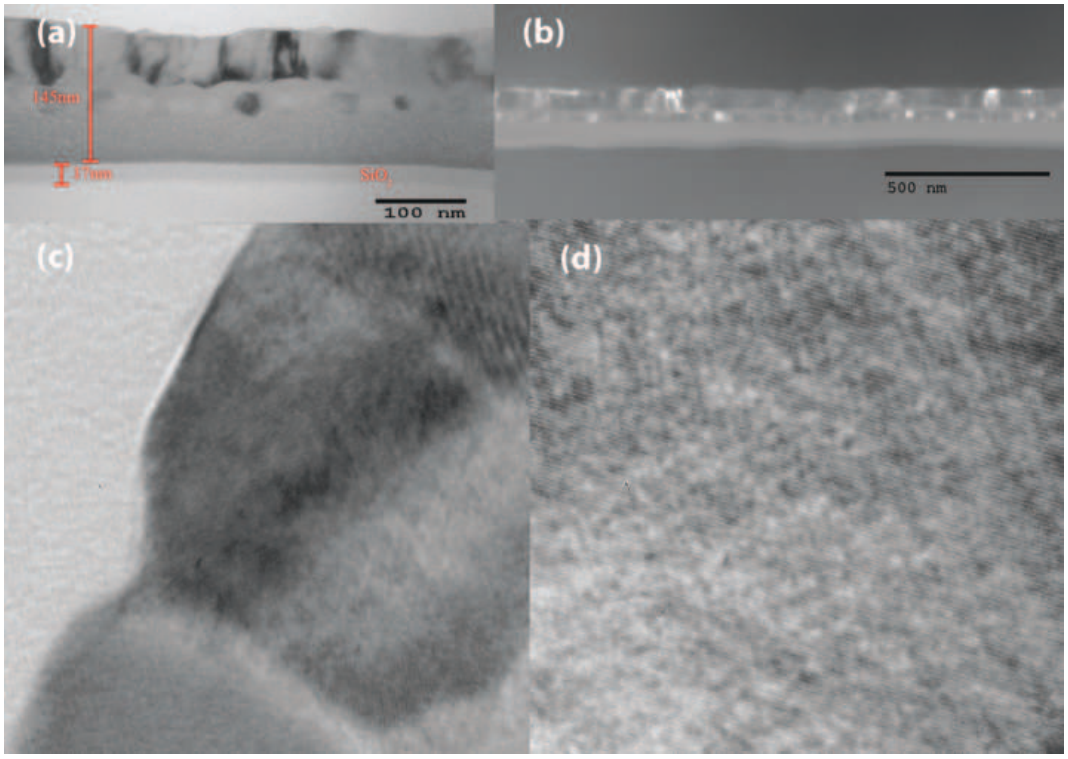

Figure 6.2: (a) TEM micrograph of LBM_s thin film. (b) Dark field of the thin film. Brighter spots show the crystalline areas, in different layers, caused by changing the growth conditions, (c) grain structure and the crystallized region of the top layer, (d) the amorphous structure of bottom layer of the LBM_s film.

6.1.2 Magnetometry and Magnetoresistance

All the measurements in this section were done on the sample, with the dimension of 9 (mm) × 4.5(mm) × 145 (nm). The temperature dependence of the resistivity, ρ(T), and magnetization, M(T), for LBM_s are shown in Figure 6.4 and Figure 6.9. The sample

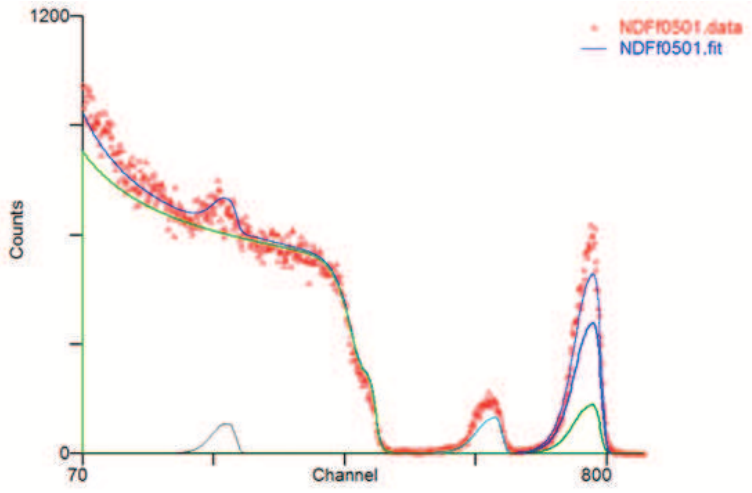

Figure 6.3: (Up) RBS data and simulation, (down) PIXE data of LBM_s thin film.

presents the insulator-like behaviour in whole temperature range, from 150 to 300 K, while the cross-over temperature of low temperature and high temperature region, T_C^R, show the ferromagnetic-paramagnetic transition of the film on Si, at 216.9 K. However, the T_C^M, driven from magnetic measurements, shows the transition temperature at 194.6 K.

The temperature dependence of the magnetization of the sample was measured with an applied field H=100 Oe after zero-field-cooling and field-cooling, as described in Section 3.4.7. The results are presented in Figure 6.4. Moreover; the separation between ZFC and the FC curves, associated with irreversibility, happens around 130.6 K.

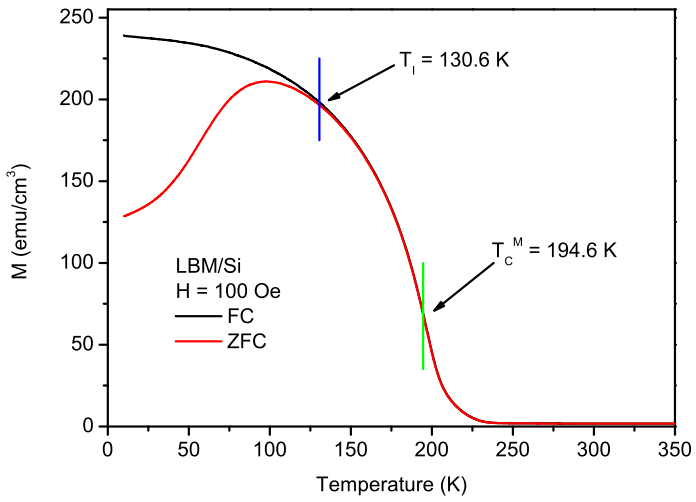

Figure 6.4: Temperature dependence of the magnetization of LBM_s thin film deposited on Si.

In comparison with the same thin film on Al_2O_3 substrate, LBM_a, at 100 Oe, magnetization has decreased slightly for the film on Si, ~20 emu/cm^3 from 190 to 170 emu/cm^3, as shown in Figure 5.13. The decrease in the magnetization can be due to the lower degree of crystallinity of the films [92, 176, 177], which in this case, referring to the TEM images, Figure 6.2, the film on Al_2O_3 substrate is more crystalline. The higher deposition rate in LBM_s thin film, leads to lower degree of crystallinity, which leads to lower magnetization.

Figure 6.5 shows the Curie-Weiss fit, done on LBM_s thin film, where there is a non-linear region in the temperature range of 270 – 350 K. The fit shows a mixed behaviour, regarding some remaining background in the mentioned temperature range. This extra phase mixture interferes with the linear behaviour of paramagnetic and cannot be fitted by Curie-Weiss fit.

Figure 6.6 shows the hysteresis loops at different temperatures for the sample, after subtracting the diamagnetic contribution from the substrate. It is obvious from the

figure that there is a saturation magnetization at all temperatures, with the maximum value of 277.8 emu/cm^3, at 20K. The coercivities for the LBM films deposited on Al_2O_3 and Si substrate are 250 and 130 Oe at 20 K, respectively. It can be seen that the coercivities for the LBM film on Si are lower than those deposited on Al_2O_3 substrate. Therefore, considering the change in the elemental composition, and the crystallite structure in the film, both originated from the strain between film and substrate, the reduction in the magnetic properties of the sample is unavoidable. Higher crystallinity in LBM$_a$ thin film leads to higher magnetization in the film.

Figure 6.6(c) illustrates the coercivities at different temperatures, where H_{c+} and H_{c-} represent coercivity at positive and negative magnetic field, with the close look around H=0 Oe, in Figure 6.7. The comparison between H_{c+} and H_{c-} shows that there is no exchange-bias in the sample. The small opening of H_{c+} and H_{c-} at T = 200 K is smaller than the remanent field of the superconducting coil, as seen before, therefore it is correctable. However, coercivity shows different behaviour around T_C^M. The measured remanent field of used system in this thesis was done in M(H) measurements of paramagnetic Pd reference sample on cycling μ_0H in ±7 T. Before the measurement, the coil was demagnetized, using Magnet reset option, provided on the software. The remanent of such 7 T coil was measured μ_0 H_{rem}=± 30 E-4 T (30 Oe), as described before.

By comparing the results, it is confirmed that the decrease of H_c around T_C is due to the superconducting coil. The corrected coercivity plot is shown in Figure 6.8.

Figure 6.9(a) shows the temperature dependence of the electrical resistivity, where figure shows the insulator-like behavior, the electrical resistivity increases with decreasing

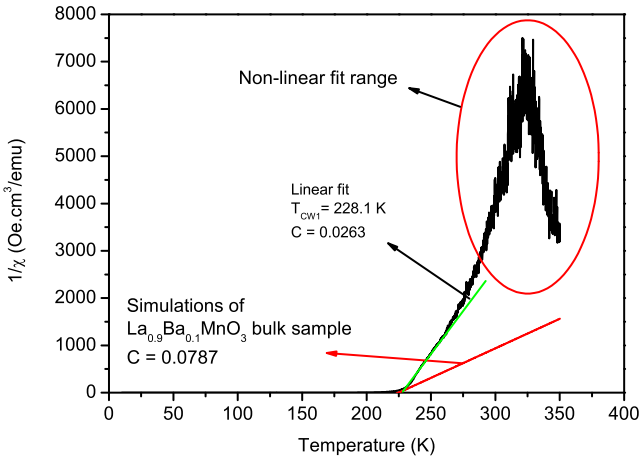

Figure 6.5: Temperature dependence of inverse of magnetization in LBM$_s$ thin film, after removing the contribution of substrate and background.

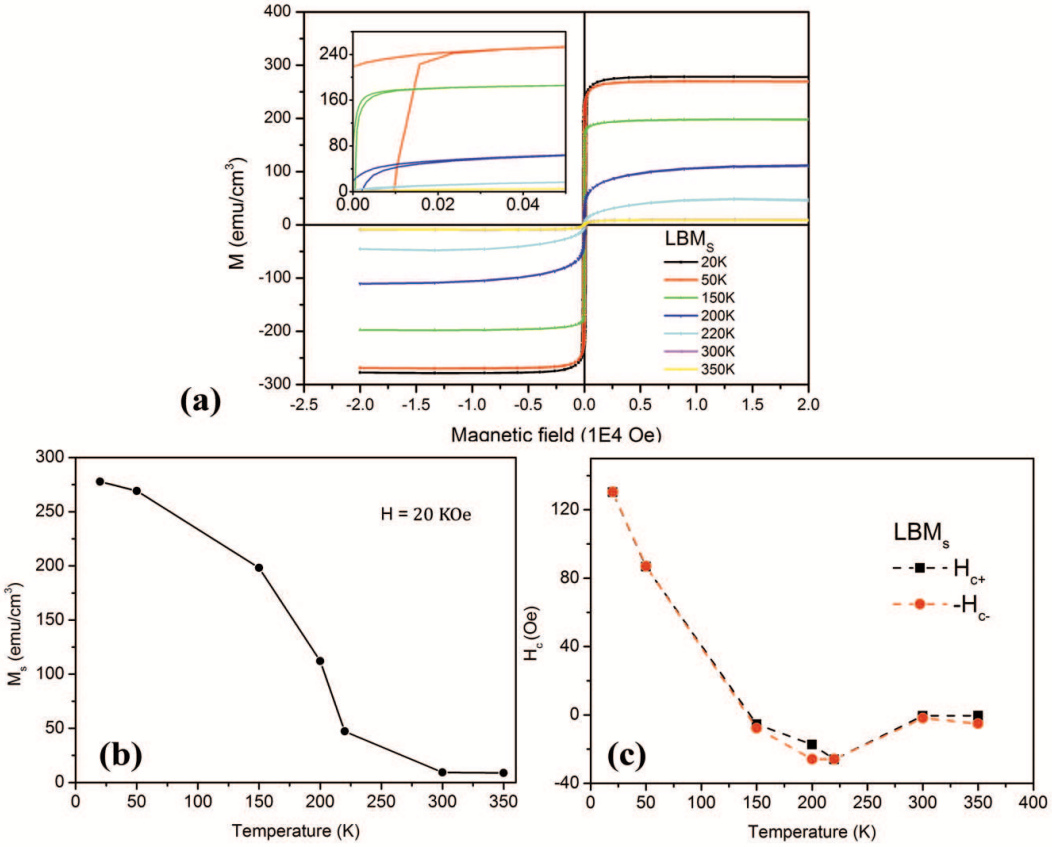

Figure 6.6: Magnetic hysteresis cycles of LBM_s thin film, (b) Temperature dependence of the saturation magnetization and (c) the coercive field behaviour vs. temperature for the LBM_s thin film.

temperature. By looking at ln (ρ(T)), for the LBM_s, the cross-over temperature for this sample is found to be at 216.9 K. The change of the T_C^R between the films grown on Al_2O_3 and Si can be due to difference in lattice mismatch between film and the substrates, where in more crystallized film, LBM_a, the resistivity is lower than LBM_s film, as expected.

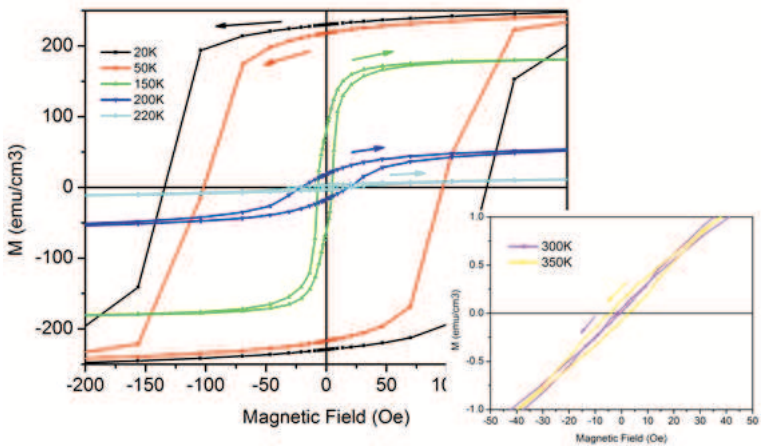

Figure 6.7: M-H curves of LBM_s show the origin of negative coercive field, shown in Figure 6.6.

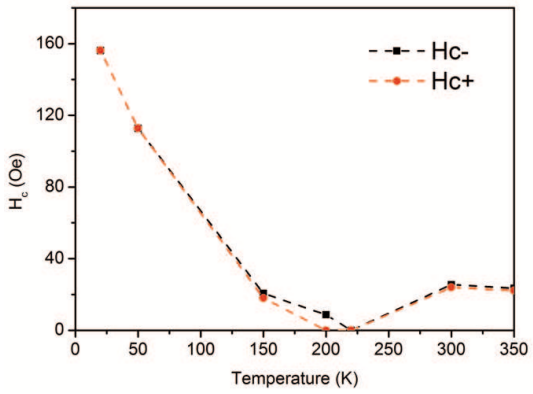

Figure 6.8: Corrected coercivity plot of LBM_s thin film on Si substrate.

The magnetoresistance of the film was measured between 0.0 to 1.0 T, with the setup, described in section 3.4.8. Figure 6.10 shows the magnetoresistance curves obtained in this film on silicon between 150 K and 270 K.

The temperature dependence of the magnetoresistance at a field of 0.2, 0.5 and 1.0 T is shown in Figure 6.10(b), in which the graphs at 0.2 T and 0.5 T are multiplied by a factor of 5 and 2, respectively. Figure 6.10(b) portrays a large drop in temperature range of 210 to 230K, in temperature dependence of magnetoresistance, where we can claim that T_c^R exists in this range. Also, existence of a cross-point in magnetoresistance graphs, at T = 215.3 K, coincides with the cross-over temperature, obtained from temperature dependence of resistivity, Figure 6.9(b). Looking back to single LBM_a layer on Al_2O_3, Figure 5.12(b), the change of curvature is in 180 to 240 K range, where the resistivity of LBM_s increased for 50 Ω.cm from the LBM_a film, from 30 Ω.cm to 80 Ω.cm. A magnetoresistance of -10.7% is observed at 150 K, while in the LBM_a sample, the magnitude of MR is bigger than the film on Si substrate, MR_{LBM_a}=17.3%, which is due to higher crystallinity of the LBM_a thin film and also magnetic domain rearrangements in the thin film, by applying external magnetic field, as it can be seen

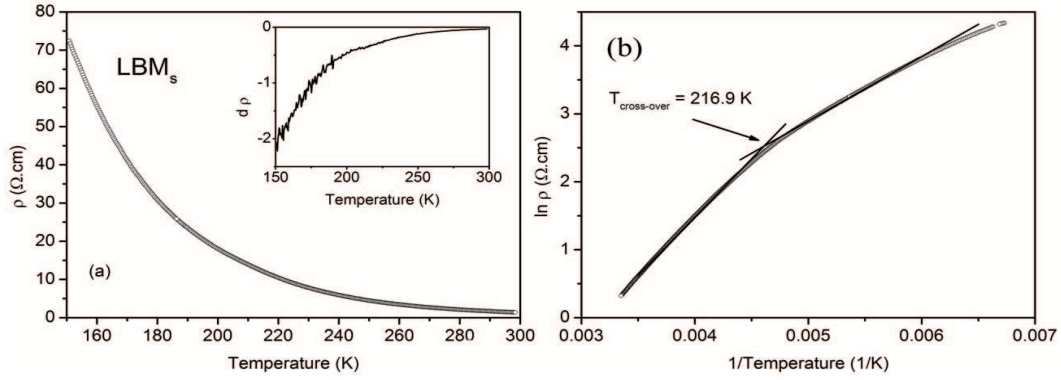

Figure 6.9: (a) Temperature dependence of the resistivity of LBM_s thin film on Si substrate, (b) plot of ln ρ vs. (1/T) and corresponding linear fits for the calculation of the transition temperature.

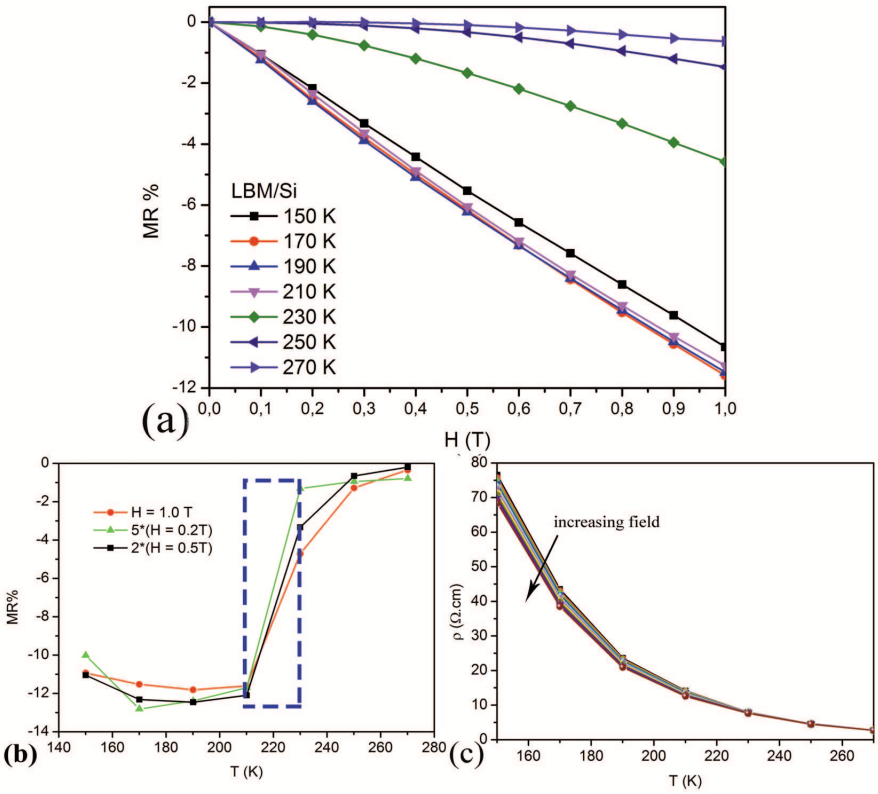

Figure 6.10: (a) Field dependence of magnetoresistance, (b) temperature dependence of the magnetoresistance at 5×(H=0.2T), 2×(H=0.5T) and H=1.0T and (c) resistivity plot of LBM thin film deposited on Si versus temperature.

in Figure 6.10(c), with increasing external magnetic field, the magnetoresistance starts to decrease. As stated before, comparing TEM analysis of LBM_a and LBM_s shows higher degree of crystallinity in LBM_a thin film. Lower crystallinity in thin film, causes an increase in electron traps density, which make mobile electrons face more scattering centres. Therefore, due to the increase in electron scattering, the resistivity is expected to increase in less crystalline thin film, LBM_s [176].

6.1.3 Surface analysis

The AFM images presented in this section, shown in Figure 6.11(a) and (b), were taken at room temperature using contact AFM, operated in the frequency modulation mode [175], to detect the grain size in the LBM_s film and the morphology of the surface. The average size of the grain structure on the surface of the film is in the range of 400 nm to 600 nm, as the profile of a sample grain is presented in Figure 6.11(c).

The main difference in topography of the LBM_s film, measured by AFM, is within their grain size, as shown in Figure 6.11(c) for Si substrate and Figure 5.19(c) for Al_2O_3 substrate. The histogram of the AFM images shows the height distribution of

the topography, as shown in Figure 6.11(d) and Figure 5.19(d). By comparison of the histograms, we can see that the film on Si substrate has wider range of height distribution. Also, the average roughness is 4.91 nm and 1.23 nm, respectively.

Some previous studies revealed the role of surface roughness on the coercivity [178, 179], where the rough surface will lead to formation of more defects [180] and therefore the defects can act as the domain-pinning sites [181]. The domain-pinning sites make extra barrier to the magnetization reversal and increase in the coercivity [99, 182, 183, 184]. Looking at Figure 5.19(d) and Figure 6.11(d), the average roughness of the surface of LBM film on Si is larger than that on Al_2O_3 substrate. As stated before, the LBM_s thin film has lower degree of crystallinity, inter-diffusion and also higher degree of roughness, as proved by XRD, RBS and TEM results. These factors changed the magnetic properties of the thin film, especially in coercivity. By comparing the temperature dependence of coercive field for LBM_a and LBM_s, at T =20 K the LBM_a has higher coercivity, while at T = 50 K the LBM_s shows higher coercive field. This states the role of temperature in the magnetic structure is more important than topography and domain pinning in the samples.

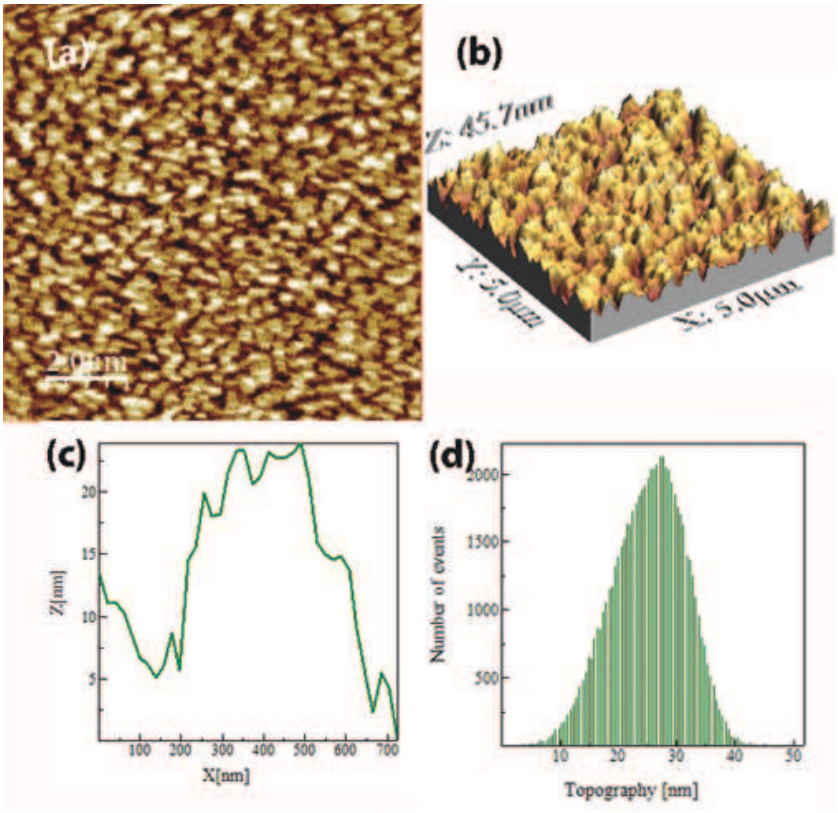

Figure 6.11: Topographic non-contact AFM image of the LBM6/Si surface (a) 2D view, (b) 3D view, (c) profile of one of the grains, the average size of ∼450 nm and (d) histogram of the topography.

6.2 $BaTiO_3$ single layer

6.2.1 X-Ray Diffraction and microstructural analysis

Figure 6.12 shows the X-ray diffraction spectra of BTO thin film deposited on (100)-Si/SiO_2 substrates. The (202) growth direction is obvious on the film on Si substrate. The planar distances, dhkl, for the film on Si substrate is close to the structure of $BaTiO_{2.67}$, hexagonal, P3m1 (156) space group, from ICDD database.

The d_{202}, crystallographic interplanar distance, is extracted from XRD data, 2.04457 Å, which in comparison with the same planes in the bulk form shows -1.36% compressive stress. According to XRD pattern, BTO has grown in crystalline form, with (202) preferred orientation over silicon.

Table 6.3 shows the crystallite size and inter-planar distances of (202) and (404) directions of the BTO film on silicon substrate. Based on the use of $Cu_{k_\alpha 1}$ and $Cu_{k_\alpha 2}$ lines in X-ray diffraction, the values suffer from high error.

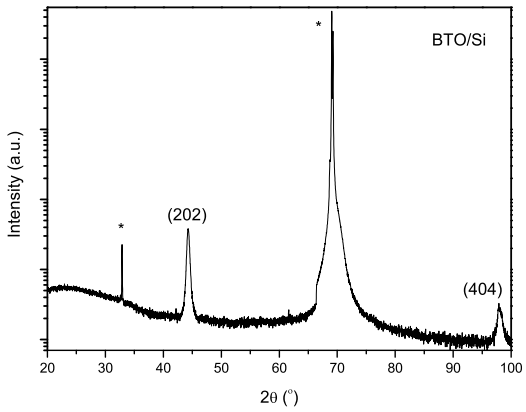

Figure 6.12: X-ray diffraction of the BTO thin film on silicon substrate. The substrate peaks are indicated by asterisk.

TEM analysis of the BTO film shows the $\sim$ 40 nm thickness in the observed area, and the absence of SiO_2 layer. Also it is notable that the crystallinity of the film may vary from one point to another.

Table 6.3: Parameters, crystallite size and inter-planar distance, obtained from the X-ray diffractograms of BTO thin film deposited on silicon.

Sample	Plane	$2\theta_{hkl}(^\circ)$	β_M (°)	β_s (°)	d_{hkl} (Å)	τ (nm)
BTO	(202)	44.29	0.491	0.063	2.04	18.40
BTO	(404)	97.99	1.230	0.063	1.02	10.29

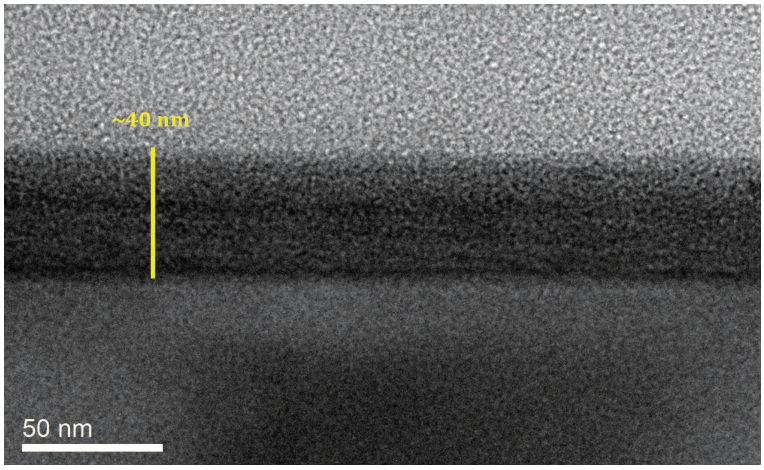

Figure 6.13: BTO film structure on Si substrate. The thickness of the film is shown as 5.7nm.

Table 6.4: The results of fitting on RBS spectrum of LBMBT (LBM (110nm)/BTO (30 nm)/LBM (10nm)/Al_2O_3 substrate.

Layer	t	Thickness (XRR)	Density	La	Mn	O	Ba	Ti
	10^{15} atom/cm^2	nm	10^{22} atom/cm^3					
1 (top LBM)	400.211	40	10.005	14.4134	20.0000	60.0000	5.5866	0.0000
2 (BTO)	391.140	30	13.038	0.0000	0.0000	63.8750	8.3749	27.7501
3 (bottom LBM)	365.801	40	9.145025	14.4134	20.0000	60.0000	5.5866	0.0000

6.3 LBM/$BaTiO_3$/ LBM ($LBMBT_s$) heterostructure

6.3.1 X-ray diffraction characterization and Microstructure analysis

The X-ray pattern of $LBMBT_s$ heterostructure on (100)-oriented single crystal silicon shows the crystalline growth of the LBM layer, mostly in the direction of (101) on the (100) plane of Si substrate. The peaks marked with asterisks, are related with the substrate. In comparison with single LBM layer on Si substrate, the heterostructure shows more crystallinity. The peak of (303) shows the compression of -4.45%, regarding (400) plane of substrate.

RBS was done on the heterostructure and the spectrum and the fit is shown in Figure 6.15, using ZBL stopping powers [166]. Also the fit data is shown in Table 6.4 [165]. The simulation results show lower concentration of Ba in middle layer, approved by comparing the sputtering rate of Ba to Ti.

STEM analysis of the $LBMBT_s$ heterostructure is shown in Figure 6.16, where the bottom LBM layer is showing crystalline structure, Figure 6.16(a). The intermediate BTO layer is grown amorphously, while the top LBM layer is showing some crystallinty in its structure, Figure 6.16(b).

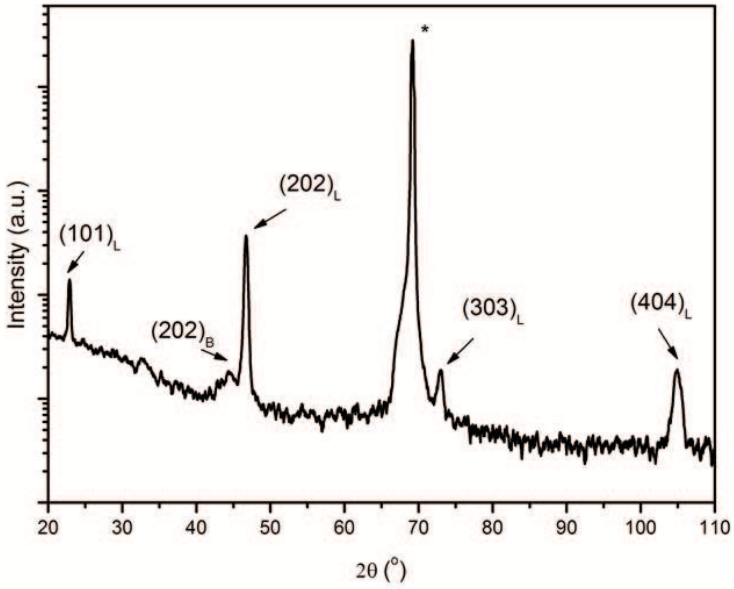

Figure 6.14: X-ray diffraction pattern of LBMBT$_s$ heterostructure on Si substrate. The peaks marked with asterisk, are correspond to substrate.

6.3.2 Magnetometry and magnetoresistance

All the magnetic and magnetoresistivity measurements on LBMBT$_s$ sample were done on (0.38 cm)×(0.275 cm)×(40+40) nm sample, where in magnetoresistivity measurements the thickness of top layer is considered, which is 40 nm. The temperature dependence of the magnetization of LBMBT$_s$ heterostructure on silicon substrate, under

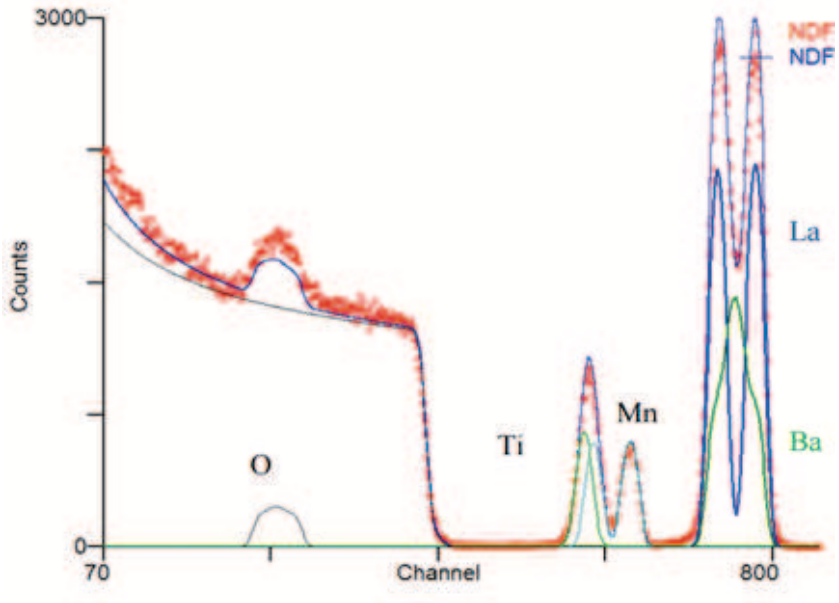

Figure 6.15: RBS analysis and simulation of data of LBMBT$_s$ heterostructure.

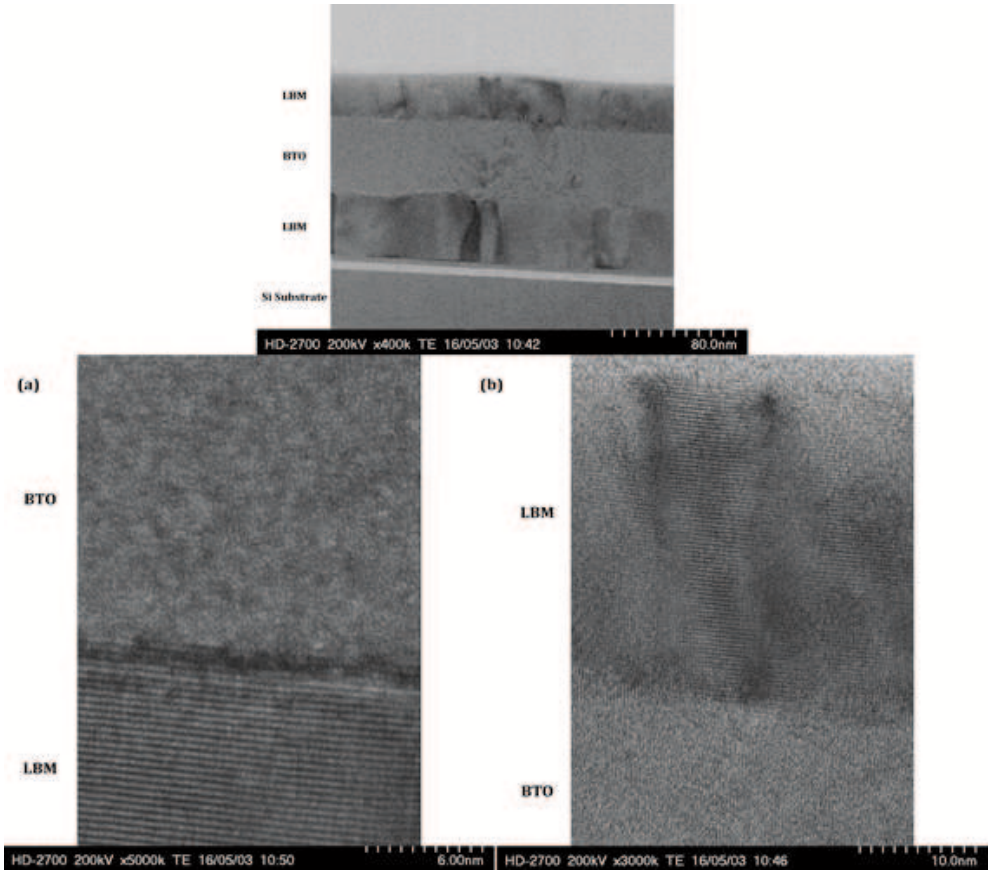

Figure 6.16: TEM micrograph of $LBMBT_s$ heterostructure on Si/SiO_2 substrate shows the crystalline growth of bottom LBM layer and amorphous BTO layer (a) and crystalline top LBM layer (b).

a small magnetic field of H=100 Oe, is plotted in Figure 6.17. The heterostructure shows the T_C^M=213.5 K, which in comparison with the single layer of LBM on an identical substrate, does not show any major difference, meanwhile the saturation magnetization has decreased drastically, around $\sim$ 130 emu/cm^3.

Figure 6.18 shows the Curie-Weiss fitted plot of temperature dependence of inverse magnetization of $LBMBT_s$ heterostructure. Like the $LBMBT_a$ heterostructure, the linear behaviour of paramagnetism is not observed in the temperature range of 280 – 380 K.

Figure 6.19(a) plots the magnetic field dependence of magnetization of $LBMBT_s$ heterostructure. The coercive field behaviour vs. temperature is shown in Figure 6.19(b), where there is a drop at 220 K, near the T_c of the heterostructure. Comparing with $LBMBT_a$ heterostructure on Al_2O_3 substrate, $LBMBT_s$ shows a drastic decrease in saturation magnetization, a drop of $\sim$ 130 emu/cm^3 at applying field of 20 kOe. Therefore $LBMBT_s$ shows weaker ferromagnetic signal than $LBMBT_a$.

The reciprocal temperature dependence of the logarithmic scale of resistivity is shown in Figure 6.21. From the linear fits of high and low temperature regions, the

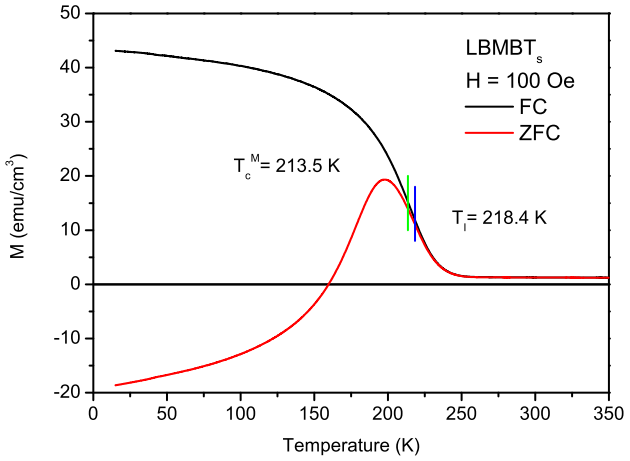

Figure 6.17: Temperature dependence of the magnetization of LBMBT$_s$ heterostructure deposited on Si.

T_C^R = 211.3 K is extracted. Regarding the T_C^R of the single LBM$_s$ layer and LBMBT$_s$ heterostructure on the identical substrate of Si, both show nearly the same value.

The magnetic field and temperature dependence of the magnetoresistance are shown in Figure 6.22(a) and (b). Figure 6.22 shows the change of the behaviour of the MR, from linear to quadratic, in the range of 210 K to 250 K, Figure 6.22(b) and (c). In comparison with LBM$_s$ thin film or LBMBT$_a$ heterostructure, LBMBT$_s$ has the smoothest change in magnetoresistance versus temperature. This is probably due to the least crystallinity of this sample, in comparison with other samples. Also the fittings,

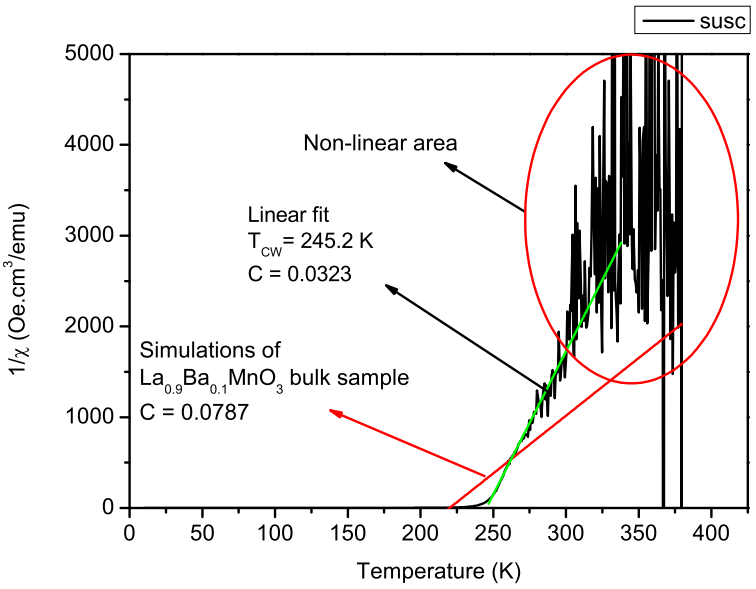

Figure 6.18: Curie-Weiss fitted plot of LBMBT$_s$ heterostructure deposited on Si.

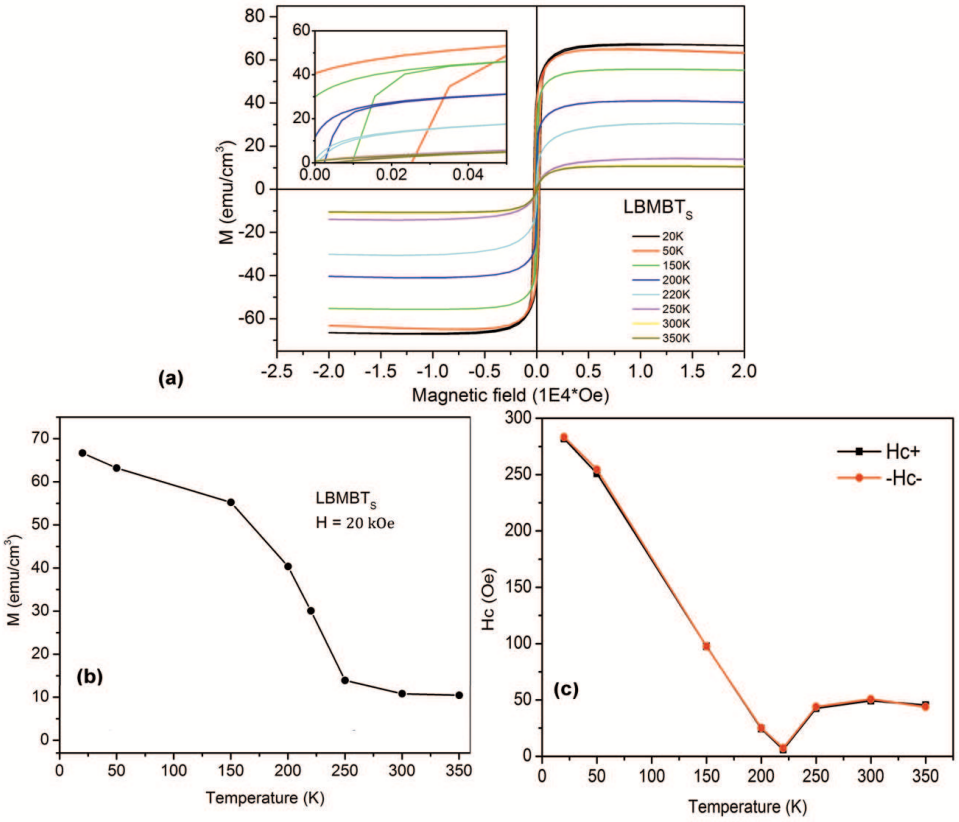

Figure 6.19: (a) Magnetic hysteresis cycles of $LBMBT_s$ heterostructure, (b) temperature dependence of the saturation magnetization at H = 2.0T, and (c) Temperature dependence of the coercive field of $LBMBT_s$ heterostructure on Si substrate.

to find the cross-over temperature, T_C^R, are less defined in comparison with LBM_s single

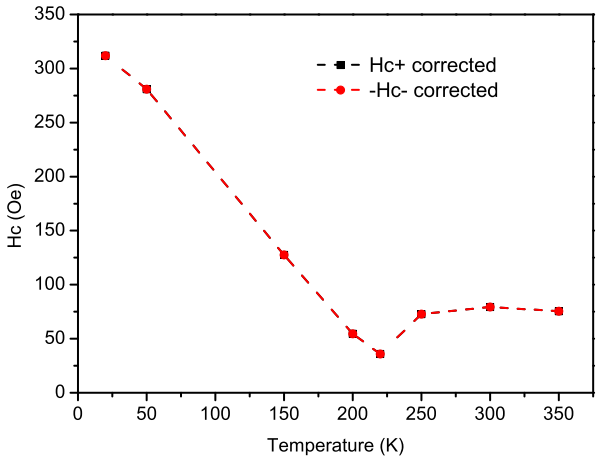

Figure 6.20: (a) Temperature dependence of the resistivity, (inset) first derivative of resistivity versus temperature, and (b) logarithmic scale of resistivity versus inverse of temperature, in $LBMBT_s$ heterostructure on Si substrate.

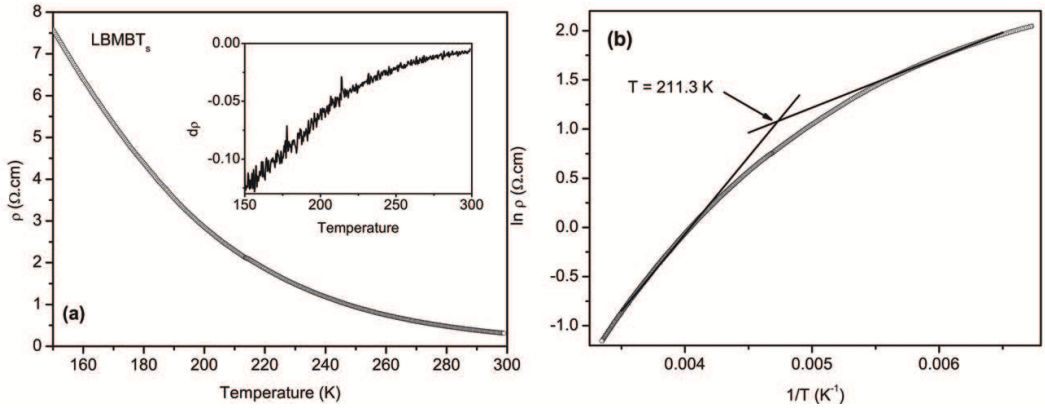

Figure 6.21: (a) Temperature dependence of the resistivity, (inset) first derivative of resistivity versus temperature, and (b) logarithmic scale of resistivity versus inverse of temperature, in LBMBT$_s$ heterostructure on Si substrate.

layer or the structures on Al_2O_3 substrate, as shown in Figure 6.21(b).

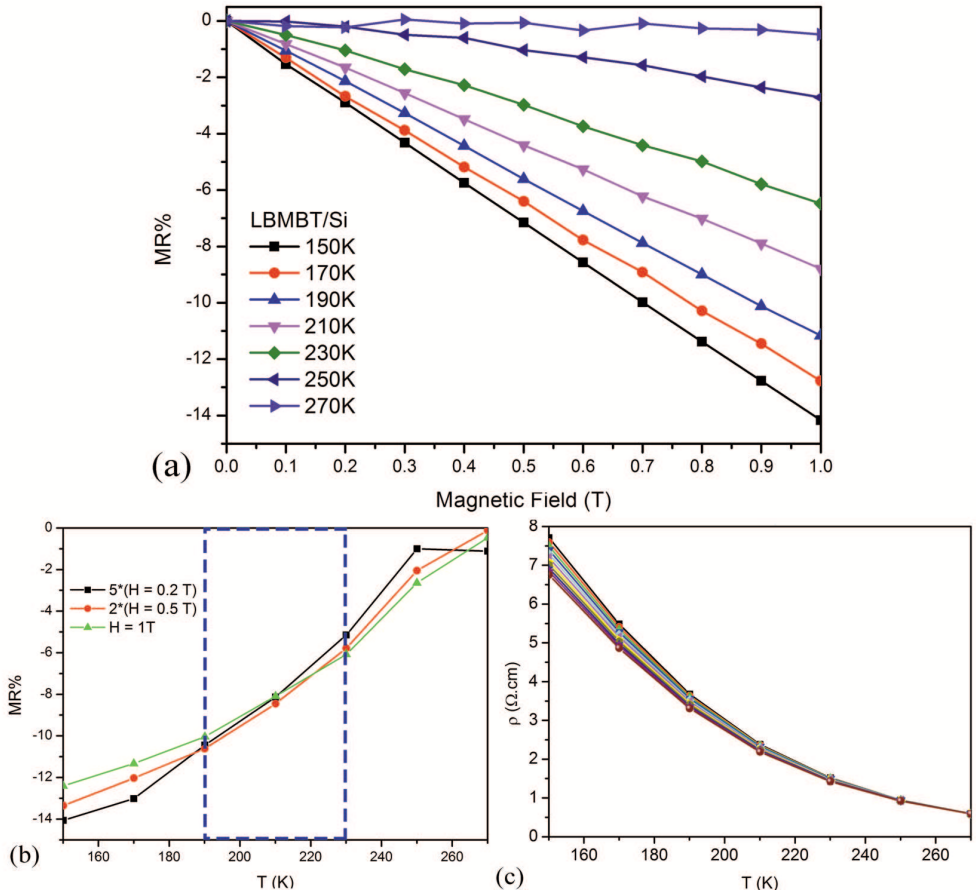

Figure 6.22: (a) Field dependence of magnetoresistance and (b) Temperature dependence of the magnetoresistance at 1.0T of LBMBT$_s$ heterostructure, deposited on Si.

Chapter 7

Surface and piezoresponse analysis

The piezoresponse force microscopy (PFM) is a unique method in probing the coupling between electrical field and mechanical strain, while the most obvious application of this technique is to map domains in ferroelectric materials [185]. Coupling between electric fields and mechanical strain reinforces a broad range of phenomena in ferroelectrics and other polar materials. Morphological changes due to the poling treatment had been previously observed and attributed to the interaction between conductive probe and the trapped charges injected into the film, during poling process in polymers [183] and PZT/LSMO thin film [184].

In this chapter the effect of poling the ferroelectric BTO thin film and LBMBT heterostructure on Si substrate, by PFM is shown, both on piezoresponse and on the surface topography of the film and multiferroic heterostructure. This illustrates a creative way of modifying the surface of the film, by PFM technique.

7.1 $BaTiO_3$

7.1.1 Single crystal (100)-$BaTiO_3$

The topography, PFM amplitude and PFM phase of (100)-single crystal $BaTiO_3$ is shown in Figure 7.1(a), (b) and (c), respectively. The ferroelectric domain structure is obvious at the single crystal structure.

To analyse the effect of poling, the sample was poled by 15, 17, 18 and 20 V. The sample does not show any changes in the piezoresponse amplitude, neither in the piezoresponse phase. This reveals the strength of ferroelectric domains inside the single crystal sample, which cannot be modified by mentioned dc-bias voltage.

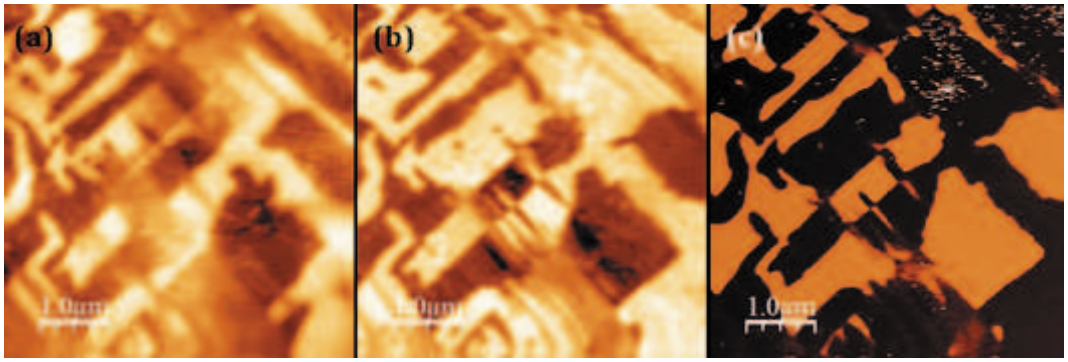

Figure 7.1: (a) Topography, (b) piezoresponse amplitude and (c) piezoresponse phase of $BaTiO_3$ substrate.

7.1.2 $BaTiO_3$ on Si Substrate

The topography of the BTO thin film is shown in Figure 7.2(a), with the root-mean-square (RMS) of 0.18 nm, and the average height of 1.65 nm, derived from the histogram of the AFM raster, Figure 7.2. The corresponding PFM amplitude ($d_{1\omega}$) shows no response of domain structure in the film, confirming that the film is not a spontaneous ferroelectric material in its preliminary state, at room temperature.

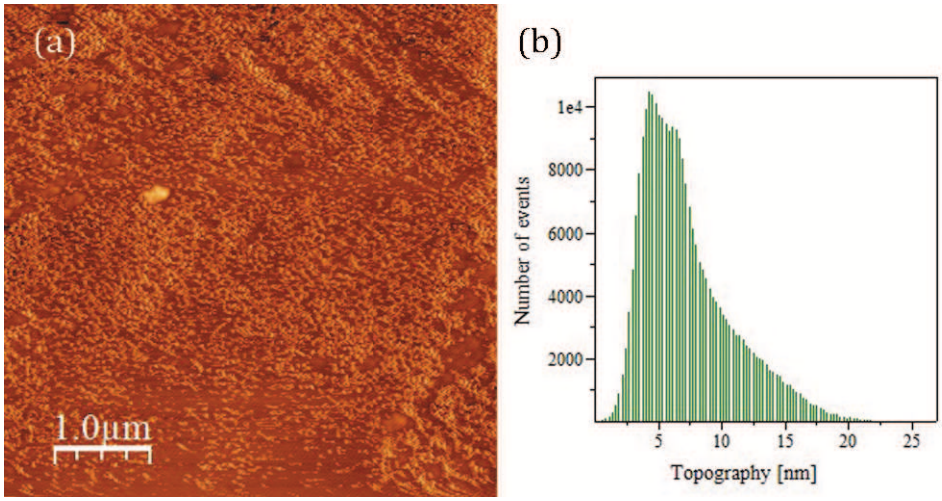

Figure 7.2: Topography of the BTO thin film before poling, with RMS roughness of 0.27 nm, with average height of 2.50 nm.

To analyse the evolution of structure and induced ferroelectricity in the 40 nm BTO thin film, local dc poling was done in two $3\mu m \times 3\mu m$ square areas, which were poled in one direction by the application of a dc-bias while scanning 256 lines at rate of 0.004 line per second at -20V and +30V. Then entire region was imaged with an ac bias to detect the effect of poling. Topography, PFM amplitude and phase (ϕ) images of the sample after local dc poling are shown in Figure 7.3(a), (b) and (c), respectively. The AFM topography image (Figure 7.3(a)) shows highly planar film, with a RMS

roughness of 0.32 nm, which can be due to the modification of the surface after make a contact mode scanning. It is also proven, by TEM micrograph, that the thin film has a smooth surface. The PFM amplitude image (Figure 7.3(b)) shows the dc bias poled area. In the PFM phase image (Figure 7.3(c)), a blue region corresponds to a single domain, polarized toward the substrate (-20V), while the green area corresponds to a region polarized away from the substrate (+30V).

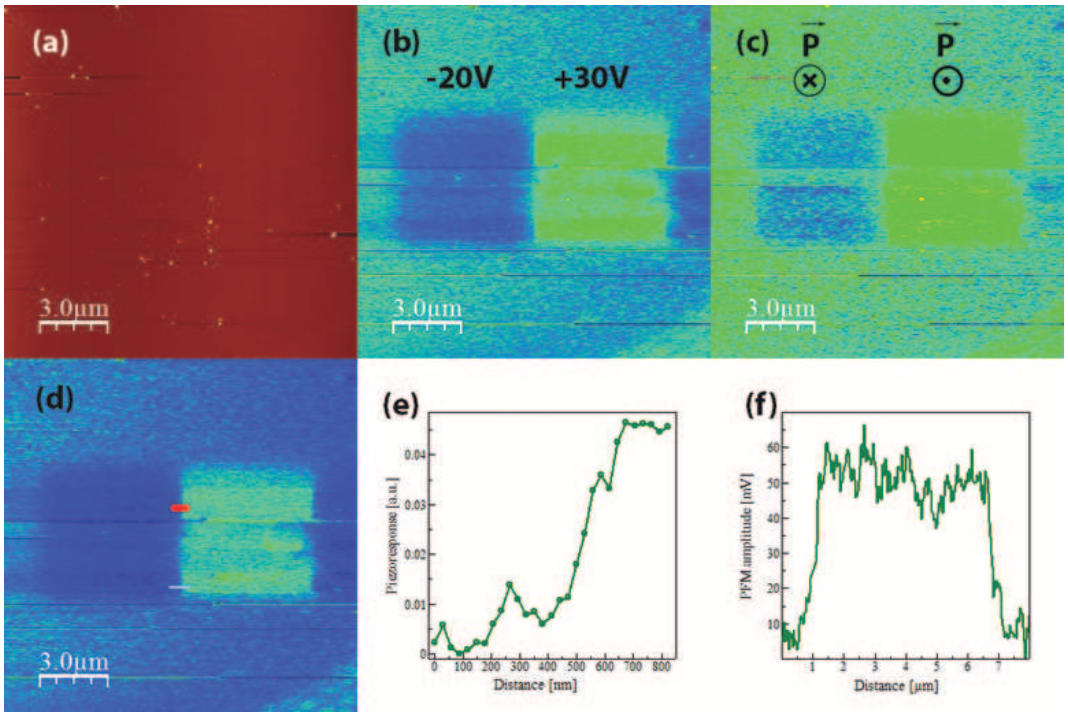

Figure 7.3: PFM data of written patterns with the tip bias of -20V (blue area) and +30V (green area) in $BaTiO_3$ film: (a) topography; (b) PFM amplitude; (c) PFM phase; (d) composite (amplitude×cos(phase)) PFM; (e) line scan of the composite image along the red bar, (f) intensity profile of PFM amplitude of the +30V poled area.

To illustrate imaging resolution, a composite image (Figure 7.3(d)) of the mixed piezoresponse, PR = $d_{1\omega}\times\cos(\phi)$ is created, from the amplitude and phase images (Figure 7.3(b), (c)). The composite image clearly shows domains of opposing polarization as blue up polarized and green down polarized. An intensity profile across one of these grain boundaries is shown in Figure 7.3(e). The width of the transition from positive to negative piezoresponse shows approximately 600 nm. A schematic diagram of the PFM measurement is shown as an inset in Figure 7.3(e). Figure 7.3(f) shows the intensity profile along the +30V poled area, showing the average change of 50 mV.

The strain gradient induced by the tip is illustrated in Figure 7.4, showing the direction of applied strain on the film structure. Previous works have shown the possibility of successful writing and detection of nano-size ferroelectric domains by means of piezoresponse scanning force microscopy (SFM) [186, 187, 188]. Also studies

on $BaTiO_3$ show the coupling between polarization and homogenous in-plane stress, to tune the symmetry and properties of ferroelectric thin film by strain engineering [189, 190, 182]. Stress can be used to influence electrical polarization, where a large local deformation can be done by forcing a sharp tip of AFM against the surface of a film, causing a large stress concentration near the tip-sample contact [182, 191].

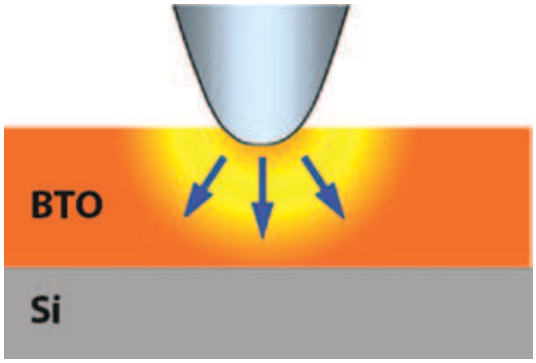

Figure 7.4: Sketch of strain gradient induced by the AFM tip, pushing on the surface of the $BaTiO_3$ thin film.

In polycrystalline piezoelectric thin film, such as PZT, it is shown that the suppression of the piezoelectric response under a sufficiently high loading force happens with almost complete recovery after stress release [191, 118, 117]. Also, the effect of application of an external electrical bias and tip-induced stress, named poling, simultaneously, on the polycrystalline thin films is described in other works [118, 117]. However, the stress from the adjacent grains can make the effect recover upon the release of the tip pressure, therefore no permanent writing was achieved.

Changing the size of the poled area, a $\pm$18 V dc poling was done over 2μm$\times 0.2\mu$m area. As mentioned above, the loading force, caused by the tip on the surface of the film, results in compressive stress. In this experiment, the poling in small area, causes a change in the topography, as well of the PFM amplitude, as shown in Figure 7.5(a). The rise of 5 nm in the topography is visible in the intensity profile across the +18 V poled area. By comparing to the TEM micrograph of BTO thin film, Figure 6.13, the rising of the film is almost equal to the thickness of the film, itself. By comparing to the adjacent region of the poled area, the surface structure remained unchanged, which means that the poled region is modifying its structure to build the new feature. Figure 7.5(b) shows the intensity profile of BTO thin film, before and after +18 V dc-bias-poling. Looking closely at the topography modification of the +18 V poled region, Figure 7.6, the modified area is wider than poled region. Poling was done on a 0.2 μm distance, while the width of the modified region is $\sim$ 0.8 μm. This comparison makes clear the required relaxation region for the poled region. Also asymmetry in the modified region is visible.

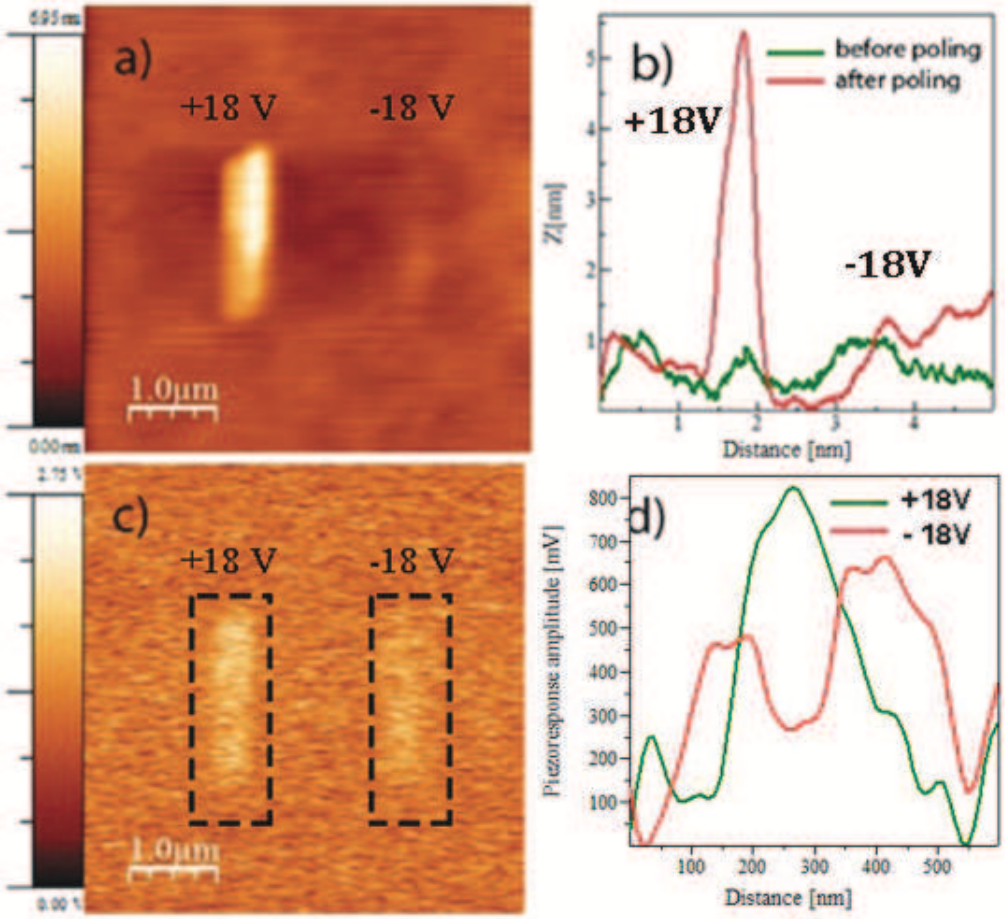

Figure 7.5: (a) Topography of $BaTiO_3$ thin film, after applying local 18V on the surface, (b) Corresponding height of the poled area, the green line shows the topography before poling and the red line shows after poling, (c) the PFM image of the poled area, (d) the height of the PFM image shows on positive and negatively poled area, +18V poled area shows higher polarization.

In comparison with nano indentation experiment on single crystal $BaTiO_3$, where the pressure threshold, to change the topography of sample, is of the order of GPa [192], the thin film shows much smaller threshold, ∼MPa. The Figure 7.5(c) and (d) shows the PFM amplitude of the poled area and the intensity profile across the area, respectively. It is important to remark that 800 mV difference of the piezoresponse amplitude is much stronger than in the case of poling large scale area, shown in Figure 7.3, which is around 55 mV and 25 mV, for +30V and -20V poled area, respectively.

On the other hand, on negatively poled area (-18 V), the modification of topography has not observed noticeably. The change in the PFM is in order of ∼800 mV for positively poled and ∼600 mV for negatively-poled region. The asymmetrical polarization in piezoresponse amplitude is visible, in Figure 7.5(d), where the negatively poled area shows lower piezoresponse.

Two alternative explanations can be noted for the asymmetrical response to positive and negative poled area. First of all, this effect can be attributed to the presence of an

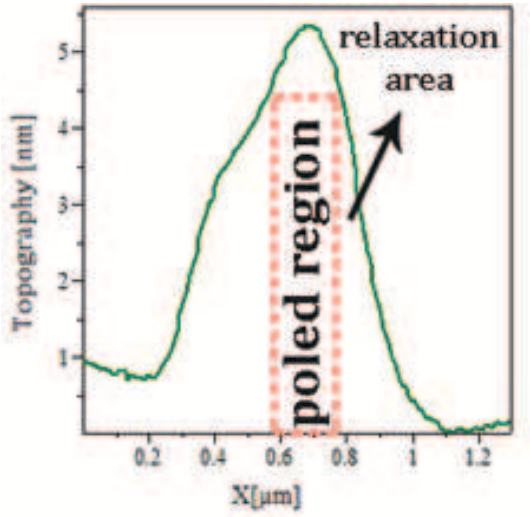

Figure 7.6: A close look at the topography modified of +18 V dc-poled area shows that the modified area is wider than poled region. Also asymmetry in the modified region is visible.

internal built-in electric field, Ebi, in the heterostructure. This field is not polarization dependent and is always pointing in one direction. The applied voltage is not enough to reverse the polarization of the E_{bi}. Figure 7.7 illustrates the formation of a counter domain in the structure, by applying an antiparallel external field, compared to E_{bi}.

The second explanation involves consideration of the mechanical stress exerted on the thin film by the tip. It is obvious that the local stress, caused by the tip, is very large, estimated by dividing the loading force between the tip and the film by the effective tip-sample contact area ($\sim$100 nm^2). The resulting compressive stress is about 10 MPa and it is high enough to produce a domain rearrangement [117]. However, it seems that the applied pressure is still below the threshold for irreversible plastic deformation of the surface.

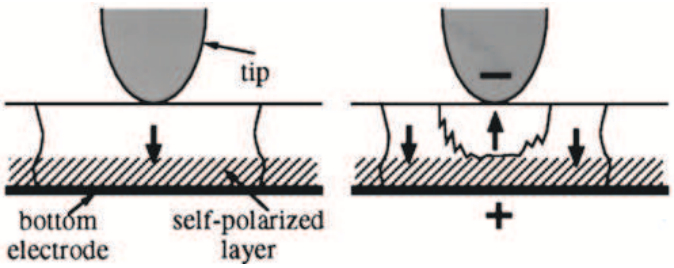

Figure 7.7: A scheme of incomplete switching of a positive domain under a negative applied voltage and formation of a counter domain due to the presence of E_{bi} near the bottom electrode.

To investigate further, increasing the DC voltage of poling to +20V, results in similar range of signal in piezoresponse amplitude, changing to $< sim1$ V, shown in Figure 7.8(b). A line profile across topography of +20 V poled area is shown in Figure 7.8(c). It is obvious that the poled region, for 20 lines, is in the middle of

deformed area, and a relaxed region is formed on both sides, which made the deformed area to be 0.8 μm at bottom and 0.3 μm on top.

Also, a line profile of the composite raster, Figure 7.8(d), along the marked line, on +20 V poling, is shown in Figure 7.8(e). The width of the transition gives the imaging resolution of the scan, which is about 150 nm. Furthermore, the composite raster, shows that both positive and negative poling, create a domain, with up polarization.

We then analysed the stability of the effect, where Figure 7.9 shows the evolution of the +20V modified area, over time. The changes in the PFM amplitude is negligible, that it is safe to say that the modified area can keep the polarization constantly, over the measuring time. However, slight change in the topography is shown in Figure 7.9(a). After 30 minutes, the topography reduced to 83% of its height in the as-poled sample, while after 90 minutes the height seems to stabilize near 80% of its starting value, Figure 7.9(c). The deformed area did not show the tendency to relax to its original state, before poling. In fact the FWHM changes only by ∼12.5% in 90 minutes, Figure 7.9(b).

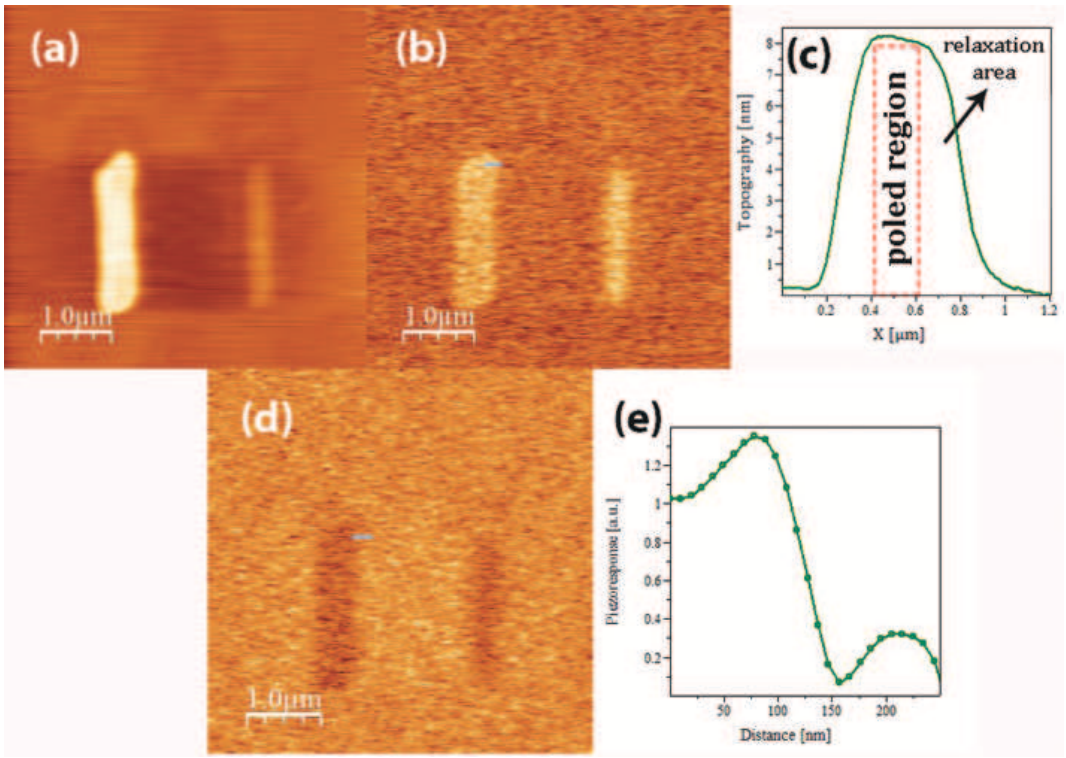

Figure 7.8: (a) Topography and PFM data of written patterns with the tip bias of +20V (left side) and -20V (right side) in $BaTiO_3$ film: (a) topography; (b) piezoresponse amplitude; (c) line scan of the topography, across +20V poled area, (d) Composite (amplitude×cos (phase)) PFM of the poled area by +20V; (e) intensity profile scan of the composite image along the red bar.

It is notable that the applied force on the tip is the same on all the poling process, therefore, it is obvious that the main factor on modifying the topography cannot be the mechanical stress on the thin film, as explained before. Looking back at the

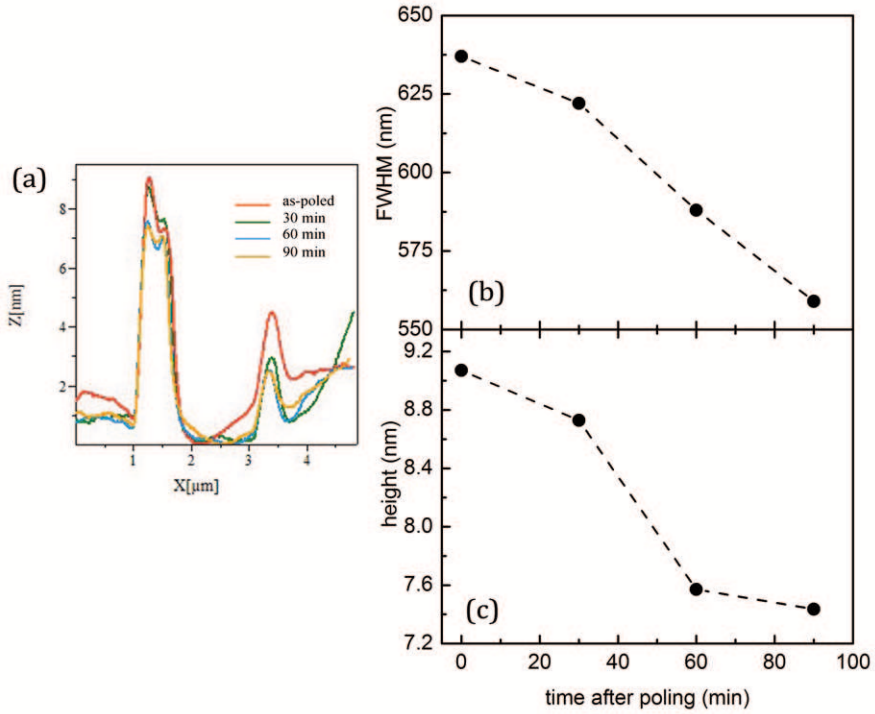

Figure 7.9: (a) The height of the topography, and (b) FWHM and (c) height of the peak, created by the +20V poled area, over time.

modifications, created by poling at 18 V and 20 V, it seems that the key point is the applied voltage during poling. Increasing applied voltage from 18 to 20 V, the height of the modified region, increased from ∼5 nm to ∼9 nm. To make a controlled and detailed study, the experiment was repeated with 10 V field, with the same applied force on tip as previous poling, but no effect of piezoresponse change was observed, Figure 7.10. Also, the topography of the film remained unchanged after poling. Following the trend, Vapp =12 V was also checked for effect of surface modification, which, the same as 10 V, did not show any effect.

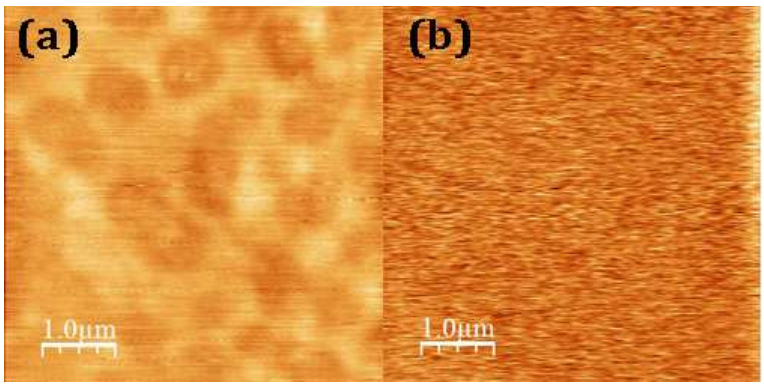

Figure 7.10: (a) Topography and (b) piezoresponse of BTO thin film on Si substrate, after applying 10 Vdc in the area. No changes on topography and piezoresponse amplitude was observed.

In order to find the threshold voltage/electric field to modify the topography, wide area of 200 nm×3μm was poled with voltages between 14 V to 20 V, as shown in Figure 7.11. The response to V_{app} <16 V is not very obvious in the PR images, and also not quite visible in the topography, however, it is enough to verify that the modification is already started in V_{app} = 14 V. Following the trend of increasing applied voltages, above 16 V, there is an obvious change in topography of the area, in a very clear step, shown in Figure 7.11 for different voltages.

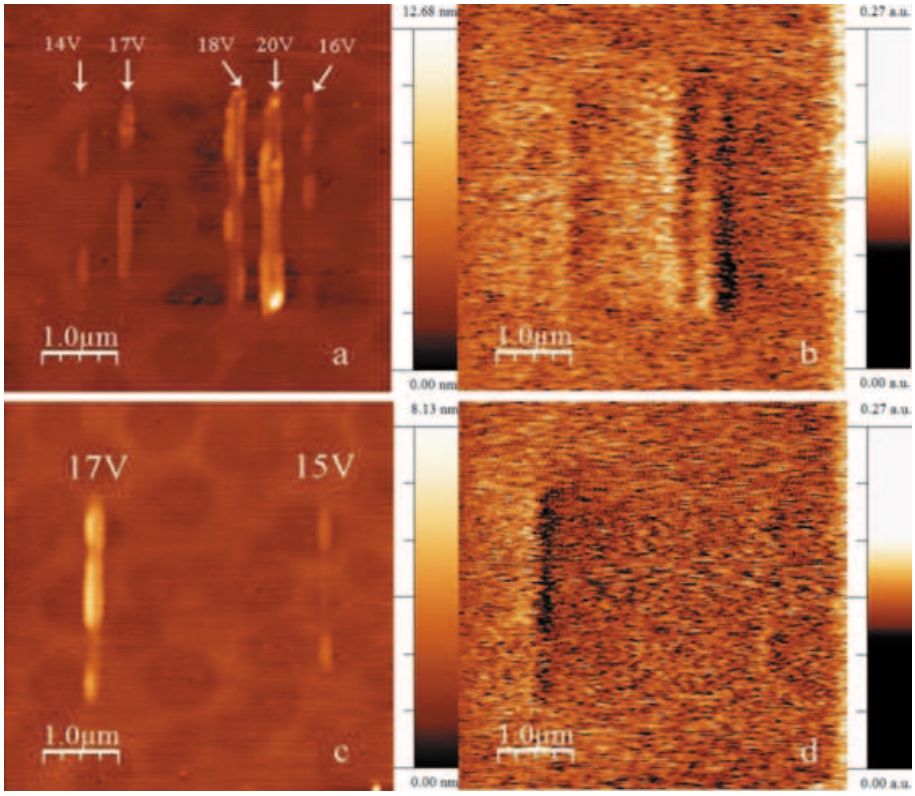

Figure 7.11: 400 nm × 8 μm strips of modified region by applying voltages, between 14V to 20V, on topography. Threshold voltage, seems to be around 15 V. Voltage was applied in a region of a 200 nm×3 μm area.

The changes in the topography, tracked by AFM, is shown in Figure 7.12, where it indicates the linear dependence of the topography change with dc applied voltage during poling, where it extrapolates to zero at V$\sim$ 12 V. For all the experiments, poling was done for 20 lines, 200nm×3μm region, with the rate of 0.25 line/sec in 3 μm length area. The result was a 250 nm to 400 nm×3μm modified area with the height of the poled area depending on the voltage.

Figure 7.12(a) shows the right edge thickness of 20 V-poled region, as an example, which is defined as the distance between the highest and lowest point of peak in the topography raster. It is obvious that by increasing the applied voltage, the height of the poled area increases, as seen in Figure 7.12(b) and plotted in Figure 7.12(c). The

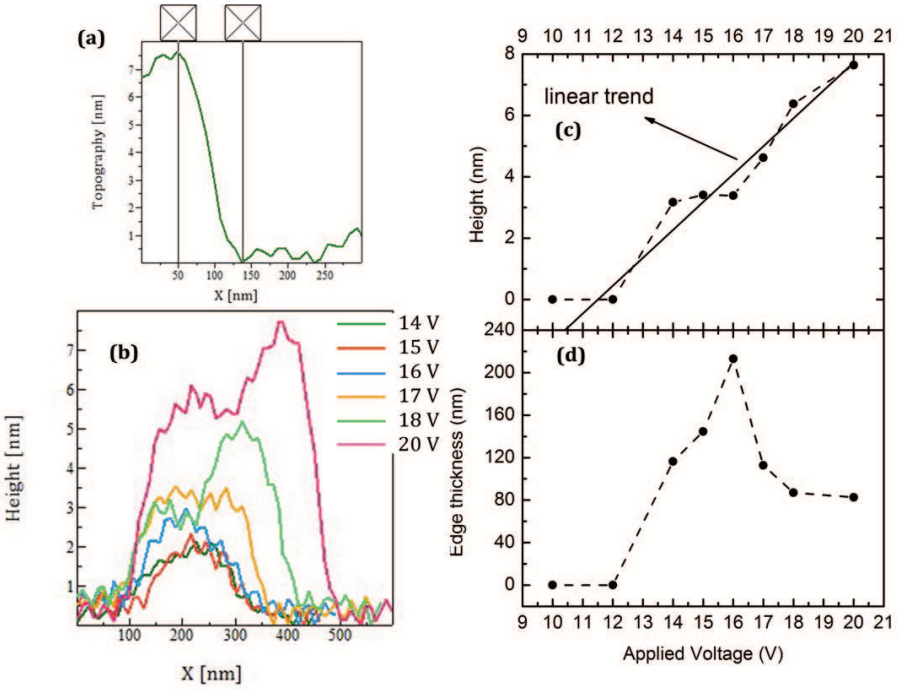

Figure 7.12: (a) Edge thickness of 20 V-poled region, (b) The topography evolution of the 5.6nm $BaTiO_3$ thin film with different applied voltage, (c) dependence of the topography evolution on dc applied voltage, (d) the edge thickness dependence on applied voltage.

values are extracted from software analysis (WSxM 5.0, Nanotec) of topography raster. Furthermore, the definition of the edges is less clear at $V_{app} = 16$ V, where it peaks at 213 nm. The evolution of edge thickness is shown in Figure 7.12(d).

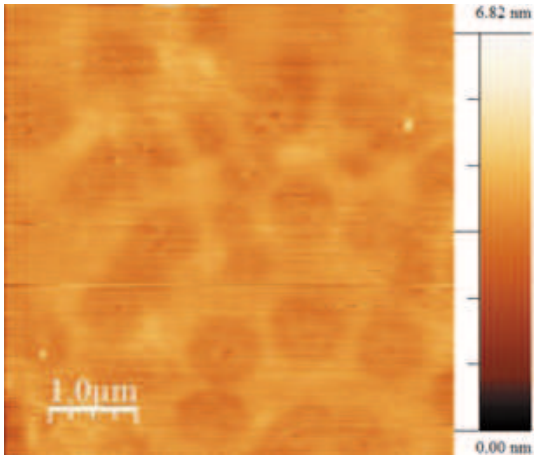

Figure 7.13: AFM raster of the BTO sample, before heating treatment. The circular areas are due to air exposure and were disappeared after heating up, for six hours, at 200 °C.

A close look to Figure 7.11 shows circular areas, obvious at the topography, which are related with the exposing of the BTO surface with air and humidity, Figure 7.12. It is clear from the Figure 7.11, that the circular areas present an enhanced modification of the surface, by means of applied field. However, these areas disappeared after heating

up the sample, for six hours, at 200 °C.

To verify the threshold of the applied voltage to modify the surface, by poling, in local scale (point measurements), the switching spectroscopy measurements, with different applied voltage, from 9 V to 20 V were done to plot the hysteresis loops. Figure 7.14 shows the results, with the measured points (9, 10, 14, 15, 16, 17, 18 and 20 V). One can see that at 9 and 10 V, the loop cannot be formed or in comparison with higher voltages, the intensity of the response is too small. In the range of 14 V $\leq$ V_{app} $\leq$ 20 V the loops are well formed with remarkable response, where above 15 V, the area of the loops decrease again and the loop starts to close back. It is considerable that, although the maximum local stress is very large, at the poled area, it seems still to be below the threshold (∼20 GPa) for irreversible plastic damage of the BTO surface [192], where the local stress cause by the tip is ∼10 MPa in this situation. This proves the enormous role of applied voltage on creating the modification of topography. Poling with higher voltages caused the total damage and plastic deformation of the surface. Figure 7.15 shows the destroyed surface, after poling of 30 V.

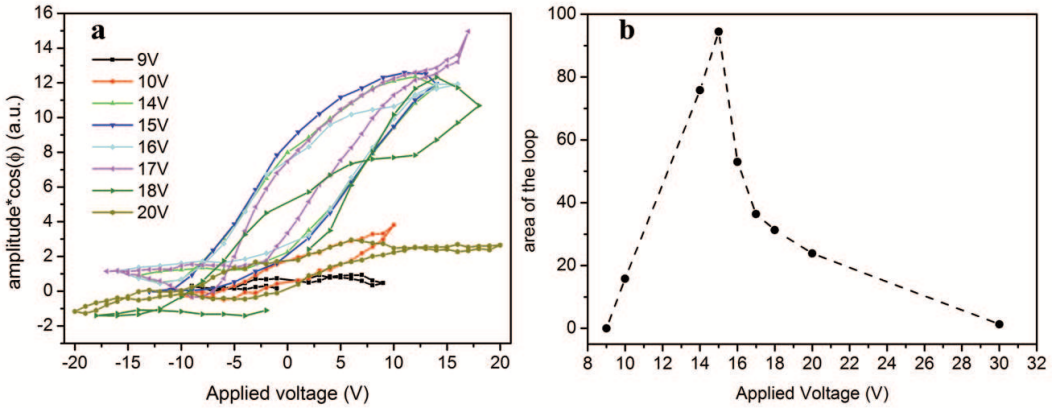

Figure 7.14: (a) The hysteresis loops of the BTO film, under different applied voltages, (b) area of the obtained loops versus applied voltage shows the maximum response at 15V.

In addition, the fact that the loops are located in positive regions of the piezoresponse shows that the applied charges, eq=E=V/d, stay in the poled regions and make a charge accumulated region. This was also proved by measuring the piezoresponse of the poled area, for V_{app} = 20V. During 90 minutes of measurements, the piezoresponse of the poled area did not change, which shows very slow, or negligible dissipation of PR with time, as shown in Figure 7.16.

By comparing the height of the poled area, and also the area of the loop, created by the same applying voltage, Figure 7.17, it is obvious that both curves change their trend at ∼15 V. The highest value in loop area corresponds to the least height, which means the piezoresponse has inverse dependence with the deformation caused by poling, for V$\geqslant$ 15 V.

As discussed before, in several studies, it has been reported that applying external dc voltage in the local area of the ferroelectric material can change its polarization [182, 193, 194, 195]. However, a systematic study on the modification of the topography of ferroelectric film was missing. In this work, we studied the effect of applied force by tip and also applied dc voltage (electric field) on the thin film, which shows modification of the surface. This modification can be the result of delocalizing of atoms, in poled area, near tip. However, the deformed area relaxes to 80% of its as-poled height, after 90 minutes, but it keeps its structure and does not regain its initial structure, in measured time.

Also it is important to note that the number of lines of poling is another factor to deform the surface. All the results, for small area poling were done for 20 lines of poling, where for a tip with 10 nm diameter, it will lead to a region with at least 200 nm (0.2μm) in width. Experiments done with lower number of lines, for V_{app}=20 V, below 10 lines did not show any form of deformation, on the surface. However, we did not check for 10 <lines< 20. This can be related with atoms dislocation and the required energy for regaining their initial positions. The atoms gain an energy of voltage $\times$ current $\times$ time, where by increasing the number of lines, and consequently time, their energy increases. Therefore, they become excited and leave their positions, and lead to a visible deformation of topography. Further studies are needed to follow the behaviour of the atoms, such as high resolution TEM in poled region, to track the change in the structure and/or atomic positions in deformed region. However, such studies would be difficult, due to the damages on the local modified area, during sample preparation.

This behaviour can be understood as either vacancy injection into the thin film. Also it should be noted that the material transfer from the tip can not be the reason for this phenomenon, because no degredation of image quality is observed after repetitive

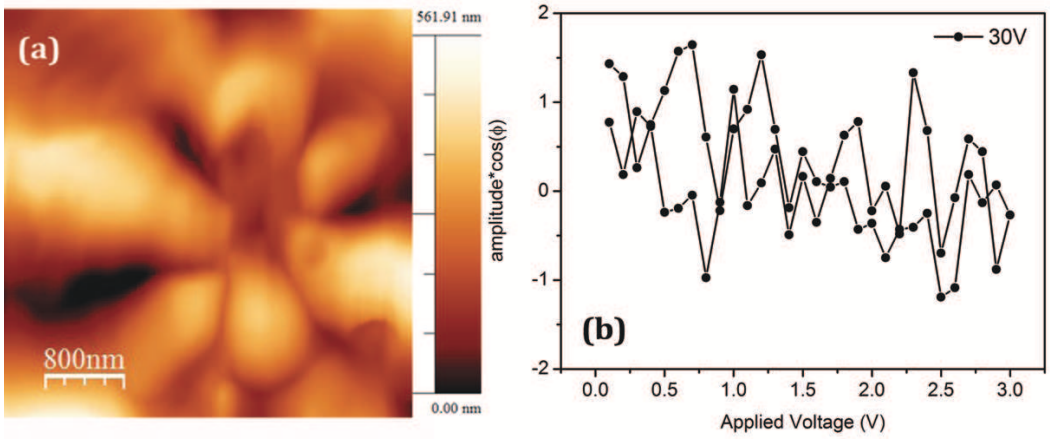

Figure 7.15: (a) Topography of +30V poled area. The surface of the film had changed completely, and (b) hysteresis loop of 30 V on BTO film. The loop does not show any opening.

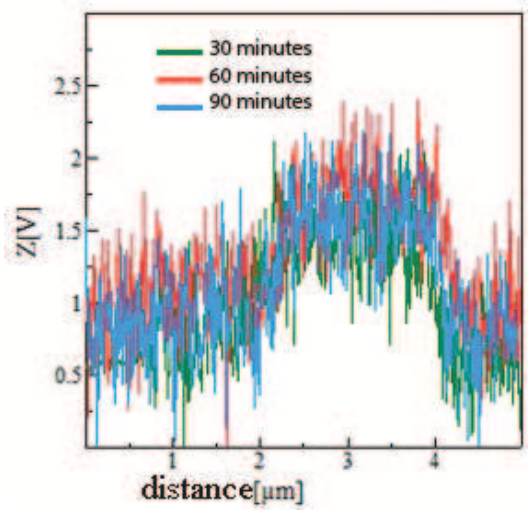

Figure 7.16: The piezoresponse of the 20V poled region shows the stability of the response during the measurement time.

scanning, while the topographical scans shows significant amouns of deposited material within the scanned region.

This method of producing modified surfaces on thin films can open up a way to build an array of nanoscale structures, to be used in ferroelectric memory bits, using electrical bias, in data-storage devices. In comparison with other lithography methods, such as molecular beam epitaxy (MBE), the new method provides a low-cost and more feasible way to achieve the desired surface in industry. Also the time and energy saving of this method can be an advantage in industrial scale.

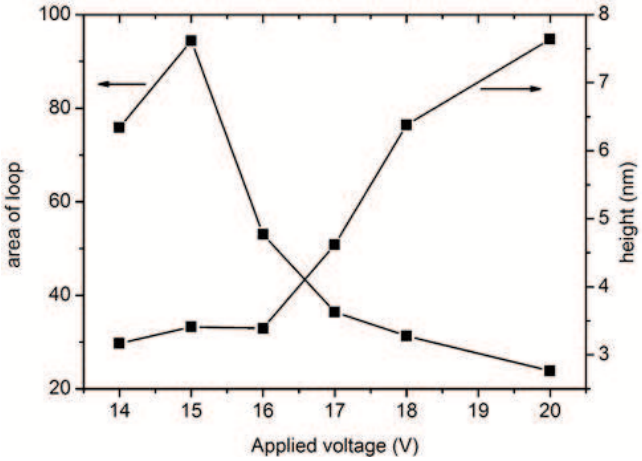

Figure 7.17: The loop area and the height of the poled area with applied voltage.

7.1.3 $BaTiO_3$ thin film on Si/SiO_2 substrate

The poling procedure was also done on the $BaTiO_3$ thin film, deposited on the layer of SiO_2 layer. Figure 7.18 shows the results of the point poled area with 16 V dc voltage, poled for 50 s, 10 s and 100 s.

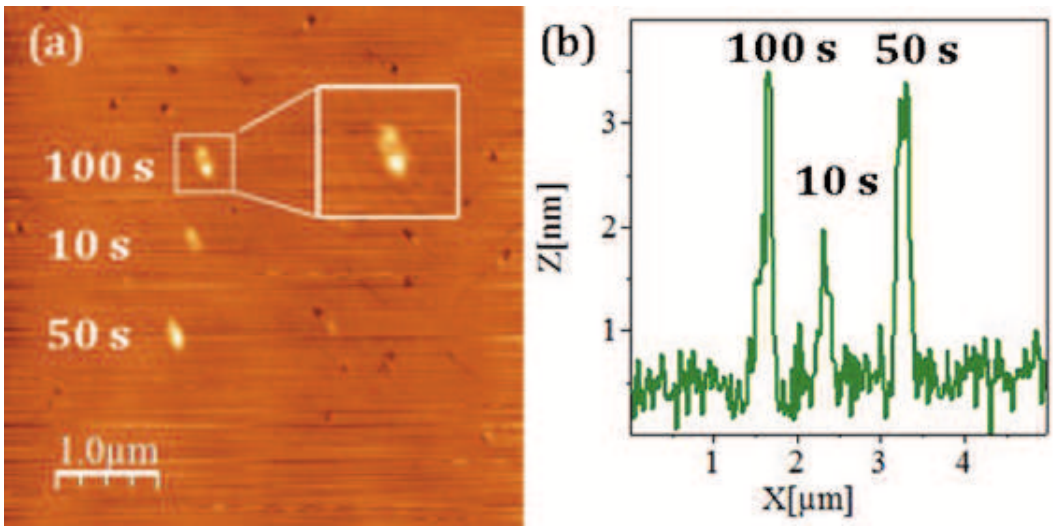

Figure 7.18: Poling of BTO thin film, deposited on Si/SiO2 substrate, by applying a dc-bias voltage of 16 V.

The results shows the change of ∼2 nm after applying the dc voltage for 10 s, while after applying it for 50 s and 100 s, the height of the modified point increases to ∼3.5 nm. It is obvious that the height does not change between 50 s and 100 s, however, small change in the shape of poled area, shown in enlarged view in Figure 7.18. Comparing with the height of 16 V-poled area on the BTO film without SiO_2 layer, Figure 7.12(b), the film without SiO_2 layer shows higher value.

7.2 LBMBT heterostructure on Si substrate

The topography of the $LBMBT_s$ heterostructure on Si substrate is shown in Figure 7.19(a) and (b) in 2D and 3D view, with the roughness RMS of 0.75 nm, and the average height of 4.94 nm, derived from the histogram of the AFM raster, Figure 7.19(c). The corresponding PFM amplitude ($d_{1\omega}$) shows no response of the domain structure visible in the film. Two neighbouring grains are considered to check the grain size of the surface, Figure 7.19(d), showing the grain size is in the order of 250 nm.

We have also explored the switching of polarization of the heterostructure by poling process. Furthermore, we found that the topography of the heterostructure was also modified in a controlled way, even though the applied loading force remained below threshold pressure for topography modifying the sample.

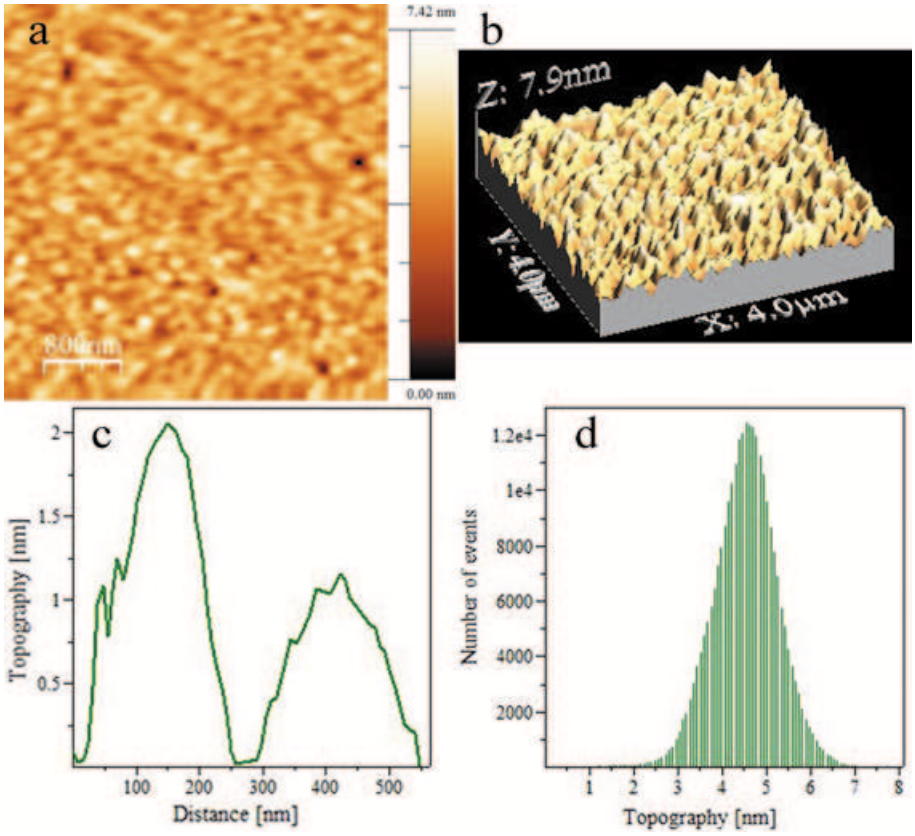

Figure 7.19: Topographic non-contact AFM image of the LBMBT$_s$ surface (a) 2D view, (b) 3D view, (c) profile of two neighbouring grains, the average size of ∼250 nm and (d) histogram of the topography.

To study the effect of local poling on the surface of LBMBT$_s$ heterostructure, two domain patterns of the ± 8V and ± 7V strips were made conventionally with an electrically biased PFM tip. After that, the topography of the sample has not changed, Figure 7.20 (left), while the piezoresponse amplitude has changed clearly for negatively poled regions and less for the positive poled regions, Figure 7.20(right) and Figure 7.21, which is clearly contrary to single layer of BTO on Si substrate.

As mentioned before, the asymmetry in piezoresponse amplitude can be mentioned by existing of an internal built-in electric field, in the heterostructure. However, in single layer of $BaTiO_3$ on Si substrate, change in polarization does not show difference in sign of polarization, where in heterostructure the amplitude of piezoresponse change by the sign, as well. This confirms that the asymmetry in piezoresponse is due to the first hypothesis, which is existing of an internal built-in electric field, in the direction of bottom electrode. In this case the polarization reversal occurs in the upper part of the film and forms a non-through counter domain. Therefore, the formed domain leads to less reversed polarization.

In other scanning region, a point poling of +10V was done on the surface, Figure 7.22.

We find that the poling of +10V changed the surface of the heterostructure, in form of a block with 10 nm height, as it can be seen in Figure 7.22(a) and (c). Figure 7.22(b) shows the topography of the surface over the modified area, and its evaluation over the 90 minutes measurement.

As it can be seen from the comparison of the height in as-poled LBMBT$_s$ heterostructure and BTO thin film, the obtained height in heterostructure is higher than thin film, which changed from 8nm in 20V poling in single layer to ∼10.5nm in heterostructure. This shows some amplification of the poling effect in the heterostructure, although we have a layer of LBM on top of the BTO layer.

The piezoresponse amplitude of the 10V-poled area is shown in Figure 7.23, with modified PR of 385 mV, where comparing with the modified piezoresponse of +7V and +8V the change shows linear behaviour with increasing the applied dc voltage.

Figure 7.24 shows the relaxation of the height and the volume of the poled area over the measurement time, illustrating the decay of the poled area. By fitting an exponential curve on the data, the stable value for the volume is obtained around 30 minutes after poling. By extrapolation of the fit done on the height of the poled area, the complete relaxation of the region is not reaching to its original value, before poling, by passing time. So, it is safe to state that by applying +10 V$_{dc}$, a (Meta) stable deformation on LBMBT$_s$ is achieved.

In mentioned design for LBMBT$_s$ heterostructure the top LBM layer, acts as a top electrode and reinforces the effect of applied voltage. Also, it is worth to keep in mind that the change in the topography of BTO layer in LBMBT$_s$ heterostructure is visible through 40-nm top LBM layer, meaning that the modification of heterostructure can be equal to modification of BTO + modification of top LBM layer, caused by BTO. This idea is shown in Figure 7.25.

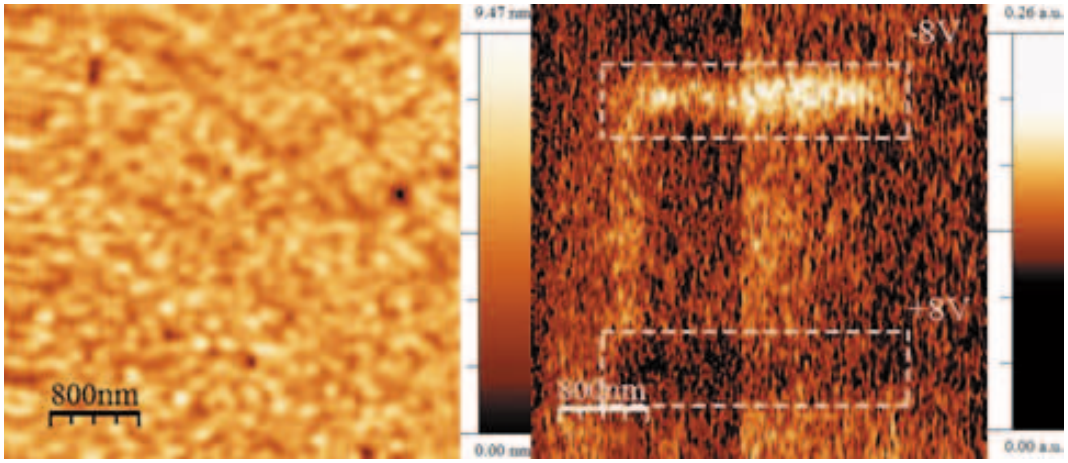

Figure 7.20: (Left) Topographic non-contact AFM image of the LBMBT$_s$/Si surface after poling of +8V and -8V and (right) piezoresponse of the poled area.

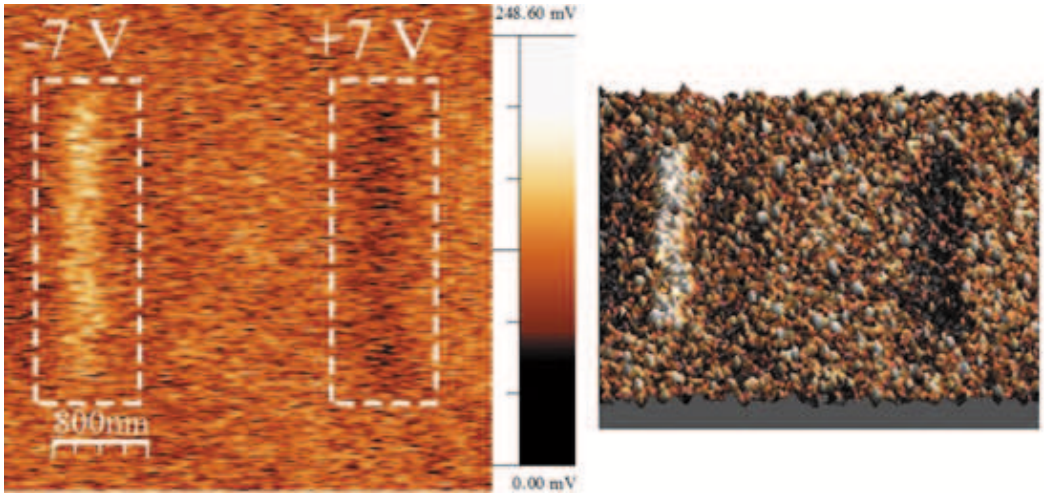

Figure 7.21: Piezoresponse amplitude raster of the LBMBT$_s$/Si surface after poling of +7V and -7V poled area (left) 2D and (right) 3D.

The comparison with the poling results in $BaTiO_3$ thin film, we should consider the difference in thickness of BTO layer, which is almost 6 times more than BTO single layer. Bearing in mind that the LBM layers act as top and bottom electrodes, and:

$$E = \frac{V}{d}. \tag{7.1}$$

we can see that, with assuming the similar electric field is needed to start the modification of the surface, we can see that we need higher applied voltage to reach the desired condition. Meanwhile, the experiment shows that the required voltage is

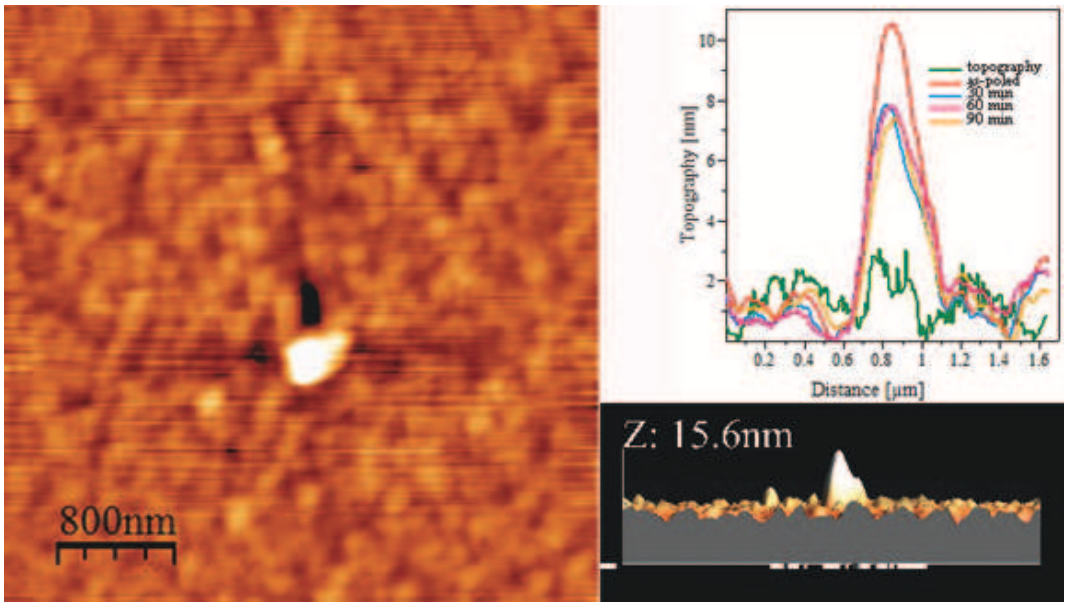

Figure 7.22: (a) Topographic deformation caused by 10V poling on the surface of the LBMBT$_s$ heterostructure, (b) change of the topography over the time, (c) 3D topography of as-poled region.

lower in heterostructure. Referring to the threshold voltage for the BTO single layer, we can say that the required electric field to excite the structure of the film and change the topography is equal to $\sim$ 2.5E9 V/m, while in the heterostructure it is $\sim$ 0.33E9 V/m. Comparing these values, we can see that the required electric field for modifying LBMBT$_s$ is one order of magnitude smaller than BTO single layer. This proves the role of LBM layer as an electrode, to amplify the effect of poling on the topography.

Considering the poling results from single layer of $BaTiO_3$ and LBMBT$_s$ heterostructure, it is obvious that the threshold value for irreversible plastic damage of the structure is higher in single layer. Obviously, this is more dependent on applied voltage than tip-applied force. The effect of the putting BTO layer in a sandwich of LBM layers is increasing the energy and therefore it decreases the threshold of deformed topology.

Rodriguez *et al.* showed that electrochemical reactions may explain the amplified topography change in the heterostructure [193]. By applying the positive voltage on the tip, the charge distribution of the heterostructure changes, consequently. The redistribution of the mobile ions results in changes in volume of the layer and development of local strains. The strains developing under the applied bias voltage result in surface displacement, detectable by PFM tip. Knowing that in the perovskite thin films, the mobile charges are related to the oxygen, with negative charge, which accumulates on the surface, near the tip. This rearranges the charge distribution of LBM layer and consequently on BTO layer. Comparing to the single layer of BTO, in heterostructure, we have more mobile ions, therefore, we may have more deformation in perovskite structure of the LBM and BTO layer.

Although lithography process has already been used with PFM equipement on different materials, few works showed the changes in the topography of the samples. Our approach can be called as the first one in the field, gradually followed the effect

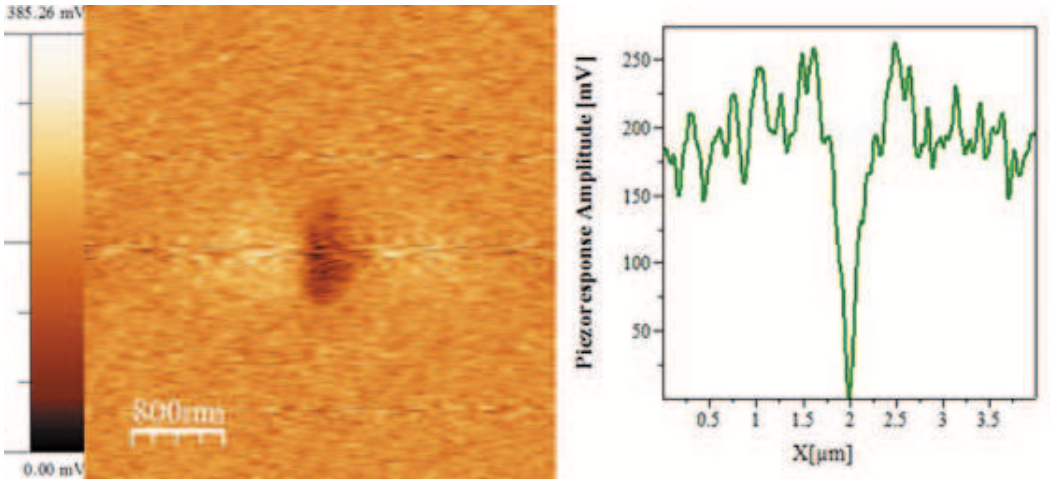

Figure 7.23: Piezoresponse of the 10 V poled area on LBMBT$_s$ heterostructure on Si substrate.

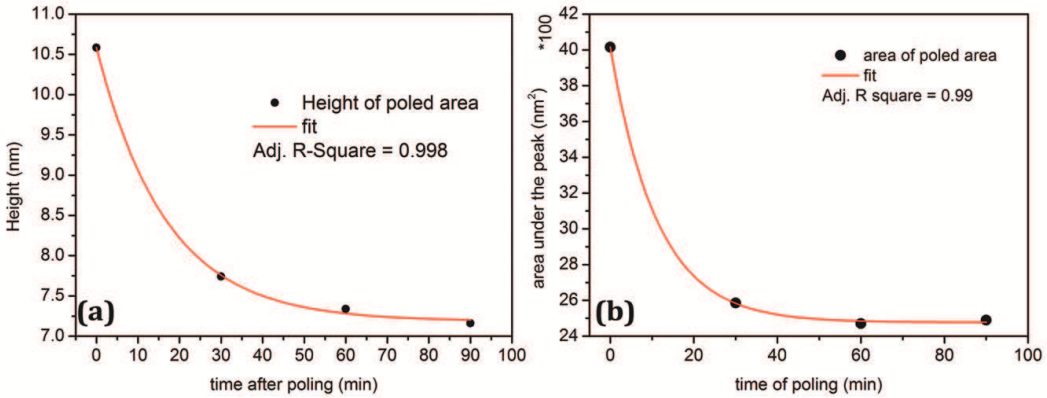

Figure 7.24: (a) Time dependence of height of the poled area, (b) time dependence of the area, under the peak, shown in Figure 7.22(b).

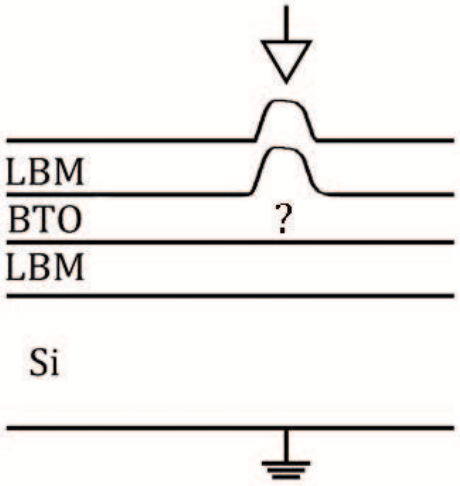

Figure 7.25: The hypothetical arrangement of LBMBT$_s$ heterostructure, after poling of 10V dc voltage, showing the change of topography.

of applied voltage and the time of poling on the modification of the surface of BTO thin film. However, the actual physics of the phenomena is still unclear and under study, due to different variables, which can play important roles in the process, such as thickness of the BTO layer, tip diameter, applied voltages, tip forcing load and etc. Meanwhile, the result of the experiment can be a breakthrough in industry, related with lithography, where it can reduce the expenses, save time and energy, which are very important factors in industry.

Chapter 8

Conclusions and future works

The research done within the PhD work was an experimental approach to study the ferromagnetic manganite thin films of $La_{1-x}Sr_xMnO_3$ (LSMO), with x$\sim$0.33, $La_{1-x}Ba_xMnO_3$ (LBM), where x$\sim$0.1, and ferroelectric thin film of $BaTiO_3$ (BTO), deposited on $SrTiO_3$, Al_2O_3 and Si single crystal substrates, respectively. The combination of ferromagnetic layer and ferroelectric film was also studied within the LBM/BTO/LBM (LBMBT) heterostructures. The study combined the structural, magnetic and electrical measurement for better understanding of the effect of crystallinity of the film on the properties of the final structure, which is originated from the substrate-induced strain. Also, deformation of the topography on the BTO thin film and LBMBT heterostructure on Si substrate, due to applied voltage/electric field in a local region, was observed and studied for the first time.

The LSMO thin films, grown on single crystal $SrTiO_3$ by pulsed laser ablation, demonstrate the existence of an epitaxially oriented layer. Different phases were confirmed, using XRD and EELS-mapping measurements. The growth direction of the phases are labeled as $(002)_R$ of $La_{0.7}Sr_{0.3}MnO_3$ rhombohedral and $(024)_O$ of $La_{0.98}Sr_{0.02}MnO_3$ orthorhombic phase. Measured magnetic and electric transport properties of the as-processed thin films show an abnormal behaviour in temperature dependent magnetization, M(T), below antiferrodistortive $SrTiO_3$ phase transition. The $\sim$100 nm thickness in films is believed to be the critical thickness for the change in magnetic properties from in-excess to in-defect magnetization, in the same temperature range. TEM results show a transition from epitaxial film, to inclinated columnar film, and then to branched structure, by increasing the thickness of film, from 13.5 nm to 320 nm film. HRTEM results depict an epitaxial film with small deformation in the interface of the film and substrate. In thicker films, 45 nm and 200 nm, the inclinated columnar structure is obvious, by basal plane, rotated for $\sim 67^\circ$ in respect to the interface. The EFTEM analysis on 45 nm film show a slight change in the composition of the La and

Mn ions, near boundaries. In 200 nm film, the width of columns is ∼20 nm. An epitaxial interface is obvious, while after ∼40 nm from the interface, small inclination, by ∼4° in 10 nm scale, is observed in the film. This is the basis of the columnar structure of the film. In thicker film, over 300 nm, the columnar structure tend to change to branched one. After ∼80 nm from the interface, a Mn-deficient layer is visible which bases the branched structure. This branched structure is associated to the change in the elemental composition, proved by STEM-EELS mapping. The in-defect magnetization observed for the films above 100 nm is due to the formation of the magnetic domain reconstructions, in the branched form, because of the film relaxation.

The LBM thin film and LBMBT heterostructure on Al_2O_3 substrate, prepared by RF magnetron sputtering, were highly oriented. The ratio of the La/Ba was increased during deposition, comparing to the provided target, caused by the lower mobility of Ba ions, during deposition. This was also proved by RBS analysis, and confirmed by comparison of Curie temperature of the film with phase diagram. The produced film and heterostructure presented a ferromagnetic-paramagnetic transition and their Curie temperatures, at 203 K and 194 K, respectively, while they show lower saturation magnetization than calculation for a $La_{0.9}Ba_{0.1}MnO_3$ sample. This difference provess the existence of extra phases of Mn ions in the thin film, as also detected in high magnetic field FC measurement. In comparison with LBM_s thin film, grown on Si, the LBMa presents higher T_C^M, beside the lower average roughness and RMS value.

The LBM_s and BTO thin films and $LBMBT_s$ heterostructure on Si substrate show low crystallinity, with lower Ba content, the same as structures on Al_2O_3 substrate. A comparison of the T_C^M and T_C^R of the films and heterostructures show a slight difference in the values, which is due to the different structure of the single layer and top LBM layer.

In the magnetoresistance measurements, the transition temperatures were in the same range for single layers and heterostructures, all ranged in vicinity of 214.7 K. The T_C^M of the heterostructures were increased, regarding the single layers on an identical substrate, while T_C^R shows slightly different behaviour. It seems that the lower crystallinity in the top LBM layer, deposited on BTO layer, is the key component to the magnetoresistance behaviour. The degree of crystallinity is confirmed by TEM micrographs.

In the $BaTiO_3$ thin film, deposited on Si substrate, the thin film showed low degree of crystallinity, where the surface analysis showed a very smooth surface. For the first time, a study of topography deformation by dc-bias poling was made, showing the ability of modifying the local structure and consequently the surface of the film, by controlling the applied voltage in PFM measurements. The film showed the capability

of a controlled modification of the surface, with applying voltage by contact AFM tip in PFM mode, in the range of 14 V $< V_{app} <$ 20V, where single crystal $BaTiO_3$ substrate is showing no topographical response to the applied voltage. The ferroelectric hysteresis cycles showed the thin film was already in the initial polarized state, where in measured applied voltages, it already started at positive region. The combination of applying external electric field and the strain, caused by the tip, produce the surface of the film to have a plastic deformation. The evolution of the relaxation of the poled region, showed slightly slow procedure, where it reached its 80% of its as-poled height in 30 minutes and stabilized afterward. This makes the technique an in-expensive method for the lithography purposes, in nano scale.

The asymmetrical response in the PFM to the positive and negatively poled area was explained by the existence of an internal built-in electric field, which is not polarization dependant, and it is always in one direction.

The $LBMBT_s$ heterostructure on Si showed the identical behaviour of plastic deformation of the surface, by applying external electric field, in comparison with single layer BTO on Si, in PFM. Comparing with BTO single layer, in $LBMBT_s$ heterostructure, the top LBM layer acts as top electrode, and enhances the poling procedure and, which makes the deformation possible with lower applied voltage, ∼10 V. The required external field for modifying the BTO single layer is ∼2.5E9 V/m while in $LBMBT_s$ the value decreases to ∼0.33E9 V/m. Decreasing the required field to make the same effect on the topography leads to importance of other factors, such as the design of the studied system, where the top electrode in the BTO single layer is the tip with 10 nm radius and in $LBMBT_s$ heterostructure, the top electrode is a plate, parallel to bottom electrode. The difference in the physics of these two arrangements can play a role in physics of the phenomena.

8.1 Future work

The role of oxygen vacancy in the structure of oxide thin films could not be appropriately clarified, within the limits of this research. For more accurate oxygen content, using post-annealing is suggested. Meanwhile optimization of the sputtering conditions to increase Ba content, in $La_{1-x}Ba_xMnO_3$ film is advised. In order to achieve a better understanding of the effect of substrate-induced strain in the LBM thin film on Al_2O_3 and Si single crystal substrates, the deposition and characterization of films with thickness value higher than 100 nm (Al_2O_3 substrate) and lower than 100 nm (Si substrate) is suggested. Also, the different thicknesses of LBM and BTO layers, on the heterostructures should be deposited and characterized for the TMR applications. In

BTO films, the growth of thicker films on Si and investigating of the poling effect on thin films is desirable, to check the effect of thickness on the threshold of topography modification phenomena. Improvement on the data collection for EFTEM mapping is undergoing to get both larger statistics and the highest possible magnification of the JEOL microscope. Using the HAADF detector in new Hitachi HD2700B STEM microscope with high field EDS we also expect that interface study in films may create images of even better quality and thus help us to explain the properties of the films. This same microscopy analysis would be useful in backing more advanced microscopy using aberration corrected microscopes in collaborative Institutions to extract information of the local chemical environment on interfaces.

Number of complementary methods, such as X-ray measurements of rocking curve and reciprocal space on the rest of the samples, should be done to have a more detailed insight on the in-plane texture and the evolution of stress with the increasing of thickness of the films. The elemental composition of the thin films may be studied by using Rutherford Backscattering Spectroscopy (RBS) and channelling RBS. However, oxygen deficiency is not detectable by RBS. Also, vibrational spectroscopy, like Raman spectroscopy can be used to reveal the nature of phase transitions in the manganite thin films. Raman spectroscopy, by using different wavelengths can be useful to determine the stress of each layer, in the heterostructure.

In magnetoresistance measurements, high magnetic field and low temperature, down to 4 K, are necessary to complete studies and find out the transition temperature from insulator to metallic phase.

On the BTO thin films, the studies can be continued using smaller radius tips, with different loading forces on the film. Also electron backscatter diffraction (EBSD) can be used to check the change of the structure inside the poled area. Long-time measurements may be useful to track the changes on the topography after several days. It is also an objective of future studies to eliminate the produced domains, by loading pressure, in AFM method.

It is within our goals to perform further studies with HRTEM on modified structure of BTO thin film, to find out changes in structure. Combining experimental data with First-principle modelling of the interfaces, we would be able to figure out the physical phenomenon, beneath deformed area. Extending this study toward thicker films, can give a better perspective over the threshold conditions to grow nanostructures. Further research on other common piezoelectric thin film, such as PZT, would give extra perspective on the materials, which can provide the condition. Our methodology on studying concerned multiferroic properties in current PhD thesis would be of use in similar studies.

Appendix A

Appendices

A.1 Low-angle X-ray reflectivity in thin films

X-ray reflectivity is a very useful technique in thin films and layered samples for determining layer thickness, vertical spacing between layers, surface and interface roughness, and estimating electronic density of these samples [196, 197, 198].

In the X-ray region, the refraction index of a material may be generally written as [196, 197]:

$$n = 1 - \delta - i\beta \tag{A.1}$$

where:

$$\delta = \frac{\lambda^2 r_e \rho_e}{2\pi} \tag{A.2}$$

and β is due to absorption, λ is the X-ray wavelength ($\lambda_{CuK\alpha}$=0.154056 nm), r_e is the classical electron radius and ρ_e is the electronic density of the material.

When light travels from a medium with a refraction index ni to a medium with ntr, impinging the surface at an angle θ_i with the surface, the angle θ_{tr} of the transmitted wave is given by Snell law [197, 199]:

$$n_i \cos\theta_i = n_{tr} \cos\theta_{tr} \tag{A.3}$$

If $n_{tr} < n_i$, there is a critical angle for total reflection, θ_c. This implies for incidence angle $\theta_i < \theta_c$, all radiation is reflected. The critical angle is obtained, by using n_i=1 and $\cos\theta_i$=1 [197, 198, 199]:

$$1 - \delta = \cos\theta_c = 1 - \frac{\theta_c^2}{2} \tag{A.4}$$

$$\theta_c \approx \sqrt{2\delta} \tag{A.5}$$

Since the refraction index of the matter is below the index of air, the impinging X-ray beams with sufficiently low incident angle cannot penetrate the film and is totally reflected. The results is a plateau for low angle X-ray reflectivity spectrum, for δ_i <0.5° [197].

The reflectivity coefficient, which allows determining the X-ray of a thin film sample, may be calculated using suitable boundary conditions for the reflections and refractions at the interface, as well as the translation within each layer of the sample [197].

A.1.1 Film thickness

For the incident angles higher than critical angle, the X-ray penetrates inside the film. Therefore reflections occurs at the top and the bottom surface of the film. The interference between the reflected rays results in interference fringes, which are angle dependent. The mth interference for a path difference Δ=mλ maximizes at:

$$\theta_m^2 \approx m^2\frac{\lambda^2}{4d^2} + 2\delta = m^2\frac{\lambda^2}{4d^2} + \theta_c^2 \tag{A.6}$$

If the substrate is optically denser than the film, a phase difference of π occurs at the reflection film/substrate interface and m is substituted with m+$\frac{1}{2}$. The thickness of the film can be determined by:

$$d \approx \frac{\lambda}{2}\frac{1}{\sqrt{\theta_{m+1}^2 - \theta_c^2} - \sqrt{\theta_m^2 - \theta_c^2}} = \frac{\lambda^2}{2}\frac{1}{\theta_{m+1} - \theta_m} \tag{A.7}$$

A.1.2 Surface Roughness

Another important quantity that can be determined from XRR measurements is the surface and interface-roughness. Roughness gives rise to diffuse scattering, resulting to a less intensity in the reflected beam. In one of the general scattering formalism, the roughness is calculated by assuming non-homogenous thickness. It assumes a Gaussian

distribution for thickness, with a mean d and a standard deviation of σ. With this assumption, the Fresnel coefficients of reflection can be corrected by $\rho_{\nu h}$, as:

$$\rho_{\nu h}.exp(-\frac{d}{2\sigma^2}) \tag{A.8}$$

The influence of roughness in Tungsten oxide film on glass is shown in Figure A.1.

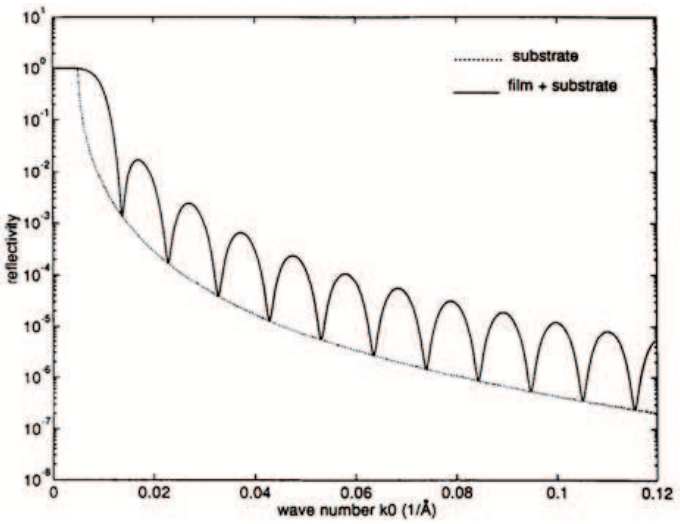

Figure A.1: The reflectivity calculated for the geometry. The dotted line is the Fresnel reflectivity of a bare substrate. The difference between the solid line and the dotted line is the contribution due to the film XRR measurements and simulation of a Tungsten oxide film on glass [200].

A.2 Grown samples

The LBM and BTO thin films, and LBMBT heterostructures were sputtered with a RF magnetron sputtering system, on well-cleaned substrates of Al_2O_3 (0001), $SrTiO_3$ (100), Si (100), $LaAlO_3$ (100), PMN-PT, glass and MgO (100).

Table A.1, Table A.2 and Table A.3 summarize the used substrates and the sputtering conditions for whole series of produced LBM, BTO thin films and LBMBT heterostructures. The used samples are highlighted in the tables.

Table A.1: Substrate characteristics and sputtering deposition parameters for LBM produced samples.

Sample	Substrate	Base pressure	Deposition					
			Temperature	dc bias	Distance	P_{Ar}	P_{O_2}	Time
		mbar	±5°C	V	mm	mbar	mbar	min
LBM 4a	Al_2O_3 (0001)	4.8E-08	696	127	115	5.0E-03	5.0E-04	120
LBM 4b	$SrTiO_3$ (110)	4.8E-08	696	127	115	5.0E-03	5.0E-04	120
LBM 4c	MgO (100)	4.8E-08	696	127	115	5.0E-03	5.0E-04	120
LBM 4d	$SrTiO_3$ (100)	4.8E-08	696	127	115	5.0E-03	5.0E-04	120
LBM 5a	Al_2O_3 (0001)	3.1E-08	696	139	115	5.0E-03	1.0E-03	17
LBM 5b	$LaAlO_3$ (100)	3.1E-08	696	139	115	5.0E-03	1.0E-03	17
LBM 5c	MgO (100)	3.1E-08	696	139	115	5.0E-03	1.0E-03	17
LBM 5d	$SrTiO_3$ (100)	3.1E-08	696	139	115	5.0E-03	1.0E-03	17
LBM 6a	Al_2O_3 (0001)	3.1E-08	696	127	105	5.0E-03	1.0E-03	105
LBM 6b	100 Si-SiO_2	3.1E-08	696	127	105	5.0E-03	1.0E-03	105
LBM 6c	MgO (100)	3.1E-08	696	127	105	5.0E-03	1.0E-03	105
LBM 6d	100 Si-SiO_2	3.1E-08	696	127	105	5.0E-03	1.0E-03	105
LBM 7a	MgO (100)	3.6E-08	696	124	100	5.0E-03	1.0E-03	40
LBM 7b	MgO (100)	3.6E-08	696	124	100	5.0E-03	1.0E-03	40
LBM 7c	$SrTiO_3$ (100)	3.6E-08	696	124	100	5.0E-03	1.0E-03	40
LBM 7d	Al_2O_3 (0001)	3.6E-08	696	124	100	5.0E-03	1.0E-03	40

Table A.2: Substrate characteristics and sputtering deposition parameters for BTO produced samples.

Sample	Substrate	Base pressure	Deposition					
			Temperature	dc bias	Distance	P_{Ar}	P_{O_2}	Time
		mbar	±5°C	V	mm	mbar	mbar	min
BTO 1a	Al_2O_3 (0001)	8.7E-08	633	134	95	5.0E-03	5.0E-04	40
BTO 1b	$SrTiO_3$ (100)	8.7E-08	633	134	95	5.0E-03	5.0E-04	40
BTO 1c	100 Si-SiO_2	8.7E-08	633	134	95	5.0E-03	5.0E-04	40
BTO 1d	MgO (100)	8.7E-08	633	134	95	5.0E-03	5.0E-04	40
BTO 2a	MgO (100)	4.7E-08	633	122	97	5.0E-03	5.0E-04	60
BTO 2b	$SrTiO_3$ (100)	4.7E-08	633	122	97	5.0E-03	5.0E-04	60
BTO 2c	Al_2O_3 (0001)	4.7E-08	633	122	97	5.0E-03	5.0E-04	60
BTO 2d	100 Si-SiO_2	4.7E-08	633	122	97	5.0E-03	5.0E-04	60
BTO 3a	$SrTiO_3$ (100)	3.4E-08	712	124	90	5.0E-03	1.0E-03	60
BTO 3b	MgO (100)	3.4E-08	712	124	90	5.0E-03	1.0E-03	60
BTO 3c	MgO (100)	3.4E-08	712	124	90	5.0E-03	1.0E-03	60
BTO 3d	PMN-PT	3.4E-08	712	124	90	5.0E-03	1.0E-03	60
BTO 4g	Glass	7.7E-08	463	123	100	5.0E-03	1.0E-03	60
BTO 5a	$SrTiO_3$ (100)	2.9E-08	665	135	90	5.0E-03	5.0E-04	30
BTO 5b	MgO (100)	2.9E-08	665	135	90	5.0E-03	5.0E-04	30
BTO 5c	Al_2O_3 (0001)	2.9E-08	665	135	90	5.0E-03	5.0E-04	30
BTO 5d	$SrTiO_3$ (100)	2.9E-08	665	135	90	5.0E-03	5.0E-04	30
BTO 6a	$SrTiO_3$ (100)	3.5E-08	595	135	90	5.0E-03	5.0E-04	17
BTO 6b	MgO (100)	3.5E-08	595	135	90	5.0E-03	5.0E-04	17
BTO 6c	Si (100)	3.5E-08	595	135	90	5.0E-03	5.0E-04	17
BTO 6d	Al_2O_3 (0001)	3.5E-08	595	135	90	5.0E-03	5.0E-04	17
BTO 7a	MgO (100)	3.9E-08	557	135	90	5.0E-03	5.0E-04	17
BTO 7b	$SrTiO_3$ (100)	3.9E-08	557	135	90	5.0E-03	5.0E-04	17
BTO 7c	Al_2O_3 (0001)	3.9E-08	557	135	90	5.0E-03	5.0E-04	17
BTO 7d	Si (100)	3.9E-08	557	135	90	5.0E-03	5.0E-04	17
BTO 8a	MgO (100)	3.4E-08	674	130	90	5.0E-03	2.5E-03	17
BTO 8b	100 Si	3.4E-08	674	130	90	5.0E-03	2.5E-03	17
BTO 8c	Al_2O_3 (0001)	3.4E-08	674	130	90	5.0E-03	2.5E-03	17
BTO 8d	$SrTiO_3$ (100)	3.4E-08	674	130	90	5.0E-03	2.5E-03	17
BTO 9a	MgO (100)	5.7E-08	557	122	90	5.0E-03	2.5E-03	10
BTO 9b	Si (100)	5.7E-08	557	122	90	5.0E-03	2.5E-03	10
BTO 9c	$SrTiO_3$ (100)	5.7E-08	557	122	90	5.0E-03	2.5E-03	10
BTO 9d	Al_2O_3 (0001)	5.7E-08	557	122	90	5.0E-03	2.5E-03	10
BTO 10a	MgO (100)	4.0E-08	712	127	90	5.0E-03	2.5E-03	8
BTO 10b	Si (100)	4.0E-08	712	127	90	5.0E-03	2.5E-03	8
BTO 10c	$SrTiO_3$ (100)	4.0E-08	712	127	90	5.0E-03	2.5E-03	8
BTO 10d	Al_2O_3 (0001)	4.0E-08	712	127	90	5.0E-03	2.5E-03	8
BTO 11a	MgO (100)	2.3E-08	712	126	90	5.0E-03	5.0E-04	6
BTO 11b	Si (100)	2.3E-08	712	126	90	5.0E-03	5.0E-04	6
BTO 11c	$SrTiO_3$ (100)	2.3E-08	712	126	90	5.0E-03	5.0E-04	6
BTO 11d	Al_2O_3 (0001)	2.3E-08	712	126	90	5.0E-03	5.0E-04	6
BTO 12	100 Si-SiO_2	4.9E-08	696	110	85	2.5E-03	5.0E-3	8

Table A.3: Substrate characteristics and sputtering deposition parameters for LBMBT produced samples.

Sample	Substrate	Base pressure	Deposition					
			Temp.	dc bias	Distance	P_{Ar}	P_{O_2}	Time
		mbar	±5°C	V	mm	mbar	mbar	min
LBMBT 1a	MgO (100)	6.5E-08	696	123/123/123	100/100/100	5.0E-03	1.0E-03	3/20/90
LBMBT 1b	Al_2O_3 (0001)	6.5E-08	696	123/123/123	100/100/100	5.0E-03	1.0E-03	3/20/90
LBMBT 1c	$SrTiO_3$ (100)	6.5E-08	696	123/123/123	100/100/100	5.0E-03	1.0E-03	3/20/90
LBMBT 1d	100 Si-SiO_2	6.5E-08	568	123/123/123	100/100/100	5.0E-03	1.0E-03	3/20/90
LBMBT 2a	MgO (100)	5.2E-08	641	146/146/146	105/105/105	5.0E-03	1.5E-03	10/30/120
LBMBT 2b	$SrTiO_3$ (100)	5.2E-08	641	146/146/146	105/105/105	5.0E-03	1.5E-03	10/30/120
LBMBT 2c	Al_2O_3 (0001)	5.2E-08	641	146/146/146	105/105/105	5.0E-03	1.5E-03	10/30/120
LBMBT 2d	100 Si-SiO_2	5.2E-08	523	146/146/146	105/105/105	5.0E-03	1.5E-03	10/30/120
LBMBT 3a	$SrTiO_3$ (100)	6.9E-08	715	119/140/161	105/105/105	5.0E-03	1.5E-03	10/30/110
LBMBT 3b	MgO (100)	6.9E-08	715	119/140/161	105/105/105	5.0E-03	1.5E-03	10/30/110
LBMBT 3c	Al_2O_3 (0001)	6.9E-08	715	119/140/161	105/105/105	5.0E-03	1.5E-03	10/30/110
LBMBT 3d	100 Si-SiO_2	6.9E-08	583	119/140/161	105/105/105	5.0E-03	1.5E-03	10/30/110
LBMBT 4a	MgO (100)	3.9E-08	641	155/155/155	105/100/105	6.0E-03	5.0E-04	30/30/30
LBMBT 4b	$SrTiO_3$ (100)	3.9E-08	523	155/155/155	105/100/105	6.0E-03	5.0E-04	30/30/30
LBMBT 4c	100 Si-SiO_2	3.9E-08	523	155/155/155	105/105/105	6.0E-03	5.0E-04	30/30/30
LBMBT 4d	Al_2O_3 (0001)	3.9E-08	641	155/155/155	105/105/105	6.0E-03	5.0E-04	30/30/30

A.3 PDF files, used in the thesis

The PDF files, used in the thesis are:

04-010-6477 Jul 8, 2016 2:46 PM (rosarios)

Status Alternate **QM:** Indexed **Pressure/Temperature:** Ambient **Chemical Formula:** Al2 O3
Empirical Formula: Al2 O3 **Weight %:** Al52.93 O47.07 **Atomic %:** Al40.00 O60.00 **ANX:** A2X3
Compound Name: Aluminum Oxide **Mineral Name:** Corundum, syn

Radiation: CuKα1 **λ:** 1.5406 Å **d-Spacing:** Calculated **Intensity:** Calculated **I/Ic:** 0.93 **I/Ic - ND:** 0.92

SYS: Rhombohedral **SPGR:** R-3c (167)
Author's Cell [AuthCell a: 4.757 Å **AuthCell c:** 12.988 Å **AuthCell Vol:** 254.53 Å³ **AuthCell Z:** 6.00
AuthCell MolVol: 42.42 **]** **Author's Cell Axial Ratio [c/a:** 2.730 **]**
Density [Dcalc: 3.991 g/cm³ **Dstruc:** 3.99 g/cm³ **]** **SS/FOM:** F(30) = 999.9(0.0000, 30)
Temp: 298.0 K (Ambient temperature assigned by ICDD editor)

Space Group: R-3c (167) **Molecular Weight:** 101.96
Crystal Data [XtlCell a: 4.757 Å **XtlCell b:** 4.757 Å **XtlCell c:** 12.988 Å **XtlCell α:** 90.00°
XtlCell β: 90.00° **XtlCell γ:** 120.00° **XtlCell Vol:** 254.53 Å³ **XtlCell Z:** 6.00 **]**
Crystal Data Axial Ratio [c/a: 2.730 **a/b:** 1.000 **c/b:** 2.730 **]**
Reduced Cell [RedCell a: 4.757 Å **RedCell b:** 4.757 Å **RedCell c:** 5.127 Å **RedCell α:** 62.36°
RedCell β: 62.36° **RedCell γ:** 60.00° **RedCell Vol:** 84.84 Å³ **]**

Crystal (Symmetry Allowed): Centrosymmetric

SG Symmetry Operators:

Seq	Operator	Seq	Operator	Seq	Operator	Seq	Operator	Seq	Operator	Seq	Operator
1	x,y,z	3	-y,x-y,z	5	-x+y,-x,z	7	-y,-x,z+1/2	9	x,x-y,z+1/2	11	-x+y,y,z+1/2
2	-x,-y,-z	4	y,-x+y,-z	6	x-y,x,-z	8	y,x,-z+1/2	10	-x,-x+y,-z+1/2	12	x-y,-y,-z+1/2

Atomic Coordinates:

Atom	Num	Wyckoff	Symmetry	x	y	z	SOF	IDP	AET
Al	1	12c	3.	0.0	0.0	0.3522	1.0		
O	2	18e	.2	0.30627	0.30627	0.25	1.0		

Subfile(s): Cement and Hydration Product, Common Phase, Forensic, Inorganic, Metals & Alloys, Mineral Related (Mineral , Synthetic), Pharmaceutical (Excipient), Superconducting Material

Former PDF's #: 01-075-6776 **LPF Prototype Structure [Formula Order]:** Al2 O3,hR30,167
LPF Prototype Structure [Alpha Order]: Al2 O3,hR30,167
Mineral Classification: Corundum (Supergroup), corundum (Group) **Pearson Symbol:** hR10.00

Cross-Ref PDF #'s: 00-001-1243 (Deleted), 00-002-1227 (Deleted), 00-002-1373 (Deleted), 00-003-1033 (Deleted), 00-005-0712 (Alternate), 00-010-0173 (Primary), 00-011-0661 (Deleted), 00-042-1468 (Deleted), 00-043-1484 (Deleted), 00-046-1212 (Primary), 01-070-5679 (Alternate), 01-070-7049 (Alternate), 01-070-7050 (Alternate), 01-070-7346 (Alternate), 01-071-1683 (Alternate), 01-071-1684 (Alternate), 01-071-6478 (Alternate), 01-073-1512 (Alternate), 01-073-5928 (Alternate), 01-073-6190 (Alternate), 01-074-0323 (Alternate), 01-074-1081 (Alternate), 01-075-1862 (Alternate), 01-075-1863 (Alternate), 01-076-8186 (Alternate), 01-077-2135 (Alternate), 01-082-1399 (Alternate), 01-083-2080 (Alternate), 01-088-0826 (Alternate), 01-089-3072 (Alternate), 01-089-7715 (Alternate), 01-089-7716 (Alternate), 01-089-7717 (Alternate), ✓04-002-3621 (Alternate), ✓04-002-5941 (Alternate), ✓04-002-8135 (Alternate), ✓04-003-2497 (Alternate), ✓04-003-5819 (Alternate), ✓04-004-2852 (Primary), ✓04-004-5100 (Alternate), ✓04-004-5285 (Alternate), ✓04-004-5286 (Alternate), ✓04-004-5287 (Alternate), ✓04-004-5288 (Alternate), ✓04-004-5289 (Alternate), ✓04-004-5290 (Alternate), ✓04-004-5291 (Alternate), ✓04-004-5292 (Alternate), ✓04-004-5434 (Alternate), ✓04-004-8977 (Alternate), ✓04-005-4213 (Alternate), ✓04-005-4311 (Alternate), ✓04-005-4497 (Alternate), ✓04-005-4498 (Alternate), ✓04-005-4499 (Alternate), ✓04-005-4500 (Alternate), ✓04-005-4501 (Alternate), ✓04-005-4502 (Alternate), ✓04-005-4503 (Alternate), ✓04-005-4505 (Alternate), ✓04-006-0815 (Alternate), ✓04-006-2060 (Alternate), ✓04-006-3495 (Alternate), ✓04-006-9359 (Alternate), ✓04-006-9730 (Alternate), ✓04-007-1400 (Alternate), ✓04-007-4873 (Alternate), ✓04-007-5143 (Alternate), ✓04-007-9625 (Alternate), ✓04-007-9764 (Alternate), ✓04-007-9768 (Alternate), ✓04-007-9769 (Alternate), ✓04-007-9906 (Alternate), ✓04-008-3293 (Alternate), ✓04-010-6476 (Alternate), ✓04-012-1370 (Alternate), ✓04-012-1371 (Alternate), ✓04-012-1372 (Alternate), ✓04-012-1373 (Alternate), ✓04-013-1687 (Alternate), ✓04-014-1368 (Alternate), ✓04-014-8419 (Alternate), ✓04-015-7243 (Alternate), ✓04-015-8608 (Alternate), ✓04-015-8609 (Alternate), ✓04-015-8610 (Alternate), ✓04-015-8611 (Alternate), ✓04-015-8642 (Alternate), ✓04-015-8993 (Alternate), ✓04-015-8994 (Alternate), ✓04-015-8995 (Alternate), ✓04-015-8996 (Alternate)

Entry Date: 09/01/2007 **Last Modification Date:** 09/01/2012 **Last Modifications:** CellVolume

References:

Type	DOI	Reference
Primary Reference		Calculated from LPF using POWD-12++.
Structure		"Equation of State of α-Al2O3 (Corundum) from Quasi-Harmonic Atomistic Simulations". Catti, M., Pavese, A. Acta Crystallogr., Sec. B: Struct. Sci. 54, 741,749 (1998).

Database Comments: ANX: A2X3. LPF Collection Code: 1412926. Minor Warning: No R factors reported/abstracted. No e.s.d reported/abstracted on the cell dimension. Unit Cell Data Source: Powder Diffraction.

04-010-6477 Jul 8, 2016 2:46 PM (rosarios)

d-Spacings (56) - Al2 O3 - 04-010-6477 (Stick, Fixed Slit Intensity) - Cu Kα1 1.54056 Å

2θ (°)	d (Å)	I	h	k	l	*	2θ (°)	d (Å)	I	h	k	l	*	2θ (°)	d (Å)	I	h	k	l	*
25.5855	3.478740	661	0	1	2		83.2535	1.159580	5	0	3	6		116.1697	0.907459	67	3	2	4	
35.1622	**2.550130**	999	1	0	4		84.3961	1.146770	38	2	2	3		116.6611	0.905050	24	0	1	14	
37.7920	2.378500	461	1	1	0		85.1808	1.138200	2	1	3	1		117.9250	0.898988	37	4	1	0	
41.6901	2.164670	5	0	0	6		86.3933	1.125310	28	3	1	2		120.2875	0.888159	2	2	3	5	
43.3706	**2.084610**	957	1	1	3		86.5409	1.123770	21	1	2	8		122.1154	0.880212	22	4	1	3	
46.1968	1.963440	14	2	0	2		89.0341	1.098640	51	0	2	10		124.6758	0.869684	13	0	4	8	
52.5717	1.739370	453	0	2	4		90.7447	1.082330	13	0	0	12		127.7647	0.857876	71	1	3	10	
57.5209	**1.600920**	866	1	1	6		91.2326	1.077810	59	1	3	4		129.9613	0.850044	27	0	3	12	
59.7665	1.546020	22	2	1	1		94.8653	1.045890	3	3	1	5		131.1833	0.845882	28	2	0	14	
61.1560	1.514180	31	1	2	2		95.2947	1.042310	114	2	2	6		132.3125	0.842157	2	3	2	7	
61.3237	1.510440	65	0	1	8		98.4443	1.017210	15	0	4	2		132.7106	0.840871	2	2	1	13	
66.5465	1.404000	318	2	1	4		101.1222	0.997381	79	2	1	10		136.1837	0.830237	102	1	4	6	
68.2397	1.373230	479	3	0	0		102.8706	0.985133	2	1	1	12		139.4775	0.821086	1	3	1	11	
70.4459	1.335530	10	1	2	5		103.3718	0.981719	14	4	0	4		141.1411	0.816795	3	2	3	8	
74.3294	1.275070	11	2	0	8		104.6938	0.972915	1	1	3	7		142.4248	0.813631	13	1	1	15	
76.9021	1.238700	127	1	0	10		109.6034	0.942628	3	3	2	1		145.3039	0.806989	39	4	0	10	
77.2654	1.233780	69	1	1	9		109.9154	0.940825	2	1	2	11		148.4326	0.800461	1	2	2	12	
80.4524	1.192740	6	2	1	7		111.0496	0.934385	21	3	1	8		149.3779	0.798626	26	0	5	4	
80.7372	1.189250	47	2	2	0		114.1321	0.917767	14	2	2	9								

04-007-8736 Jul 8, 2016 2:47 PM (rosarios)

Status Alternate **QM:** Indexed **Pressure/Temperature:** Ambient **Chemical Formula:** Si
Empirical Formula: Si **Weight %:** Si100.00 **Atomic %:** Si100.00 **ANX:** N **Compound Name:** Silicon
Mineral Name: Silicon, syn

Radiation: CuKα1 **λ:** 1.5406 Å **d-Spacing:** Calculated **Intensity:** Calculated **I/Ic:** 4.55 **I/Ic - ND:** 0.48

SYS: Cubic **SPGR:** Fd-3m (227)
Author's Cell [AuthCell a: 5.43054(17) Å **AuthCell Vol:** 160.15 Å³ **AuthCell Z:** 8.00 **AuthCell MolVol:** 20.02 **]** **Density [Dcalc:** 2.33 g/cm³ **Dstruc:** 2.33 g/cm³ **]** **SS/FOM:** F(12) = 999.9(0.0002, 13)
Temp: 298.0 K (Author provided temperature)

Space Group: Fd-3m (227) **Molecular Weight:** 28.09
Crystal Data [XtlCell a: 5.431 Å **XtlCell b:** 5.431 Å **XtlCell c:** 5.431 Å **XtlCell α:** 90.00°
XtlCell β: 90.00° **XtlCell γ:** 90.00° **XtlCell Vol:** 160.15 Å³ **XtlCell Z:** 8.00 **]**
Crystal Data Axial Ratio [a/b: 1.000 **c/b:** 1.000 **]**
Reduced Cell [RedCell a: 3.840 Å **RedCell b:** 3.840 Å **RedCell c:** 3.840 Å **RedCell α:** 60.00°
RedCell β: 60.00° **RedCell γ:** 60.00° **RedCell Vol:** 40.04 Å³ **]**

Origin: O2 **Crystal (Symmetry Allowed):** Centrosymmetric

SG Symmetry Operators:

Seq	Operator	Seq	Operator	Seq	Operator	Seq	Operator	Seq	Operator
1	x,y,z	11	z,-x+1/4,-y+1/4	21	-y+1/4,z,-x+1/4	31	-x+1/4,-z+1/4,y	41	z,y,x
2	-x,-y,-z	12	-z,x+3/4,y+3/4	22	y+3/4,-z,x+3/4	32	x+3/4,z+3/4,-y	42	-z,-y,-x
3	x,-y+1/4,-z+1/4	13	-z+1/4,x,-y+1/4	23	-y+1/4,-z+1/4,x	33	y,x,z	43	z,-y+1/4,-x+1/4
4	-x,y+3/4,z+3/4	14	z+3/4,-x,y+3/4	24	y+3/4,z+3/4,-x	34	-y,-x,-z	44	-z,y+3/4,x+3/4
5	-x+1/4,y,-z+1/4	15	-z+1/4,-x+1/4,y	25	x,z,y	35	y,-x+1/4,-z+1/4	45	-z+1/4,y,-x+1/4
6	x+3/4,-y,z+3/4	16	z+3/4,x+3/4,-y	26	-x,-z,-y	36	-y,x+3/4,z+3/4	46	z+3/4,-y,x+3/4
7	-x+1/4,-y+1/4,z	17	y,z,x	27	x,-z+1/4,-y+1/4	37	-y+1/4,x,-z+1/4	47	-z+1/4,-y+1/4,x
8	x+3/4,y+3/4,-z	18	-y,-z,-x	28	-x,z+3/4,y+3/4	38	y+3/4,-x,z+3/4	48	z+3/4,y+3/4,-x
9	z,x,y	19	y,-z+1/4,-x+1/4	29	-x+1/4,z,-y+1/4	39	-y+1/4,-x+1/4,z		
10	-z,-x,-y	20	-y,z+3/4,x+3/4	30	x+3/4,-z,y+3/4	40	y+3/4,x+3/4,-z		

Atomic Coordinates:

Atom	Num	Wyckoff	Symmetry	x	y	z	SOF	IDP	AET
Si	1	8a	-43m	0.125	0.125	0.125	1.0		4-a

Subfile(s): Ceramic (Semiconductor), Common Phase, Forensic, Inorganic, Metals & Alloys, Mineral Related (Mineral , Synthetic)

Former PDF's #: 01-073-2534 **Prototype Structure [Formula Order]:** C **Prototype Structure [Alpha Order]:** C
LPF Prototype Structure [Formula Order]: C,cF8,227 **LPF Prototype Structure [Alpha Order]:** C,cF8,227
Mineral Classification: Diamond (Supergroup), 2C-diamond (Group) **Pearson Symbol:** cF8.00

Cross-Ref PDF #'s: 00-001-0787 (Deleted), 00-001-0791 (Deleted), 00-002-0561 (Deleted), 00-003-0529 (Deleted), 00-005-0565 (Alternate), 00-026-1481 (Alternate), 00-027-1402 (Primary), 01-070-5680 (Alternate), 01-071-3770 (Alternate), 01-071-4631 (Alternate), 01-073-6978 (Alternate), 01-075-0589 (Alternate), 01-077-2108 (Alternate), 01-077-2109 (Alternate), 01-077-2110 (Alternate), 01-077-2111 (Alternate), 01-089-2749 (Alternate), 01-089-2955 (Alternate), ✓03-065-1060 (Alternate), ✓04-001-7247 (Primary), ✓04-002-0118 (Alternate), ✓04-002-0891 (Alternate), ✓04-002-2831 (Alternate), ✓04-003-1456 (Alternate), ✓04-003-3352 (Alternate), ✓04-003-3353 (Alternate), ✓04-003-4734 (Alternate), ✓04-004-5099 (Alternate), ✓04-004-6896 (Alternate), ✓04-005-9699 (Alternate), ✓04-006-2527 (Alternate), ✓04-006-2591 (Alternate), ✓04-006-4528 (Alternate), ✓04-006-6436 (Alternate), ✓04-007-5232 (Alternate), ✓04-010-2410 (Alternate), ✓04-012-0806 (Alternate), ✓04-012-7888 (Alternate), ✓04-013-4795 (Alternate), ✓04-014-0211 (Alternate), ✓04-014-0247 (Alternate), ✓04-014-8844 (Alternate), ✓04-016-4861 (Alternate), ✓04-016-5305 (Alternate)

Entry Date: 09/01/2005 **Last Modification Date:** 09/01/2011 **Last Modifications:** Reflections

References:

Type	DOI	Reference
Primary Reference		Calculated from LPF using POWD-12++.
Structure		"Results of the I.U.Cr. precision lattice-parameter project". Parrish W. Acta Crystallogr. 13, 838 (1960).

Database Comments: ANX: N. LPF Collection Code: 1500920. Sample Preparation: STARTING MATERIALS:Si. Temperature of Data Collection: 298 K. Minor Warning: No R factor reported/abstracted. Unit Cell Data Source: Powder Diffraction.

d-Spacings (12) - Si - 04-007-8736 (Stick, Fixed Slit Intensity) - Cu Kα1 1.54056 Å

2θ (°)	d (Å)	I	h	k	l	*	2θ (°)	d (Å)	I	h	k	l	*	2θ (°)	d (Å)	I	h	k	l	*
28.4438	**3.135320**	999	1	1	1		69.1336	1.357640	74	4	0	0		106.7161	0.959993	37	4	4	0	
47.3051	**1.919990**	586	2	2	0		76.3808	1.245850	103	3	3	1		114.1009	0.917929	64	5	3	1	
56.1254	**1.637370**	321	3	1	1		88.0361	1.108500	126	4	2	2		127.5560	0.858644	55	6	2	0	
58.8596	1.567660	1	2	2	2		94.9585	1.045110	66	5	1	1		136.9075	0.828150	26	5	3	3	

04-012-7345 Jul 8, 2016 2:47 PM (rosarios)

2θ (°)	d (Å)	I	h	k	l	*	2θ (°)	d (Å)	I	h	k	l	*	2θ (°)	d (Å)	I	h	k	l	*
75.0984	1.263910	13	2	4	0		95.1683	1.043360	19	1	3	6		113.2866	0.922200	m	6	0	0	
76.0868	1.249930	34	3	3	2		96.1001	1.035700	26	3	1	6		113.5884	0.920607	11	3	3	6	
76.2818	1.247220	23	2	4	1		97.3481	1.025720	3m	0	2	7		115.3522	0.911532	9	0	2	8	
76.5316	1.243770	24m	0	4	3		97.3481	1.025720	m	1	4	5		115.8659	0.908963	11m	2	0	8	
76.5316	1.243770	m	4	2	0		97.5251	1.024330	1	4	3	3		115.8659	0.908963	m	3	4	5	
77.7084	1.227850	7	4	2	1		97.8956	1.021440	14m	1	5	3		116.1926	0.907346	1	1	6	2	
78.2402	1.220830	46	1	1	6		97.8956	1.021440	m	5	2	1		116.5799	0.905446	10	3	5	3	
78.6070	1.216050	10	2	2	5		98.8328	1.014250	1	2	5	2		116.8250	0.904253	1m	4	3	5	
79.4027	1.205850	1	3	2	4		99.0537	1.012580	1	4	1	5		116.8250	0.904253	m	6	1	1	
79.8002	1.200840	1	2	4	2		99.5932	1.008540	1	1	2	7		117.2374	0.902262	10	1	5	5	
80.6219	1.190660	1	4	1	3		99.9456	1.005930	1	2	1	7		117.6151	0.900457	1	2	4	6	
81.2097	1.183520	8	4	2	2		100.3669	1.002840	6	3	3	5		117.8150	0.899508	1m	1	2	8	
81.9315	1.174910	13	3	3	3		100.7124	1.000330	1	5	1	3		117.8150	0.899508	m	2	3	7	
82.3943	1.169480	6	0	2	6		101.3035	0.996086	1	5	2	2		117.9992	0.898638	1	5	0	5	
82.5231	1.167980	13	1	3	5		102.0022	0.991150	5m	2	3	6		118.3859	0.896825	3m	3	2	7	
82.8613	1.164070	6	2	0	6		102.0022	0.991150	m	4	4	0		118.3859	0.896825	m	6	0	2	
83.4569	1.157270	2	3	1	5		102.5021	0.987670	1	3	2	6		118.6717	0.895496	5	5	3	3	
84.7274	1.143130	10m	0	4	4		103.1774	0.983038	10	4	4	1		119.1954	0.893085	3	4	2	6	
84.7274	1.143130	m	1	2	6		104.0825	0.976950	7	2	4	5		119.8420	0.890152	10	2	6	1	
85.5847	1.133860	19	2	4	3		104.6936	0.972916	1	2	5	3		120.1804	0.888636	6	0	6	3	
86.5860	1.123300	21	4	0	4		104.8887	0.971641	1	3	4	4		120.8067	0.885864	1	6	1	2	
86.9773	1.119250	7m	1	4	4		105.5203	0.967556	2m	3	5	0		121.8877	0.881182	7	4	4	4	
86.9773	1.119250	m	4	2	3		105.5203	0.967556	m	4	2	5		122.8391	0.877166	7m	1	6	3	
87.5468	1.113430	1m	1	5	0		106.3337	0.962387	6m	0	0	8		122.8391	0.877166	m	6	2	0	
87.5468	1.113430	m	3	4	1		106.3337	0.962387	m	2	2	7		123.8947	0.872823	1m	2	6	2	
88.3269	1.105600	1	4	3	1		106.6959	0.960119	11m	3	5	1		123.8947	0.872823	m	4	5	1	
88.6941	1.101970	19m	1	5	1		106.6959	0.960119	m	4	4	2		124.2150	0.871528	3	6	2	1	
88.6941	1.101970	m	4	1	4		107.2237	0.956850	1	5	2	3		124.6628	0.869736	3	0	4	7	
89.2068	1.096960	1	2	3	5		107.4347	0.955555	1	5	3	0		125.0266	0.868295	1	2	5	5	
89.3699	1.095380	1	5	0	1		107.9684	0.952309	1	0	4	6		125.6771	0.865752	14	2	2	8	
89.7861	1.091380	1	3	2	5		108.6409	0.948280	6	5	3	1		127.4092	0.859187	1	1	4	7	
89.9874	1.089460	2	3	3	4		109.0276	0.945993	5	5	1	4		127.7516	0.857924	1	6	1	3	
90.3275	1.086240	4	5	1	0		110.0336	0.940145	6m	0	6	1		128.3108	0.855886	1m	4	5	2	
90.9576	1.080350	1	3	4	2		110.0336	0.940145	m	4	0	6		128.3108	0.855886	m	5	3	4	
91.3000	1.077190	5	2	2	6		110.3252	0.938477	5m	1	4	6		128.4884	0.855245	2	6	2	2	
91.4745	1.075590	1	5	1	1		110.3252	0.938477	m	3	5	2		129.6300	0.851196	1m	4	1	7	
91.7686	1.072910	1	4	3	2		110.5081	0.937437	6	1	3	7		129.6300	0.851196	m	5	4	2	
92.1360	1.069590	5	1	5	2		110.8993	0.935228	3	1	1	8		130.0055	0.849891	1	0	6	4	
93.2357	1.059840	2	1	1	7		111.5007	0.931873	1	3	1	7		130.5890	0.847889	1	1	3	8	
93.6209	1.056490	12	2	4	4		112.3147	0.927411	15m	1	6	1		131.1296	0.846062	8m	2	6	3	
94.9214	1.045420	34	5	1	2		112.3147	0.927411	m	5	3	2		131.1296	0.846062	m	3	4	6	
95.0147	1.044640	31m	0	4	5		112.8376	0.924592	7	4	4	3		131.3314	0.845387	6m	1	0	9	
95.0147	1.044640	m	4	2	4		113.2866	0.922200	4m	2	5	4		131.3314	0.845387	m	3	3	7	

04-012-7345 Jul 8, 2016 2:47 PM (rosarios)

2θ (°)	d (Å)	I	h	k	l	*	2θ (°)	d (Å)	I	h	k	l	*	2θ (°)	d (Å)	I	h	k	l	*
75.0984	1.263910	13	2	4	0		95.1683	1.043360	19	1	3	6		113.2866	0.922200	m	6	0	0	
76.0868	1.249930	34	3	3	2		96.1001	1.035700	26	3	1	6		113.5884	0.920607	11	3	3	6	
76.2818	1.247220	23	2	4	1		97.3481	1.025720	3m	0	2	7		115.3522	0.911532	9	0	2	8	
76.5316	1.243770	24m	0	4	3		97.3481	1.025720	m	1	4	5		115.8659	0.908963	11m	2	0	8	
76.5316	1.243770	m	4	2	0		97.5251	1.024330	1	4	3	3		115.8659	0.908963	m	3	4	5	
77.7084	1.227850	7	4	2	1		97.8956	1.021440	14m	1	5	3		116.1926	0.907346	1	1	6	2	
78.2402	1.220830	46	1	1	6		97.8956	1.021440	m	5	2	1		116.5799	0.905446	10	3	5	3	
78.6070	1.216050	10	2	2	5		98.8328	1.014250	1	2	5	2		116.8250	0.904253	1m	4	3	5	
79.4027	1.205850	1	3	2	4		99.0537	1.012580	1	4	1	5		116.8250	0.904253	m	6	1	1	
79.8002	1.200840	1	2	4	2		99.5932	1.008540	1	1	2	7		117.2374	0.902262	10	1	5	5	
80.6219	1.190660	1	4	1	3		99.9456	1.005930	1	2	1	7		117.6151	0.900457	1	2	4	6	
81.2097	1.183520	8	4	2	2		100.3669	1.002840	6	3	3	5		117.8150	0.899508	1m	1	2	8	
81.9315	1.174910	13	3	3	3		100.7124	1.000330	1	5	1	3		117.8150	0.899508	m	2	3	7	
82.3943	1.169480	6	0	2	6		101.3035	0.996086	1	5	2	2		117.9992	0.898638	1	5	0	5	
82.5231	1.167980	13	1	3	5		102.0022	0.991150	5m	2	3	6		118.3859	0.896825	3m	3	2	7	
82.8613	1.164070	6	2	0	6		102.0022	0.991150	m	4	4	0		118.3859	0.896825	m	6	0	2	
83.4569	1.157270	2	3	1	5		102.5021	0.987670	1	3	2	6		118.6717	0.895496	5	5	3	3	
84.7274	1.143130	10m	0	4	4		103.1774	0.983038	10	4	4	1		119.1954	0.893085	3	4	2	6	
84.7274	1.143130	m	1	2	6		104.0825	0.976950	7	2	4	5		119.8420	0.890152	10	2	6	1	
85.5847	1.133860	19	2	4	3		104.6936	0.972916	1	2	5	3		120.1804	0.888636	6	0	6	3	
86.5860	1.123300	21	4	0	4		104.8887	0.971641	1	3	4	4		120.8067	0.885864	1	6	1	2	
86.9773	1.119250	7m	1	4	4		105.5203	0.967556	2m	3	5	0		121.8877	0.881182	7	4	4	4	
86.9773	1.119250	m	4	2	3		105.5203	0.967556	m	4	2	5		122.8391	0.877166	7m	1	6	3	
87.5468	1.113430	1m	1	5	0		106.3337	0.962387	6m	0	0	8		122.8391	0.877166	m	6	2	0	
87.5468	1.113430	m	3	4	1		106.3337	0.962387	m	2	2	7		123.8947	0.872823	1m	2	6	2	
88.3269	1.105600	1	4	3	1		106.6959	0.960119	11m	3	5	1		123.8947	0.872823	m	4	5	1	
88.6941	1.101970	19m	1	5	1		106.6959	0.960119	m	4	4	2		124.2150	0.871528	3	6	2	1	
88.6941	1.101970	m	4	1	4		107.2237	0.956850	1	5	2	3		124.6628	0.869736	3	0	4	7	
89.2068	1.096960	1	2	3	5		107.4347	0.955555	1	5	3	0		125.0266	0.868295	1	2	5	5	
89.3699	1.095380	1	5	0	1		107.9684	0.952309	1	0	4	6		125.6771	0.865752	14	2	2	8	
89.7861	1.091380	1	3	2	5		108.6409	0.948280	6	5	3	1		127.4092	0.859187	1	1	4	7	
89.9874	1.089460	2	3	3	4		109.0276	0.945993	5	5	1	4		127.7516	0.857924	1	6	1	3	
90.3275	1.086240	4	5	1	0		110.0336	0.940145	6m	0	6	1		128.3108	0.855886	1m	4	5	2	
90.9576	1.080350	1	3	4	2		110.0336	0.940145	m	4	0	6		128.3108	0.855886	m	5	3	4	
91.3000	1.077190	5	2	2	6		110.3252	0.938477	5m	1	4	6		128.4884	0.855245	2	6	2	2	
91.4745	1.075590	1	5	1	1		110.3252	0.938477	m	3	5	2		129.6300	0.851196	1m	4	1	7	
91.7686	1.072910	1	4	3	2		110.5081	0.937437	6	1	3	7		129.6300	0.851196	m	5	4	2	
92.1360	1.069590	5	1	5	2		110.8993	0.935228	3	1	1	8		130.0055	0.849891	1	0	6	4	
93.2357	1.059840	2	1	1	7		111.5007	0.931873	1	3	1	7		130.5890	0.847889	1	1	3	8	
93.6209	1.056490	12	2	4	4		112.3147	0.927411	15m	1	6	1		131.1296	0.846062	8m	2	6	3	
94.9214	1.045420	34	5	1	2		112.3147	0.927411	m	5	3	2		131.1296	0.846062	m	3	4	6	
95.0147	1.044640	31m	0	4	5		112.8376	0.924592	7	4	4	3		131.3314	0.845387	6m	1	0	9	
95.0147	1.044640	m	4	2	4		113.2866	0.922200	4m	2	5	4		131.3314	0.845387	m	3	3	7	

04-012-7799 Jul 8, 2016 2:48 PM (rosarios)

Status Alternate **QM:** Star **Pressure/Temperature:** Ambient **Chemical Formula:** Sr0.3 La0.7 Mn O3
Empirical Formula: La0.7 Mn O3 Sr0.3 **Weight %:** La42.94 Mn24.26 O21.19 Sr11.61
Atomic %: La14.00 Mn20.00 O60.00 Sr6.00 **ANX:** ABX3
Compound Name: Strontium Lanthanum Manganese Oxide

Radiation: CuKα1 **λ:** 1.5406 Å **d-Spacing:** Calculated **Intensity:** Calculated **I/Ic:** 5.71 **I/Ic - ND:** 0.63

SYS: Rhombohedral **SPGR:** R-3c (167)
Author's Cell [AuthCell a: 5.5023(3) Å **AuthCell c:** 13.3569(7) Å **AuthCell Vol:** 350.21 Å³
AuthCell Z: 6.00 **AuthCell MolVol:** 58.37] **Author's Cell Axial Ratio [c/a:** 2.428]
Density [Dcalc: 6.443 g/cm³ **Dstruc:** 6.44 g/cm³] **SS/FOM:** F(30) = 508.2(0.0019, 31)
Temp: 298.0 K (Ambient temperature assigned by ICDD editor) **R-factor:** 0.031

Space Group: R-3c (167) **Molecular Weight:** 226.46
Crystal Data [XtlCell a: 5.502 Å **XtlCell b:** 5.502 Å **XtlCell c:** 13.357 Å **XtlCell α:** 90.00°
XtlCell β: 90.00° **XtlCell γ:** 120.00° **XtlCell Vol:** 350.21 Å³ **XtlCell Z:** 6.00]
Crystal Data Axial Ratio [c/a: 2.428 **a/b:** 1.000 **c/b:** 2.428]
Reduced Cell [RedCell a: 5.469 Å **RedCell b:** 5.469 Å **RedCell c:** 5.469 Å **RedCell α:** 60.40°
RedCell β: 60.40° **RedCell γ:** 60.40° **RedCell Vol:** 116.73 Å³]

ADP: B **Crystal (Symmetry Allowed):** Centrosymmetric

SG Symmetry Operators:

Seq	Operator	Seq	Operator	Seq	Operator	Seq	Operator	Seq	Operator	Seq	Operator
1	x,y,z	3	-y,x-y,z	5	-x+y,-x,z	7	-y,-x,z+1/2	9	x,x-y,z+1/2	11	-x+y,y,z+1/2
2	-x,-y,-z	4	y,-x+y,-z	6	x-y,x,-z	8	y,x,-z+1/2	10	-x,-x+y,-z+1/2	12	x-y,-y,-z+1/2

Atomic Coordinates:

Atom	Num	Wyckoff	Symmetry	x	y	z	SOF	Biso	AET
La	1	6a	32	0.0	0.0	0.25	0.7	0.29	
Sr	2	6a	32	0.0	0.0	0.25	0.3	0.29	
Mn	3	6b	-3.	0.0	0.0	0.0	1.0	0.37	
O	4	18e	.2	0.4556	0.0	0.25	1.0	0.84	

Subfile(s): Ceramic (Ferroelectric, Perovskite), Inorganic **Former PDF's #:** 01-074-8358
LPF Prototype Structure [Formula Order]: La Al O3,hR30,167
LPF Prototype Structure [Alpha Order]: Al La O3,hR30,167 **Pearson Symbol:** hR10.00

Cross-Ref PDF #'s: 00-050-0308 (Primary), 00-051-0409 (Alternate), ✓00-064-0177 (Primary), 01-070-8668 (Alternate), 01-071-5288 (Alternate), 01-071-5289 (Alternate), 01-072-7896 (Alternate), 01-075-3216 (Alternate), 01-078-2865 (Alternate), 01-078-2866 (Alternate), 01-078-2867 (Alternate), 01-080-3278 (Alternate), 01-089-8093 (Alternate), 01-089-8094 (Alternate), 01-089-8095 (Alternate), 01-089-8096 (Alternate), 01-089-8097 (Alternate), 01-089-8098 (Alternate), ✓04-002-5475 (Alternate), ✓04-006-7892 (Alternate), ✓04-006-9515 (Alternate), ✓04-008-2551 (Primary), ✓04-008-4421 (Alternate), ✓04-012-5784 (Alternate), ✓04-012-5785 (Alternate), ✓04-013-6882 (Alternate), ✓04-013-6891 (Alternate), ✓04-013-6895 (Alternate), ✓04-014-1819 (Alternate), ✓04-014-7254 (Alternate), ✓04-015-2353 (Alternate), ✓04-015-6977 (Alternate), ✓04-015-9729 (Alternate), ✓04-019-4873 (Alternate)

Entry Date: 09/01/2009 **Last Modification Date:** 09/01/2011 **Last Modifications:** Reflections

References:

Type	DOI	Reference
Primary Reference		Calculated from LPF using POWD-12++.
Structure		"Structure, magnetic and magnetoresistive properties of La0.7Sr0.3Mn1-xSnxO3 samples (0 <= x <= 0.20)". Kallel N., Frohlich K., Pignard S., Oummezzine M., Vincent H. J. Alloys Compd. 399, 20,26 (2005).

Database Comments: ANX: ABX3. LPF Collection Code: 1908038. Sample Preparation: Compound Preparation: heated at 1173 K for 72 h, then at 1473 K for 24 h, then at 1673 K for 2 d with intermediate grindings. ATMOSPHERE: air. Unit Cell Data Source: Powder Diffraction.

d-Spacings (74) - Sr0.3 La0.7 Mn O3 - 04-012-7799 (Stick, Fixed Slit Intensity) - Cu Kα1 1.54056 Å

2θ (°)	d (Å)	I	h	k	l	*	2θ (°)	d (Å)	I	h	k	l	*	2θ (°)	d (Å)	I	h	k	l	*
22.9077	3.878970	203	0	1	2		68.1071	1.375580	140	2	2	0		82.7728	1.165090	19	0	2	10	
32.5186	**2.751150**	986	1	1	0		68.5762	1.367310	146	2	0	8		86.7092	1.122020	59	4	0	4	
32.7207	**2.734620**	999	1	0	4		71.7020	1.315190	3m	1	3	1		87.5823	1.113070	21	0	0	12	
38.4313	2.340390	15	1	1	3		71.7020	1.315190	m	2	2	3		89.9780	1.089550	1	3	2	1	
40.1507	2.244040	240	2	0	2		72.0463	1.309750	1	2	1	7		90.3042	1.086460	1	1	3	7	
40.4875	2.226150	87	0	0	6		72.2749	1.306170	1	1	1	9		91.1208	1.078840	15	2	3	2	
46.8010	**1.939490**	590	0	2	4		72.9022	1.296470	19	3	1	2		91.7752	1.072850	12	2	1	10	
51.1324	1.784900	4	2	1	1		73.1302	1.292990	25	0	3	6		95.5937	1.039840	81	4	1	0	
52.5860	1.738930	54	1	2	2		73.5848	1.286120	10	1	0	10		95.7032	1.038940	86	3	2	4	
52.8600	1.730560	47	1	1	6		77.6325	1.228860	117	1	3	4		96.0324	1.036250	66	3	1	8	
58.0180	1.588380	204	3	0	0		77.9664	1.224430	122	1	2	8		96.5806	1.031820	64	1	1	12	
58.1463	1.585180	345	2	1	4		81.1226	1.184570	2	3	1	5		99.0524	1.012590	1m	2	3	5	
58.5304	1.575690	162	0	1	8		82.1132	1.172770	17	0	4	2		99.0524	1.012590	m	4	1	3	
62.1028	1.493350	2	1	2	5		82.3325	1.170200	34	2	2	6		99.5488	1.008870	1	2	2	9	

04-012-7799 Jul 8, 2016 2:48 PM (rosarios)

2θ (°)	d (Å)	I	h	k	l	*	2θ (°)	d (Å)	I	h	k	l	*	2θ (°)	d (Å)	I	h	k	l	*
99.8251	1.006820	1	1	2	11		118.0934	0.898195	1m	2	4	1		130.2929	0.848901	9	1	5	2	
105.1809	0.969743	37	0	4	8		118.0934	0.898195	m	3	3	3		130.5793	0.847922	8	3	3	6	
108.5951	0.948552	1	3	2	7		118.9613	0.894159	1	3	1	11		131.1553	0.845976	11	3	2	10	
109.4589	0.943468	8	5	0	2		119.3348	0.892449	14m	2	1	13		132.0291	0.843081	9	1	2	14	
109.6901	0.942126	20	4	1	6		119.3348	0.892449	m	4	2	2		136.5949	0.829046	45	5	1	4	
110.1535	0.939458	9	1	3	10		120.0873	0.889052	8	4	0	10		137.0726	0.827680	28	5	0	8	
110.8513	0.935498	5	0	1	14		120.8457	0.885693	9	2	0	14		139.0280	0.822283	23	1	0	16	
114.2706	0.917050	31	3	3	0		124.7314	0.869463	58	2	4	4		141.8480	0.815037	1	1	5	5	
114.3901	0.916433	36	0	5	4		125.7988	0.865281	62	2	2	12		142.9189	0.812447	1	2	3	11	
114.7494	0.914589	56	2	3	8		128.8102	0.854091	1	5	1	1		143.4644	0.811161	1	1	3	13	
115.3506	0.911540	53	3	0	12		129.5125	0.851607	1	4	1	9								

04-008-1880 May 17, 2016 3:01 PM (jbastos)

Status Alternate **QM:** Prototyping **Pressure/Temperature:** Ambient **Chemical Formula:** Ba Ti O3
Empirical Formula: Ba O3 Ti **Weight %:** Ba58.89 O20.58 Ti20.53 **Atomic %:** Ba20.00 O60.00 Ti20.00
ANX: ABX3 **Compound Name:** Barium Titanium Oxide

Radiation: CuKα1 **λ:** 1.5406 Å **d-Spacing:** Calculated **Intensity:** Calculated **I/Ic:** 7.46 **I/Ic - ND:** 0.68

SYS: Tetragonal **SPGR:** P4mm (99)
Author's Cell [AuthCell a: 3.986 Å **AuthCell c:** 4.026 Å **AuthCell Vol:** 63.97 Å³ **AuthCell Z:** 1.00
AuthCell MolVol: 63.97 **]** **Author's Cell Axial Ratio [c/a:** 1.010 **]**
Density [Dcalc: 6.055 g/cm³ **Dstruc:** 6.05 g/cm³ **]** **SS/FOM:** F(30) = 336.9(0.0029, 31)
Temp: 298.0 K (Ambient temperature assigned by ICDD editor)

Space Group: P4mm (99) **Molecular Weight:** 233.23
Crystal Data [XtlCell a: 3.986 Å **XtlCell b:** 3.986 Å **XtlCell c:** 4.026 Å **XtlCell α:** 90.00°
XtlCell β: 90.00° **XtlCell γ:** 90.00° **XtlCell Vol:** 63.97 Å³ **XtlCell Z:** 1.00 **]**
Crystal Data Axial Ratio [c/a: 1.010 **a/b:** 1.000 **c/b:** 1.010 **]**
Reduced Cell [RedCell a: 3.986 Å **RedCell b:** 3.986 Å **RedCell c:** 4.026 Å **RedCell α:** 90.00°
RedCell β: 90.00° **RedCell γ:** 90.00° **RedCell Vol:** 63.97 Å³ **]**

Crystal (Symmetry Allowed): Non-centrosymmetric - Pyro / Piezo (p), Piezo (2nd Harm.)

SG Symmetry Operators:

Seq	Operator	Seq	Operator	Seq	Operator	Seq	Operator
1	x,y,z	3	-x,y,z	5	y,x,z	7	-y,x,z
2	-x,-y,z	4	x,-y,z	6	-y,-x,z	8	y,-x,z

Atomic Coordinates:

Atom	Num	Wyckoff	Symmetry	x	y	z	SOF	IDP	AET
O	1	2c	2mm.	0.5	0.0	0.0329	1.0		2#a
Ba	2	1b	4mm	0.5	0.5	0.5224	1.0		12-b
Ti	3	1a	4mm	0.0	0.0	0.0	1.0		6-a
O	4	1a	4mm	0.0	0.0	0.5468	1.0		2#b

Subfile(s): Ceramic (Ferroelectric, Perovskite), Common Phase, Inorganic
LPF Prototype Structure [Formula Order]: Ba Ti O3,tP5,99
LPF Prototype Structure [Alpha Order]: Ba O3 Ti,tP5,99 **Pearson Symbol:** tP5.00

Cross-Ref PDF #'s: 00-005-0626 (Primary), 01-070-9164 (Alternate), 01-075-1606 (Alternate), 01-076-0744 (Alternate), 01-076-8447 (Alternate), 01-079-6629 (Alternate), 01-081-8524 (Alternate), 01-082-8580 (Alternate), 01-082-9237 (Alternate), 01-089-1428 (Alternate), ✓04-002-3176 (Alternate), ✓04-002-3207 (Alternate), ✓04-002-3209 (Alternate), ✓04-002-8615 (Alternate), ✓04-002-9075 (Alternate), ✓04-002-9077 (Alternate), ✓04-002-9127 (Alternate), ✓04-005-5601 (Alternate), ✓04-005-7623 (Alternate), ✓04-005-8494 (Alternate), ✓04-006-0175 (Alternate), ✓04-006-0818 (Alternate), ✓04-006-2615 (Alternate), ✓04-006-2812 (Alternate), ✓04-006-6504 (Alternate), ✓04-006-6505 (Alternate), ✓04-006-6548 (Alternate), ✓04-006-9685 (Alternate), ✓04-006-9860 (Alternate), ✓04-006-9936 (Alternate), ✓04-006-9982 (Alternate), ✓04-007-2685 (Alternate), ✓04-007-4173 (Alternate), ✓04-007-5010 (Alternate), ✓04-007-5133 (Alternate), ✓04-007-5230 (Alternate), ✓04-007-8509 (Alternate), ✓04-007-8512 (Alternate), ✓04-007-8514 (Alternate), ✓04-007-9921 (Alternate), ✓04-008-2230 (Alternate), ✓04-008-2416 (Alternate), ✓04-008-4641 (Alternate), ✓04-008-6891 (Alternate), ✓04-008-6892 (Alternate), ✓04-008-6893 (Alternate), ✓04-008-6894 (Alternate), ✓04-009-3215 (Alternate), ✓04-009-3216 (Alternate), ✓04-009-3217 (Alternate), ✓04-009-3218 (Alternate), ✓04-009-3219 (Alternate), ✓04-009-3220 (Alternate), ✓04-012-0310 (Alternate), ✓04-012-0312 (Alternate), ✓04-012-8127 (Primary), ✓04-012-8129 (Alternate), ✓04-012-8130 (Alternate), ✓04-013-5282 (Alternate), ✓04-013-5283 (Alternate), ✓04-013-5890 (Alternate), ✓04-013-5891 (Alternate), ✓04-013-5892 (Alternate), ✓04-013-6990 (Alternate), ✓04-014-0448 (Alternate), ✓04-014-2985 (Alternate), ✓04-014-7603 (Alternate), ✓04-015-2322 (Alternate), ✓04-015-6089 (Alternate), ✓04-015-6090 (Alternate), ✓04-016-2037 (Alternate), ✓04-016-2038 (Alternate), ✓04-016-2039 (Alternate), ✓04-016-2040 (Alternate), ✓04-016-2041 (Alternate), ✓04-016-2042 (Alternate), ✓04-016-6602 (Alternate)

Entry Date: 09/01/2005 **Last Modification Date:** 09/01/2011 **Last Modifications:** Reflections

References:

Type	DOI	Reference
Primary Reference		Calculated from LPF using POWD-12++.
Structure		"Preparation and Properties of Some Novel Perovskite-Type Ferroelectrics". Brixner L.H. J. Solid State Chem. 1, 59 (1969).

Database Comments: ANX: ABX3. LPF Collection Code: 1700378. Sample Preparation: Compound Preparation: solid-state reaction.

d-Spacings (56) - Ba Ti O3 - 04-008-1880 (Stick, Fixed Slit Intensity) - Cu Kα1 1.54056 Å

2θ (°)	d (Å)	I	h	k	l	*	2θ (°)	d (Å)	I	h	k	l	*	2θ (°)	d (Å)	I	h	k	l	*
22.0604	4.026000	101	0	0	1		31.5592	**2.832560**	999	1	0	1		38.9758	**2.308940**	343	1	1	1	
22.2846	3.986000	185	1	0	0		31.7204	**2.818530**	522	1	1	0		44.9962	2.013000	153	0	0	2	

04-008-1880 May 17, 2016 3:01 PM (jbastos)

2θ (°)	d (Å)	I	h	k	l	*	2θ (°)	d (Å)	I	h	k	l	*	2θ (°)	d (Å)	I	h	k	l	*
45.4729	1.993000	299	2	0	0		83.7050	1.154470	56	2	2	2		110.0544	0.940026	m	4	1	1	
50.7678	1.796860	45	1	0	2		87.5735	1.113160	8	2	0	3		113.9404	0.918764	19	3	1	3	
51.0946	1.786130	44	2	0	1		87.9962	1.108900	8	3	0	2		114.6833	0.914927	9	3	3	1	
51.2034	1.782590	43	2	1	0		88.3350	1.105520	7	3	2	0		118.0432	0.898431	22	2	0	4	
56.0978	1.638110	154	1	1	2		91.8535	1.072140	52	2	1	3		119.2000	0.893064	24	4	0	2	
56.4029	1.629970	299	2	1	1		92.2764	1.068330	53	3	1	2		119.5884	0.891297	24	4	2	0	
65.8957	1.416280	141	2	0	2		92.5306	1.066060	53	3	2	1		123.0129	0.876443	9	2	1	4	
66.2661	1.409260	72	2	2	0		99.8684	1.006500	8	0	0	4		124.2322	0.871459	8	4	1	2	
70.0563	1.342000	4	0	0	3		101.2455	0.996500	16	4	0	0		124.5398	0.870226	8	4	2	1	
70.5060	1.334540	30	2	1	2		104.2452	0.975870	6	1	0	4		129.0392	0.853276	28	3	2	3	
70.7747	1.330130	16m	2	2	1		104.8572	0.971847	5	2	2	3		129.5859	0.851350	14	3	3	2	
70.7747	1.330130	m	3	0	0		105.2953	0.969004	10	3	2	2		140.2544	0.819055	19	2	2	4	
74.5495	1.271850	53	1	0	3		105.5586	0.967310	6	4	0	1		141.8700	0.814983	40	4	2	2	
75.2506	1.261730	61	3	0	1		105.6465	0.966747	6	4	1	0		146.1285	0.805200	1	0	0	5	
75.3382	1.260480	61	3	1	0		108.7089	0.947876	16	1	1	4		147.5203	0.802292	4	3	0	4	
78.9472	1.211660	27	1	1	3		109.3355	0.944188	17	3	0	3		148.6405	0.800052	4	4	0	3	
79.6354	1.202910	48	3	1	1		110.0544	0.940026	37m	3	3	0								

04-012-5563 May 17, 2016 3:02 PM (jbastos)

Status Primary **QM:** Indexed **Pressure/Temperature:** Ambient **Chemical Formula:** Ba0.3 La0.7 Mn O3
Empirical Formula: Ba0.3 La0.7 Mn O3 **Weight %:** Ba17.07 La40.29 Mn22.76 O19.89
Atomic %: Ba6.00 La14.00 Mn20.00 O60.00 **ANX:** ABX3
Compound Name: Barium Lanthanum Manganese Oxide

Radiation: CuKα1 **λ:** 1.5406 Å **d-Spacing:** Calculated **Intensity:** Calculated **I/Ic:** 11.86 **I/Ic - ND:** 0.82

SYS: Cubic **SPGR:** Pm-3m (221)
Author's Cell [AuthCell a: 3.91(5) Å **AuthCell Vol:** 59.78 Å³ **AuthCell Z:** 1.00 **AuthCell MolVol:** 59.78]
Density [Dcalc: 6.705 g/cm³ **Dstruc:** 6.7 g/cm³] **SS/FOM:** F(21) = 999.9(0.0004, 21)
Temp: 293.0 K (Author provided temperature) **R-factor:** 0.056

Space Group: Pm-3m (221) **Molecular Weight:** 241.37
Crystal Data [XtlCell a: 3.910 Å **XtlCell b:** 3.910 Å **XtlCell c:** 3.910 Å **XtlCell α:** 90.00°
XtlCell β: 90.00° **XtlCell γ:** 90.00° **XtlCell Vol:** 59.78 Å³ **XtlCell Z:** 1.00]
Crystal Data Axial Ratio [a/b: 1.000 **c/b:** 1.000]
Reduced Cell [RedCell a: 3.910 Å **RedCell b:** 3.910 Å **RedCell c:** 3.910 Å **RedCell α:** 90.00°
RedCell β: 90.00° **RedCell γ:** 90.00° **RedCell Vol:** 59.78 Å³]

Crystal (Symmetry Allowed): Centrosymmetric

SG Symmetry Operators:

Seq	Operator	Seq	Operator	Seq	Operator	Seq	Operator	Seq	Operator	Seq	Operator	Seq	Operator
1	x,y,z	8	-x,-z,-y	15	z,-x,-y	22	-y,x,z	29	-y,z,-x	36	z,-y,x	43	-x,-z,y
2	-x,-y,-z	9	y,x,z	16	-z,x,y	23	z,-y,-x	30	y,-z,x	37	-x,-y,z	44	x,z,-y
3	z,x,y	10	-y,-x,-z	17	y,-z,-x	24	-z,y,x	31	-x,z,-y	38	x,y,-z	45	-y,-x,z
4	-z,-x,-y	11	z,y,x	18	-y,z,x	25	-x,y,-z	32	x,-z,y	39	-z,-x,y	46	y,x,-z
5	y,z,x	12	-z,-y,-x	19	x,-z,-y	26	x,-y,z	33	-y,x,-z	40	z,x,-y	47	-z,-y,x
6	-y,-z,-x	13	x,-y,-z	20	-x,z,y	27	-z,x,-y	34	y,-x,z	41	-y,-z,x	48	z,y,-x
7	x,z,y	14	-x,y,z	21	y,-x,-z	28	z,-x,y	35	-z,y,-x	42	y,z,-x		

Atomic Coordinates:

Atom	Num	Wyckoff	Symmetry	x	y	z	SOF	IDP	AET
La	1	1a	m-3m	0.0	0.0	0.0	0.7		
Ba	2	1a	m-3m	0.0	0.0	0.0	0.3		
Mn	3	1b	m-3m	0.5	0.5	0.5	1.0		
O	4	3c	4/mm.m	0.5	0.5	0.0	1.0		

Subfile(s): Inorganic **Former PDF's #:** 01-075-7700 **Prototype Structure [Formula Order]:** Ca Ti O3
Prototype Structure [Alpha Order]: Ca O3 Ti **LPF Prototype Structure [Formula Order]:** Ca Ti O3,cP5,221
LPF Prototype Structure [Alpha Order]: Ca O3 Ti,cP5,221 **Pearson Symbol:** cP5.00 **Entry Date:** 09/01/2009
Last Modification Date: 09/01/2011 **Last Modifications:** Reflections

References:

Type	DOI	Reference
Primary Reference		Calculated from LPF using POWD-12++.
Structure		"Synthesis, structural and transport properties of nanocrystalline La1-xBaxMnO3 (0.0 <= x <= 0.3) powders". Nagabhushana B.M., Chandrappa G.T., Sreekanth Chakradhar R.P., Ramesh K.P., Shivakumara C. Solid State Commun. 136, 427,432 (2005).

Database Comments: ANX: ABX3. LPF Collection Code: 1813946. Sample Preparation: Compound Preparation: burned with oxyalyl dihydrazide in furnace heated at 573 K, heated at 1173 K for 6 h. Calculated Pattern Original Remarks: z(O) is assumed to be misprinted as 1/2 instead of 0;in table 1;(agreement with structure type). LPF Editor Comment: editor assigned an approximate value to the La/Ba ratio of site La,Ba based on the nominal composition. Temperature of Data Collection: 293 K. Minor Warning: Minor warning from the LPF Editor exist. Magnitude of e.s.d. on cell dimension is >1000 ppm. Unit Cell Data Source: Powder Diffraction.

d-Spacings (21) - Ba0.3 La0.7 Mn O3 - 04-012-5563 (Stick, Fixed Slit Intensity) - Cu Kα1 1.54056 Å

2θ (°)	d (Å)	I	h	k	l	*	2θ (°)	d (Å)	I	h	k	l	*	2θ (°)	d (Å)	I	h	k	l	*
22.7235	3.910000	145	1	0	0		72.4573	1.303330	27	2	2	1		108.6352	0.948314	16	3	2	2	
32.3537	**2.764790**	999	1	1	0		77.0677	1.236450	104	3	1	0		113.4007	0.921596	53	4	1	1	
39.9022	2.257440	191	1	1	1		81.5943	1.178910	40	3	1	1		118.3449	0.897016	16	3	3	1	
46.4079	**1.955000**	302	2	0	0		86.0687	1.128720	37	2	2	2		123.5317	0.874303	48	4	2	0	
52.2728	1.748610	61	2	1	0		90.5190	1.084440	11	3	2	0		129.0516	0.853232	13	4	2	1	
57.7049	**1.596250**	304	2	1	1		94.9728	1.044990	104	3	2	1		135.0432	0.833615	29	3	3	2	
67.7260	1.382390	139	2	2	0		103.9999	0.977500	16	4	0	0		149.6418	0.798125	42	4	2	2	

04-006-8863 May 17, 2016 3:03 PM (jbastos)

Status Primary **QM:** Indexed **Pressure/Temperature:** Ambient **Chemical Formula:** Ba0.075 La0.925 Mn O3
Empirical Formula: Ba0.075 La0.925 Mn O3 **Weight %:** Ba4.26 La53.16 Mn22.73 O19.86
Atomic %: Ba1.50 La18.50 Mn20.00 O60.00 **ANX:** ABX3
Compound Name: Barium Lanthanum Manganese Oxide

Radiation: CuKα1 **λ:** 1.5406 Å **d-Spacing:** Calculated **Intensity:** Calculated **I/Ic:** 8.01 **I/Ic - ND:** 0.37

SYS: Orthorhombic **SPGR:** Pnma (62)
Author's Cell [AuthCell a: 5.5079(7) Å **AuthCell b:** 7.816(2) Å **AuthCell c:** 5.5516(8) Å
AuthCell Vol: 238.99 Å³ **AuthCell Z:** 4.00 **AuthCell MolVol:** 59.75 **]**
Author's Cell Axial Ratio [c/a: 1.008 **a/b:** 0.705 **c/b:** 0.710 **]**
Density [Dcalc: 6.718 g/cm³ **Dstruc:** 6.72 g/cm³ **]** **SS/FOM:** F(30) = 151.0(0.0057, 35)
Temp: 298.0 K (Ambient temperature assigned by ICDD editor)

Space Group: Pcmn (62) **Molecular Weight:** 241.72
Crystal Data [XtlCell a: 5.552 Å **XtlCell b:** 7.816 Å **XtlCell c:** 5.508 Å **XtlCell α:** 90.00°
XtlCell β: 90.00° **XtlCell γ:** 90.00° **XtlCell Vol:** 238.99 Å³ **XtlCell Z:** 4.00 **]**
Crystal Data Axial Ratio [c/a: 0.992 **a/b:** 0.710 **c/b:** 0.705 **]**
Reduced Cell [RedCell a: 5.508 Å **RedCell b:** 5.552 Å **RedCell c:** 7.816 Å **RedCell α:** 90.00°
RedCell β: 90.00° **RedCell γ:** 90.00° **RedCell Vol:** 238.99 Å³ **]**

Crystal (Symmetry Allowed): Centrosymmetric

SG Symmetry Operators:

Seq	Operator	Seq	Operator	Seq	Operator	Seq	Operator
1	x,y,z	3	x+1/2,-y+1/2,-z+1/2	5	-x,y+1/2,-z	7	-x+1/2,-y,z+1/2
2	-x,-y,-z	4	-x+1/2,y+1/2,z+1/2	6	x,-y+1/2,z	8	x+1/2,y,-z+1/2

Atomic Coordinates:

Atom	Num	Wyckoff	Symmetry	x	y	z	SOF	IDP	AET
La	1	4c	.m.	0.488	0.25	-0.001	0.925		8-b
Mn	2	4a	-1	0.0	0.0	0.0	1.0		6-a
O	3	4c	.m.	0.006	0.25	0.05	1.0		4-a
O	4	8d	1	0.276	-0.039	0.27	1.0		2#a
Ba	5	4c	.m.	0.488	0.25	-0.001	0.075		8-b

Subfile(s): Inorganic **Former PDF's #:** 01-070-5873 **Prototype Structure [Formula Order]:** Gd Fe O3
Prototype Structure [Alpha Order]: Fe Gd O3 **LPF Prototype Structure [Formula Order]:** Gd Fe O3,oP20,62
LPF Prototype Structure [Alpha Order]: Fe Gd O3,oP20,62 **Pearson Symbol:** oP20.00
Entry Date: 09/01/2005 **Last Modification Date:** 09/01/2011 **Last Modifications:** Reflections

References:

Type	DOI	Reference
Primary Reference		Calculated from LPF using POWD-12++.
Structure		"Phase Equilibria in the LaCoO3-LaMnO3-BaCoOz-BaMnO3 System". Cherepanov V.A., Filonova E.A., Voronin V.I., Berger I.F. J. Solid State Chem. 153, 205 (2000).

Database Comments: ANX: ABX3. LPF Collection Code: 1001321. Polymorphism/Phase Transition: orthorhombic. Sample Preparation: STARTING MATERIALS:Mn2O3,La2O3,BaCO3. Compound Preparation: heated at 1123 K for 24 h, 1223 K for 24 h, and then at 1373 K for 120-160 h with intermediate grindings in alcohol, quenched. CRUCIBLE: alumina. ATMOSPHERE: air. Minor Warning: No R factor reported/abstracted. LPF Editor Comment: editor took La/Ba ratio for mixed site from nominal composition. Unit Cell Data Source: Powder Diffraction.

d-Spacings (198) - Ba0.075 La0.925 Mn O3 - 04-006-8863 (Stick, Fixed Slit Intensity) - Cu Kα1 1.54056 Å

2θ (°)	d (Å)	I	h	k	l	*	2θ (°)	d (Å)	I	h	k	l	*	2θ (°)	d (Å)	I	h	k	l	*
19.5974	4.526070	1	0	1	1		47.9251	1.896590	5	2	1	2		61.4026	1.508690	1	0	3	3	
22.7233	3.910030	215m	0	2	0		48.0322	1.892610	4	2	3	0		61.5835	1.504690	1m	0	5	1	
22.7233	3.910030	m	1	0	1		50.6504	1.800750	1	0	1	3		61.5835	1.504690	m	3	1	2	
25.4505	3.496880	9	1	1	1		50.7984	1.795850	1	1	3	2		63.9257	1.455090	1	1	3	3	
32.2219	2.775800	290	0	0	2		50.9345	1.791370	2	2	3	1		64.1026	1.451500	1	1	5	1	
32.3622	**2.764090**	999	1	2	1		52.0947	1.754170	20	1	0	3		64.2384	1.448760	4	3	3	1	
32.4846	**2.753950**	310	2	0	0		52.2783	1.748440	59m	1	4	1		65.2087	1.429530	1	2	2	3	
34.5016	2.597430	3	2	1	0		52.2783	1.748440	m	2	2	2		65.4021	1.425770	1	3	2	2	
36.2084	2.478810	1	1	0	2		52.4500	1.743120	17	3	0	1		67.4210	1.387900	32	0	0	4	
36.3865	2.467080	1	2	0	1		53.4919	1.711600	1	1	1	3		67.7449	1.382050	115	2	4	2	
38.1243	2.358530	8m	0	3	1		53.8411	1.701320	6	3	1	1		68.0284	1.376980	32	4	0	0	
38.1243	2.358530	m	1	1	2		57.5433	1.600350	166	1	2	3		69.0280	1.359460	1	2	5	0	
38.2231	2.352660	4	2	1	1		57.6429	1.597820	108	0	4	2		69.2239	1.356090	2	4	1	0	
39.7995	2.263030	125	0	2	2		57.8759	1.591940	164m	2	4	0		69.8279	1.345830	1	1	0	4	
40.0185	2.251150	125	2	2	0		57.8759	1.591940	m	3	2	1		70.3884	1.336480	1	4	0	1	
41.6207	2.168120	1	1	3	1		59.0225	1.563720	1	2	3	2		71.0093	1.326310	1	1	1	4	
43.1827	2.093240	1	1	2	2		60.1974	1.535980	1m	1	4	2		71.2047	1.323150	1m	1	5	2	
43.3367	2.086160	1	2	2	1		60.1974	1.535980	m	2	0	3		71.2047	1.323150	m	2	3	3	
46.4074	**1.955020**	367m	0	4	0		60.3996	1.531320	1m	2	4	1		71.3725	1.320450	2m	2	5	1	
46.4074	**1.955020**	m	2	0	2		60.3996	1.531320	m	3	0	2		71.3725	1.320450	m	3	3	2	

04-006-8863 May 17, 2016 3:03 PM (jbastos)

2θ (°)	d (Å)	I	h	k	l	*	2θ (°)	d (Å)	I	h	k	l	*	2θ (°)	d (Å)	I	h	k	l	*
72.1661	1.307870	6	0	2	4		91.2097	1.078020	1	1	1	5		110.1116	0.939698	2m	3	7	1	
72.3281	1.305340	13	1	4	3		91.6871	1.073650	1	1	7	1		110.1116	0.939698	m	5	1	3	
72.4567	1.303340	9m	0	6	0		92.0538	1.070330	2	5	1	1		110.7600	0.936012	1	1	6	4	
72.4567	1.303340	m	3	0	3		92.6239	1.065230	1	3	2	4		111.3248	0.932849	1	4	6	1	
72.6233	1.300760	11	3	4	1		92.8702	1.063050	1	4	2	3		112.7118	0.925267	5	0	0	6	
72.7556	1.298720	6	4	2	0		94.5528	1.048520	31	1	2	5		113.0984	0.923199	18	3	2	5	
73.6202	1.285590	2	3	1	3		94.7783	1.046620	34	2	4	4		113.4447	0.921364	29m	2	8	0	
74.5056	1.272490	1	1	2	4		94.8725	1.045830	34	1	6	3		113.4447	0.921364	m	3	6	3	
75.0524	1.264570	1	4	2	1		95.2020	1.043080	44m	3	6	1		113.7110	0.919963	18	5	2	3	
76.8507	1.239400	26	2	0	4		95.2020	1.043080	m	4	4	2		114.0905	0.917983	5	6	0	0	
77.0714	1.236400	90m	1	6	1		95.3998	1.041440	25	5	2	1		114.6278	0.915211	1	4	3	4	
77.0714	1.236400	m	3	2	3		96.2160	1.034760	1	2	7	0		115.3155	0.911717	1	6	1	0	
77.2832	1.233540	28	4	0	2		96.4003	1.033270	1	4	5	0		116.4000	0.906326	1m	1	1	6	
77.9907	1.224110	1	2	1	4		97.5800	1.023900	1	5	0	2		116.4000	0.906326	m	5	4	2	
78.2348	1.220900	1	2	5	2		97.8969	1.021430	1	0	3	5		116.5310	0.905685	1m	0	5	5	
78.4216	1.218460	2m	4	1	2		97.9588	1.020950	1	2	1	5		116.5310	0.905685	m	6	0	1	
78.4216	1.218460	m	4	3	0		98.0932	1.019910	1	1	5	4		117.0526	0.903152	1m	2	7	3	
79.2680	1.207560	1	2	4	3		98.2164	1.018960	1	3	3	4		117.0526	0.903152	m	3	5	4	
79.4469	1.205290	1	3	4	2		98.4404	1.017240	1m	2	7	1		117.2583	0.902162	1m	3	7	2	
80.2111	1.195720	1	1	3	4		98.4404	1.017240	m	4	3	3		117.2583	0.902162	m	4	5	3	
80.3372	1.194160	1	0	5	3		98.6263	1.015820	1m	4	5	1		117.6323	0.900375	3	0	2	6	
80.7454	1.189150	1	4	3	1		98.6263	1.015820	m	5	1	2		118.1513	0.897923	5	2	6	4	
81.3852	1.181410	15	2	2	4		100.1659	1.004310	1	1	3	5		118.6307	0.895686	5	4	6	2	
81.5650	1.179260	8	0	6	2		100.6144	1.001040	1	3	5	3		119.0699	0.893660	3m	1	5	5	
81.7069	1.177570	9	2	6	0		101.0244	0.998082	2	5	3	1		119.0699	0.893660	m	6	2	0	
81.8114	1.176330	15	4	2	2		102.0997	0.990468	1	5	2	2		119.3034	0.892592	1	3	3	5	
82.7260	1.165630	1	3	3	3		103.9987	0.977508	15m	0	8	0		119.9504	0.889665	2	5	3	3	
82.8865	1.163780	1	3	5	1		103.9987	0.977508	m	4	0	4		120.1341	0.888843	2m	1	2	6	
83.8243	1.153130	1	1	6	2		104.9591	0.971183	1	2	5	4		120.1341	0.888843	m	5	5	1	
83.9306	1.151940	1	2	6	1		105.1487	0.969952	1m	2	7	2		121.6266	0.882301	1	6	2	1	
85.8042	1.131520	22	0	4	4		105.1487	0.969952	m	4	1	4		122.8580	0.877087	10	2	0	6	
86.3685	1.125570	22	4	4	0		105.3961	0.968354	1	4	5	2		123.5522	0.874219	30m	2	8	2	
86.9812	1.119210	1	2	3	4		106.1936	0.963270	1	3	4	4		123.5522	0.874219	m	4	4	4	
87.4031	1.114890	2	4	3	2		106.4500	0.961657	1	4	4	3		124.2073	0.871559	9m	2	1	6	
88.0491	1.108370	1	1	4	4		107.0889	0.957681	1	2	3	5		124.2073	0.871559	m	6	0	2	
88.1712	1.107150	1	3	0	4		107.3581	0.956024	1	0	7	3		125.2872	0.867271	1	4	7	0	
88.4176	1.104700	1	4	0	3		108.2088	0.950861	5	1	4	5		125.5642	0.866190	2m	6	1	2	
88.5764	1.103130	1	4	4	1		108.3374	0.950090	5m	0	6	4		125.5642	0.866190	m	6	3	0	
89.2841	1.096210	1m	2	5	3		108.3374	0.950090	m	3	0	5		126.4373	0.862834	1	5	0	4	
89.2841	1.096210	m	3	1	4		108.7120	0.947858	6m	1	8	1		126.8726	0.861189	1	1	3	6	
89.4455	1.094650	1m	0	7	1		108.7120	0.947858	m	4	2	4		127.2038	0.859950	1	2	5	5	
89.4455	1.094650	m	4	1	3		108.9748	0.946304	5m	4	6	0		127.8334	0.857624	1m	0	9	1	
90.0969	1.088420	4	1	0	5		108.9748	0.946304	m	5	0	3		127.8334	0.857624	m	5	1	4	
90.5595	1.084060	13m	2	6	2		109.0991	0.945573	4	5	4	1		128.3351	0.855798	3m	2	2	6	
90.5595	1.084060	m	3	4	3		109.5139	0.943148	1	3	1	5		128.3351	0.855798	m	6	3	1	
90.9404	1.080510	2	5	0	1		109.7222	0.941940	1	1	7	3		128.7123	0.854441	4	3	4	5	

04-015-3539 May 17, 2016 3:01 PM (jbastos)

Status Primary **QM:** Indexed **Pressure/Temperature:** Ambient **Chemical Formula:** Ba Ti O2.67
Empirical Formula: Ba O2.67 Ti **Weight %:** Ba60.25 O18.74 Ti21.01 **Atomic %:** Ba21.41 O57.17 Ti21.41
ANX: AB2C3X8 **Compound Name:** Barium Titanium Oxide

Radiation: CuKα1 **λ:** 1.5406 Å **d-Spacing:** Calculated **Intensity:** Calculated **I/Ic:** 5.84 **I/Ic - ND:** 0.45

SYS: Hexagonal **SPGR:** P3m1 (156)
Author's Cell [AuthCell a: 5.7 Å **AuthCell c:** 7 Å **AuthCell Vol:** 196.96 Å³ **AuthCell Z:** 3.00
AuthCell MolVol: 65.65] **Author's Cell Axial Ratio [c/a:** 1.228]
Density [Dcalc: 5.765 g/cm³ **Dstruc:** 5.76 g/cm³] **SS/FOM:** F(30) = 782.1(0.0012, 33)
Temp: 298.0 K (Ambient temperature assigned by ICDD editor)

Space Group: P3m1 (156) **Molecular Weight:** 227.95
Crystal Data [XtlCell a: 5.700 Å **XtlCell b:** 5.700 Å **XtlCell c:** 7.000 Å **XtlCell α:** 90.00°
XtlCell β: 90.00° **XtlCell γ:** 120.00° **XtlCell Vol:** 196.96 Å³ **XtlCell Z:** 3.00]
Crystal Data Axial Ratio [c/a: 1.228 **a/b:** 1.000 **c/b:** 1.228]
Reduced Cell [RedCell a: 5.700 Å **RedCell b:** 5.700 Å **RedCell c:** 7.000 Å **RedCell α:** 90.00°
RedCell β: 90.00° **RedCell γ:** 120.00° **RedCell Vol:** 196.96 Å³]

Crystal (Symmetry Allowed): Centrosymmetric

SG Symmetry Operators:

Seq	Operator	Seq	Operator	Seq	Operator	Seq	Operator	Seq	Operator	Seq	Operator
1	x,y,z	2	-y,x-y,z	3	-x+y,-x,z	4	-y,-x,z	5	x,x-y,z	6	-x+y,y,z

Atomic Coordinates:

Atom	Num	Wyckoff	Symmetry	x	y	z	SOF	IDP	AET
Ba	1	1a	3m.	0.0	0.0	0.0	1.0		
Ba	2	1b	3m.	0.33333	0.66666	0.66666	1.0		
Ba	3	1c	3m.	0.66666	0.33333	0.33333	1.0		
Ti	4	1a	3m.	0.0	0.0	0.5	1.0		
Ti	5	1b	3m.	0.33333	0.66666	0.16666	1.0		
Ti	6	1c	3m.	0.66666	0.33333	0.83333	1.0		
O	7	3d	.m.	0.5	0.0	0.0	1.0		
O	8	3d	.m.	0.83333	0.66666	0.66666	1.0		
O	9	3d	.m.	0.16666	0.33333	0.33333	0.667		

Subfile(s): Inorganic **Former PDF's #:** 01-073-7322
LPF Prototype Structure [Formula Order]: Ba Ti O2.67,hP15,156
LPF Prototype Structure [Alpha Order]: Ba O2.67 Ti,hP15,156 **Pearson Symbol:** hP14.01
Entry Date: 09/01/2011

References:

Type	DOI	Reference
Primary Reference		Calculated from LPF using POWD-12++.
Structure		"Vacancy ordering in reduced barium titanate". Woodward D.I., Reaney I.M., Yang G.Y., Dickey E.C., Randall C.A. Appl. Phys. Lett. 84, 4650,4652 (2004).

Database Comments: ANX: AB2C3X8. LPF Collection Code: 1815490. Sample Preparation: Compound Preparation: multilayer ceramic capacitor were fabricated, fired at 1573 K under reduced oxygen atmosphere, annealed at 1073 K, heated at 568 K under an electric field of 103 kV·mm-1. Minor Warning: No R factors reported/abstracted. No e.s.d reported/abstracted on the cell dimension. Unit Cell Data Source: Powder Diffraction.

d-Spacings (85) - Ba Ti O2.67 - 04-015-3539 (Stick, Fixed Slit Intensity) - Cu Kα1 1.54056 Å

2θ (°)	d (Å)	I	h	k	l	*	2θ (°)	d (Å)	I	h	k	l	*	2θ (°)	d (Å)	I	h	k	l	*
12.6352	7.000000	4	0	0	1		57.4867	1.601790	1	0	3	1		85.4418	1.135390	1	0	1	6	
17.9546	4.936340	1	1	0	0		62.1977	1.491300	1	1	1	4		86.9239	1.119800	11	1	2	5	
22.0153	4.034150	299	1	0	1		62.2998	1.489100	1	3	0	2		87.1047	1.117940	11	3	2	1	
25.4275	3.500000	1	0	0	2		63.8227	1.457190	1	1	2	3		88.3874	1.105000	1	2	2	4	
31.3031	**2.855150**	997	0	1	2		65.3088	1.427580	115	0	2	4		91.0278	1.079700	46	1	1	6	
31.3611	**2.850000**	999	1	1	0		65.4418	1.425000	114	2	2	0		91.1783	1.078310	59	1	3	4	
33.9334	2.639610	1	1	1	1		66.9584	1.396360	1	2	2	1		91.2684	1.077480	83m	2	3	2	
36.3699	2.468170	1	2	0	0		68.4741	1.369100	1	3	1	0		91.2684	1.077480	m	4	1	0	
38.5522	2.333330	108	0	0	3		69.7656	1.346880	14	0	1	5		93.8202	1.054770	1	0	2	6	
38.6489	2.327710	249	0	2	1		69.8940	1.344720	31	0	3	3		96.8657	1.029540	1	1	4	2	
40.7966	2.209990	1	1	1	2		69.9583	1.343640	30	1	3	1		99.5932	1.008540	24	4	0	4	
42.8325	2.109540	1	0	1	3		71.4131	1.319800	1	2	2	2		100.9425	0.998671	1	2	2	5	
44.9004	**2.017070**	447	2	0	2		74.2389	1.276400	94	2	1	4		103.6128	0.980092	4	1	0	7	
48.7681	1.865760	1	2	1	0		74.3328	1.275020	94	3	1	2		103.7993	0.978840	10	3	1	5	
50.5098	1.805430	75	1	1	3		77.2424	1.234090	1	4	0	0		103.9236	0.978009	17m	0	5	1	
50.5881	1.802820	75	2	1	1		78.4768	1.217740	22	2	0	5		103.9236	0.978009	m	4	1	3	
52.2282	1.750000	1	0	0	4		78.6000	1.216140	43m	2	2	3		108.0666	0.951717	30	0	3	6	
54.0381	1.695580	1	0	2	3		78.6000	1.216140	m	4	0	1		108.2253	0.950762	35	3	2	4	
55.6795	1.649420	149	1	0	4		81.4336	1.180830	1	3	1	3		108.3207	0.950190	32m	3	3	0	
55.7891	1.646440	320m	1	2	2		82.6361	1.166670	16	0	0	6		108.3207	0.950190	m	5	0	2	
55.7891	1.646440	m	3	0	0		82.8795	1.163860	43	0	4	2		111.3191	0.932881	1	4	2	0	

04-015-3539 May 17, 2016 3:01 PM (jbastos)

2θ (°)	d (Å)	I	h	k	l	*	2θ (°)	d (Å)	I	h	k	l	*	2θ (°)	d (Å)	I	h	k	l	*
112.4240	0.926819	7	0	2	7		122.2675	0.879567	10	5	1	1		138.6807	0.823219	m	6	0	0	
112.6199	0.925761	8	0	4	5		123.3620	0.875000	1	0	0	8		142.8546	0.812600	1	2	3	6	
112.8163	0.924706	13	2	4	1		125.5573	0.866217	1	2	4	3		145.0590	0.807530	5	1	3	7	
117.1432	0.902715	36	2	2	6		126.7716	0.861569	11	0	1	8		145.3767	0.806829	3	5	0	5	
117.4148	0.901412	36	4	2	2		127.3388	0.859448	25	1	5	2		145.6965	0.806131	5	4	3	1	
120.6408	0.886594	1	5	1	0		130.6178	0.847791	1	4	0	6		148.2137	0.800895	1	0	6	2	
121.8402	0.881385	6	2	1	7		138.1351	0.824709	16	2	0	8								
122.0537	0.880474	8	2	3	5		138.6807	0.823219	33m	2	4	4								

Bibliography

[1] R. Vonhelmolt, J. Wecker, B. Holzapfel, L. Schultz, and K. Samwer. Giant negative magnetoresistance in perovskitelike $la_{2/3}ba_{1/3}mno_x$ ferromagnetic-films. *Physical Review Letters*, 71(14):2331–2333, 1993.

[2] V. Laukhin, V. Skumryev, X. Marti, D. Hrabovsky, F. Sanchez, M. V. Garcia-Cuenca, C. Ferrater, M. Varela, U. Lueders, J. F. Bobo, and J. Fontcuberta. Electric-field control of exchange bias in multiferroic epitaxial heterostructures. *Physical Review Letters*, 97(22):227201, 2006.

[3] Martin Weisheit, Sebastian Faehler, Alain Marty, Yves Souche, Christiane Poinsignon, and Dominique Givord. Electric field-induced modification of magnetism in thin-film ferromagnets. *Science*, 315(5810):349–351, 2007.

[4] D. Chiba, M. Sawicki, Y. Nishitani, Y. Nakatani, F. Matsukura, and H. Ohno. Magnetization vector manipulation by electric fields. *Nature*, 455(7212):515–518, 2008.

[5] Chun-Gang Duan, Julian P. Velev, R. F. Sabirianov, W. N. Mei, S. S. Jaswal, and E. Y. Tsymbal. Tailoring magnetic anisotropy at the ferromagnetic/ferroelectric interface. *Applied Physics Letters*, 92(12):122905, 2008.

[6] T. Maruyama, Y. Shiota, T. Nozaki, K. Ohta, N. Toda, M. Mizuguchi, A. A. Tulapurkar, T. Shinjo, M. Shiraishi, S. Mizukami, Y. Ando, and Y. Suzuki. Large voltage-induced magnetic anisotropy change in a few atomic layers of iron. *Nature Nanotechnology*, 4(3):158–161, 2009.

[7] P. Borisov, A. Hochstrat, X. Chen, W. Kleemann, and C. Binek. Magnetoelectric switching of exchange bias. *Physical Review Letters*, 94(11):117203, 2005.

[8] D. V. Efremov, J. Van den Brink, and D. I. Khomskii. Bond-versus site-centred ordering and possible ferroelectricity in manganites. *Nature Materials*, 3(12):853–856, 2004.

[9] Evgeny Y. Tsymbal and Hermann Kohlstedt. Applied physics - tunneling across a ferroelectric. *Science*, 313(5784):181–183, 2006.

[10] Julian P. Velev, Chun-Gang Duan, J. D. Burton, Alexander Smogunov, Manish K. Niranjan, Erio Tosatti, S. S. Jaswal, and Evgeny Y. Tsymbal. Magnetic tunnel junctions with ferroelectric barriers: Prediction of four resistance states from first principles. *Nano Letters*, 9(1):427–432, 2009.

[11] K. Dorr. Ferromagnetic manganites: spin-polarized conduction versus competing interactions. *Journal of Physics D-Applied Physics*, 39(7):R125–R150, 2006.

[12] K. H. Ahn, T. Lookman, and A. R. Bishop. Strain-induced metal-insulator phase coexistence in perovskite manganites. *Nature*, 428(6981):401–404, 2004.

[13] H. L. Ju, K. M. Krishnan, and D. Lederman. Evolution of strain-dependent transport properties in ultrathin $la_{0.67}sr_{0.33}mno_3$ films. *Journal of Applied Physics*, 83(11):7073–7075, 1998.

[14] P. Murugavel, J. H. Lee, J. G. Yoon, T. W. Noh, J. S. Chung, M. Heu, and S. Yoon. Origin of metal-insulator transition temperature enhancement in underdoped lanthanum manganite films. *Applied Physics Letters*, 82(12):1908–1910, 2003.

[15] O. I. Lebedev, G. Van Tendeloo, S. Amelinckx, B. Leibold, and H. U. Habermeier. Structure and microstructure of la1-xcaxmno3-delta thin films prepared by pulsed laser deposition. *Physical Review B*, 58(12):8065–8074, 1998.

[16] A. Biswas, M. Rajeswari, R. C. Srivastava, Y. H. Li, T. Venkatesan, R. L. Greene, and A. J. Millis. Two-phase behavior in strained thin films of hole-doped manganites. *Physical Review B*, 61(14):9665–9668, 2000.

[17] E. Dagotto. Complexity in strongly correlated electronic systems. *Science*, 309(5732):257–262, 2005.

[18] Evgeny Y. Tsymbal, Elbio R. A. Dagotto, Chang-Beom Eom, and Ramamoorthy Ramesh. *A brief introduction to strongly correlated electronic materials*. OUP Oxford, 2012.

[19] T. V. Ramakrishnan. Strongly correlated electrons in solids. *Current Science*, 95(9):1284–1309, 2008.

[20] R. Ramesh and Nicola A. Spaldin. Multiferroics: progress and prospects in thin films. *Nature Materials*, 6(1):21–29, 2007.

[21] H. Schmid. Magnetic ferroelectric materials. *Bulletin of Materials Science*, 17(7):1411–1414, 1994.

[22] M. Fiebig. Revival of the magnetoelectric effect. *Journal of Physics D-Applied Physics*, 38(8):R123–R152, 2005.

[23] W. Eerenstein, N. D. Mathur, and J. F. Scott. Multiferroic and magnetoelectric materials. *Nature*, 442(7104):759–765, 2006.

[24] R. E. Cohen. Origin of ferroelectricity in perovskite oxides. *Nature*, 358(6382):136–138, 1992.

[25] L. W. Martin and R. Ramesh. Overview no. 151 multiferroic and magnetoelectric heterostructures. *Acta Materialia*, 60(6-7):2449–2470, 2012.

[26] L. W. Martin, S. P. Crane, Y. H. Chu, M. B. Holcomb, M. Gajek, M. Huijben, C. H. Yang, N. Balke, and R. Ramesh. Multiferroics and magnetoelectrics: thin films and nanostructures. *Journal of Physics-Condensed Matter*, 20(43):434220, 2008.

[27] John B Goodenough. *Magnetism and the Chemical Bond*, volume Volume 1 of Interscience monographs on chemistry. Inorganic chemistry section. R. E. Krieger Publishing Company, reprint edition, 1976.

[28] V. M. Goldschmidt. The laws of crystal chemistry. *Naturwissenschaften*, 14:477–485, 1926.

[29] G. H. Jonker and J. H. Vansanten. Ferromagnetic compounds of manganese with perovskite structure. *Physica*, 16(3):337–349, 1950.

[30] C. A. Randall, A. S. Bhalla, T. R. Shrout, and L. E. Cross. Classification and consequences of complex lead perovskite ferroelectrics with regard to b-site cation order. *Journal of Materials Research*, 5(4):829–834, 1990.

[31] A. M. Haghiri-Gosnet and J. P. Renard. Cmr manganites: physics, thin films and devices. *Journal of Physics D-Applied Physics*, 36(8):R127–R150, 2003.

[32] J. M. D. Coey, M. Viret, and S. von Molnar. Mixed-valence manganites. *Advances in Physics*, 48(2):167–293, 1999.

[33] H. Y. Hwang, S. W. Cheong, N. P. Ong, and B. Batlogg. Spin-polarized intergrain tunneling in $la_{2/3}sr_{1/3}mno_3$. *Physical Review Letters*, 77(10):2041–2044, 1996.

[34] Richard J. D. Tilley. *Defects in Solids: Volume 4 of Special Topics in Inorganic Chemistry*. John Wiley & Sons, 2008.

[35] J. M. D. Coey. *Magnetism and Magnetic Materials*. Cambridge University Press, illustrated, reprint edition, 2010.

[36] B. D. Cullity. *Introduction to magnetic materials*. Wiley, 2, illustrated edition, 2009.

[37] Stephen Blundell. *Magnetism in Condensed Matter*. OUP Oxford, 2001.

[38] N. Cusak. *The Electrical and Magnetic Properties of Solids: An Introductory Textbook*. Textbook Publishers, 2003.

[39] Y. Tokura. *Colossal Magnetoresistive Oxides*. Advances in Condensed Matter Science. CRC Press, illustrated edition, 2000.

[40] T. Hotta, S. Yunoki, M. Mayr, and E. Dagotto. A-type antiferromagnetic and c-type orbital-ordered states in lamno$_3$ using cooperative jahn-teller phonons. *Physical Review B*, 60(22):15009–15012, 1999.

[41] E. O. Wollan and W. C. Koehler. Neutron diffraction study of the magnetic properties of the series of perovskite-type compounds (1-x)la,xca mno$_3$. *Physical Review*, 100(2):545–563, 1955.

[42] C. Zener. Interaction between the d-shells in the transition metals .2. ferromagnetic compounds of manganese with perovskite structure. *Physical Review*, 82(3):403–405, 1951.

[43] P. W. Anderson and H. Hasegawa. Considerations on double exchange. *Physical Review*, 100(2):675–681, 1955.

[44] J. Hemberger, A. Krimmel, T. Kurz, H. A. K. von Nidda, V. Y. Ivanov, A. A. Mukhin, A. M. Balbashov, and A. Loidl. Structural, magnetic, and electrical properties of single-crystalline la$_{1-x}$sr$_x$mno$_3$ ($0.4 < x < 0.85$). *Physical Review B*, 66(9), 2002.

[45] A. J. Millis, P. B. Littlewood, and B. I. Shraiman. Double exchange alone does not explain the resistivity of la$_{1-x}$sr$_x$mno$_3$. *Physical Review Letters*, 74(25):5144–5147, 1995.

[46] J. B. Goodenough. Theory of the role of covalence in the perovskite-type manganites la,m(ii) mno$_3$. *Physical Review*, 100(2):564–573, 1955.

[47] P. G. Degennes. Effects of double exchange in magnetic crystals. *Physical Review*, 118(1):141–154, 1960.

[48] Y. Tokura and Y. Tomioka. Colossal magnetoresistive manganites. *Journal of Magnetism and Magnetic Materials*, 200(1-3):1–23, 1999.

[49] M. Ziese. Extrinsic magnetotransport phenomena in ferromagnetic oxides. *Reports on Progress in Physics*, 65(2):143–249, 2002.

[50] T. Okuda, Y. Tomioka, A. Asamitsu, and Y. Tokura. Low-temperature properties of $la_{1-x}ca_xmno_3$ single crystals: comparison with $la_{1-x}sr_xmno_3$. *Physical Review B*, 61(12):8009–8015, 2000.

[51] J. P. Renard and A. Anane. Experimental studies of colossal magnetoresistance manganites: effects of oxygen non-stoichiometry, mn-55 nuclear magnetic resonance, slow relaxation near the metal-insulator phase transition. *Materials Science and Engineering B-Solid State Materials for Advanced Technology*, 63(1-2):22–29, 1999.

[52] P. Curie. Sur la possibilité d'existence de la conductibilité magnétique et du magnétisme libre. page 415, 1894.

[53] P. Debye. Remark to some new trials on a magneto-electrical direct effect. *Zeitschrift Fur Physik*, 36(4):300–301, 1926.

[54] L.D. Landau and E.M. Lifshitz. *The Classical Theory of Fields*, volume 2. Butterworth Heinemann, 1975.

[55] Craig J. Fennie and Karin M. Rabe. Magnetic and electric phase control in epitaxial $eutio_3$ from first principles. *Physical Review Letters*, 97(26):267602, 2006.

[56] W. Eerenstein, M. Wiora, J. L. Prieto, J. F. Scott, and N. D. Mathur. Giant sharp and persistent converse magnetoelectric effects in multiferroic epitaxial heterostructures. *Nature Materials*, 6(5):348–351, 2007.

[57] Chun-Gang Duan, Ce-Wen Nan, S. S. Jaswal, and E. Y. Tsymbal. Universality of the surface magnetoelectric effect in half-metals. *Physical Review B*, 79(14):140403, 2009.

[58] James M. Rondinelli, Massimiliano Stengel, and Nicola A. Spaldin. Carrier-mediated magnetoelectricity in complex oxide heterostructures. *Nature Nanotechnology*, 3(1):46–50, 2008.

[59] J. D. Burton and E. Y. Tsymbal. Prediction of electrically induced magnetic reconstruction at the manganite/ferroelectric interface. *Physical Review B*, 80(17):174406, 2009.

[60] E. Dagotto, T. Hotta, and A. Moreo. Colossal magnetoresistant materials: The key role of phase separation. *Physics Reports-Review Section of Physics Letters*, 344(1-3):1–153, 2001.

[61] M. E. Lines and A. M. Glass. *Principles and Applications of Ferroelectrics and Related Materials*. OUP Oxford, illustrated, reprint edition, 2001.

[62] Kwan-Chi Kao. *Dielectric Phenomena in Solids: With Emphasis on Physical Concepts of Electronic Processes,*. Referex Engineering. Academic Press, 2004.

[63] Y. M. Shkel and D. J. Klingenberg. Material parameters for electrostriction. *Journal of Applied Physics*, 80(8):4566–4572, 1996.

[64] Neil W. Ashcroft and N. David Mermin. *Solid state physics*. Holt-Saunders International Editions: Science : Physics. Saunders College, 1976.

[65] D. Damjanovic. Ferroelectric, dielectric and piezoelectric properties of ferroelectric thin films and ceramics. *Reports on Progress in Physics*, 61(9):1267–1324, 1998.

[66] Standards on piezoelectric crystals, 1949. *Proceedings of the Institute of Radio Engineers*, 37(12):1378–1395, 1949.

[67] C. Adamo, X. Ke, H. Q. Wang, H. L. Xin, T. Heeg, M. E. Hawley, W. Zander, J. Schubert, P. Schiffer, D. A. Muller, L. Maritato, and D. G. Schlom. Effect of biaxial strain on the electrical and magnetic properties of (001) $la_{0.7}sr_{0.3}mno_3$ thin films. *Applied Physics Letters*, 95(11):112504, 2009.

[68] F. Tsui, M. C. Smoak, T. K. Nath, and C. B. Eom. Strain-dependent magnetic phase diagram of epitaxial $la_{0.67}sr_{0.33}mno_3$ thin films. *Applied Physics Letters*, 76(17):2421–2423, 2000.

[69] M. Ziese, H. C. Semmelhack, and K. H. Han. Strain-induced orbital ordering in thin $la_{0.70}ca_{0.30}mno_3$ films on $srtio_3$. *Physical Review B*, 68(13):134444, 2003.

[70] M. Bibes, L. Balcells, S. Valencia, J. Fontcuberta, M. Wojcik, E. Jedryka, and S. Nadolski. Nanoscale multiphase separation at $la_{2/3}ca_{1/3}mno_3/srtio_3$ interfaces. *Physical Review Letters*, 87(6):672101–672104, 2001.

[71] A. Tebano, A. Orsini, P. G. Medaglia, D. Di Castro, G. Balestrino, B. Freelon, A. Bostwick, Young Jun Chang, G. Gaines, E. Rotenberg, and N. L. Saini. Preferential occupation of interface bands in $la_{2/3}sr_{1/3}mno_3$ films as seen via angle-resolved photoemission. *Physical Review B*, 82(21):214407, 2010.

[72] Marie-Bernadette Lepetit, Bernard Mercey, and Charles Simon. Interface effects in perovskite thin films. *Physical Review Letters*, 108(8):087202, 2012.

[73] A. Biswas, M. Rajeswari, R. C. Srivastava, T. Venkatesan, R. L. Greene, Q. Lu, A. L. de Lozanne, and A. J. Millis. Strain-driven charge-ordered state in $la_{0.67}ca_{0.33}mno_3$. *Physical Review B*, 63(18):1844241–1844247, 2001.

[74] M. Huijben, L. W. Martin, Y. H. Chu, M. B. Holcomb, P. Yu, G. Rijnders, D. H. A. Blank, and R. Ramesh. Critical thickness and orbital ordering in ultrathin $la_{0.7}sr_{0.3}mno_3$ films. *Physical Review B*, 78(9):094413, 2008.

[75] A. Tebano, C. Aruta, S. Sanna, P. G. Medaglia, G. Balestrino, A. A. Sidorenko, R. De Renzi, G. Ghiringhelli, L. Braicovich, V. Bisogni, and N. B. Brookes. Evidence of orbital reconstruction at interfaces in ultrathin $la_{0.67}sr_{0.33}mno_3$ films. *Physical Review Letters*, 100(13):137401, 2008.

[76] Rajesh V. Chopdekar, Elke Arenholz, and Y. Suzuki. Orientation and thickness dependence of magnetization at the interfaces of highly spin-polarized manganite thin films. *Physical Review B*, 79(10):104417, 2009.

[77] M. Avellaneda and G. Harshe. Magnetoelectric effect in piezoelectric magnetostrictive multilayer (2-2) composites. *Journal of Intelligent Material Systems and Structures*, 5(4):501–513, 1994.

[78] G. Srinivasan, E. T. Rasmussen, B. J. Levin, and R. Hayes. Magnetoelectric effects in bilayers and multilayers of magnetostrictive and piezoelectric perovskite oxides. *Physical Review B*, 65(13):1344021–1344027, 2002.

[79] P. Murugavel, M. P. Singh, W. Prellier, B. Mercey, C. Simon, and B. Raveau. The role of ferroelectric-ferromagnetic layers on the properties of superlattice-based multiferroics. *Journal of Applied Physics*, 97(10):103914, 2005.

[80] M. I. Bichurin, V. M. Petrov, and G. Srinivasan. Theory of low-frequency magnetoelectric coupling in magnetostrictive-piezoelectric bilayers. *Physical Review B*, 68(5):13, 2003.

[81] C. Binek and B. Doudin. Magnetoelectronics with magnetoelectrics. *Journal of Physics-Condensed Matter*, 17(2):L39–L44, 2005.

[82] S. A. Wolf, D. D. Awschalom, R. A. Buhrman, J. M. Daughton, S. von Molnar, M. L. Roukes, A. Y. Chtchelkanova, and D. M. Treger. Spintronics: A spin-based electronics vision for the future. *Science*, 294(5546):1488–1495, 2001.

[83] Teruya Shinjo. *Nanomagnetism and Spintronics*. Oxford: Elsevier, 2009.

[84] Sang-Wook Cheong and Maxim Mostovoy. Multiferroics: a magnetic twist for ferroelectricity. *Nature Materials*, 6(1):13–20, 2007.

[85] Silvia Picozzi and Claude Ederer. First principles studies of multiferroic materials. *Journal of Physics-Condensed Matter*, 21(30):303201, 2009.

[86] A. Vailionis, H. Boschker, W. Siemons, E. P. Houwman, D. H. A. Blank, G. Rijnders, and G. Koster. Misfit strain accommodation in epitaxial abo$_3$ perovskites: Lattice rotations and lattice modulations. *Physical Review B*, 83(6):064101, 2011.

[87] Darrell G. Schlom, Long-Qing Chen, Chang-Beom Eom, Karin M. Rabe, Stephen K. Streiffer, and Jean-Marc Triscone. Strain tuning of ferroelectric thin films. *Annual Review of Materials Research*, 37:589–626, 2007.

[88] L. F. Mattheiss, E. M. Gyorgy, and D. W. Johnson. Superconductivity above 20 k in the ba-k-bi-o system. *Physical Review B*, 37(7):3745–3746, 1988.

[89] Y. Moritomo, A. Asamitsu, H. Kuwahara, and Y. Tokura. Giant magnetoresistance of manganese oxides with a layered perovskite structure. *Nature*, 380(6570):141–144, 1996.

[90] S. Ishihara, T. Hatakeyama, and S. Maekawa. Magnetic ordering, orbital ordering, and resonant x-ray scattering in perovskite titanates. *Physical Review B*, 65(6):644421–644429, 2002.

[91] H. L. Ju, J. Gopalakrishnan, J. L. Peng, Q. Li, G. C. Xiong, T. Venkatesan, and R. L. Greene. Dependence of giant magnetoresistance on oxygen stoichiometry and magnetization in polycrystalline $la_{0.67}ba_{0.33}mno_z$. *Physical Review B*, 51(9):6143–6146, 1995.

[92] W. Prellier, M. P. Singh, and P. Murugavel. The single-phase multiferroic oxides: from bulk to thin film (vol 17, pg 803, 2005). *Journal of Physics-Condensed Matter*, 17(48):7753–7753, 2005.

[93] C. N. R. Rao, A. Arulraj, A. K. Cheetham, and B. Raveau. Charge ordering in the rare earth manganates: the experimental situation. *Journal of Physics-Condensed Matter*, 12(7):R83–R106, 2000.

[94] R. P. Borges, W. Guichard, J. G. Lunney, J. M. D. Coey, and F. Ott. Magnetic and electric "dead" layers in $(la_{0.7}sr_{0.3})mno_3$ thin films. *Journal of Applied Physics*, 89(7):3868–3873, 2001.

[95] J. Dho, N. H. Hur, I. S. Kim, and Y. K. Park. Oxygen pressure and thickness dependent lattice strain in $la_{0.7}sr_{0.3}mno_3$ films. *Journal of Applied Physics*, 94(12):7670–7674, 2003.

[96] M. Belmeguenai, S. Mercone, C. Adamo, P. Moch, D. G. Schlom, and P. Monod. Structural and magnetic properties of $la_{0.7}sr_{0.3}mno_3$ thin films integrated onto si(100) substrates with $srtio_3$ as buffer layer. *Journal of Applied Physics*, 109(7):07C120, 2011.

[97] I. C. Infante, F. Sanchez, J. Fontcuberta, M. Wojcik, E. Jedryka, S. Estrade, F. Peiro, J. Arbiol, V. Laukhin, and J. P. Espinos. Elastic and orbital effects on thickness-dependent properties of manganite thin films. *Physical Review B*, 76(22):224415, 2007.

[98] I. C. Infante, F. Sanchez, J. Fontcuberta, S. Fusil, K. Bouzehouane, G. Herranz, A. Barthelemy, S. Estrade, J. Arbiol, F. Peiro, R. J. O. Mossanek, M. Abbate, and M. Wojcik. Structural and functional characterization of (110)-oriented epitaxial $la_{2/3}ca_{1/3}mno_3$ electrodes and $srtio_3$ tunnel barriers. *Journal of Applied Physics*, 101(9), 2007.

[99] Y. S. Du, B. Wang, T. Li, D. B. Yu, and H. Yan. Effects of annealing procedures on the structural and magnetic properties of epitaxial $la_{0.7}sr_{0.3}mno_3$ films. *Journal of Magnetism and Magnetic Materials*, 297(2):88–92, 2006.

[100] A. J. Millis, T. Darling, and A. Migliori. Quantifying strain dependence in "colossal" magnetoresistance manganites. *Journal of Applied Physics*, 83(3):1588–1591, 1998.

[101] J. Z. Sun, D. W. Abraham, R. A. Rao, and C. B. Eom. Thickness-dependent magnetotransport in ultrathin manganite films. *Applied Physics Letters*, 74(20):3017–3019, 1999.

[102] D. Varshney, E. Khan, and D. Choudhary. Interpretation of temperature-dependent thermoelectric power behaviour of la0.67ba0.33mno3manganites. *Molecular Physics*, 112(24):3183–3188, 2014.

[103] N. Moutis, I. Panagiotopoulos, M. Pissas, and D. Niarchos. Structural and magnetic properties of $la_{0.67}(ba_xca_{1-x})_{0.33})mno_3$ perovskites (o <= x <= 1). *Physical Review B*, 59(2):1129–1133, 1999.

[104] P. G. Radaelli, G. Iannone, M. Marezio, H. Y. Hwang, S. W. Cheong, J. D. Jorgensen, and D. N. Argyriou. Structural effects on the magnetic and transport properties of perovskite $a_{1-x}a_xmno_3$ (x=0.25, 0.30). *Physical Review B*, 56(13):8265–8276, 1997.

[105] B. Raveau, C. Martin, A. Maignan, and M. Hervieu. Insulator-metal like transition in air-synthesized mn^{4+}-rich $la_{1-x}ba_xmno_3$: grain boundary phase effect. *Journal of Physics-Condensed Matter*, 14(6):1297–1306, 2002.

[106] J. Zhang, H. Tanaka, T. Kanki, J. H. Choi, and T. Kawai. Strain effect and the phase diagram of $la_{1-x}ba_xmno_3$ thin films. *Physical Review B*, 64(18):6275–6279, 2001.

[107] A. Barnabe, F. Millange, A. Maignan, M. Hervieu, B. Raveau, G. Van Tendeloo, and P. Laffez. Barium-based manganites $ln_{1-x}ba_xmno_3$ with ln = Pr, La: Phase transitions and magnetoresistance properties. *Chemistry of Materials*, 10(1):252–259, 1998.

[108] K. Koch, R. O. Kuzian, K. Koepernik, I. V. Kondakova, and H. Rosner. Analysis of the electric field gradient in the perovskites $srtio_3$ and $batio_3$: Density functional and model calculations. *Physical Review B*, 80(12), 2009.

[109] M. M. Vijatovic, J. D. Bobic, and B. A. Stojanovic. History and challenges of barium titanate: Part i. *Science of Sintering*, 40(2):155–165, 2008.

[110] B. Dabrowski, S. Kolesnik, A. Baszczuk, O. Chmaissem, T. Maxwell, and J. Mais. Structural, transport, and magnetic properties of $rmno_3$ perovskites (r = la, pr, nd, sm, eu-153, dy). *Journal of Solid State Chemistry*, 178(3):629–637, 2005.

[111] I. Fina, N. Dix, J. M. Rebled, P. Gemeiner, X. Marti, F. Peiro, B. Dkhil, F. Sanchez, L. Fabrega, and J. Fontcuberta. The direct magnetoelectric effect in ferroelectric-ferromagnetic epitaxial heterostructures. *Nanoscale*, 5(17):8037–8044, 2013.

[112] Fabio Gabriel Nazario Figueiras. *Study of multiferroic materials*. Thesis, 2011.

[113] H. Bea, M. Gajek, M. Bibes, and A. Barthelemy. Spintronics with multiferroics. *Journal of Physics-Condensed Matter*, 20(43), 2008.

[114] Rakesh Dhama, Chiranjib ayek, Ch Thirmal, and P. Murugavel. Enhanced magnetic properties in low doped la $la_{1-x}ba_xmno_3$+delta (x=0, 0.1 and 0.2) nanoparticles. *Journal of Magnetism and Magnetic Materials*, 364:125–128, 2014.

[115] D A Mota, Y. Romaguera Barcelay, A M R Senos, C M Fernandes, P B Tavares, I T Gomes, P Sá, L Fernandes, B G Almeida, F Figueiras, P Mirzadeh Vaghefi, V S Amaral, A Almeida, J Pérez de la Cruz, and J Agostinho Moreira. Unravelling the effect of $srtio_3$ antiferrodistortive phase transition on the magnetic properties of $la_{0.7}sr_{0.3}mno_3$ thin films. *Journal of Physics D: Applied Physics*, 47(43):435002, 2014.

[116] T. Tybell, C. H. Ahn, and J. M. Triscone. Ferroelectricity in thin perovskite films. *Applied Physics Letters*, 75(6):856–858, 1999.

[117] A. Gruverman and A. Kholkin. Nanoscale ferroelectrics: processing, characterization and future trends. *Reports on Progress in Physics*, 69(8):2443–2474, 2006.

[118] A. L. Kholkin, V. V. Shvartsman, A. Y. Emelyanov, R. Poyato, M. L. Calzada, and L. Pardo. Stress-induced suppression of piezoelectric properties in $pbtio_3$: La thin films via scanning force microscopy. *Applied Physics Letters*, 82(13):2127–2129, 2003.

[119] R. Garcia and R. Perez. Dynamic atomic force microscopy methods. *Surface Science Reports*, 47(6-8):197–301, 2002.

[120] J. Seidel, L. W. Martin, Q. He, Q. Zhan, Y. H. Chu, A. Rother, M. E. Hawkridge, P. Maksymovych, P. Yu, M. Gajek, N. Balke, S. V. Kalinin, S. Gemming, F. Wang, G. Catalan, J. F. Scott, N. A. Spaldin, J. Orenstein, and R. Ramesh. Conduction at domain walls in oxide multiferroics. *Nature Materials*, 8(3):229–234, 2009.

[121] Armandina Maria Lima Lopes. *Estudos de distorções da rede e correlações electrónicas em manganites utilizando sondas lociais.* Thesis, 2006.

[122] Isabel Alexandra Domingues Tarroso Gomes. *Manganite thin films deposited on piezoelectric substrates.* Thesis, 2013.

[123] I. W. Boyd. Thin film growth by pulsed laser deposition. *Ceramics International*, 22(5):429–434, 1996.

[124] R. K. Singh and J. Narayan. Pulsed-laser evaporation technique for deposition of thin-films - physics and theoretical-model. *Physical Review B*, 41(13):8843–8859, 1990.

[125] J. Schou. Physical aspects of the pulsed laser deposition technique: The stoichiometric transfer of material from target to film. *Applied Surface Science*, 255(10):5191–5198, 2009.

[126] G. Lawes and G. Srinivasan. Introduction to magnetoelectric coupling and multiferroic films. *Journal of Physics D-Applied Physics*, 44(24):243001, 2011.

[127] D. H. Wang, L. Yan, C. K. Ong, and Y. W. Du. Bifeo$_3$ film deposited on si substrate buffered with la$_{0.7}$sr$_{0.3}$mno$_3$ electrode. *Applied Physics Letters*, 89(18):182905, 2006.

[128] J. J. Yang, Y. G. Zhao, H. F. Tian, L. B. Luo, H. Y. Zhang, Y. J. He, and H. S. Luo. Electric field manipulation of magnetization at room temperature in multiferroic cofe$_2$o$_4$/pb(mg$_{1/3}$nb$_{2/3}$)$_{(0.7)}$ti$_{0.3}$o$_3$ heterostructures. *Applied Physics Letters*, 94(21):212504, 2009.

[129] K. M. Satyalakshmi, R. M. Mallya, K. V. Ramanathan, X. D. Wu, B. Brainard, D. C. Gautier, N. Y. Vasanthacharya, and M. S. Hegde. Epitaxial metallic lanio$_3$ thin-films grown by pulsed laser deposition. *Applied Physics Letters*, 62(11):1233–1235, 1993.

[130] X. D. Wu, S. R. Foltyn, R. C. Dye, Y. Coulter, and R. E. Muenchausen. Properties of epitaxial srruo3 thin-films. *Applied Physics Letters*, 62(19):2434–2436, 1993.

[131] H. S. Choi, J. S. Ahn, J. H. Jung, T. W. Noh, and D. H. Kim. Mid-infrared properties of a vo2 film near the metal-insulator transition. *Physical Review B*, 54(7):4621–4628, 1996.

[132] K. Ueda, H. Tabata, and T. Kawai. Magnetic and electric properties of transition-metal-doped zno films. *Applied Physics Letters*, 79(7):988–990, 2001.

[133] Robert Eason. *Pulsed Laser Deposition of Thin Films: Applications-Led Growth of Functional Materials*. John Wiley & Sons, 2007.

[134] J. A. Venables, G. D. T. Spiller, and M. Hanbucken. Nucleation and growth of thin-films. *Reports on Progress in Physics*, 47(4):399–459, 1984.

[135] J. C. S. Kools, T. S. Baller, S. T. Dezwart, and J. Dieleman. Gas-flow dynamics in laser ablation deposition. *Journal of Applied Physics*, 71(9):4547–4556, 1992.

[136] Milton Ohring. *Materials Science of Thin Films*. Academic Press, 2 edition, 2001.

[137] M. N. R. Ashfold, F. Claeyssens, G. M. Fuge, and S. J. Henley. Pulsed laser ablation and deposition of thin films. *Chemical Society Reviews*, 33(1):23–31, 2004.

[138] Richard F. Haglund, John C. Miller, Thomas Lucatorto, and Marc De Graef. *Laser Ablation and Desorption*, volume 30. Academic Press, 1997.

[139] S. Swann. Magnetron sputtering. *Physics in Technology*, 19(2):67–75, 1988.

[140] Ladislaus Marton. *ADV ELECTRONC/ELECTRON PHYSICS V28B APL*. Academic Press, 1969.

[141] G. H. Rue and H. K. Kim. A two-inch dc/rf circular magnetron sputtering gun for a miniature chamber for an in situ experiment. *Review of Scientific Instruments*, 69(4):1616–1621, 1998.

[142] Donald Smith. *Thin-Film Deposition: Principles and Practice*. McGraw Hill Professional, 1995.

[143] Reiner Waser. *Nanoelectronics and Information Technology*. Wiley, 2005.

[144] A. Paoletti and A. Tucciarone. *The Physics of Diamond*. IOS Press, 1997.

[145] R Egerton. *Physical Principles of Electron Microscopy: An Introduction to TEM, SEM, and AEM*. Springer Science & Business Media, 2006.

[146] R. Guiebretière. *X-Ray Diffraction by Polycrystalline Materials*. Wiley, 2010.

[147] N. P. Barradas, C. Jeynes, R. P. Webb, U. Kreissig, and R. Grotzschel. Unambiguous automatic evaluation of multiple ion beam analysis data with simulated annealing. *Nuclear Instruments & Methods in Physics Research Section B-Beam Interactions with Materials and Atoms*, 149(1-2):233–237, 1999.

[148] Eugene A. Eliseev, Sergei V. Kalinin, Stephen Jesse, Svetlana L. Bravina, and Anna N. Morozovska. Electromechanical detection in scanning probe microscopy: Tip models and materials contrast. *Journal of Applied Physics*, 102(1):014109, 2007.

[149] S. Jesse, A. P. Baddorf, and S. V. Kalinin. Dynamic behaviour in piezoresponse force microscopy. *Nanotechnology*, 17(6):1615–1628, 2006.

[150] C. R. Brundle, Charles A. Evans, and Shaun Wilson. *Encyclopedia of Materials Characterization: Surfaces, Interfaces, Thin Films*. Gulf Professional Publishing, illustrated edition, 1992.

[151] A. P. Schuetze, W. Lewis, C. Brown, and W. J. Geerts. A laboratory on the four-point probe technique. *American Journal of Physics*, 72(2):149–153, 2004.

[152] F. M. Smits. Measurement of sheet resistivities with the 4-point probe. *Bell System Technical Journal*, 37(3):711–718, 1958.

[153] P de Sousa. *Manganite based magnetoresistive ceramics* $La_{1-x}Sr_xMnO_3$. Thesis, 2011.

[154] S. J. Hibble, S. P. Cooper, A. C. Hannon, I. D. Fawcett, and M. Greenblatt. Local distortions in the colossal magnetoresistive manganates $la_{0.70}ca_{0.30}mno_3$, $la_{0.80}ca_{0.20}mno_3$ and $la_{0.70}sr_{0.30}mno_3$ revealed by total neutron diffraction. *Journal of Physics-Condensed Matter*, 11(47):9221–9238, 1999.

[155] L. Ranno, A. Llobet, R. Tiron, and E. Favre-Nicolin. Strain-induced magnetic anisotropy in epitaxial manganite films. *Applied Surface Science*, 188(1-2):170–175, 2002.

[156] D. Pesquera, V. Skumryev, F. Sanchez, G. Herranz, and J. Fontcuberta. Magnetoelastic coupling in $la_{2/3}sr_{1/3}mno_{33}$. *Physical Review B*, 84(18):184412, 2011.

[157] M. Cesaria, A. P. Caricato, G. Maruccio, and M. Martino. *LSMO - growing opportunities by PLD and applications in spintronics*, volume 292 of *Journal of Physics Conference Series*, page 012003. 2011.

[158] Maurizio Martino, Maura Cesaria, Anna Paola Caricato, Giuseppe Maruccio, Adriano Cola, and Isabella Farella. $La_{0.7}sr_{0.3}mno_3$ thin films deposited by pulsed laser ablation for spintronic applications. *Physica Status Solidi a-Applications and Materials Science*, 208(8):1817–1820, 2011.

[159] S. Farokhipoor, C. Magen, S. Venkatesan, J. Iniguez, C. J. M. Daumont, D. Rubi, E. Snoeck, M. Mostovoy, C. de Graaf, A. Mueller, M. Doeblinger, C. Scheu, and B. Noheda. Artificial chemical and magnetic structure at the domain walls of an epitaxial oxide. *Nature*, 515(7527):379–+, 2014.

[160] A. R. C. Westwood. Surface sensitive properties. *Lubrication Engineering*, 32(8):438–438, 1976.

[161] J. A. Thornton. Influence of apparatus geometry and deposition conditions on structure and topography of thick sputtered coatings. *Journal of Vacuum Science & Technology*, 11(4):666–670, 1974.

[162] Jin Fang and Yimin Cui. Magnetic and transport properties of samples of the approximate composition $la_{0.9}ba_{0.1}mno_3$ with different cation deficiencies. *Journal of Alloys and Compounds*, 432(1-2):15–17, 2007.

[163] Sérgio Manuel de Sousa Pereira. *Estudo de propriedades estruturais e ópticas de multicamadas epitaxiais emissoras de luz baseadas em InGaN/GaN*. Thesis, 2005.

[164] T. Metzger, R. Hopler, E. Born, O. Ambacher, M. Stutzmann, R. Stommer, M. Schuster, H. Gobel, S. Christiansen, M. Albrecht, and H. P. Strunk. Defect structure of epitaxial gan films determined by transmission electron microscopy and triple-axis x-ray diffractometry. *Philosophical Magazine a-Physics of Condensed Matter Structure Defects and Mechanical Properties*, 77(4):1013–1025, 1998.

[165] N. P. Barradas and C. Jeynes. Advanced physics and algorithms in the iba datafurnace. *Nuclear Instruments & Methods in Physics Research Section B-Beam Interactions with Materials and Atoms*, 266(8):1875–1879, 2008.

[166] James F. Ziegler, M. D. Ziegler, and J. P. Biersack. Srim - the stopping and range of ions in matter (2010). *Nuclear Instruments & Methods in Physics Research Section B-Beam Interactions with Materials and Atoms*, 268(11-12):1818–1823, 2010.

[167] P. Orgiani, C. Adamo, C. Barone, A. Galdi, S. Pagano, A. Yu Petrov, O. Quaranta, C. Aruta, R. Ciancio, M. Polichetti, D. Zola, and L. Maritato. Epitaxial growth of $la_{0.7}ba_{0.3}mno_3$ thin films on mgo substrates: Structural, magnetic, and transport properties. *Journal of Applied Physics*, 103(9):093902, 2008.

[168] M. Kanai, H. Tanaka, and T. Kawai. Origin of metal-insulator transition temperature enhancement in $la_{0.8}ba_{0.2}mno_3$ thin films as determined by structural analysis. *Physical Review B*, 70(12):125109, 2004.

[169] M. Mayr, A. Moreo, J. A. Verges, J. Arispe, A. Feiguin, and E. Dagotto. Resistivity of mixed-phase manganites. *Physical Review Letters*, 86(1):135–138, 2001.

[170] J. A. Turcaud, A. M. Pereira, K. G. Sandeman, J. S. Amaral, K. Morrison, A. Berenov, A. Daoud-Aladine, and L. F. Cohen. Spontaneous magnetization above t-c in polycrystalline $la_{0.7}ca_{0.3}mno_3$ and $la_{0.7}ba_{0.3}mno_3$. *Physical Review B*, 90(2):024410(1)–024410(7), 2014.

[171] S. Das, J. S. Amaral, K. De, M. Willinger, J. N. Goncalves, A. Roy, P. Dhak, S. Giri, S. Majumder, C. J. R. Silva, M. J. M. Gomes, P. K. Mahapatra, and V. S.

Amaral. Strain induced enhanced ferromagnetic behavior in inhomogeneous low doped $la_{0.95}sr_{0.05}mno_{3+delta}$. *Applied Physics Letters*, 102(11):112408, 2013.

[172] R. C. Budhani, C. Roy, L. H. Lewis, Q. A. Li, and A. R. Moodenbaugh. Magnetic ordering and granularity effects in $la_{1-x}ba_xmno_3$. *Journal of Applied Physics*, 87(5):2490–2496, 2000.

[173] N. J. O. Silva and V. S. Amaral. Comment on "magnetization reversal in europium sulfide nanocrystals" appl. phys. lett. 89, 222501 (2006). *Applied Physics Letters*, 92(2), 2008.

[174] F. J. Giessibl. Advances in atomic force microscopy. *Reviews of Modern Physics*, 75(3):949–983, 2003.

[175] T. R. Albrecht, P. Grutter, D. Horne, and D. Rugar. Frequancy-modulation detection using high-q cantilevers for enhanced force microscope sensitivity. *Journal of Applied Physics*, 69(2):668–673, 1991.

[176] W. Prellier, P. Lecoeur, and B. Mercey. Colossal-magnetoresistive manganite thin films. *Journal of Physics-Condensed Matter*, 13(48):R915–R944, 2001.

[177] F. Stobiecki and T. Stobiecki. The effect of crystallinity on temperature dependences of magnetization, resistivity and anomalous hall constant in thin amorphous $fe_{1-X}b_x$ films. *Journal of Magnetism and Magnetic Materials*, 40(1-2):111–116, 1983.

[178] M. Li, G. C. Wang, and H. G. Min. Effect of surface roughness on magnetic properties of co films on plasma-etched si(100) substrates. *Journal of Applied Physics*, 83(10):5313–5320, 1998.

[179] J. Swerts, K. Temst, M. J. Van Bael, C. Van Haesendonck, and Y. Bruynseraede. Magnetic domain wall trapping by in-plane surface roughness modulation. *Applied Physics Letters*, 82(8):1239–1241, 2003.

[180] Q. Jiang, H. N. Yang, and G. C. Wang. Effect of interface roughness on hysteresis loops of ultrathin co films from 2 to 30 ml on cu(001) surfaces. *Surface Science*, 373(2-3):181–194, 1997.

[181] M. Pardavihorvath. Coercivity of epitaxial magnetic garnet crystals. *Ieee Transactions on Magnetics*, 21(5):1694–1699, 1985.

[182] H. Lu, C. W. Bark, D. E. de los Ojos, J. Alcala, C. B. Eom, G. Catalan, and A. Gruverman. Mechanical writing of ferroelectric polarization. *Science*, 336(6077):59–61, 2012.

[183] Lija K. Joy, Senoy Thomas, and M. R. Anantharaman. A study on the magnetic properties of gd-sr based low bandwidth manganites in their bulk and thin film forms and evidence for magnetization reversal in bulk $gd_{0.7}sr_{0.3}mno_3$. *Journal of Magnetism and Magnetic Materials*, 398:174–182, 2016.

[184] L. S. Uspenskaya, T. Nurgaliev, and S. Miteva. Magnetization reversal of thin $la_{0.7}sr_{0.3}mno_3$ manganite films grown on laalo3. *Journal of Physics D-Applied Physics*, 42(18), 2009.

[185] Chengliang Lu, Shuai Dong, Zhengcai Xia, Hui Luo, Zhibo Yan, Haowen Wang, Zhaoming Tian, Songliu Yuan, Tao Wu, and Junming Liu. Polarization enhancement and ferroelectric switching enabled by interacting magnetic structures in $dymno_3$ thin films. *Scientific Reports*, 3:1–7, 2013.

[186] A. Gruverman, O. Auciello, and H. Tokumoto. Imaging and control of domain structures in ferroelectric thin films via scanning force microscopy. *Annual Review of Materials Science*, 28:101–123, 1998.

[187] T. Hidaka, T. Maruyama, I. Sakai, M. Saitoh, L. A. Wills, R. Hiskes, S. A. Dicarolis, J. Amano, and C. M. Foster. Characteristics of pzt thin films as ultra-high density recording media. *Integrated Ferroelectrics*, 17(1-4):319–327, 1997.

[188] C. Harnagea, A. Pignolet, M. Alexe, K. M. Satyalakshmi, D. Hesse, and U. Gosele. Nanoscale switching and domain structure of ferroelectric $babi_4ti_4o{-}15$ thin films. *Japanese Journal of Applied Physics Part 2-Letters*, 38(11A):L1255–L1257, 1999.

[189] K. J. Choi, M. Biegalski, Y. L. Li, A. Sharan, J. Schubert, R. Uecker, P. Reiche, Y. B. Chen, X. Q. Pan, V. Gopalan, L. Q. Chen, D. G. Schlom, and C. B. Eom. Enhancement of ferroelectricity in strained $batio_3$ thin films. *Science*, 306(5698):1005–1009, 2004.

[190] G. Catalan, A. Janssens, G. Rispens, S. Csiszar, O. Seeck, G. Rijnders, D. H. A. Blank, and B. Noheda. Polar domains in lead titanate films under tensile strain. *Physical Review Letters*, 96(12), 2006.

[191] G. Zavala, J. H. Fendler, and S. TrolierMcKinstry. Characterization of ferroelectric lead zirconate titanate films by scanning force microscopy. *Journal of Applied Physics*, 81(11):7480–7491, 1997.

[192] Y. Gaillard, A. Hurtado Macias, J. Munoz-Saldana, M. Anglada, and G. Trapaga. Nanoindentation of batio$_3$: dislocation nucleation and mechanical twinning. *Journal of Physics D-Applied Physics*, 42(8):085502, 2009.

[193] Brian J. Rodriguez, Stephen Jesse, Sergei V. Kalinin, Jihee Kim, Stephen Ducharme, and V. M. Fridkin. Nanoscale polarization manipulation and imaging of ferroelectric langmuir-blodgett polymer films. *Applied Physics Letters*, 90(12), 2007.

[194] Yongbo Yuan, Pankaj Sharma, Zhengguo Xiao, Shashi Poddar, Alexei Gruverman, Stephen Ducharme, and Jinsong Huang. Understanding the effect of ferroelectric polarization on power conversion efficiency of organic photovoltaic devices. *Energy & Environmental Science*, 5(9):8558–8563, 2012.

[195] N. A. Pertsev, A. Petraru, H. Kohlstedt, R. Waser, I. K. Bdikin, D. Kiselev, and A. L. Kholkin. Dynamics of ferroelectric nanodomains in batio$_3$ epitaxial thin films via piezoresponse force microscopy. *Nanotechnology*, 19(37):375703, 2008.

[196] J. Daillant and M. Alba. High-resolution x-ray scattering measurements: I. surfaces. *Reports on Progress in Physics*, 63(10):1725–1777, 2000.

[197] Alain Gibaud. *X-Ray and Neutron Reflectivity: Principles and Applications*. Lecture Notes in Physics Monographs. Springer-Verlag Berlin Heidelberg, 1999.

[198] Ullrich Pietsch, Vaclav Holy, and Tilo Baumbach. *High-Resolution X-Ray Scattering: From Thin Films to Lateral Nanostructures*. Advanced Texts in Physics. Springer, 2004.

[199] M. Born and E. Wolf. *Principles of Optics: Electromagnetic Theory of Propagation, Interference and Diffraction of Light*. Cambridge University Press, 1999.

[200] X. L. Zhou and S. H. Chen. Theoretical foundation of x-ray and neutron reflectometry. *Physics Reports-Review Section of Physics Letters*, 257(4-5):223–348, 1995.